学位論文

Micro-architectures of Quantum Information Processor

（量子情報処理装置のマイクロアーキテクチャ）

by

Hiroto Mukai
向井　寛人

Submitted to the Department of Physics
in partial fulfillment of the requirements for the degree of
DOCTOR OF SCIENCE
at the
TOKYO UNIVERSITY OF SCIENC
March 2021

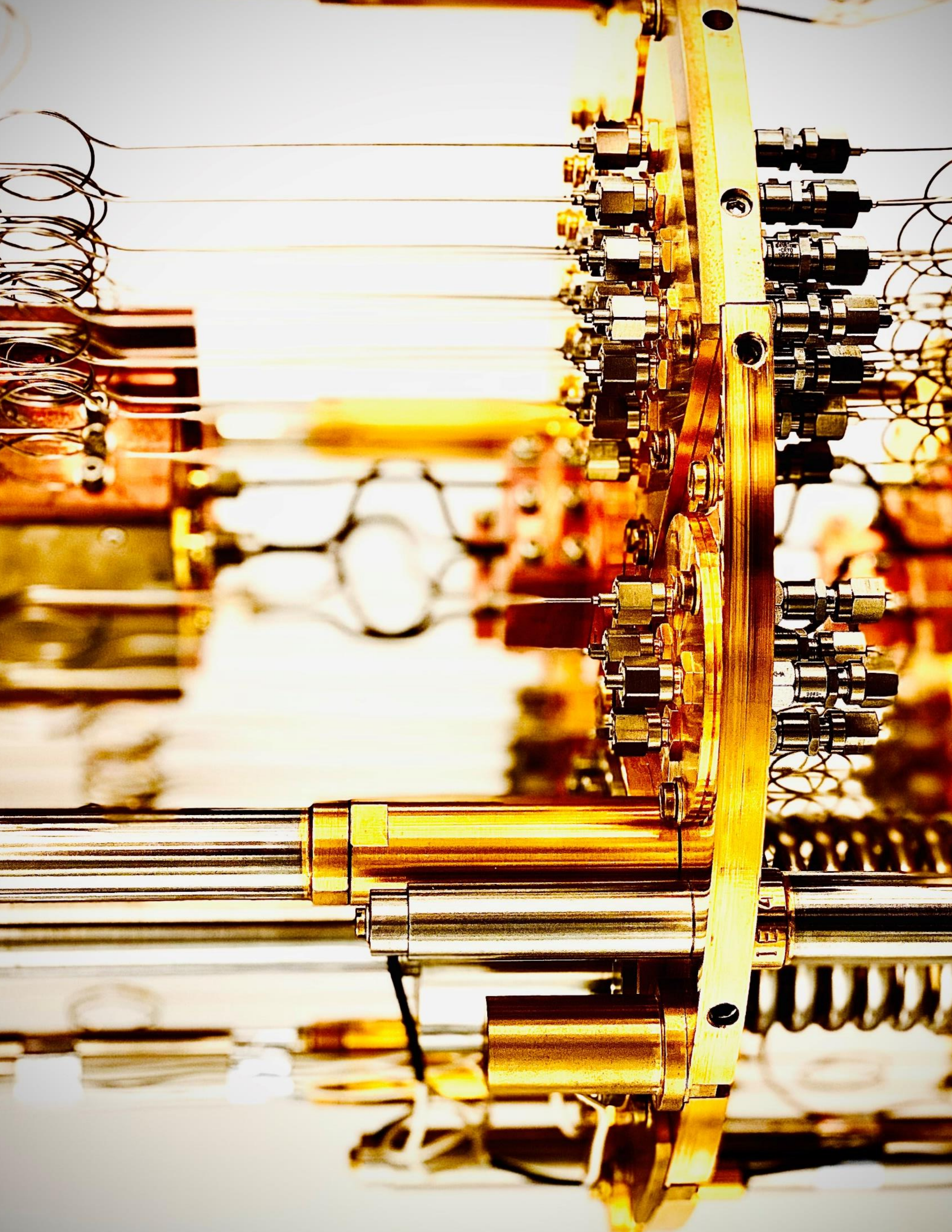

Micro-architectures of Quantum Information Processor

by

Hiroto Mukai

Submitted to the Department of Physics
in partial fulfillment of the requirements for the degree of

DOCTOR OF SCIENCE

at the

TOKYO UNIVERSITY OF SCIENCE

March 2021

Author . . . .
Department of Physics
February 17, 2021

Certified by . . . .
Jaw-Shen Tsai
Professor
Thesis Supervisor

Revised at February 1, 2021.

Micro-architectures of Quantum Information Processor

by

Hiroto Mukai

Submitted to the Department of Physics
on February 17, 2021, in partial fulfillment of the
requirements for the degree of
DOCTOR OF SCIENCE

Abstract

Among the many potential hardware platforms, superconducting quantum circuits have become the leading contender for constructing a scalable quantum computing system. Not only have we seen significant advances in recent years in reliable fabrication and control technology, but the quality of the qubits themselves have increased by many orders of magnitude. Almost all current architecture designs necessitate a two-dimensional arrangement of superconducting qubits with nearest-neighbor interactions, that is compatible with powerful quantum error-correction using the surface code. A major hurdle for scalability in superconducting systems is the so-called wiring problem, where internal qubits of a chipset become inaccessible for external control/readout lines.

The current consensus within the superconducting quantum circuit field is that the control wiring for such chips should be fabricated in the third dimension, utilizing several techniques to place bias, readout and control wires orthogonal to the plane of the chip itself. This technique has shown much promises, but it is also very unclear and still a significant engineering challenge if these intricate, three-dimensional wiring and packaging technology control fabrication techniques are compatible with maintaining high fidelity operations and increasing chip size. The largest concern is the ability to reduce cross-talk and control line contamination of neighbouring qubits to the degree necessary to achieve fidelities of 99% or higher across the chip. In other words, these approaches resort to intricate, three-dimensional wiring and packaging technology, which is a significant engineering challenge to realize while maintaining qubit fidelity.

In this thesis, we present a revolutionary new large-scale micro-architecture design that completely side-steps this issue. We propose a pseudo-2D arrangement architecture of superconducting qubits. This bi-linear array allows each physical qubit to be biased, measured and controlled using wiring that remains in-plane with the chip (eliminating completely the need for 3D control line fabrication and packaging).

Utilizing the micro-architecture bi-linear arrangement of superconducting qubits, we also show how a large Raussendorf cluster can be produced, which realizes the cluster state model of surface code quantum error correction while maintaining planar access of control lines to each individual qubit. This architecture realizes the cluster state model of surface code quantum error correction, without the need for 3-dimensional control wiring. Moreover, we propose that bi-linear transformed arrangement with additional qubits can be generate a 3D-cluster-state on completely planer circuit with some overhead.

A novel architecture for superconducting circuits is also proposed to improve the efficiency of a quantum annealing system. To increase the capability of a circuit, it is desirable for a qubit to be coupled not only with adjacent qubits but also with other qubits located far away. We introduce a circuit that uses a lumped element resonator coupled each with one qubit. The resonator-qubit pairs are coupled by rf-superconducting quantum interference device (SQUID) based couplers. These pairs make a large quantum system for quantum annealer. This system could prepare the problem Hamiltonian and tune the parameters for quantum annealing procedure.

Thesis Supervisor: Jaw-Shen Tsai
Title: Professor

Micro-architectures of Quantum Information Processor
量子情報処理装置のマイクロアーキテクチャ

向井　寛人　著

要旨

数あるハードウェアプラットフォームの中でも、超伝導量子回路は、スケーラブルな量子コンピューティングシステムを構築するための有力な候補となっています。 近年、信頼性の高い製造技術や制御技術が大幅に進歩しただけでなく、量子ビット自体の品質も桁違いに向上しています。 現在のほとんどのアーキテクチャ設計では、最近接相互作用を持つ超伝導量子ビットの 2 次元配列が必要とされており、表面コードを用いた強力な量子エラー訂正との互換性があります。超伝導システムにおけるスケーラビリティの大きなハードルは、チップセットの内部量子ビットが外部の制御/読み出し線にアクセスできなくなる、いわゆる配線の問題です。

超伝導量子回路分野における現在の見解は、このようなチップの配線（バイアス、読み出し、および制御配線）をチップ自体の平面に直交するように配置するいくつかの技術を利用して、3 次元で製造されるべきであるということです。 この技術は多くの期待を示してきましたが、これらの複雑な三次元配線およびパッケージング技術の制御製造技術が、高忠実度動作の維持およびチップサイズの増大と互換性があるかどうかは、非常に不明確であり、依然として重要な工学上の課題であるとされています。最大の懸念事項は、チップ全体で 99%以上の忠実度を達成するために必要な程度に、クロストークを低減し、隣接する量子ビットへの混線を制御する能力です。言い換えれば、これらのアプローチは、複雑な三次元配線やパッケージング技術に頼っており、量子ビットの忠実度を維持しながら実現することは、大きな課題となっています。

本論文では、この問題を完全に回避する画期的な新しい大規模マイクロアーキテクチャを提案します。本論文では、超伝導量子ビットの擬似 2 次元配列アーキテクチャを提案します。このバイリニアな配列により、チップと面内に残る配線を用いて、各物理量子ビットのバイアス、測定、制御を行うことが可能となります。(3 次元制御ラインの製作やパッケージングの必要性を完全に排除することができます)。

超伝導量子ビットのバイリニア配列を利用するマイクロアーキテクチャによって、個々の量子ビットへの制御線の平面的なアクセスを維持しながら、クラスター状態モデルによる表面符号量子エラー訂正を実現する大規模なラウッセンドルフクラスターを生成する方法も示しています。 このアーキテクチャは、3次元制御配線を必要とせず、クラスター状態モデルによる表面符号量子誤り訂正を実現できます。さらに、量子ビットを追加したバイリニア変換配置を行うことでも完全平面回路上で 3 次元クラスター状態を生成することが可能であることを提案しています。

また、量子アニーリング装置の効率を向上させるために、超伝導回路のための新しいアーキテク

チャを提案する。量子アニーリングに対する回路の性能を向上させるためには、隣接する量子ビットだけでなく、離れた位置にある他の量子ビットとも結合することが望ましいとされています。本研究では、1つのクビットに1つずつ結合された集積素子共振器を用いた回路についても提案しています。RF 型超伝導量子干渉素子(SQUID)をベースとした結合器によって結合された、共振子と量子ビットの対を集積することで、量子アニーラーのための大規模な量子システムを構築できます。この系において、目的関数のハミルトニアンを準備し、量子アニーリングのためのパラメータを調整することができることを示しています。

Acknowledgments

This thesis work would not have been possible without the help of many who have advise me during my five years at Tokyo university of science. First of all, I would like to thank Professor Jaw-Shen Tsai for opening me the opportunity to work in his group, and for his guidance, and patience with my poorly and slowly writing manuscripts, throughout my graduating time science I was as undergraduate student.

I would like express my thanks to all members of Tsai Laboratory, especially Akiyoshi Tomonaga who gives me many help and discussion for everything, and Dr. Yu Zhou who gives huge suggestion and build up experimental system together.

As for micro-architecture of pseudo-2D surface code and cluster state, we thank Prof. F. Nori, Prof. O. V. Astafiev, Dr. D. Zhang, Dr. A. F. Kockum and Dr. S. J. Devitt for discussions. We also thank Dr. M. Hidaka for providing wafers with a Nb film. As for micro-architecture of quantum annealing, we thank Dr. Z. H. Peng, Dr. R. Wang, Dr. F. Yoshihara, Dr. T. Yamamoto, Dr. M. Maezawa, Dr. S. Watabe, Prof. T. Nikuni, Dr. K. Imafuku, Dr. S. Kawabata, Dr. Y. Matsuzaki, Dr. Y. Seki, for their thoughtful comments on this research.

This work is based on results obtained from a project commissioned by the New Energy and Industrial Technology Development Organization (NEDO). Support from CREST, JST (Grant No. JPMJCR1676), and the ImPACT Program of Council for Science, Technology and Innovation (Cabinet Office, Government of Japan) is also appreciated.

Finally, I wish to deeply thankful my parents and family for their enormous and continuous support and understanding for a long time.

Contents

Introduction

Quantum information processing has the ability to potentially outperform previous classical von Neumann-type computers through computation based on the principles of quantum mechanics. Quantum computers are increasingly attracting the attention of scientists in fields such as physics and chemistry, as well as industrialists in the pharmaceutical, aerospace, and automotive industries. Globally, the laboratories of companies like Google and IBM are devoting vast resources to improve quantum computers. Since quantum computers use the fundamentals of quantum mechanics and have ability to process large amounts of information potentially much faster than classical computers, once error-correcting and fault-tolerant quantum computing will have been realized, scientific and technological advances are expected to occur on an unprecedented scale. However, tremendous challenges remain to be overcome in order to realize the quantum computer that will support the next generation of society and make a significant contribution to the development of human history.

Superconducting quantum circuits have long been expected to be one of the candidates for quantum computer devices owing to their extremely high integration potential and design freedom. Superconducting quantum circuits can be fabricated on a substrate, and quantum systems can be artificially fabricated while granting quantum mechanical degrees of freedom by devising the circuit structure. The quantum systems on the circuit are precisely controlled using microwave technology, which has been developed in fields such as information and communications. In addition, the fabrication process can use semiconductor fabrication techniques such as electron beam lithography [80, 221, 29, 238], metal film deposition [118, 176, 226], [215, 179, 56] and cleaning [134, 166, 192], which have been highly developed in the past.

Initially, coherence times of less than nanoseconds in 1999 were a concern for superconducting devices [175], but they have now reached milliseconds [187, 42, 192, 235]. In addition, in recent years, research groups at large companies such as Google, IBM, and Intel have reported the fabrication of tens of qubit circuits one after another. The "quantum supremacy" of quantum computers over classical computers [198, 1] has been demonstrated by Google team [177, 4]. What will be demonstrable at this stage in the near future, however, is the supremacy of quantum computers for a very limited number of small-scale problems [24, 16, 66, 67]. There is still a great deal of work to be done if quantum computers are to solve societally useful problems as fast as the public expects.

The heart of quantum computer research is the attempt to protect the quantum state from the environment. Although coherence times have increased significantly in the last 20 years, they are not yet at the stage where they can be put to practical use. In addition, quantum error correction is necessary to perform quantum computation that can handle many problems. The computational accuracy of a quantum computer depends on the product of the success probability of each operation, such as gate manipulation and readout of qubit states. Therefore, in the absence of error correction, the computation accuracy decreases exponentially by a number of gate operations (a depth of algorithm). In addition, since the operation of a quantum computer is analog, the required resolution is fine, and the error threshold for each operation requires an error rate of less than 1%, even for the most promising candidate, surface code error correction [74, 114, 76, 110, 156]. Therefore, research groups have so far worked on improving the accuracy of readout [229, 206, 82, 168, 163, 147, 117, 126, 14, 105, 124, 158, 122, 141, 36, 84, 49, 190] and gate operations [22, 100, 135, 213, 244, 242, 162, 152, 39] as well as the coherence time of the qubits, and have achieved values below this threshold.

However, as integration progresses, errors increase due to increased fabrication processes and the effects of increased interference and noise with increased interconnect complexity. Despite the fact that a million to 100 million qubits are needed, currently the 53-qubit chip by Google's group is the largest integrated circuit that has been below the threshold, where 53 qubits have work well in 54 qubits on the chip, one qubit have been failed. Therefore, groups aiming to realize large scale quantum computers are looking for new circuit designs to solve this problem.

In this thesis, we will explore how to construct novel quantum processing circuits based on the demands of aspects of the actual implementation of such superconducting quantum circuits, as well as the demands of the theoretical aspects of quantum information processing. The thesis is separated into two part. One is **Part** $|0\rangle$ giving the review for the superconducting quantum computing, which composes the Chapter1 to 4. The other is **Part** $|1\rangle$ giving the main result of the micro-architecture of quantum information processors, which composes the Chapter 5 to 8.

Chapter 1 gives a brief summary of the fundamentals of quantum mechanics and the specification of qubits, which are essential for understanding the dynamics of superconducting quantum circuits and figuring out quantum information processing.

Chapter 2 summarizes the most basic aspects of superconducting quantum circuits. This chapter covers superconductivity and microwave engineering in the context of quantum mechanics. Then the superconducting quantum circuits that combine them are described.

Chapter 3 summarizes the basics of quantum information processing theory. In particular, quantum gate operations and error correction are described, which are necessary to realize a universal quantum computer. Quantum annealing is introduced, which is different from the universal type. Although these two schemes are completely independent concepts, the same techniques can be used to implement each of them in the superconducting quantum circuits that this thesis aims at.

Chapter 4 describes the configuration of an experimental system for cryogenic and ultra-low noise microwave operations and measurements using a dilution refrigerator, which is required for experiments of superconducting quantum circuits. Simple measurement results for qubits in the system are presented. The evaluation method and results of the microwave resonator are also expressed, which is an important element in superconducting quantum circuits in addition to qubits.

Chapter 5 discusses the micro-architecture of quantum information processing, the main topic of this thesis, in three ways:

Chapter 6 propose and analyse a micro-architecture for the surface code, which is the most common quantum error correction and planar arrangement of qubits in the realization of quantum computers, and the implementation of qubits in superconducting quantum circuits and physical systems alongside them.

Chapter 7 gives proposal and instruction of the one-way-quantum-computation using clustered states, which are known to be equivalent to surface codes, and how their micro-architecture can be organized and operated in superconducting quantum circuits.

Chapter 8 micro-architectures of quantum annealing machines are proposed with a much larger number of connections compared to commercially available machines. This system has the potential to be developed further, not only as quantum annealing but also as an fully coupled gated quantum computer.

Finally, a comparison of these micro-architectures are made and future improvements in micro-architecture are discussed.

Part $|0\rangle$

Background for Superconducting Quantum Information Processor

Chapter 1

Overview of Quantum Physics

1.1 Fundamental Quantum Theory

In this chapter, most fundamental and general theory of quantum physics are briefly introduced as starting point to derive superconducting quantum circuit (Chapter 2) and quantum information (Chapter 3). Quantum mechanics has been described mathematically in several ways, starting with the most famous Schrödinger equation using the wave function and Heisenberg matrix mechanics using linear algebra, or interaction picture and density operators (master equations) describing the dissipative dynamics with the environment. All of these are essentially equivalent, but need to be used appropriately for the phenomenon or physical quantity of interest. This quantum mechanics governs microscopic and even macroscopic physical systems, which have been tested by experiments, and countless tools have been developed to apply quantum mechanics for superconducting quantum circuit and quantum information.

1.1.1 Quantum state and observable

In quantum mechanics, to describe system and dynamics, Hilbert space and sates are defined. We use the braket notation for the quantum state, which has been establishing and correcting quantum theory and mathematical notations. Then, operator and projective measurement are introduced. Moreover, we briefly introduce quantization by Hamiltonian.

Quantum state vector

For arbitrary quantum state, its state vector $|\psi\rangle$ can be decomposed by set of basis $\{|\phi_k\rangle : \langle\phi_k|\phi_l\rangle = \delta_{kl}\}$ on the Hilbert space $\mathbb{H}$,

$$|\psi\rangle = \sum_k c_k |\phi_k\rangle \ , \tag{1.1.1}$$

where c_k is complex and called as probability amplitude. The probability amplitude satisfies $\sum_k |c_k|^2 = 1$.

Quantum observable

For any observable $\mathscr{A}$, an arbitrary compact operator $\hat{\mathcal{A}}$ on the Hilbert space $\mathbb{H}$ are decomposed by using the orthonormal basis as

$$\hat{\mathcal{A}} = \sum_{k,l} \alpha_{kl} |\phi_k\rangle\langle\phi_l| \ , \tag{1.1.2}$$

with the matrix element of kl

$$\alpha_{kl} = \langle\phi_k|\hat{\mathcal{A}}|\phi_l\rangle \ . \tag{1.1.3}$$

Hermitian conjugate $\hat{\mathcal{A}}^\dagger$ is defined as the operator satisfying $\langle\psi|\hat{\mathcal{A}}^\dagger|\phi\rangle = \langle\phi|\hat{\mathcal{A}}|\psi\rangle^*$ for arbitrarily state vectors $|\psi\rangle$ and $|\phi\rangle$. In the matrix representation, Hermitian conjugate corresponds to complex conjugated matrix. The matrix of $\hat{\mathcal{A}}$ has eigenvalues λ_k and eigenvectors $|\lambda_k\rangle$ certainly: $\mathcal{A}|\lambda_k\rangle = \lambda_k |\lambda_k\rangle$. These eigenvectors $\{|\lambda_k\rangle\}$ also satisfies orthonormal condition. In addition, the eigenvectors satisfy completeness $\sum_k |\lambda_k\rangle\langle\lambda_k| = \hat{\mathcal{I}}$, where $\hat{\mathcal{I}}$ is the identity operator on the Hilbert space.

Projective measurement and Born's rule

When one measures an arbitrary observable $\mathscr{A}$, projection operator $\mathcal{P}_k := |\lambda_k\rangle\langle\lambda_k|$ is defined to get amount of parts of probability amplitude of the eigenvalue corresponding the eigenvector $|\lambda_k\rangle$. For instance, an arbitrarily quantum state $|\psi\rangle = \sum_k c_k |\lambda_k\rangle$ is projected by

$$\mathcal{P}_k |\psi\rangle = |\lambda_k\rangle\langle\lambda_k|\,\psi\rangle = c_k |\lambda_k\rangle \ . \tag{1.1.4}$$

An Helmitian operator $\hat{\mathcal{A}}$ of the observable can be spectral decomposed by the projection operator $\hat{P}_k$ into the eigenspace, where projection operator satisfies completeness

$\sum_k \hat{\mathcal{P}}_k = \hat{\mathcal{I}}$:

$$\hat{\mathcal{A}} = \sum_k \lambda_k \hat{\mathcal{P}}_k \tag{1.1.5}$$

Measuring the observable $\mathscr{A}$ with the state vector $|\psi\rangle$, outcome is chosen from one of the eigenvalue of the operator $\hat{\mathcal{A}}$. Then the probability that the outcome α_k is assumed to follow the Born's rule,

$$p(k) = \langle\psi|\hat{\mathcal{P}}_k|\psi\rangle \ . \tag{1.1.6}$$

According to this rule, expectation value of observable $\mathscr{A}$ is calculated as

$$\langle\mathcal{A}\rangle = \sum_k p(k)\lambda_k = \sum_k \langle\psi|\alpha_k\hat{\mathcal{P}}_k|\psi\rangle = \langle\psi|\hat{\mathcal{A}}|\psi\rangle \ , \tag{1.1.7}$$

where $p(k)$ satisfies the normalization condition:

$$\sum_k p(k) = \sum_k \langle\psi|\hat{\mathcal{P}}_k|\psi\rangle = 1 \, . \tag{1.1.8}$$

Product state and entangle state

Let two Hilbert spaces $\mathbb{H}_A$ and $\mathbb{H}_B$ be two partial spaces of a product space $\mathbb{H}_{AB}$ of two quantum systems with orthnormal basis $\{\left|\phi_i^A\right\rangle\}$ and $\{\left|\phi_i^B\right\rangle\}$, respectably. A state on the product space $\mathbb{H}_{AB}$ is expressed as

$$\left|\phi^{AB}\right\rangle = \left|\phi^A\right\rangle \otimes \left|\psi^B\right\rangle \text{ , or } \left|\psi^A\right\rangle \left|\phi^B\right\rangle \tag{1.1.9}$$

When states of A and B are $\left|\psi^A\right\rangle = \sum_i a_i \left|\phi_i^A\right\rangle$ and $\left|\psi^B\right\rangle = \sum_i b_i \left|\phi_i^B\right\rangle$, respectably, product state $\left|\phi^{AB}\right\rangle$ is

$$\left|\phi^{AB}\right\rangle = \sum_{ij} a_i b_j \left|\phi_i^A\right\rangle \left|\phi_j^B\right\rangle \ . \tag{1.1.10}$$

This kind of state is also called separable state since the product state decomposes the system into partial systems. On the other hand, when the state cannot be decomposed as separable state, it is called entangle state, for instance $\sum_i c_i \left|\phi_i^A\right\rangle \left|\phi_i^B\right\rangle$.

Lagrangian and Hamiltonian in classical and quantum physics

To analyze a system, firstly the Lagrangian $\mathcal{L}$ is classically defined as the difference between the kinetic energy $\mathscr{T}$ and potential energy $\mathscr{U}$ of the system with generalised coordinates $\mathbf{q} = (q_i)$ and generalised velocities $\dot{\mathbf{q}} = (\dot{q}_i)$ of the system.

$$\begin{aligned} \mathcal{L} &= \mathcal{L}(\mathbf{q}, \dot{\mathbf{q}}, t) \qquad (1.1.11) \\ &= \mathscr{T}(\mathbf{q}, \dot{\mathbf{q}}, t) - \mathscr{U}(\dot{\mathbf{q}}, t) \qquad (1.1.12) \end{aligned}$$

Introducing the generalized momentum $\mathbf{p} = (p_i)$ conjugate to q_i by,

$$p_i = \frac{\partial \mathcal{L}(\mathbf{q}, \dot{\mathbf{q}}, t)}{\partial \dot{q}_i} \,. \qquad (1.1.13)$$

One can derive the Hamiltonian from the Lagrangian by Legendre transformation,

$$\mathcal{H}(\mathbf{q}, \mathbf{p}, t) = \mathbf{p}\dot{\mathbf{q}} - \mathcal{L}(\mathbf{q}, \dot{\mathbf{q}}, t) \,. \qquad (1.1.14)$$

Canonical equation of motion is given by

$$\begin{aligned} \frac{\mathrm{d}p_i}{\mathrm{d}t} &= -\frac{\partial \mathcal{H}(\mathbf{p}, \mathbf{q})}{\partial q_i} \,, \qquad (1.1.15) \\ \frac{\mathrm{d}q_i}{\mathrm{d}t} &= \frac{\partial \mathcal{H}(\mathbf{p}, \mathbf{q})}{\partial p_i} \,. \qquad (1.1.16) \end{aligned}$$

Using Poisson Bracket $\{f, g\}$ for arbitrarily function $f(q_i, p_i)$ and $g(q_i, p_i)$, a dynamics of physical quantity $\mathcal{A}$ in the canonical space is expressed as

$$\begin{aligned} \frac{\mathrm{d}\mathcal{A}}{\mathrm{d}t} &= \{\mathcal{A}, \mathcal{H}\} \,, \qquad (1.1.17) \\ \{f, g\} &:= \sum_i \left(\frac{\partial f}{\partial q_i}\frac{\partial g}{\partial p_i} - \frac{\partial g}{\partial q_i}\frac{\partial f}{\partial p_i} \right) \qquad (1.1.18) \end{aligned}$$

Then a transition from classical to quantum mechanics requires quantization based on the uncertainty principle, which can be mathematically represented by introducing non-commutative relations as constraints on the Lagrangian and Hamiltonian canonical variables in the commutation relations,

$$\begin{aligned} [\hat{q}_j, \hat{p}_k] &= i\hbar\delta_{jk} \,, \qquad (1.1.19) \\ [\hat{q}_j, \hat{q}_k] = [\hat{p}_j, \hat{p}_k] &= 0 \qquad (1.1.20) \end{aligned}$$

where $\hbar = h/2\pi$ is reduced Planck constant, h is Planck constant and $\hat{\bullet}$ represent quantum operator and variables, however, in trivial cases, $\hat{\bullet}$ notation are ignored.

1.1.2 Schrödinger picture

Schrödinger equation for time-independent Hamiltonian

For a given Hamiltonian $\hat{\mathcal{H}}$ of a isolated system, the dynamics of the quantum state $|\psi(t)\rangle$ is expressed as the time-depending Schrödinger equation,

$$i\hbar\frac{\mathrm{d}}{\mathrm{d}t}|\psi(t)\rangle = \hat{\mathcal{H}}|\psi(t)\rangle \ . \tag{1.1.21}$$

If the Hamiltonian does not depend on time, equation (1.1.21) can be formally solved as,

$$|\psi(t)\rangle = \exp\left(-i\frac{\hat{\mathcal{H}}}{\hbar}t\right)|\psi(0)\rangle \tag{1.1.22}$$

$$= \hat{\mathcal{U}}(t)|\psi(0)\rangle \tag{1.1.23}$$

where the time evolution operator $\hat{\mathcal{U}}(t) := \exp\left(-i\hat{\mathcal{H}}t/\hbar\right)$ is introduced. The Hermitian operator is defined as

$$\hat{\mathcal{A}} \subset \hat{\mathcal{A}}^{\dagger} \tag{1.1.24}$$

i.e.,

$$\mathrm{dom}\hat{\mathcal{A}} \subset \mathrm{dom}\hat{\mathcal{A}}^{\dagger} \text{ , and } \forall x \in \mathrm{dom}\hat{\mathcal{A}} \text{, } \hat{\mathcal{A}}x = \hat{\mathcal{A}}^{\dagger}x \, , \tag{1.1.25}$$

where self-adjoin operator is also defined as $\mathcal{A} = \mathcal{A}^{\dagger}$. Since the Hamiltonian $\hat{\mathcal{H}}$ is the Hermitian operator, the time evolution operator is the unitary operator, i.e., $\hat{\mathcal{U}}(t)\hat{\mathcal{U}}^{\dagger}(t) = \exp\left(-i\hat{\mathcal{H}}t/\hbar\right)\exp\left(i\hat{\mathcal{H}}t/\hbar\right) = \hat{\mathcal{I}}$.

Schrödinger equation for time-dependent Hamiltonian

When the Hamiltonian depends on time $\mathcal{H}(t)$, equation (1.1.21) is expressed as,

$$i\hbar\frac{\mathrm{d}}{\mathrm{d}t}|\psi(t)\rangle = \mathcal{H}(t)|\psi(t)\rangle \ . \tag{1.1.26}$$

Schrödinger equation for time-dependent Hamiltonian is assumed to be solved as,

$$|\psi(t)\rangle = \mathcal{U}(t)|\psi(0)\rangle \ , \tag{1.1.27}$$

where $\mathcal{U}$ satisfies the boundary condition $\mathcal{U}(0) = \mathcal{I}$. Substituting this solution (1.1.27) into the Schrödinger equation (1.1.26) leads

$$i\hbar\frac{\mathrm{d}}{\mathrm{d}t}\mathcal{U}(t) = \mathcal{H}(t)\mathcal{U}(t) \, . \tag{1.1.28}$$

Then integrating both sides of equation by time provides

$$\mathcal{U}(t) = \mathcal{I} + \int_0^t \mathrm{d}t'\, \mathcal{H}(t')\mathcal{U}(t')\,. \tag{1.1.29}$$

This integration can be calculated one by one from different time t_i to same span t,

$$\begin{aligned}\mathcal{U}(t) =& \mathcal{I} - \frac{i}{\hbar}\int_0^t \mathrm{d}t'\, \mathcal{H}(t') + \left(-\frac{i}{\hbar}\right)^2 \int_0^t \mathrm{d}t' \int_0^{t'} \mathrm{d}t''\, \mathcal{H}(t')\mathcal{H}(t'') + \cdots && (1.1.30)\\ =& \sum_{k=0}^{\infty} \left(-\frac{i}{\hbar}\right)^k \int_0^t \mathrm{d}t_1 \int_0^{t_1} \mathrm{d}t_2 \cdots \int_0^{t_{n-1}} \mathrm{d}t_n \mathcal{H}(t_1)\mathcal{H}(t_2)\cdots\mathcal{H}(t_k) && (1.1.31)\end{aligned}$$

where the term of $k = 0$ is identity operator $\mathcal{I}$. Generally, the Hamiltonian at different time does not commute. Time ordered product (T-product) are introduced,

$$\begin{aligned}&\mathrm{T}\left[\exp\left(-\frac{i}{\hbar}\int_0^t \mathcal{H}(t')\mathrm{d}t'\right)\right] && (1.1.32)\\ &:= \sum_{k=0}^{\infty} \left(-\frac{i}{\hbar}\right)^k \int_0^t \mathrm{d}t_1 \int_0^{t_1} \mathrm{d}t_2 \cdots \int_0^{t_{k-1}} \mathrm{d}t_k \mathcal{H}(t_1)\mathcal{H}(t_2)\cdots\mathcal{H}(t_k) && (1.1.33)\\ &= \mathcal{U}(t)\,, && (1.1.34)\end{aligned}$$

where $\mathrm{T}[\cdot]$ represent time ordered product and $t > t_1 > t_2 > \cdots > t_{k-1} > t_k > 0$. This time ordered product is defined as,

$$\mathrm{T}[\mathcal{A}(t_1)\mathcal{B}(t_2)] := \begin{cases} \mathcal{A}(t_1)\mathcal{B}(t_2) & (t_1 > t_2) \\ \mathcal{B}(t_2)\mathcal{A}(t_1) & (t_1 < t_2) \end{cases}$$

where $\mathcal{A}$ and $\mathcal{B}$ are arbitrary operators.

From both results (1.1.23) and (1.1.27) of Schrödinger equation, it is well understood that in this Schrödinger picture, quantum state vector are time evolving instead of observable. For given observable $\mathcal{A}$, its expectation value $\langle \mathcal{A} \rangle$ is calculated as,

$$\begin{aligned}\langle \mathcal{A} \rangle &= \langle \psi(t)|\mathcal{A}|\psi(t)\rangle && (1.1.35)\\ &= \left\langle \psi(0)\middle|\mathcal{U}^\dagger(t)\mathcal{A}\mathcal{U}(t)\middle|\psi(0)\right\rangle\,. && (1.1.36)\end{aligned}$$

1.1.3 Heisenberg picture

Of the analogy and expansion of the classical canonical equation of motion (1.1.17) is $\{f,g\} \to \frac{1}{i\hbar}[f,g]$

$$\frac{\mathrm{d}}{\mathrm{d}t}\hat{\mathcal{A}}(t) = \frac{1}{i\hbar}\left[\hat{\mathcal{H}}, \hat{\mathcal{A}(t)}\right] \tag{1.1.37}$$

In this Heisenberg picture, wave function is not time evolved $|\psi(t)\rangle = |\psi(0)\rangle$, but observable evolve on time, At time t, observable $\hat{\mathcal{A}}$ is described as,

$$\hat{\mathcal{A}}(t) = \hat{\mathcal{U}}^\dagger(t)\hat{\mathcal{A}}\hat{\mathcal{U}}(t)\,. \tag{1.1.38}$$

Then expectation value of $\hat{\mathcal{A}}$ is

$$\begin{aligned}\left\langle\hat{\mathcal{A}}\right\rangle &= \langle\psi(0)|\hat{\mathcal{A}}(t)|\psi(0)\rangle && (1.1.39)\\ &= \langle\psi(0)|\hat{\mathcal{U}}^\dagger(t)\hat{\mathcal{A}}\hat{\mathcal{U}}(t)|\psi(0)\rangle && (1.1.40)\end{aligned}$$

This shows the equivalence between Heisenberg picture and Schrödinger picture.

Unitary transformation

In the classical physics, to understand clearly and easily the dynamics on a rotating system, taking a frame co-rotating with the system of interest allows us to remove complexity arising from rotation and draw simply the dynamics accompanied extra-force. Analogous to this classical physics, in quantum physics, it is often better and useful to introduce rotating frame. Unitary transformation represents the coordinate transformation, therefore, a transformation into rotating frame for interesting system is one of the unitary transformations.

Schrödinger equation is describe as (1.1.21). Unitary operator $\mathcal{U}$ is introduced as,

$$|\psi'\rangle = \mathcal{U}^\dagger\,|\psi\rangle\ . \tag{1.1.41}$$

Applying this unitary operator into Schrödinger equation (1.1.21) is written as,

$$\begin{aligned} i\hbar\frac{\mathrm{d}}{\mathrm{d}t}\left|\psi'\right\rangle &= i\hbar\frac{\mathrm{d}\mathcal{U}^\dagger}{\mathrm{d}t}\left|\psi\right\rangle + i\hbar\mathcal{U}^\dagger\frac{\mathrm{d}}{\mathrm{d}t}\left|\psi\right\rangle & (1.1.42)\\ &= \left(i\hbar\frac{\mathrm{d}\mathcal{U}^\dagger}{\mathrm{d}t}\mathcal{U} + \mathcal{U}^\dagger\mathcal{H}\mathcal{U}\right)\left|\psi'\right\rangle & (1.1.43)\\ &= \left(-i\hbar\mathcal{U}^\dagger\frac{\mathrm{d}\mathcal{U}}{\mathrm{d}t} + \mathcal{U}^\dagger\mathcal{H}\mathcal{U}\right)\left|\psi'\right\rangle & (1.1.44)\\ &\equiv \mathcal{H}'\left|\psi'\right\rangle , & (1.1.45)\end{aligned}$$

where to transform from second equation to third equation, definition of the unitary operator is used,

$$\frac{\mathrm{d}\mathcal{I}}{\mathrm{d}t} = \frac{\mathrm{d}\mathcal{U}^\dagger\mathcal{U}}{\mathrm{d}t} = \frac{\mathrm{d}\mathcal{U}^\dagger}{\mathrm{d}t}\mathcal{U} + \mathcal{U}^\dagger\frac{\mathrm{d}\mathcal{U}}{\mathrm{d}t} = 0\,. \tag{1.1.46}$$

Finally, the unitary transformed Hamiltonian $\mathcal{H}'$ is given by,

$$\mathcal{H}' = -i\hbar\mathcal{U}^\dagger\frac{\mathrm{d}\mathcal{U}}{\mathrm{d}t} + \mathcal{U}^\dagger\mathcal{H}\mathcal{U}\,. \tag{1.1.47}$$

Especially, if $\mathcal{U}$ does not depend on time, $(\mathrm{d}\mathcal{U}/\mathrm{d}t = 0)$, the transformed Hamiltonian is simply written as,

$$\mathcal{H}' = \mathcal{U}^\dagger\mathcal{H}\mathcal{U}\,. \tag{1.1.48}$$

1.1.4 Interaction picture

To consider interaction between systems or perturbation of system from external environment, it is sometimes useful to take mixed picture of two Schrödinger and Heisenbarg so called interaction picture. Let Hamiltonian $\mathcal{H}$ be separated into two parts, the main physical system $\mathcal{H}_0$ and the interaction $\mathcal{H}_{\mathrm{int}}$

$$\mathcal{H} = \mathcal{H}_0 + \mathcal{H}_{\mathrm{int}}\,. \tag{1.1.49}$$

In the interaction picture, state vector $\left|\psi^I(t)\right\rangle$ and observable $\mathcal{A}^I(t)$ both depend on time, and are defined as

$$\begin{aligned} \left|\psi^I(t)\right\rangle &= \exp\left(\frac{i}{\hbar}\mathcal{H}_0 t\right)\left|\psi(t)\right\rangle\ , & (1.1.50)\\ \mathcal{A}^I(t) &= \exp\left(\frac{i}{\hbar}\mathcal{H}_0 t\right)\mathcal{A}\exp\left(-\frac{i}{\hbar}\mathcal{H}_0 t\right). & (1.1.51)\end{aligned}$$

Then Schrödinger equation in the interaction picture can be expressed,

$$i\hbar\frac{\mathrm{d}}{\mathrm{d}t}\left|\psi^I(t)\right\rangle = \mathcal{H}^I_{int}(t)\left|\psi^I(t)\right\rangle \tag{1.1.52}$$

The formal solution of this equation is given by

$$\left|\psi^I(t)\right\rangle = \exp\left(\frac{i}{\hbar}\mathcal{H}_0 t\right)\exp\left(-\frac{i}{\hbar}\mathcal{H}t\right)\left|\psi(0)\right\rangle\ . \tag{1.1.53}$$

On the other hand, the observable $\mathcal{A}^I(t)$ still follows the equation of motion analogous to (1.1.37),

$$\frac{\mathrm{d}\mathcal{A}^I(t)}{\mathrm{d}t} = \frac{i}{\hbar}\left[\mathcal{H}_0, \mathcal{A}^I(t)\right]\ . \tag{1.1.54}$$

Therefore, in the interaction picture, the time evolution of the state vector is governed by the main Hamiltonian $\mathcal{H}_0$ (1.1.50), while the time evolution of the observable is governed by the interaction (1.1.51).

1.1.5 Mixed state and Density Matrix

A system is usually written probabilistically by combination set of wavefunction $|\psi_k\rangle$ and classical probability q_i appearing in the wavefunction ($1 \leq k \leq s$, where s is the number of pure eigenstates of the system). It is called "Mixed state", that pure states are mixed with classical probability. Usually this classical probability comes from classical noise of environment and so on. To understand and describe this mixed state, it is useful that density operator $\hat{\rho}$ is introduced.

Density matrix

For state vector $|\psi_i\rangle$ of quantum system with classical probability q_i, density operator is defined as

$$\hat{\rho} := \sum_i q_i \left|\psi_i\rangle\!\langle\psi_i\right|\ . \tag{1.1.55}$$

From Born' rule for measurement, probability that the measurement of the observable $\hat{\mathcal{A}}$ with the state vector $|\psi_i\rangle$ gives the result λ_k is

$$p(k) = \sum_k q_k \langle\psi_i|\hat{\mathcal{P}}_k|\psi_i\rangle\ . \tag{1.1.56}$$

Moreover to analyze this probability, "trace" is introduced to sum up diagonal element of matrix of interest. For an arbitrarily operator $\mathcal{A}$, with orthogonal basis $\{|\lambda_k\rangle\}$

$$\mathrm{tr}\left[\hat{\mathcal{A}}\right] := \sum_k \langle\lambda_k|\hat{\mathcal{A}}|\lambda_k\rangle \ . \tag{1.1.57}$$

Then measurement probability with classical probability is rewritten and linked to density operator

$$\begin{aligned} p(k) &= \sum_i q_i \langle\psi_i|\hat{\mathcal{P}}_k|\psi_i\rangle && (1.1.58)\\ &= \sum_i \mathrm{tr}\left[\hat{\mathcal{P}}_k q_i |\psi_i\rangle\langle\psi_i|\right] && (1.1.59)\\ &= \mathrm{tr}\left[\hat{\mathcal{P}}_k\hat{\rho}\right] . && (1.1.60) \end{aligned}$$

On the other hand, the superposition state $|\psi\rangle = \sum_i c_i |\psi_i\rangle$ is expressed using the density operator $\hat{\rho}'$

$$\begin{aligned} \hat{\rho}' &= |\psi\rangle\langle\psi| && (1.1.61)\\ &= \sum_{i,j} c_i c_j^* |\psi_i\rangle\langle\psi_j| && (1.1.62)\\ &= \sum_j |c_j|^2 |\psi_j\rangle\langle\psi_j| + \sum_{i\neq j} c_i c_j^* |\psi_i\rangle\langle\psi_j| \ , && (1.1.63) \end{aligned}$$

where last term represents non diagonal element of the density matrix. The diagonal elements are determined by state probability, not by classical probability.

When a quantum state undergoes unitary time evolution $|\psi\rangle \rightarrow \mathcal{U}|\psi\rangle$, its density of states is $\hat{\rho} = |\psi\rangle\langle\psi| \rightarrow \mathcal{U}|\psi\rangle\langle\psi|\mathcal{U}^\dagger = \mathcal{U}\hat{\rho}\mathcal{U}^\dagger$.

Quantum master equation

In a closed system with the Hamiltonian $\mathcal{H}$, each state vector $|\psi_k\rangle$ in the density matrix $\hat{\rho} = \sum_k q_k |\psi_k\rangle\langle\psi_k|$ satisfies Schrödinger equation $i\hbar\frac{\mathrm{d}}{\mathrm{d}t}|\psi_k\rangle = \mathcal{H}|\psi_k\rangle$. Then time evolution of the density matrix are derived as

$$i\hbar\frac{\mathrm{d}}{\mathrm{d}t}\hat{\rho} = i\hbar\frac{\mathrm{d}}{\mathrm{d}t}\sum_{k=1}^{s} q_k \left|\psi_k\middle\rangle\middle\langle\psi_k\right| \tag{1.1.64}$$

$$= \sum_{k=1}^{s} q_k\hat{\mathcal{H}} \left|\psi_k\middle\rangle\middle\langle\psi_k\right| - \sum_{k=1}^{s} q_k \left|\psi_k\middle\rangle\middle\langle\psi_k\right| \hat{\mathcal{H}} \tag{1.1.65}$$

$$= \left[\hat{\mathcal{H}}, \hat{\rho}\right], \tag{1.1.66}$$

This is called "Liouville–von-Neumann" equation.

When a system of interest $\mathcal{S}$ interacts with environment of not interest $\mathcal{E}$, the state of the system $|\psi_{\mathcal{S}}\rangle$ is effected from and leak into the environment, it is so-called decoherence. To analyse this decoherence dynamics, time evolution of density matrix of the system $\hat{\rho_S}$ is expressed as Master equation (Lindblad eqation) [89, 153, 88, 50]:

$$\frac{\mathrm{d}}{\mathrm{d}t}\hat{\rho}_{\mathcal{S}}(t) = -\frac{i}{\hbar}\left[\hat{\mathcal{H}}_{\mathcal{S}}, \hat{\rho}_{\mathcal{S}}(t)\right] + \frac{1}{2}\sum_{j}\left[2\hat{L}_j\hat{\rho}_{\mathcal{S}}(t)\hat{L}_j^{\dagger} - \left\{\hat{L}_j^{\dagger}\hat{L}_j, \hat{\rho}_{\mathcal{S}}(t)\right\}\right], \tag{1.1.67}$$

where the operators $\hat{L}_j$, called as Lindblad operator, usually correspond to "jump operators" to other state. The first term represents the "Liouville–von-Neumann" equation and describes the unitary evolution of the density matrix. The second term represents the non-unitary evolution such as decoherence by environment.

1.2 Quantum Bit

The most fundamental and smallest unit of quantum information is called as the quantum bit or "qubit".

1.2.1 Basics of Quantum bits

A classical bit can take one of two different states "0" or "1" such as "off" or "on" of switch, low" or "high" voltage of transistor, or "empty" or "full" of a capacitor. A qubit, however, unlike those classical bit, can represent a coherent superposition of the two states, denoted as $|0\rangle$ and $|1\rangle$, which are two orthonormal basis states. This two state system also has two energy levels corresponding to either $|0\rangle$ or $|1\rangle$. When the difference between two levels is $\hbar\omega_{\mathrm{q}}$, its Hamiltonian is written as $\mathcal{H}_{\mathrm{q}} = \hbar\omega_{\mathrm{q}}\sigma_z/2$, where $\sigma_z := |0\rangle\langle 0| - |1\rangle\langle 1|$. This qubit corresponds to various physical systems, for example, as directions of persistent current in a superconducting loop $\{|\circlearrowleft\rangle, |\circlearrowright\rangle\}$ [186, 119, 193, 245, 103, 117, 148, 189, 241, 17, 18], the number of cooper pairs of two superconductors $\{|n_{\mathrm{cp}}\rangle, |n_{\mathrm{cp}}+1\rangle\}$ [175, 140], an ion trapped by a laser $\{|\uparrow\rangle, |\downarrow\rangle\}$ [23], or optical polarization $\{|H\rangle, |V\rangle\}$, and so on. An individual qubit has an arbitrary state, $|\psi\rangle$ expressed by,

$$|\psi\rangle = \alpha|0\rangle + \beta|1\rangle \ , \ (\alpha, \beta \in \mathbb{C}, |\alpha|^2 + |\beta|^2 = 1) \tag{1.2.1}$$

where α and β are complex numbers and normalized. α and β represent the weight of $|0\rangle$ and $|1\rangle$ states in the superposition state, and are called complex probability amplitudes.

Bloch sphere

Although the representation (1.2.1) of the qubit state using the complex number is helpful in calculating quantum state, it is still not easy to imagine geometrically. To illustrate the state of a qubit, complex probability amplitudes α and β are replaced with real numbers a, b, θ_a, θ_b: $\alpha = a\mathrm{e}^{i\theta_a}$ and $\beta = b\mathrm{e}^{i\theta_b}$. Then the state of qubit $|\psi\rangle$ is expressed as

$$\begin{aligned} |\psi\rangle &= \alpha|0\rangle + \beta|1\rangle \\ &= a\mathrm{e}^{i\theta_a}|0\rangle + b\mathrm{e}^{i\theta_b}|1\rangle \\ &= \mathrm{e}^{i\theta_a}\left(a|0\rangle + b\mathrm{e}^{i(\theta_b-\theta_a)}|1\rangle\right) \\ &\equiv \mathrm{e}^{i\theta_g}\left(a|0\rangle + b\mathrm{e}^{i\phi}|1\rangle\right), \end{aligned} \tag{1.2.2}$$

where θ_g represents the global phase, and $\phi = \theta_a - \theta_b$ represents the relative phase between the two states. Usually only relative phase can be observed physically. Another angular variable θ introduced by $a = \cos(\theta/2)$, $b = \sin(\theta/2)$ with normalization condi-

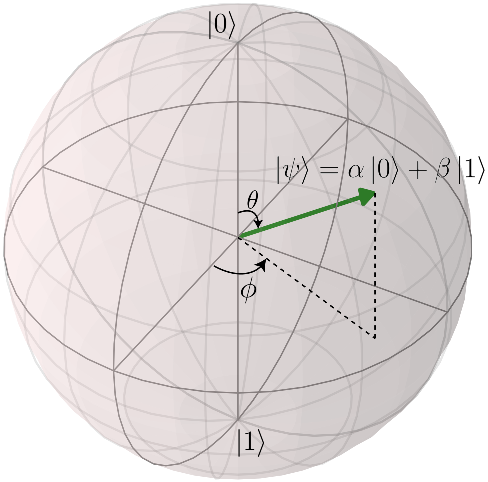

Figure 1.2.1: Bloch's sphere

tion imposed on α and β,

$$1 = |\alpha|^2 + |\beta|^2 \tag{1.2.3}$$

$$= \left|a\mathrm{e}^{i\theta_a}\right|^2 + \left|b\mathrm{e}^{i\theta_b}\right|^2 = a^2 + b^2 \tag{1.2.4}$$

$$= \cos^2(\theta/2) + \sin^2(\theta/2)\,, (0 \le \theta \le \pi)\,. \tag{1.2.5}$$

Therefore, physically distinguishable states are represented by only two angular variables θ and ϕ. The global phase θ_d can be ignored because $\mathrm{e}^{i\theta_g}|\psi\rangle = |\psi\rangle$, then arbitraly state of qubit are expressed as,

$$|\psi\rangle = \cos(\theta/2)\,|0\rangle + \mathrm{e}^{i\phi}\sin(\theta/2)\,|1\rangle \tag{1.2.6}$$

$$(0 \le \theta \le \pi, 0 \le \phi < 2\pi) \tag{1.2.7}$$

where a range of θ is reduced due to unique representation for state. Illustrating these θ and ϕ as polar and azimuthal angle in the spherical coordinate shown in figure 1.2.1, a physical pure state is mapped onto a point on the surface of the Bloch sphere.

Then in order to represent a unitary operation of a qubit on the Bloch sphere, it is useful to describe the state as density operator ρ:

$$\rho = |\psi\rangle\langle\psi| = \begin{pmatrix} \cos^2\frac{\theta}{2} & \mathrm{e}^{-i\phi}\cos\frac{\theta}{2}\sin\frac{\theta}{2} \\ \mathrm{e}^{i\phi}\cos\frac{\theta}{2}\sin\frac{\theta}{2} & \sin^2\frac{\theta}{2} \end{pmatrix} \tag{1.2.8}$$

$$= \begin{pmatrix} 1+\cos\theta & \cos\phi\sin\theta - i\sin\phi\sin\theta \\ \cos\phi\sin\theta + i\sin\phi\sin\theta & 1-\cos\theta \end{pmatrix}. \tag{1.2.9}$$

Pauli operators

A two level system defined by basis $|0\rangle$ and $|1\rangle$. In this space, creation and annihilation operators are defined as

$$\sigma_+ := |1\rangle\langle 0|\;, \tag{1.2.10}$$

$$\sigma_- := |0\rangle\langle 1|\;. \tag{1.2.11}$$

To control qubit, most basic operation are represented by Pauli operators, and when both state vector are represented as $|0\rangle \to (1\ 0)^{\mathrm{T}}$ and $|1\rangle \to (0\ 1)^{\mathrm{T}}$, matrix of Pauli operators are described by using creation and annihilation operators:

$$\sigma_x = \sigma_+ + \sigma_- = |0\rangle\langle 1| + |1\rangle\langle 0| \to \begin{pmatrix} 0 & 1 \\ 1 & 0 \end{pmatrix}, \tag{1.2.12}$$

$$\sigma_y = -i(\sigma_+ - \sigma_-) = i\,|0\rangle\langle 1| - i\,|1\rangle\langle 0| \to \begin{pmatrix} 0 & -i \\ i & 0 \end{pmatrix}, \tag{1.2.13}$$

$$\sigma_z = \sigma_+\sigma_- - \sigma_-\sigma_+ = |0\rangle\langle 0| - |1\rangle\langle 1| \to \begin{pmatrix} 1 & 0 \\ 0 & -1 \end{pmatrix}, \tag{1.2.14}$$

$$\sigma_0 = \sigma_+\sigma_- + \sigma_-\sigma_+ = |0\rangle\langle 0| + |1\rangle\langle 1| = \begin{pmatrix} 1 & 0 \\ 0 & 1 \end{pmatrix}. \tag{1.2.15}$$

Acting on the state $|0\rangle$ or $|1\rangle$, σ_z gives eigenvalue of qubit ± 1, $\sigma_{x,y}$ changes state and phase each other, and σ_i does not change the state.

The density operator of qubit (1.2.9) can be decomposed by those Pauli operators as

$$\rho = \frac{1}{2}(\sigma_0 + \sigma_x \cos\phi \sin\theta + \sigma_y \sin\phi \sin\theta + \sigma_z \cos\theta) \tag{1.2.16}$$

$$= \frac{1}{2}(\sigma_0 + \mathbf{r}_\rho \cdot \boldsymbol{\sigma}), \tag{1.2.17}$$

where $\mathbf{r} := (r_x \ r_y \ r_z) = (\cos\phi \sin\theta \ \ \sin\phi \sin\theta \ \ \cos\theta)$ is Bloch vector and $\boldsymbol{\sigma} = (\sigma_x \ \sigma_y \ \sigma_z)^{\mathrm{T}}$ is vector of the Pauli operators. Then on the Bloch sphere, the Bloch vector is rotated by unitary operation of Pauli operators about x, y, and z axes by given angle η:

$$\mathcal{R}_x(\eta) := \mathrm{e}^{-i\frac{\eta}{2}\sigma_x} = \cos\frac{\eta}{2}\sigma_0 - i\sin\frac{\eta}{2}\sigma_x = \begin{pmatrix} \cos\frac{\eta}{2} & -i\sin\frac{\eta}{2} \\ -i\sin\frac{\eta}{2} & \cos\frac{\eta}{2} \end{pmatrix}, \tag{1.2.18}$$

$$\mathcal{R}_y(\eta) := \mathrm{e}^{-i\frac{\eta}{2}\sigma_y} = \cos\frac{\eta}{2}\sigma_0 - i\sin\frac{\eta}{2}\sigma_y = \begin{pmatrix} \cos\frac{\eta}{2} & -\sin\frac{\eta}{2} \\ -i\sin\frac{\eta}{2} & \cos\frac{\eta}{2} \end{pmatrix}, \tag{1.2.19}$$

$$\mathcal{R}_z(\eta) := \mathrm{e}^{-i\frac{\eta}{2}\sigma_z} = \cos\frac{\eta}{2}\sigma_0 - i\sin\frac{\eta}{2}\sigma_z = \begin{pmatrix} \mathrm{e}^{-i\eta/2} & 0 \\ 0 & \mathrm{e}^{i\eta/2} \end{pmatrix}. \tag{1.2.20}$$

For example, the state ρ is evolved by $\mathcal{R}_z(\eta)$ around z-axis:

$$\begin{aligned}
\rho' &= \mathcal{R}_z(\eta)\rho\mathcal{R}_z^\dagger(\eta) && (1.2.21)\\
&= \mathcal{R}_z(\eta)\frac{1}{2}(\sigma_0 + \mathbf{r}_\rho \cdot \boldsymbol{\sigma})\mathcal{R}_z^\dagger(\eta) && (1.2.22)\\
&= \frac{1}{2}\big[\mathcal{R}_z(\eta)\sigma_0\mathcal{R}_z^\dagger(\eta) + \mathcal{R}_z(\eta)(\mathbf{r}_\rho \cdot \boldsymbol{\sigma})\mathcal{R}_z^\dagger(\eta)\big] && (1.2.23)\\
&= \frac{1}{2}[\sigma_0 + (r_x\cos\eta - r_y\sin\eta)\sigma_x + (r_x\sin\eta + r_y\cos\eta)\sigma_y + r_z\sigma_z] && (1.2.24)\\
&= \frac{1}{2}(\sigma_0 + \mathbf{r}_{\rho'} \cdot \boldsymbol{\sigma}), && (1.2.25)
\end{aligned}$$

where $\mathbf{r} := (r'_x\ r'_y\ r'_z) = (r_x\cos\eta - r_y\sin\eta\ \ r_x\sin\eta + r_y\cos\eta\ \ r_z)$ is rotated Bloch vector. Arbitrarily rotation $\mathcal{R}_\xi(\eta)$ of a qubit for angle η around arbitrarily axis $\boldsymbol{\xi}$, which is a unit vector of the axis, can be decomposed as,

$$\begin{aligned}
\mathcal{R}_\xi(\eta) &= \cos\frac{\eta}{2}\sigma_0 - i\sin\frac{\eta}{2}\boldsymbol{\xi}\cdot\boldsymbol{\sigma} && (1.2.26)\\
&= \exp\left(-i\frac{\eta}{2}\boldsymbol{\xi}\cdot\boldsymbol{\sigma}\right). && (1.2.27)
\end{aligned}$$

Therefore, this arbitrarily rotation evolves the state ρ around the axis $\boldsymbol{\xi}$ by angle η as

$$\rho' = \mathcal{R}_\xi(\eta)\rho\mathcal{R}_\xi(\eta)^\dagger\,. \tag{1.2.28}$$

1.2.2 Qubit dynamics

Interaction between qubit and environment gives rise to decoherence due to relaxation and dephasing. Here both mechanisms are briefly derived from the master equation (1.1.67).

Qubit relaxation

Let qubit be at excited state $|1\rangle$, then it may release photon and relax into the ground state $|0\rangle$. Assuming that a rate of releasing photon into vacuum is γ_0, in the master equation, this process is described by the Lindblad operator $L_{\mathrm{rx}} = \sqrt{\gamma_0}\sigma_-$. The initial state of the qubit ρ_{rx} at $t = 0$ is expressed as

$$\rho_{\mathrm{rx}}(0) = \begin{pmatrix} \rho_0^{\mathrm{rx}} & \rho_+^{\mathrm{rx}} \\ \rho_+^{\mathrm{rx}*} & 1 - \rho_0^{\mathrm{rx}} \end{pmatrix}. \tag{1.2.29}$$

Then, the master equation describing this process is also expressed as

$$\frac{\mathrm{d}\rho_{\mathrm{rx}}}{\mathrm{d}t} = [\mathcal{H}, \rho_{\mathrm{rx}}] + \gamma_0 \left(\sigma_- \rho_{\mathrm{rx}} \sigma_+ - \frac{1}{2} \{\sigma_+ \sigma_-, \rho_{\mathrm{rx}}\} \right) . \tag{1.2.30}$$

This master equation can be solved straightforwardly as,

$$\rho_{\mathrm{rx}}(t) = \begin{pmatrix} \rho_0^{\mathrm{rx}} \mathrm{e}^{-\gamma_0 t} & \rho_+^{\mathrm{rx}} \mathrm{e}^{-\gamma_0 t/2} \\ \rho_+^{\mathrm{rx}*} \mathrm{e}^{-\gamma_0 t/2} & 1 - \rho_0^{\mathrm{rx}} \mathrm{e}^{-\gamma_0 t} \end{pmatrix} . \tag{1.2.31}$$

$$\tag{1.2.32}$$

This solution shows that the type of the Lindblad operator $L_{\mathrm{rx}} = \sqrt{\gamma_0}\sigma_-$ collapses the state from pure state at the surface of the Bloch sphere into thermally equivalent value of the environment at inside of the Bloch sphere.

Qubit dephasing

Let qubit be at a superposition state $|+\rangle = (|0\rangle + |1\rangle)/\sqrt{2}$, then it may be disturbed by environment. A rate of disturbance of phase between $|0\rangle$ and $|1\rangle$ is γ_{p} by splitting the Bloch vector due to the phasing of the qubit. Assuming that a rate of releasing photon into vacuum is γ_0, in the master equation, this process is described by the Lindblad operator $L_{\mathrm{dp}} = \sqrt{\gamma_{\mathrm{dp}}}\sigma_z$. The initial state of the qubit ρ_{dp} at $t = 0$ is expressed as

$$\rho_{\mathrm{dp}}(0) = \begin{pmatrix} \rho_0^{\mathrm{dp}} & \rho_+^{\mathrm{dp}} \\ \rho_+^{\mathrm{dp}*} & 1 - \rho_0^{\mathrm{dp}} \end{pmatrix} \tag{1.2.33}$$

Then, the master equation describing this process also expressed as

$$\frac{\mathrm{d}\rho_{\mathrm{dp}}}{\mathrm{d}t} = [\mathcal{H}, \rho_{\mathrm{dp}}] + \gamma_{\mathrm{dp}} \left(\sigma_z \rho_{\mathrm{dp}} \sigma_z - \frac{1}{2} \left\{ \sigma_z^2, \rho_{\mathrm{dp}} \right\} \right) . \tag{1.2.34}$$

This master equation can be solved as,

$$\rho_{\mathrm{dp}}(t) = \begin{pmatrix} \rho_0^{\mathrm{dp}} & \rho_+^{\mathrm{dp}} \mathrm{e}^{-\gamma_0 t} \\ \rho_+^{\mathrm{dp}*} \mathrm{e}^{-\gamma_0 t} & 1 - \rho_0^{\mathrm{dp}} \end{pmatrix} , \tag{1.2.35}$$

$$\tag{1.2.36}$$

This solution shows that the type of the Lindblad operator L_{dp} collapses the state from pure state at the surface of the Bloch sphere into zero at the center of the Bloch sphere.

1.2.3 Entanglement

Bell pairs

For two qubit system on Hilbert space $\mathbb{H}^{\otimes 2}$, there are choices of basis set. For instance, $\{|00\rangle, |01\rangle, |10\rangle, |11\rangle\}$ can be taken as orthogonal basis. Consider superposition state of two of these basis,

$$\left|\Phi^{\pm}\right\rangle_{\text{bell}} = \frac{1}{\sqrt{2}}(|00\rangle \pm |11\rangle), \tag{1.2.37}$$

$$\left|\Psi^{\pm}\right\rangle_{\text{bell}} = \frac{1}{\sqrt{2}}(|01\rangle \pm |10\rangle). \tag{1.2.38}$$

Both $|\Phi\rangle^{\pm}_{\text{bell}}$ and $|\Psi\rangle^{\pm}_{\text{bell}}$ are so called Bell pair or EPR pair. When one qubit state is determined on the basis by projection measurement, simultaneously the other qubit state is projected [65, 11, 6] .

Three qubits entanglement

To extend the number of qubit in the system [98], from two qubits to three qubits on Hilbert space $\mathbb{H}^{\otimes 3}$, there are two non-biseparable states of three-qubit states, which cannot be separated into each other by local quantum operations. one of the these states is so-called Greenberger–Horne–Zeilinger (GHZ) state [94] expressed as

$$|\text{GHZ}\rangle = \frac{1}{\sqrt{2}}(|000\rangle + |111\rangle). \tag{1.2.39}$$

The other state is so-called W state [62] expressed as

$$|\text{W}\rangle = \frac{1}{\sqrt{3}} = (|100\rangle + |010\rangle + |001\rangle). \tag{1.2.40}$$

Both are entangled state of three qubits. However, once one party of the state is traced out, the difference of the entanglement properties between GHZ and W states appear. Let both states be taken partial trace of the third qubit, for GHZ state, the reduced density operator of the two qubits is given by

$$\rho_{12}(\text{GHZ}) = \text{tr}_3(|\text{GHZ}\rangle\langle\text{GHZ}|) = \frac{1}{2}\,|00\rangle\langle 00|_{12} + \frac{1}{2}\,|11\rangle\langle 11|_{12}\,, \tag{1.2.41}$$

where $\mathrm{tr}_k(\rho)$ represents the partial trace out of the state ρ for k-th qubit. On the other hand, for W state, the reduced density operator of the two qubits is given by

$$\rho_{12}(\mathrm{W}) = \mathrm{tr}_3(|\mathrm{W}\rangle\langle\mathrm{W}|) = \frac{2}{3}\left|\Phi^+\middle\rangle\middle\langle\Phi^+\right|_{12} + \frac{1}{2}\left|00\middle\rangle\middle\langle 00\right|_{12} . \tag{1.2.42}$$

One of the most remarkable difference properties between the GHZ state and the W state is the fact that for the GHZ state, the partial trace of the only one party destroys entanglement completely, on the other hand, the partial trace of density operator contains a Bell pair in case of W state. Thus, after tracing out the one of the state of the GHZ state, two states remaining are separated which is represented by $\sum_{k,j} c_k c_j \left|\psi_k\right\rangle \otimes \left|\psi_j\right\rangle$.

Chapter 2

Review of Superconducting Circuit

2.1 Superconductivity

Superconductors are characterized by infinite electrical conductivity and the Meissner effect [167], in which magnetic fields are excluded from the superconductor's interior [224, 137]. These properties are manifested by the fact that the superconductor is in a macroscopic quantum state. This macroscopic quantum state means that the many particles in the superconductor behave as a whole in a manner described by quantum mechanics with marring two electrons so-called "Cooper pair" forming. The electrons start to move with creating order, not independently and randomly. This is called an emergent phenomenon. This order in a superconductor is governed by the number of charges n_{cp} and the phase ϕ. These two are conjugate variables. Curiously, in quantum mechanics, two conjugate variables cannot be determined simultaneously. This is called an uncertainty principle. The position x and momentum p is an example of the conjugate variables. The number of charges and the phase are also the conjugate variables.

2.1.1 BCS theory and superconducting energy gap

In the presence of the attractive interaction, the many-body electron system becomes unstable towards the formation of a new ground state, where these Cooper pairs proliferate. According to Bardeen–Cooper–Schrieffer (BCS) theory of superconductivity [48, 7, 8, 224], superconducting gap Δ_{sc} is determined at finite temperature by

$$\Delta_{\mathrm{sc}} = \frac{1}{2} v_0 \sum_k \frac{\Delta_{\mathrm{sc}}}{E_k} \tanh\left(\frac{1}{2}\beta E_k\right) \tag{2.1.1}$$

$$\Leftrightarrow 1 = \frac{1}{2} v_0 \sum_k \frac{1}{\sqrt{\xi_k^2 + |\Delta_{\mathrm{sc}}|^2}} \tanh\left[\frac{1}{2}\beta\sqrt{\xi_k^2 + |\Delta_{\mathrm{sc}}|^2}\right], \tag{2.1.2}$$

where $E_k = \sqrt{\xi_k^2 + |\Delta_{\mathrm{sc}}|^2}$ is excitation energy of the quasiparticles, $\beta = 1/k_B T$, and v_0 is coupling constant of electrons in the Cooper pair.

At $T = 0$, the the superconducting gap is given by

$$\Delta_{\mathrm{sc}}(0) = 2\hbar\omega_{\mathrm{Debye}} \exp\left(-\frac{1}{v_0 D_0}\right) \tag{2.1.3}$$

where $\hbar\omega_{\mathrm{Debye}}$ is Debye energy which represents the approximately maximum energy of the phonon in the superconductor, and D_0 is the density of state in the superconductor.

Around $T \approx T_c$, the the superconducting gap is given by

$$\frac{\Delta_{\mathrm{sc}}(T)}{\Delta_{\mathrm{sc}}(0)} \approx 1.74\left(1 - \frac{T}{T_c}\right)^{1/2}, \tag{2.1.4}$$

$$\frac{2|\Delta_{\mathrm{sc}}(0)|}{k_B T_c} \approx \frac{3}{1.13} \approx 3.54\,. \tag{2.1.5}$$

2.1.2 London equation and penetration depth

When external magnetic field is applied to a superconductor, it is only penetrating the surface of the superconductor. There are no magnetic field inside superconductor, called "Meissener effect". To represent this penetration phenomenon, London equation [159] gives the relation between current and vector potential on the superconductor.

$$\mathbf{J} = -\mu_0 \lambda_{\mathrm{L}}^2 \mathbf{A}\,, \tag{2.1.6}$$

where $\mathbf{J}$ is current density, $\mathbf{A}$ is vector potential (magnetic field is $B = \boldsymbol{\nabla} \times \mathbf{A}$), and λ_{L} is constant value representing material characters (shown later). Using both the equation (2.1.6) and Maxwell' equation $\boldsymbol{\nabla} \times B = \mu_0 \mathbf{J}$ leads

$$\nabla^2 B = \frac{B}{\lambda_{\mathrm{L}}^2} \tag{2.1.7}$$

This equation represents the penetration amplitude of the magnetic field at the depth d from surface of the superconductor:

$$B(d) = B_0 \exp\left(-\frac{d}{\lambda_{\mathrm{L}}}\right). \tag{2.1.8}$$

Here London penetration depth λ_{L} characterizes the amount of the external magnetic field penetrating and at temperature T [164, 97]

$$\lambda_{\mathrm{L}}(T) = \lambda_{\mathrm{L}}(0)\frac{1}{\sqrt{1-\left(\frac{T}{T_c}\right)^4}}\,. \tag{2.1.9}$$

$$\lambda_{\mathrm{L}}(0) = \sqrt{\frac{mc^2}{4\pi n_s e^2}}\,, \tag{2.1.10}$$

where m is a mass of the particle, c is speed of right, and n_s and $-e$ is density and charge of the electron.

2.1.3 Ginzburg–Landau equation and coherence length

To express the phenomena of thermodynamic nature and magnetic nature, usually Ginzburg–Landau (GL) equation [139] is used. The phase transition between normal conductivity and superconductivity is characterized by the order parameter (wave function) Ψ when external magnetic field is zero. The wave function is related to the electron density by

$$n_s = |\Psi|^2\,. \tag{2.1.11}$$

From a minimum condition of the difference of the free energy between normal and superconducting phase $\min f_s - f_n$, the equation that wave function satisfies is derived as

$$a(T)\Psi + b(T)\Psi|\Psi|^2 = 0, \tag{2.1.12}$$

and it gives

$$|\Psi|^2 = -\frac{a(T)}{b(T)}\,, \tag{2.1.13}$$

where $a(T)$ and $b(T)$ are satisfy for critical magnetic field $H_c(T)$ at temperature T

$$f_s - f_n = -\frac{1}{2}\frac{a(T)^2}{b(T)} = -\frac{H_c(T)^2}{8\pi}\,. \tag{2.1.14}$$

The equation of motion at the zero electromagnetic field is

$$\frac{\hbar}{2m^*}\nabla^2\Psi = a(T)\Psi + b(T)\Psi|\Psi|^2\,, \tag{2.1.15}$$

where m^* is mass of the particle. This equation is called Ginzburg–Landau (GL) equation. To evaluate Ψ, the small difference $\delta\Psi$ from equilibrium value Ψ_∞ and normalized function h are defined as

$$|\Psi_\infty|^2 := -a/b\,, \tag{2.1.16}$$

$$h := \frac{\Psi}{\Psi_\infty} = \frac{(\Psi_\infty + \delta\Psi)}{\Psi_\infty} = 1 + g(x)\,. \tag{2.1.17}$$

Then GL equation can be rewrite as

$$\xi_{\mathrm{GL}}^2 \frac{\mathrm{d}^2 g}{\mathrm{d}x^2} + (1+g) - (1 + 3g + 3g^2 + g^3) = 0\,, \tag{2.1.18}$$

$$\xi_{\mathrm{GL}}(T) = \frac{\hbar}{\sqrt{|2m^* a(T)|}} \tag{2.1.19}$$

where ξ_{GL} is called Ginzburg-Landau (GL) coherence length When g is small, higher order terms are negligible:

$$\xi^2 \frac{\mathrm{d}^2 g}{\mathrm{d}x^2} - 2g = 0\,. \tag{2.1.20}$$

Then this solution is

$$\frac{\Psi}{\Psi_\infty} + 1 = g(x) \approx \exp\left(-\sqrt{2}\frac{x}{\xi_{\mathrm{GL}}(T)}\right). \tag{2.1.21}$$

Therefore, the wave function of superconductor distributes around this GL coherence length, where probability amplitude of wave function is decreased into $1/\mathrm{e}$.

2.1.4 Josephson junction

When two superconductors are sufficiently close to each other with interrupting insulator between them, called "Josephson Junction" [128]. To analyze the this junction, wave functions of both superconductor $\Psi_{1,2}$ are assumed to represented as $\Psi_{1,2} = \sqrt{\rho_{1,2}^e}\mathrm{e}^{i\theta_{1,2}}$, where $\theta_{1,2}$ is the phases on the two sides of the junction and $\rho_{1,2}^e$ is the density of electrons at those two points.

$$i\hbar\frac{\partial \Psi_1}{\partial t} = +2eV\Psi_1 + K\Psi_1\,, \tag{2.1.22}$$

$$i\hbar\frac{\partial \Psi_2}{\partial t} = -2eV\Psi_2 + K\Psi_2\,. \tag{2.1.23}$$

The constant K represents the leakage by coupling through the junction from one side to the other. To across the junction, there is a potential difference $2eV = U_1 - U_2$ and zero energy point is set at the center of two energies. These equations are solved straightforwardly as

$$\frac{\mathrm{d}\rho_1}{\mathrm{d}t} = +\frac{2}{\hbar}K\sqrt{\rho_2\rho_1}\sin\varphi\,, \tag{2.1.24}$$

$$\frac{\mathrm{d}\rho_2}{\mathrm{d}t} = -\frac{2}{\hbar}K\sqrt{\rho_1\rho_2}\sin\varphi\,, \tag{2.1.25}$$

$$\frac{\mathrm{d}\theta_1}{\mathrm{d}t} = -\frac{1}{\hbar}K\sqrt{\frac{\rho_2}{\rho_1}}\cos\varphi - \frac{qV}{2\hbar}\,, \tag{2.1.26}$$

$$\frac{\mathrm{d}\theta_2}{\mathrm{d}t} = -\frac{1}{\hbar}K\sqrt{\frac{\rho_1}{\rho_2}}\cos\varphi + \frac{qV}{2\hbar}\,, \tag{2.1.27}$$

where phase difference is $\theta_2-\theta_1 = \varphi$. From the first two equations (2.1.24) and (2.1.25) lead that $\dot{\rho_1} = -\dot{\rho_2} := \rho_0$. When at first there is a phase difference of the wave function across the junction, the flow is happen from one side to the other side without extra electrical force because of taking balance of the electrons,. This is called the DC Josephson effect. Josephson current is given by

$$I = I_c\sin\varphi\,, \tag{2.1.28}$$

where $I_c := 2K\rho_0/\hbar$ is maximum current, called critical current, unless Cooper pairs are broken, otherwise, once the superconducting current exceeds the critical current, Cooper pairs are destroyed and suddenly quasiparticles appears. In order to operate the circuit with Josephson junction in quantum regime, current should be well below the critical current, otherwise dissipation and finite voltage appear at the junction accompanied by a resistive current.

Furthermore, the other pair of the equations (2.1.26) and (2.1.27) leads the dynamics of the phase difference.

$$\frac{\mathrm{d}\varphi}{\mathrm{d}t} = \frac{\mathrm{d}\theta_2}{\mathrm{d}t} - \frac{\mathrm{d}\theta_1}{\mathrm{d}t} = \frac{2eV}{\hbar} \tag{2.1.29}$$

When a voltage is applied between these two superconductors, the relative phase varies linearly in time as,

$$V = \frac{\hbar}{2e}\dot{\varphi} = \frac{\Phi_0}{2\pi}\dot{\varphi} = \frac{\mathrm{d}\Phi}{\mathrm{d}t}\,, \tag{2.1.30}$$

where $\Phi_0 := h/(2e)$ is flux quantum and $\Phi := \Phi_0\varphi$. According to (2.1.28), this phase variation caused the oscillating current. This phenomenon is called the AC Josephson effect. Despite the fact that the Josephson effect occurs in the a macroscopic system, Planck's constant h that is the smallest units of quantum mechanics , and the elementary charge e, are directly related to this effect.

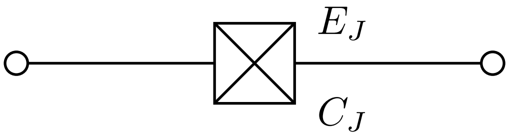

Figure 2.1.1: Circuit schematic of Josephson junction

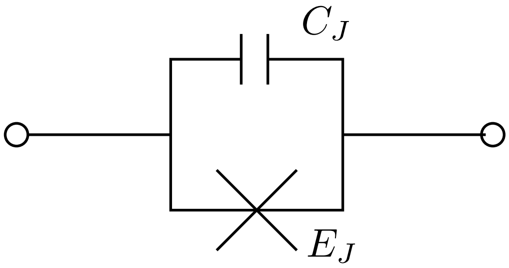

Figure 2.1.2: Circuit schematic of Josephson junction separated Junction capacitor

Ambegaokar–Baratof relation

The maximum current depends on the superconducting energy gap Δ_{sc} and resistance R_j through the relation is expressed as [2]

$$I_c = \frac{\pi\Delta_{sc}(T)}{2eR_j}\tanh\frac{\Delta_{sc}(T)}{2k_BT}\,. \tag{2.1.31}$$

Josephson inductance

When the current and the phase of the Josephson junction varies by time, using Josephson effect representations, the dynamics of the current is expressed as

$$\frac{\partial I}{\partial t} = \frac{\partial I}{\partial \varphi}\frac{\partial \varphi}{\partial t} = I_c\cos\varphi\cdot\frac{2e}{\hbar}V\,. \tag{2.1.32}$$

From this equation, the inductance relation of voltage and current is regards as

$$V = L(\varphi)\frac{\partial I}{\partial \varphi}\ , L(\varphi) = \frac{L_J}{\cos\varphi}\ , L_J = \frac{\Phi_0}{2\pi I_c}\,. \tag{2.1.33}$$

Here L_J is a characteristic parameter of the Josephson junction, called Josephson inductance.

Josephson Energy

The energy is stored in the Josephson junction with current I_J through and voltage V_J across the junction.

$$\begin{aligned}
\mathcal{E}_J &= \int_0^{t_0} I_J V_J \,\mathrm{d}t && (2.1.34)\\
&= \int_0^{t_0} I_c \sin\varphi \cdot \frac{\hbar}{2e}\frac{\mathrm{d}\varphi}{\mathrm{d}t}\,\mathrm{d}t && (2.1.35)\\
&= \frac{I_c\Phi_0}{2\pi}\int_{\varphi(0)}^{\varphi(t)} \sin\varphi \,\mathrm{d}\varphi && (2.1.36)\\
&= \mathcal{E}_{J0}(1-\cos\varphi) && (2.1.37)
\end{aligned}$$

where $\mathcal{E}_{J0} := I_c\Phi_0/2\pi$ is Josephson coupling energy.

2.1.5 Flux quantization

Ginzburg–Landau (GL) equation describes macroscopic superconducting phenomena (2.1.3). From the GL equation, a density of supercurrent $\mathbf{j}$ can be derived as

$$\Lambda\mathbf{j} = \hbar\boldsymbol{\nabla}\bar{\varphi} - 2e\mathbf{A}_{vp}\,, \tag{2.1.38}$$

where London coefficient is Λ, a phase of superconductor is φ, a vector potential is $\mathbf{A}_{vp}$. For loop superconductor with junction, line integration of equation (2.1.38) is taken alone given closed arbitrary curve C in the loop.

$$\Lambda\oint_C \mathbf{j}\cdot\mathrm{d}\mathbf{l} = \oint_C (\hbar\boldsymbol{\nabla}\bar{\varphi} - 2e\mathbf{A}_{vp})\cdot\mathrm{d}\mathbf{l} \tag{2.1.39}$$

From London equation, supercurrent is given by $j(x) = j_0\exp(-x/\lambda_L)$ at a depth x from surface of superconductor. Here, λ_L is called as London penetration depth, which is regarded as an index parameter in the analysis of actual superconductor when fabricating superconducting quantum circuit such as qubit, microwave resonator and so on. The penetration depth also depends on material and temperature. When the thickness or width of the superconductor is much less than the penetration depth, there is no current inside the superconductor, i.e., gives $\mathbf{j} = 0$, and thus (2.1.39)

$$\oint_C \boldsymbol{\nabla}\bar{\varphi}\cdot\mathrm{d}\mathbf{l} = \frac{2e}{\hbar}\oint_c \mathbf{A}_{vp}\cdot\mathrm{d}\mathbf{l}\ . \tag{2.1.40}$$

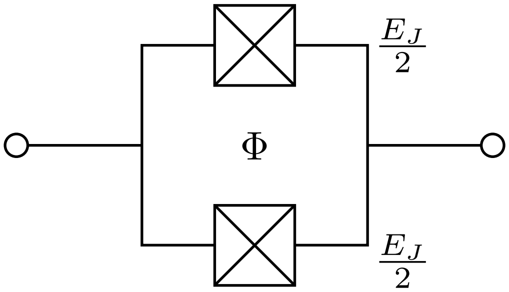

Figure 2.1.3: Circuit schematic of SQUID

The left hand side of (2.1.40) is given by phase difference of the junction. The requirement that the order parameter be single-valued leads to

$$\oint_C \boldsymbol{\nabla}\bar{\varphi}\cdot \mathrm{d}\mathbf{l} = \bar{\varphi} + 2\pi k\,(k\in\mathbb{Z}) \tag{2.1.41}$$

On the other hand, the right hand term can be rewritten by using Stokes' theorem as

$$\frac{2e}{\hbar}\oint_C \mathbf{A}_{vp}\cdot \mathrm{d}\mathbf{l} = \frac{2e}{\hbar}\int_S (\boldsymbol{\nabla}\times\mathbf{A}_{vp})\cdot \mathrm{d}\mathbf{s} \tag{2.1.42}$$

$$= \frac{2e}{\hbar}\int_S \mathbf{B}\cdot \mathrm{d}\mathbf{s} = \frac{2e}{\hbar}\Phi\,. \tag{2.1.43}$$

Using (2.1.41) and (2.1.43) in (2.1.40) gives the flux quntization

$$\Phi_0\left(\frac{\bar{\varphi}}{2\pi} + k\right) = \Phi\,, \tag{2.1.44}$$

where $\Phi_0 = h/(2e)$.

2.1.6 Superconducting quantum interference device (SQUID)

Superconducting quantum interference device (SQUID) is based on superconducting loop with Josephson junction (shown in figure 2.1.3) [3, 120, 45].

dc-SQUID

Potential energy of the dc-SQUID U_{squid} is calculated as

$$U_{\mathrm{squid}} = -\frac{E_J}{2}\cos\varphi_1 - \frac{E_J}{2}\cos\varphi_2 \tag{2.1.45}$$

$$= -E_J\cos\left(\frac{\varphi_1+\varphi_2}{2}\right)\cos\left(\frac{\varphi_1-\varphi_2}{2}\right), \tag{2.1.46}$$

where φ_i is phase drop at each junction. To quantize the flux 2.1.5, total phase is zero along the loop with external flux Φ penetrating the SQUID loop:

$$2\pi\frac{\Phi}{\Phi_0}+\varphi_1-\varphi_2=0\,. \tag{2.1.47}$$

Thus, Potential energy (2.1.46) is rewritten by

$$\begin{aligned} U_{\text{squid}} &= -E_J\cos\left(\frac{\varphi_1+\varphi_2}{2}\right)\cos\left(\pi\frac{\Phi}{\Phi_0}\right) && (2.1.48)\\ &= -E_{\text{J,squid}}(\Phi)\cos\left(\frac{\varphi_1+\varphi_2}{2}\right), && (2.1.49) \end{aligned}$$

where $E_{\text{J,squid}} := E_J\cos\left(\pi\Phi/\Phi_0\right)$. Comparing with the single Josephson junction 2.1.4, SQUID can be regarded as the tunable Josephson junction by external flux.

Screening parameter

The screening parameter [224, 195] is defined as the ratio of the loop inductance of the SQUID to the Josephson inductance,

$$\beta_{\text{s}} := \frac{L_g}{L_J}=\frac{L_gI_c}{\Phi_0/(2\pi)}\,. \tag{2.1.50}$$

Thus, when the loop inductance becomes large, circulating current does not change by external flux.

2.2 Superconducting microwave circuit

In general, cavity in circuit composes two elements, one element is capacitance C and the other is inductance L in circuit. Using superconducting material at low temperature, circuit has ideally no resistance R, which allows for the description in terms of an ideal harmonic oscillator. The other view point of resonator is characterised by angular frequency $\omega_r := 1/\sqrt{LC}$ and characteristic impedance $Z_r := \sqrt{L/C}$. On the capacitance, charge Q is stored and related to current I through charge conservation. The flux Φ along the inductance depends on voltage according to the Farady's induction law,

$$\begin{aligned} Q(t) &= \int_{t_0}^{t} I(t')\,\mathrm{d}t'\ , && (2.2.1)\\ \Phi(t) &= \int_{t_0}^{t} V(t')\,\mathrm{d}t'\ . && (2.2.2) \end{aligned}$$

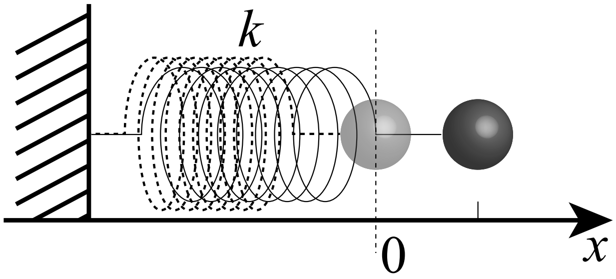

Figure 2.2.1: Harmonic oscillator

2.2.1 Harmonic oscillator

Before starting the analysis of the superconducting quantum circuit, a simple harmonic oscillator is prepared. Almost all superconducting quantum circuit can be described as the harmonic oscillator system with some perturbation. A classical mechanical oscillator with its mass m and the angular frequency ω has the kinetic and potential energy $\mathscr{T}$ and $\mathscr{U}$,

$$\mathscr{T} = \frac{1}{2}m\dot{q}^2 \, , \, \mathscr{U} = \frac{1}{2}m\omega^2 q^2 \, , \tag{2.2.3}$$

where q is the generalized coordinate. Then the Lagrangian is given by

$$\mathcal{L}(q, \dot{q}) = \mathscr{T} - \mathscr{U} = \frac{1}{2}m\dot{q}^2 - \frac{1}{2}m\omega^2 q^2 \, . \tag{2.2.4}$$

The momentum conjugate to q is given by

$$p = \frac{\partial \mathcal{L}}{\partial \dot{q}} = m\dot{q} \, , \tag{2.2.5}$$

Legendre transformation leads to the Hamiltonian

$$\begin{aligned} \mathcal{H} &= p\dot{q} - \mathcal{L} && (2.2.6) \\ &= \frac{1}{2m}p^2 + \frac{1}{2}m\omega^2 q^2 \, . && (2.2.7) \end{aligned}$$

To transform from classical physics to quantum physics, we replace the canonical valuables q and p with the operators and introduce the commutation relation,

$$[\hat{q}, \hat{p}] = i\hbar \, . \tag{2.2.8}$$

In the case of the harmonic oscillator, it is useful to introduce the ladder operators defined as

$$\hat{a} := \sqrt{\frac{m\omega}{2\hbar}}\left(\hat{q} + \frac{i}{m\omega}\hat{p}\right), \tag{2.2.9}$$

$$\hat{a}^\dagger := \sqrt{\frac{m\omega}{2\hbar}}\left(\hat{q} - \frac{i}{m\omega}\hat{p}\right). \tag{2.2.10}$$

One can show that these ladder operators satisfy the commutation relation

$$\left[\hat{a}, \hat{a}^\dagger\right] = \frac{1}{i\hbar}[\hat{q}, \hat{p}] = 1\,. \tag{2.2.11}$$

Using these ladder operators, q and p are written as,

$$\hat{q} = \sqrt{\frac{\hbar}{2}\frac{1}{m\omega}}\left(\hat{a}^\dagger + \hat{a}\right), \tag{2.2.12}$$

$$\hat{p} = i\sqrt{\frac{\hbar}{2}m\omega}\left(\hat{a}^\dagger - \hat{a}\right). \tag{2.2.13}$$

Then Hamiltonian (2.2.7) are finally written as

$$\mathcal{H} = \frac{1}{4}\hbar\omega\left(\hat{a}^\dagger + \hat{a}\right)^2 - \frac{1}{4}\hbar\omega\left(\hat{a}^\dagger - \hat{a}\right), \tag{2.2.14}$$

$$= \frac{1}{2}\hbar\omega\left(\hat{a}^\dagger\hat{a} + \hat{a}\hat{a}^\dagger\right), \tag{2.2.15}$$

$$= \hbar\omega\left(\hat{a}^\dagger\hat{a} + \frac{1}{2}\right). \tag{2.2.16}$$

The last term of Hamiltonian $1/2$ represents the zero point fluctuation. It is often omitted from the Hamiltonian because in usual physical system, it is just offset of the energy. Thus, the Hamiltonian of the harmonic oscillator is written as

$$\mathcal{H} = \hbar\omega\hat{a}^\dagger\hat{a}\,. \tag{2.2.17}$$

2.2.2 Lagrangian for the LC resonator

To analyze the dynamics of a superconducting quantum circuit, a linear LC oscillator is classically described, which has an ideal capacitor and an ideal inductor. In the LC resonator circuit shown in figure 2.2.2, electrical energy stored in the capacitance C and magnetic energy stored in the inductance L oscillate out-of-phase with each other. To contrast with Sec. 2.2.1, in this system, usually electrical energy is analogous to "kinetic energy" and magnetic energy is analogous to "potential energy" of the harmonic oscillator.

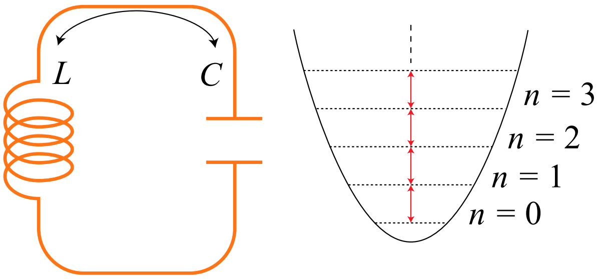

Figure 2.2.2: Schematic of LC resonator

In general, at arbitrarily time t, both electrical and magnetic energies are obtained from voltage and current, and expressed in terms of flux Φ (2.2.2) as canonical coordinate [55]

$$\mathscr{T}_{LC} := \mathscr{E}_E(t) = \int_{-\infty}^{t} CV(t')\,\mathrm{d}t' = \int_{-\infty}^{t} C\frac{\mathrm{d}\Phi(t')}{\mathrm{d}t'}\,\mathrm{d}t' = \frac{1}{2}C\dot{\Phi}^2\,, \tag{2.2.18}$$

$$\mathscr{U}_{LC} := \mathscr{E}_B(t) = \int_{-\infty}^{t} LI(t')\,\mathrm{d}t' = \int_{-\infty}^{t} L\int_{-\infty}^{t'} \frac{\mathrm{d}I(t'')}{\mathrm{d}t''}\,\mathrm{d}t'\,\mathrm{d}t'' \tag{2.2.19}$$

$$= \int_{-\infty}^{t}\int_{-\infty}^{t'} V(t'')\,\mathrm{d}t'\,\mathrm{d}t'' = \int_{-\infty}^{t} \Phi(t')\,\mathrm{d}t' = \frac{1}{2}L\Phi^2\,, \tag{2.2.20}$$

The Lagrangian of this system is defined as the difference between kinetic (electrical) and potential (magnetic) energy, and expressed as,

$$\mathcal{L}_{LC}(\Phi, \dot{\Phi}) = \mathscr{T}_{LC} - \mathscr{U}_{LC} = \frac{1}{2}C\dot{\Phi}^2 - \frac{1}{2}L\Phi^2\,. \tag{2.2.21}$$

Then the canonical conjugate valuable is

$$\frac{\mathrm{d}\mathcal{L}_{LC}}{\mathrm{d}\dot{\Phi}} = C\dot{\Phi}(t) \tag{2.2.22}$$

$$=CV(t) = \int_{-\infty}^{t} C\frac{\mathrm{d}V(t')}{\mathrm{d}t'}\,\mathrm{d}t' = \int_{-\infty}^{t} I(t')\,\mathrm{d}t' = Q\,, \tag{2.2.23}$$

where Farady' low (2.2.2) and equation (2.2.1) are used. The above equation show that the canonical conjugate valuable corresponds to the charge Q on capacitor. Hamiltonian of this system is generated by Legendre transformation of the Lagrangian with canonical valuables Q and Φ as

$$\mathcal{H}_{LC} = Q\dot{\Phi} - \mathcal{L}_{LC} = \frac{Q^2}{2C} + \frac{\Phi^2}{2L}\,. \tag{2.2.24}$$

This Hamiltonian has the same form as mechanical oscillator Hamiltonian (2.2.7). The correspondences between the canonical variables and coefficient parameters are given by,

$$q \to Q\,, p \to \Phi \tag{2.2.25}$$

$$\frac{1}{m\omega^2} \to C\,,\ m \to L\,,\ \omega \to \frac{1}{\sqrt{LC}}\,. \tag{2.2.26}$$

Then the canonical variables can be quantized by introducing the commutation relation,

$$\left[\hat{\Phi}, \hat{Q}\right] = \hat{\Phi}\hat{Q} - \hat{Q}\hat{\Phi} = i\hbar\,. \tag{2.2.27}$$

From equation (2.2.9) and (2.2.10), the standard annihilation $\hat{a}$ and creation $\hat{a}$ operators of harmonic oscillator are written as

$$\hat{\Phi} = \Phi_{\text{zpf}}\left(\hat{a}^\dagger + \hat{a}\right)\,, \tag{2.2.28}$$

$$\hat{Q} = iQ_{\text{zpf}}\left(\hat{a}^\dagger - \hat{a}\right)\,, \tag{2.2.29}$$

where characteristic zero-point fluctuations of the flux and charge are given by

$$\Phi_{\text{zpf}} = \sqrt{\frac{\hbar}{2}\frac{1}{\omega_r C}} = \sqrt{\frac{\hbar}{2}Z_r}\,, \tag{2.2.30}$$

$$Q_{\text{zpf}} = \sqrt{\frac{\hbar}{2}\omega_r C} = \sqrt{\frac{\hbar}{2}\frac{1}{Z_r}}\,. \tag{2.2.31}$$

2.2.3 Coplanar waveguide resonator

To form harmonic oscillator in superconducting circuit, there are various structures pattering on planar circuit [196]. There are several styles of planar resonators, each characterized by a unique electric and magnetic field pattern. One of the most commonly used on-chip resonator styles is the “coplanar waveguide” (CPW) resonator. An on-chip resonator is formed from thin-films deposited onto a substrate. The resonator structure is defined from the patterning of a thin metallic film which is deposited on the surface.

The coplanar waveguide is catheterized by center line (feed line) and a plane on either side, where width of center line is w, gaps between center line and ground plane is s, and thickness of the film t (shown in the figure 2.2.4). Although the capacitance and inductance of LC resonator describing above section ideally completely are separated each other so called lamped elements, coplanar waveguide have distributed small element of capacitor and inductor. The capacitance of coplanar waveguide is defined in terms of the potential difference between center line and ground plane on either side. The inductance of the coplanar waveguide is defied the parallel lines of the center line and ground plane. The

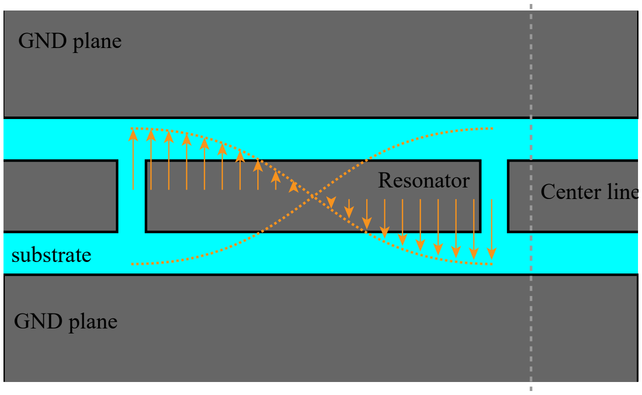

Figure 2.2.3: Schematic of the coplaner waveguide

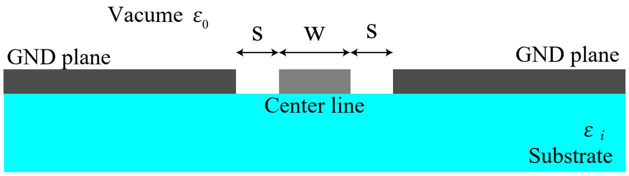

Figure 2.2.4: Cross section of the coplaner waveguide

electromagnetic field is traveling along the feed line. This structure is the 2D analogy of the coaxial cable (3D line) in 2D-planar circuit.

To generate cavity in this 2D form, one needs to prepare "mirror" for the electrical microwave. In electrical microwave circuit, there are several ways to make a mirror. When impedance has a spatial discontiunity, microwave along the feed line are refracted at the discontinuous point. For example, at open end of the feed line, voltage is maximum and there is no current because of capacitance between end of center line and across side (2.2.3). Then two such open end are produced in feed line, there is one isolated line from electrically by capacitance. In this isolated line form resonator as Fabry-Perot cavity, where capacitance act as mirror.

Transmission line resonator

To find modes of a distributed resonator, we consider telegrapher model of an open-ended transmission line resonator of length d. The i-th LC resonator have capacitance C_0 and inductance L_0. Then the electrical energy $Q_k^2/(2C_0)$ is stored in the capacitance. The magnetic energy associated with the inductance is $\Delta\Phi_k^2/(2L_0)$, where $\Delta\Phi_k = \Phi_{k+1} - \Phi_k$ is difference of flux nodes. Then classical Hamiltonian of this system corresponding figure 2.2.4 is described as,

$$\mathcal{H}_{\text{Tel}} = \sum_{k=0}^{m-1} \left[\frac{1}{2C_0} Q_k^2 + \frac{1}{2L_0} (\Delta\Phi_n)^2 \right] . \tag{2.2.32}$$

Assuming that the size of the unit cell δx be taken zero, system become a continuum limit of the Hamiltonian. For the mathematical manipulation, capacitance and inductance are rewritten $C_0 = c_0 \delta x$ and $L_0 = l_0 \delta x$, where c_0 and l_0 are the capacitance and inductance of per unit length. Then continuum flux variable $\Phi(x_k) = \Phi_k$ and charge density $Q(x_k) = Q_k/\delta x$ are defined. Taking the continuum limit $\delta x \to 0$ with maintaining the total length $d = m\delta x$ constant, we obtain the continuous Hamiltonian

$$\mathcal{H}_{\text{cpw}} = \int_0^d \left[\frac{1}{2c_0} Q(x)^2 + \frac{1}{2l_0} \left(\frac{\partial \Phi(x)}{\partial x} \right)^2 \right] \mathrm{d}x \ , \tag{2.2.33}$$

$$\tag{2.2.34}$$

where the difference of the flux nodes replacing with the spatial derivative according to

$$\frac{\partial \Phi(x)}{\partial x} = \lim_{\delta x \to 0} \frac{\Phi_{k+1} - \Phi_k}{\delta x} . \tag{2.2.35}$$

In this continuum model, propagation of the electromagnetic wave along the transmission line is described by the wave equation,

$$v_0^2 \frac{\partial^2 \Phi(x,t)}{\partial x^2} - \frac{\partial^2 \Phi(x,t)}{\partial t^2} = 0 \, , \tag{2.2.36}$$

where $v_0 = 1/\sqrt{c_0 l_0}$ is the speed of the electromagnetic wave in the medium. Equation (2.2.36) can be solved formally as

$$\Phi(x,t) = \sum_{m=0}^{\infty} u_m(x) \Phi_m(t) \, , \tag{2.2.37}$$

$$\ddot{\Phi}_m = -\omega_m^2 \Phi_m \, , \tag{2.2.38}$$

where $u_m(x) = A_{um} \cos{(k_m + \varphi_m)}$ with amplitude of the mode and wave vector $k_m = \omega_m / v_0$ and phase φ_m. Then taking into account the wave equation to solve Hamiltonian, Hamiltonian can be expressed in the decomposed form as

$$\mathcal{H}_{\text{cpw}} = \sum_{m=0}^{\infty} \left[\frac{Q_m^2}{2C_{\text{cpw}}} + \frac{1}{2} C_{\text{cpw}} \omega_m \Phi_m^2 \right] \tag{2.2.39}$$

Following the canonical quantization procedure, with characteristic impedance $Z_m = \sqrt{L_m/C_m}$ canonical conjugate operators are defined as

$$\hat{\Phi}_m = \sqrt{\frac{\hbar}{2} Z_m} \left(\hat{a}_m^\dagger + \hat{a}_m\right) , \tag{2.2.40}$$

$$\hat{Q}_m = \sqrt{\frac{\hbar}{2} \frac{1}{Z_m}} \left(\hat{a}_m^\dagger - \hat{a}_m\right) \tag{2.2.41}$$

where Φ_m and Q_m satisfy the canonical commutation relation $\left[\hat{\Phi}_m, \hat{Q}_m\right] = i\hbar$. Finally, the Hamilronian of the transmission resonator is given by

$$\mathcal{H}_{\text{cpw}} = \sum_{m=0}^{\infty} \hbar\omega_m \hat{a}_m^\dagger \hat{a}_m . \tag{2.2.42}$$

2.3 Superconducting qubit

For quantum computing, only two states are interested for computational space in the quantum system with multi levels. One of the easiest way for two energy states to be separated from other states in the system is that making the energy gap well differ from other energy gap in the system. To obtain the two level system, these anharmonic level systems having the different energy gaps emerge through a clever combination of macroscopic quantum states governing superconductors and nonlinear phenomena occurring at their interfaces (junctions), which are known as superconducting qubits. In this section, a couple of types of superconducting qubit are introduced. Dividing types, one is charge based qubit and the other is current based qubit. The charge based qubit has a island capacitively separated by Josephson junction, on the other hand, the current based qubit has the loop with the Josephson junction.

2.3.1 Charge (density) based regime

A superconducting qubit in the charge based regime has the island to confine the Cooper pair [175]. The existence probability at the island makes the superposition states.

Cooper pair box qubit

To analyse the Cooper pair box shown in figure 2.3.1, the generalized coordinate of the circuit is taken flux as the time integral of the voltage. Accompanying with magnetic flux

Φ as generalized coordinate, Kinetic energy $\mathscr{T}_{cq}$ and potential energy $\mathscr{U}_{cq}$ are expressed,

$$\begin{aligned}\mathscr{T}_{cgq} &= \frac{1}{2}C_J\dot{\Phi}^2 + \frac{1}{2}C_g\left(\dot{\Phi} - V_g\right)^2 && (2.3.1)\\ &= \frac{1}{2}\left(\frac{\hbar}{2e}\right)^2 C_J\dot{\varphi}^2 + \frac{1}{2}C_g\left(\frac{\hbar}{2e}\dot{\varphi} - V_g\right)^2, && (2.3.2)\\ \mathscr{U}_{cgq} &= -E_J\cos\left(\frac{\hbar}{2e}\frac{\Phi}{\Phi_0}\right) && (2.3.3)\\ &= -E_J\cos\left(\varphi\right). && (2.3.4)\end{aligned}$$

where $\Phi = (\hbar/2e)\varphi$ and $\dot{\Phi} = (\hbar/2e)\dot{\varphi}$ are used. Then Lagrangian of the charge qubit is given by,

$$\begin{aligned}\mathcal{L}_{cgq}(\varphi, \dot{\varphi}) &= \mathscr{T}_{cgq} - \mathscr{U}_{cgq} && (2.3.5)\\ &= \frac{1}{2}\left(\frac{\hbar}{2e}\right)^2 C_J\dot{\varphi}^2 + \frac{1}{2}C_g\left(\frac{\hbar}{2e}\dot{\varphi} - V_g\right)^2 + E_J\cos\left(\varphi\right). && (2.3.6)\end{aligned}$$

From this Lagrangian, generalized momentum q conjugate to phase difference φ is derived as

$$\begin{aligned}q = \frac{\partial\mathcal{L}_{cgq}}{\partial\dot{\varphi}} &= \left(\frac{\hbar}{2e}\right)^2 C_J\dot{\varphi} + \frac{\hbar}{2e}C_g\left(\frac{\hbar}{2e}\dot{\varphi} - V_g\right) && (2.3.7)\\ &= \frac{\hbar}{2e}Q\,, && (2.3.8)\\ & && (2.3.9)\end{aligned}$$

where

$$Q = \frac{\hbar}{2e}C_J\dot{\varphi} + C_g\left(\frac{\hbar}{2e}\dot{\varphi} - V_g\right). \qquad (2.3.10)$$

where Q is a charge in the island.

Hamiltonian is obtained by taking by Legendre transformation of the Lagrangian as

$$\begin{aligned}\mathcal{H}_{cgq} &= q\dot{\varphi} - \mathcal{L} && (2.3.11)\\ &= \frac{1}{2}\left(\frac{\hbar}{2e}\right)^2 C_J\dot{\varphi}^2 + \frac{1}{2}\left(\frac{\hbar}{2e}\right)^2 C_g\dot{\varphi}^2 - \frac{1}{2}C_gV_g^2 - E_J\cos(\varphi)\,. && (2.3.12)\end{aligned}$$

The number of the Cooper pairs n_{cp} for a charge Q is calculated as

$$n_{cp} = \frac{Q}{2e} = \frac{q}{\hbar}\,. \qquad (2.3.13)$$

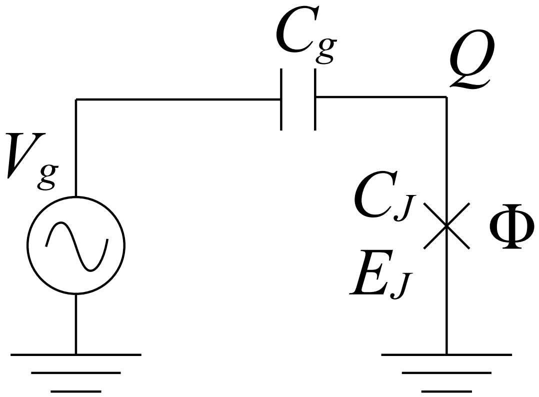

Figure 2.3.1: Schematic circuit of charge qubit

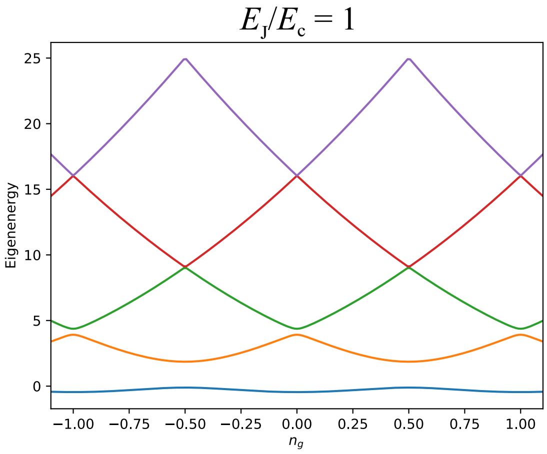

Figure 2.3.2: Energy diagram of charge qubit with $E_J/E_c = 1$

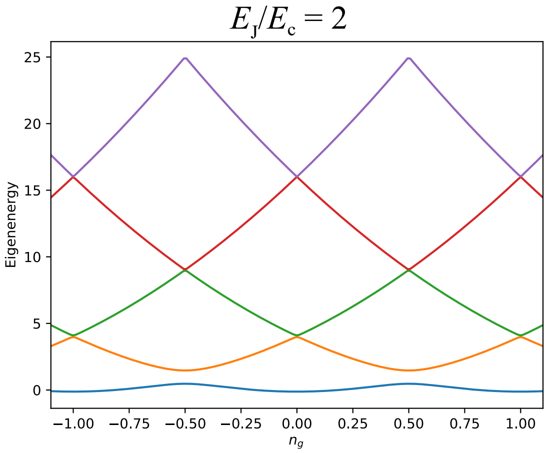

Figure 2.3.3: Energy diagram of charge qubit with $E_J/E_c = 2$

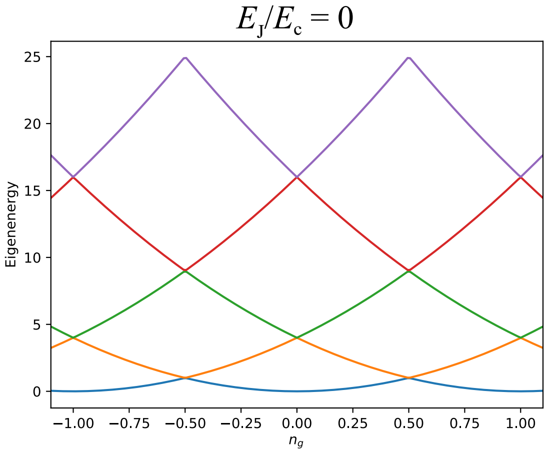

Figure 2.3.4: Energy diagram of non charge qubit with $E_J/E_c = 0$ for reference

By gate bias voltage V_g, a certain amount of number of Cooper pairs are depend on the gate voltage, with $Q_g = C_g V_g$,

$$n_g = -\frac{C_g V_g}{2e}\,. \tag{2.3.14}$$

Then Hamiltonian (2.3.11) is rewritten as,

$$\mathcal{H}_{cgq} = \frac{(2e)^2}{2(C_J + C_g)}(n - n_g)^2 - \frac{(2e)^2}{2C_g}n_g^2 - E_J\cos(\varphi) \tag{2.3.15}$$

$$= 4E_c(n - n_g)^2 - E_J\cos\varphi - \frac{(2e)^2}{2C_g}n_g^2\,, \tag{2.3.16}$$

where $E_c := e^2/(2C_\Sigma)$ is called named as Josephson charging energy and $C_\Sigma = C_J + C_g$. Since the last term of the Hamiltonian does not depend on n_{cp} or φ, it does not affect eigenstate or eigenvalue, and thus it can be omitted from the Hamiltonian as

$$\mathcal{H}_{cpg} = 4E_c(n_{cp} - n_g)^2 - E_J\cos\varphi\,. \tag{2.3.17}$$

In order to consider energy levels for quantum gate operation, commutation relation for canonical quantization is first introduced about canonical variables φ and q,

$$[\hat{\varphi}, \hat{q}] = i\hbar\,, \tag{2.3.18}$$

$$[\hat{\varphi}, \hat{n}_{cp}] = i\,, \tag{2.3.19}$$

where the definition of n_{cp} in (2.3.13) is used. The notation $\hat{\cdot}$ is used to clarify quantization. Since $\hat{n}_{cp}$ is Hermitian operator, it can be decomposed by using the eigenstate $|n_{cp}\rangle$ and eigenvalue n_{cp} as

$$\hat{n}_{cp} = \sum_{n_{cp}} n_{cp} \left| n_{cp} \right\rangle \left\langle n_{cp} \right| \ . \tag{2.3.20}$$

Raising and lowering operators of charge qubit are given by $\exp(\pm i\hat{\varphi})$ (see B.1),

$$\exp(i\hat{\varphi}) = \sum_{n_{cp}} \left| n_{cp}+1 \right\rangle \left\langle n_{cp} \right| , \ \exp(-i\hat{\varphi}) = \sum_{n_{cp}} \left| n_{cp} \right\rangle \left\langle n_{cp}+1 \right| \ . \tag{2.3.21}$$

Then the cosine function in the potential energy is decomposed by the eigenstates as

$$\cos\hat{\varphi} = \frac{1}{2}\left[\exp(i\hat{\varphi}) + \exp(-i\hat{\varphi})\right] = \frac{1}{2}\sum_{n_{cp}}\Big(\left| n_{cp}+1 \right\rangle \left\langle n_{cp} \right| + \left| n_{cp} \right\rangle \left\langle n_{cp}+1 \right| \Big) \ . \tag{2.3.22}$$

Using equations (2.3.20) and (2.3.22), the Hamiltonian of charge qubit (2.3.11) is canonically quantized as,

$$\mathcal{H}_{cgq} = 4E_c \sum_{n_{cp}} (n_{cp} - n_g)^2 \left| n_{cp} \right\rangle \left\langle n_{cp} \right| - \frac{1}{2}E_J \sum_{n_{cp}} \Big(\left| n_{cp}+1 \right\rangle \left\langle n_{cp} \right| + \left| n_{cp} \right\rangle \left\langle n_{cp}+1 \right| \Big) \ . \tag{2.3.23}$$

Then picking up the lowest two energy levels makes two level system, because other high order energy state having different energy gap [21].

$$\begin{aligned} \mathcal{H}_{cgq} &\approx 4E_c\Big[n_g^2 \left|0\right\rangle\!\left\langle 0\right| + (1-n_g)^2 \left|1\right\rangle\!\left\langle 1\right|\Big] - \frac{1}{2}E_J\Big(\left|1\right\rangle\!\left\langle 0\right| + \left|0\right\rangle\!\left\langle 1\right|\Big) && (2.3.24)\\ &= 4E_c\left(n_g - \frac{1}{2}\right)\sigma_z - \frac{1}{2}E_J\sigma_x + 2E_c\big[(1-n_g)^2 + n_g\big]\sigma_0 && (2.3.25)\\ &\to 4E_c\left(n_g - \frac{1}{2}\right)\sigma_z - \frac{1}{2}E_J\sigma_x && (2.3.26) \end{aligned}$$

where in going form (2.3.25) to (2.3.26), we have omitted the constant term, and use the Pauli operators (1.2.12)-(1.2.14).

Transmon qubit

To get more insensitive charge qubit about the flux noise, usually other shunt large capacitance C_s are added to the charge qubit. With the large capacitance, energy of the total capacitance $E_c = 2e/(C_J + C_s)$ including Josephson capacitance and shunt capacitance $C_J \ll C_s$ is much smaller than original cooper-pair-box-based qubit [140, 216, 20]. Comparing the E_c with the Josephson energy is better to consider the qubit regime about the total capacitance of the system. In the regime $E_J \gg E_c$, qubit is specially so-called

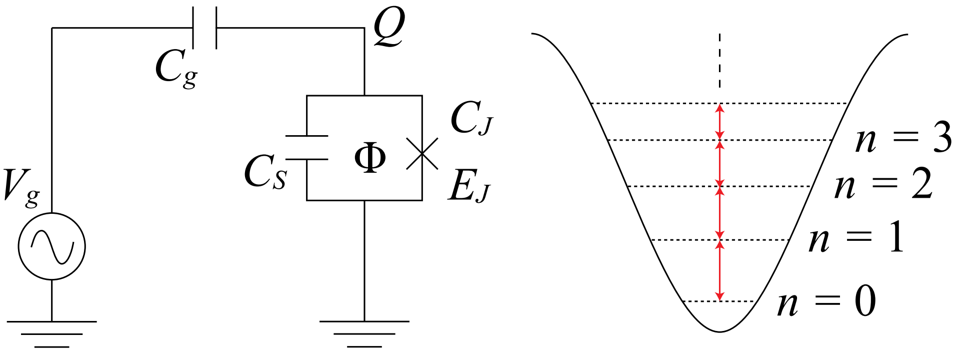

Figure 2.3.5: Circuit of Transmon qubit

Transmon. Hamiltonian of the transmon qubit are similar to that of the charge qubit, but bias voltage n_g is temporally fixed then it is offset,

$$\begin{aligned}\mathcal{H}_{tmon} &= 4E_c n_{cp}^2 - E_J \cos\varphi && (2.3.27)\\ &= 4E_c n_{cp}^2 + \frac{1}{2}E_J\varphi^2 - E_J\left(\cos\varphi + \frac{1}{2}\varphi^2\right) && (2.3.28)\\ &= 4E_c n_{cp}^2 + \frac{1}{2}E_J\varphi^2 - E_J\left(\sum_{n=0}^{\infty}\frac{(-1)^n}{(2n)!}\varphi^{2n} + \frac{1}{2}\varphi^2\right) && (2.3.29)\end{aligned}$$

Here, first two terms are the harmonic oscillator, and thus annihilation and creation operators $\hat{b}^\dagger$ and $\hat{b}$ can be introduced in the standard manner.

$$\hat{\varphi} = \left(\frac{2E_c}{E_J}\right)^{1/4}\left(\hat{b}^\dagger + \hat{b}\right), \tag{2.3.30}$$

$$\hat{n}_{cp} = \frac{i}{2}\left(\frac{E_J}{2E_c}\right)^{1/4}\left(\hat{b}^\dagger - \hat{b}\right). \tag{2.3.31}$$

In the transmon regime $E_J \gg E_c$, the phase difference is much small [140] $\Delta\hat{\varphi} = \sqrt{\langle\hat{\varphi}^2\rangle - \langle\hat{\varphi}\rangle^2} \ll 1$, the terms of higher order in $\hat{\varphi}$ can be ignored. Then transmon Hamiltonian (2.3.29) is approximated as,

$$\begin{aligned}\mathcal{H}_{tq} &\approx 4E_c n_{cp}^2 + \frac{1}{2}E_J\varphi^2 - E_J\left(-\frac{1}{2!}\varphi^2 + \frac{1}{4!}\varphi^4 + \frac{1}{2}\varphi^2\right) && (2.3.32)\\ &= 4E_c n_{cp}^2 + \frac{1}{2}E_J\varphi^2 - E_J\frac{1}{4!}\varphi^4 && (2.3.33)\\ &= \sqrt{8E_cE_J}\left(\hat{b}^\dagger\hat{b} + \frac{1}{2}\right) - \frac{E_c}{12}\left(\hat{b}^\dagger + \hat{b}\right)^4 && (2.3.34)\end{aligned}$$

Moreover using rotating wave approximation [46, 140, 20], with an unequal amount of b and $b^\dagger$ causes oscillation on rotating frame of ω_{tmon}. When oscillating frequency is lager

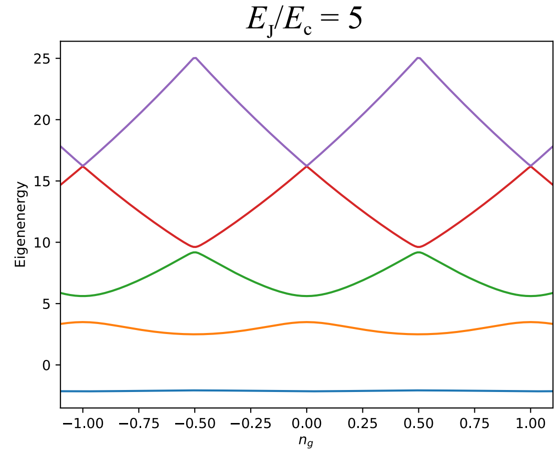

Figure 2.3.6: Energy diagram of Transmon with $E_J/E_c = 5$

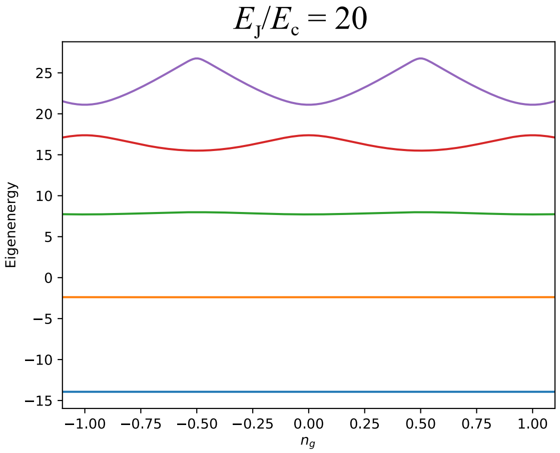

Figure 2.3.7: Energy diagram of Transmon with $E_J/E_c = 20$

than the magnitude of its term, this term is averaged out and can be ignored. After this approximation, only $(\hat{b}^\dagger + \hat{b})^4 \approx 12\hat{b}^\dagger\hat{b} + 6\hat{b}^\dagger\hat{b}^\dagger\hat{b}\hat{b}$ remain.

$$\mathcal{H}_{tq}^{\mathrm{RWA}} = \hbar\omega_{tq}\hat{b}^\dagger\hat{b} - \frac{1}{2}E_c\hat{b}^\dagger\hat{b}^\dagger\hat{b}\hat{b}\,. \tag{2.3.35}$$

2.3.2 Flux (current) based regime

Current in superconductor is flow of the aggregating cooper pairs. When superconductor is formed loop with Josephson junction and external magnetic field is applied perpendicular to the loop, flux of magnetic field through the closed loop is quantized [143]. However, when external flux is around half of flux quantum, flux through the junction and current flows both clockwise and counterclockwise directions within superposition state.

In this regime, Cooper pair is not localized in superconductor across island, completely distributed in superconductor so that current arise with one wave function.

Flux qubit

To derive flux qubit Hamiltonian, the kinetic and potential energy of the circuit with junction are given by

$$\mathscr{T}_{rf} = \frac{1}{2}C_J\dot{\Phi}^2 = \frac{1}{2}\left(\frac{\hbar}{2e}\right)^2 C_J\dot{\varphi}_{rf}^2 \tag{2.3.36}$$

$$\mathscr{U}_{rf} = \frac{1}{2}L_g I_{cir}^2 - E_J\cos\left(\frac{2e}{\hbar}\frac{\Phi}{\Phi_0}\right), \tag{2.3.37}$$

$$= \frac{1}{2}\frac{1}{L_g}\left(\frac{\hbar}{2e}\right)^2(\varphi_{rf}-\varphi_{ext})^2 - E_J\cos\left(\varphi_{rf}\right), \tag{2.3.38}$$

and then, Lagrangian is expressed as

$$\mathcal{L}_{rf} = \mathscr{T}_{rf} - \mathscr{U}_{rf} \tag{2.3.39}$$

$$= \frac{1}{2}\left(\frac{\hbar}{2e}\right)^2 C_J\dot{\varphi}_{rf}^2 - \frac{1}{2}\frac{1}{L_g}\left(\frac{\hbar}{2e}\right)^2(\varphi_{rf}-\varphi_{ext})^2 + E_J\cos\left(\varphi_{rf}\right). \tag{2.3.40}$$

Three junction qubit

The most used flux qubit has the tree junction to decrease the screening parameter β_s in section . Two of the three junctions $(j = 1, 2)$ have ideally same size of the junction $(E_{J1} = E_{J2} := E_J)$ and the other junction is small with coefficient $\alpha_J\,(0.5 < \alpha_J < 1)$, so the energy of small junction is $\alpha_J E_J$. This loop of qubit has also the self inductance L_g. The screening parameter $\beta_{s,3JJ}$ is calculated as

$$\beta_{s,3JJ} = \frac{2\pi L_g}{\Phi_0}\left(\frac{1}{I_1}+\frac{1}{I_2}+\frac{1}{I_{\alpha_J}}\right)^{-1} = \frac{\alpha_J}{2\alpha+1}\frac{L_g}{L_J}, \tag{2.3.41}$$

where $I_{1,2,\alpha_J}$ is critical current at junctions, respectably. Thus, Lagrangean of the three junctions flux qubit is given by

$$\mathcal{L}_{3JJ} = \frac{1}{2}C\left(\frac{\hbar}{2e}\right)^2\dot{\varphi}_1^2 + \frac{1}{2}C\left(\frac{\hbar}{2e}\right)^2\dot{\varphi}_2^2 + \alpha\frac{1}{2}C\left(\frac{\hbar}{2e}\right)^2(\dot{\varphi}_1-\dot{\varphi}_2)^2 \tag{2.3.42}$$

$$+ E_J\cos(\varphi_1) + E_J\cos(\varphi_2) + \alpha E_J\cos(\varphi_1-\varphi_2-2\pi\varphi_{ext}) \tag{2.3.43}$$

Then, taking generalized position as $q_i = \varphi_i$, generalized momentum is given by

$$\begin{aligned} p_1 &= \frac{\partial \mathcal{L}}{\partial \dot{\varphi}_1} = C\left(\frac{\hbar}{2e}\right)\dot{\varphi}_1 + \alpha C\left(\frac{\hbar}{2e}\right)(\dot{\varphi}_1 - \dot{\varphi}_2)^2 \\ p_2 &= \frac{\partial \mathcal{L}}{\partial \dot{\varphi}_2} = C\left(\frac{\hbar}{2e}\right)\dot{\varphi}_2 - \alpha C\left(\frac{\hbar}{2e}\right)(\dot{\varphi}_1 - \dot{\varphi}_2)^2 \end{aligned} \tag{2.3.44}$$

The Hamiltonian of the system is derived by Legendre transformation as

$$\mathcal{H}_{3JJ} = \dot{\varphi}_1 p_1 + \dot{\varphi}_2 p_2 - \mathcal{L}_{3JJ} \tag{2.3.45}$$

$$\begin{aligned} &= 4E_c\left(\frac{1+\alpha}{1+2\alpha}p_1^2 + \frac{2\alpha}{1+2\alpha}p_1p_2 + \frac{1+\alpha}{1+2\alpha}p_2^2\right) \\ &- E_J\cos(\varphi_1) - E_J\cos(\varphi_2) - \alpha E_J\cos(\varphi_1 - \varphi_2 - 2\pi\varphi_{ext}) \,. \end{aligned} \tag{2.3.46}$$

2.4 Superconducting quantum circuit

To operate and measure the superconducting qubit introduced in section 2.3, the classical microwave circuit such as coplanar waveguide introduced in section 2.2 is combined together. The combination of superconducting qubit and superconducting resonator by electromagnetic coupling is analogous to optical cavity quantum electro dynamics (cQED), in which the qubit corresponds artificial atom and resonator corresponds optical cavity. In this section, the dynamics of the this superconducting quantum circuit with qubit and resonator is introduced, such as coupling models between the qubit and the resonator, regime of coupling either for frequencies of the system or coupling strength.

2.4.1 Light-matter interaction dynamics in circuit QED

Here, two basic model of coupling between qubit and resonator are introduced. One is so-called Rabi model and the other is Jaynes–Cummings model (JC model). Rabi model describes the system completely with the atom-cavity interaction. JC model is derived from the Rabi model by using the rotating wave approximation (RWA) to ignore the high frequency terms. Using the Pauli operators of qubit $\sigma_{x,y,z}$ (1.2.12)-(1.2.14), creation and annihilation operators of qubit $\sigma_{+,-}$ (1.2.10)-(1.2.11), and creation and annihilation operators of the resonator $a, a^\dagger$ (2.2.9)-(2.2.10), the Rabi model is derived as

$$\mathcal{H}_{\mathrm{rabi}}/\hbar = \frac{1}{2}\omega_q\sigma_z + \omega_q a^\dagger a + g(\sigma_+ + \sigma_-)\left(a^\dagger + a\right) , \tag{2.4.1}$$

where ω_q is the frequency of qubit, ω_r is the frequency of resonator, and g is coupling constant between qubit and resonator.

The Jaynes–Cummings model Hamiltonian of the qubit is described as [21, 102]

$$\mathcal{H}_{\mathrm{JC}}/\hbar = \frac{1}{2}\Delta\sigma_z + \omega_q a^\dagger a + g\big(\sigma_- a^\dagger + \sigma_+ a\big)\,. \tag{2.4.2}$$

Chapter 3

Review of Quantum Information Processing

3.1 Quantum Computing in Gate model

The origin of the concept of the quantum computer would be Richard P. Feynman's 1981 lecture [70]. In this lecture, Feynman spoke about how nature can be simulated by classical computers,

> ... nature isn't classical, dammit, and if you want to make a simulation of Nature, you'd better make it quantum mechanical ...

As he expected, classical computers can still only simulate as high as 45 qubits, even today, nearly 40 years later and with such advanced technology. Remarkably, the simulation of 45-qubit combines 8,192 computational nodes and 0.5 petabytes of memory [101]. This is probably the limit of the classical computer [248]. The supremacy of the quantum computer have been demonstrated if the number of calculations beyond the limit of the classical computer can be achieved [197]].

What can a quantum computer with this advantage do? As Feynman mentioned, it can simulate quantum systems. For example, it can find the exact solution of the electronic state of a molecule, which is a complex quantum system [233, 231]. Despite the fact that this solution cannot be obtained by classical computers, it is needed not only in the fields of condensed matter physics, materials engineering, and chemistry, but also in the development of drug discovery, new catalysts, etc. Also, we may be able to elucidate mechanisms such as photosynthesis from a microscopic perspective [172].

These applications will show the advantages of quantum in small-scale circuits, and research will go further in the direction of realizing error-collected quantum computers. As is often said, we may be able to perform the prime factorization of large numbers, and

Name (abbr.)	Symbol	Operator	Matrix
Identity (I)	$\boxed{\mathrm{I}}$	$\hat{I}$	$\begin{pmatrix} 1 & 0 \\ 0 & 1 \end{pmatrix}$
Pauli X (X)	$\boxed{\mathrm{X}}$	$\hat{R}_x(\pi)$	$\begin{pmatrix} 0 & 1 \\ 1 & 0 \end{pmatrix}$
Pauli Y (Y)	$\boxed{\mathrm{Y}}$	$\hat{R}_y(\pi)$	$\begin{pmatrix} 0 & -i \\ i & 0 \end{pmatrix}$
Pauli Z (Z)	$\boxed{\mathrm{Z}}$	$\hat{R}_z(\pi)$	$\begin{pmatrix} 1 & 0 \\ 0 & -1 \end{pmatrix}$
Hadamard (H)	$\boxed{\mathrm{H}}$	$\hat{R}_x(\pi)\hat{R}_y(\pi/2)$	$\frac{1}{\sqrt{2}}\begin{pmatrix} 1 & 1 \\ 1 & -1 \end{pmatrix}$
Phase (S)	$\boxed{\mathrm{S}}$	$\hat{R}_z(\pi/2)$	$\begin{pmatrix} 1 & 0 \\ 0 & i \end{pmatrix}$
$\pi/8$ (T)	$\boxed{\mathrm{T}}$	$\hat{R}_z(\pi/4)$	$\begin{pmatrix} 1 & 0 \\ 0 & e^{i\pi/4} \end{pmatrix}$
Controlled NOT (CNOT)	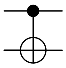	$\lvert 0\rangle\langle 0\rvert \otimes \mathrm{I} + \lvert 1\rangle\langle 1\rvert \otimes \mathrm{X}$	$\begin{pmatrix} 1 & 0 & 0 & 0 \\ 0 & 1 & 0 & 0 \\ 0 & 0 & 0 & 1 \\ 0 & 0 & 1 & 0 \end{pmatrix}$
Controlled Z (Z)	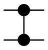	$\lvert 0\rangle\langle 0\rvert \otimes \mathrm{I} + \lvert 1\rangle\langle 1\rvert \otimes \mathrm{Z}$	$\begin{pmatrix} 1 & 0 & 0 & 0 \\ 0 & 1 & 0 & 0 \\ 0 & 0 & 1 & 0 \\ 0 & 0 & 0 & -1 \end{pmatrix}$
SWAP		U_{SWAP12}	
iSWAP	$\boxed{X}$	$\hat{R}_{xx+yy}(-\pi/2)$	$\begin{pmatrix} 1 & 0 & 0 & 0 \\ 0 & 0 & i & 0 \\ 0 & i & 0 & 0 \\ 0 & 0 & 0 & 0 \end{pmatrix}$
Measurement	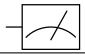	$\mathcal{P}$	

Table 3.1.1: Name, symbol in quantum circuit, operators and represented matrix of the quantum gate for qubit oeprations

solve the parallel search problems. This will require further technological advances and deeper physics exploration.

3.1.1 Gate operations

To operate qubit, quantum operators should be unitary (see Ref [182]). From characters of unitary operation, any quantum operation is reversible [146]. Then total operation of the quantum computing is reversible as well.

Single qubit operations are defined by Pauli matrices (1.2.12)-(1.2.13). For gate operation in quantum information, to simplify the notation, capital characters X, Y, Z are used

$$\mathrm{X} := \sigma_x = \begin{pmatrix} 0 & 1 \\ 1 & 0 \end{pmatrix}, \tag{3.1.1}$$

$$\mathrm{Y} := \sigma_y = \begin{pmatrix} 0 & -i \\ i & 0 \end{pmatrix}, \tag{3.1.2}$$

$$Z := \sigma_z = \begin{pmatrix} 0 & 1 \\ 1 & 0 \end{pmatrix}. \tag{3.1.3}$$

These operations represent π rotation on the Bloch sphere (3.1.1)-(3.1.3) $\mathcal{R}_{x,y,z}(\pi)$, respectably.

Hadamard gate H changes $|0\rangle$ state to $(|0\rangle + |1\rangle)/\sqrt{2}$ and $|1\rangle$ state to $(|0\rangle - |1\rangle)/\sqrt{2}$. It is described as

$$\mathrm{H} = \frac{1}{\sqrt{2}} \begin{pmatrix} 1 & 1 \\ 1 & -1 \end{pmatrix} \tag{3.1.4}$$

This operation is realized by two successive rotations on the Bloch sphere. One way is to use rotations about x and y aces as $\mathcal{R}_x(\pi)\mathcal{R}_y(\pi/2)$ or $\mathcal{R}_y(-\pi/2)\mathcal{R}_x(\pi)$. The other way is to use rotations about y and z axes as $\mathcal{R}_z(\pi)\mathcal{R}_y(-\pi/2)$.

Next, we consider the single qubit operation that change the phase, so-called phase gate S. It is realized by half rotation about Z-axis $\mathcal{R}_z(\pi/2)$. Strictly, the operator changing phase between $|0\rangle$ and $|1\rangle$ is given by

$$\mathcal{R}_\phi = \begin{pmatrix} 1 & 0 \\ 0 & \mathrm{e}^{i\phi} \end{pmatrix}. \tag{3.1.5}$$

Using rotation about z axis (3.1.3), this phase change operation is expressed as

$$\mathcal{R}_\phi = \mathrm{e}^{i\pi/2}\mathcal{R}_{\mathrm{z}}(\phi) \tag{3.1.6}$$

Thus, the phase gate S is given by

$$\mathrm{S} = \begin{pmatrix} 1 & 0 \\ 0 & \mathrm{e}^{i\frac{\pi}{2}} \end{pmatrix} = \begin{pmatrix} 1 & 0 \\ 0 & i \end{pmatrix} = \mathrm{e}^{i\pi/4}\mathcal{R}_{\mathrm{z}}\left(\frac{\pi}{2}\right). \tag{3.1.7}$$

Other specified phase gate, so-called T-gate, is change the phase by quarter of π. This T-gate is given by

$$\mathrm{T} = \begin{pmatrix} 1 & 0 \\ 0 & \mathrm{e}^{i\pi/4} \end{pmatrix} = \mathrm{e}^{i\pi/8}\mathcal{R}_{\mathrm{z}}\left(\frac{\pi}{8}\right). \tag{3.1.8}$$

When basis vector of a qubit state is represented $|0\rangle \rightarrow (1 \;\; 0)^{\mathrm{T}}$ and $|1\rangle \rightarrow (0 \;\; 1)^{\mathrm{T}}$, basis k-qubit state vector is written as product of the qubit. For example, two qubit state is represented as $|00\rangle = (1 \;\; 0 \;\; 0 \;\; 0)^{\mathrm{T}}$, $|01\rangle = (0 \;\; 1 \;\; 0 \;\; 0)^{\mathrm{T}}$, $|10\rangle = (0 \;\; 0 \;\; 1 \;\; 0)^{\mathrm{T}}$, and $|11\rangle = (0 \;\; 0 \;\; 0 \;\; 1)^{\mathrm{T}}$.

To operate two qubits or more, interaction operations are required. In general, one can show the operations on multiple qubits can be decomposed into a set of single qubit operation and two qubits operations. Commonly used two qubit gate operations are controlled-not (CNOT), controlled-phase (CZ), and iSWAP gates.

$$\mathrm{CZ} = \begin{pmatrix} 1 & 0 & 0 & 0 \\ 0 & 1 & 0 & 0 \\ 0 & 0 & 1 & 0 \\ 0 & 0 & 0 & -1 \end{pmatrix}, \tag{3.1.9}$$

$$\mathrm{iSWAP} = \begin{pmatrix} 1 & 0 & 0 & 0 \\ 0 & 0 & i & 0 \\ 0 & i & 0 & 0 \\ 0 & 0 & 0 & 1 \end{pmatrix}. \tag{3.1.10}$$

CNOT gate flips the target qubit state $|t\rangle$ depending on the state of the controlled qubit $|c\rangle$.

$$U_{\mathrm{CNOT}} = |0\rangle\langle 0| \otimes \mathrm{I} + |1\rangle\langle 1| \otimes \mathrm{X} \tag{3.1.11}$$

$$\mathrm{CNOT} = \begin{pmatrix} 1 & 0 & 0 & 0 \\ 0 & 1 & 0 & 0 \\ 0 & 0 & 0 & 1 \\ 0 & 0 & 1 & 0 \end{pmatrix}, \tag{3.1.12}$$

3.1.2 Quantum gate model

Solovay-Kitaev theorem

For the quantum computer, the universal gate set is {CNOT, X, Z} or {CZ, $R_z(-\pi/2)$, $R_z(-pi/2)$}. But for practical purpose, arbitrary one qubit unitary gate can be well approximated by Hadamard (H)-gate, S-gate, and T-gate. (Solovay-Kitaev theorem [51])

$$\mathrm{H} = |+\rangle \langle 0| + |-\rangle \langle 1| \tag{3.1.13}$$

$$\mathrm{S} = |0\rangle \langle 0| + i\,|1\rangle \langle 1| \tag{3.1.14}$$

$$\mathrm{T} = |0\rangle \langle 0| + e^{-i\frac{\pi}{4}}\,|1\rangle \langle 1| \tag{3.1.15}$$

Among these,CZ, H, and S except T is included in the group of Clifford that is projection operators between stabilizer state. Therefor, these gates have good compatibility with the stabilizer code, but logical T-gate cannot directly be operated on it. However, A quantum computer which can only operate the Clifford gates is simulated efficiently in classical computer (Gottesman-Knill theorem [91]), implementation of T-gate is inevitable. Development of stabilizer states is described by updating the group of Pauli operators and that calculation is enough to ability of classical computers.

3.1.3 Quantum algorithms

Quantum computers are capable of processing 2^n states simultaneously using n qubits through quantum mechanical superposition [52, 243]. However, this alone does not mean that the computation is "fast" because only one of the 2^n states is randomly obtained when the result is observed after the computation is completed. Therefore, in order to obtain the desired solution with high probability, it is essential to have an algorithm designed specifically for quantum computers. Such an algorithm is called a quantum algorithm [218, 12, 169].

Grover's algorithm for database search

To search data of interest from a database, Lov K. Grover proposed a quantum algorithm in 1996 [95, 96]. Using the Grover's algorithm can find the data from the database with N items by $\mathcal{O}\left(\sqrt{N}\right)$ query (calling the oracle), although using the classical computer costs $\mathcal{O}(N)$ query. Thus, Grover's algorithm have the quadratic speed up to find the data of interest from the database.

An oracle is an abstract entity that is a black box, but gives you the answer anyway, and does not care how it is implemented (nor does it require that an implementation exist). The computational complexity of a classical algorithm solving a search problem is evaluated by the number of times it asks the classical oracle $\mathscr{O}_c$ if x is a solution. In this way, a uniform evaluation is possible, independent of the details of the problem. Therefor, when the classical oracle is represent the function f_c as

$$f_c(x) = \begin{cases} 0 & \text{(not solution)} \\ 1 & \text{(solution)} \end{cases} \tag{3.1.16}$$

where each element is labeled as n-bit $x = x_1 x_2 \dots x_n$. Using this classical oracle $f(x)$ costs the number of the calling oracle $\mathcal{O}(N)$.

On the other hand, in quantum computation, the quantum oracle $\mathscr{O}_q$ is defined as the one of the unitary operator U_w for solution w. The oracle $\mathscr{O}_q$ is change the phase of ancilla qubit state:

$$|x\rangle\,|-\rangle \xrightarrow{\mathscr{O}_q} (-1)^{f_c(x)}\,|x\rangle\,|-\rangle\ . \tag{3.1.17}$$

This mean that when the input x is solution, the quantum oracle responses the phase flip of the ancilla qubit.

The Grover's algorithm is executed following steps to find M data of interest from the database with N data:

1. prepare all quantum state in the superposition $|s\rangle = \frac{1}{\sqrt{N}}\sum_x |x\rangle$
   To prepare superposition state, all qubit, which initially are $|00\ldots0\rangle$, is applied the Hadamard gate:
   $$|s\rangle := \bigotimes_k^n |H_k\rangle\,|00\ldots0\rangle = \left(\frac{1}{\sqrt{2}}\right)^n \bigotimes_k^n (|0\rangle_k + |1\rangle_k)\,. \tag{3.1.18}$$

2. apply the oracle U_w
   U_w is defined as that for input $|x\rangle$, if x is a solution, multiply by (-1) to flip the phase, if not, do nothing:
   $$U_w\,|x\rangle = \begin{cases} |x\rangle & (x \text{ is not solution}) \\ -\,|x\rangle & (x \text{ is solution}) \end{cases} \tag{3.1.19}$$
   $$U_w = \mathrm{I} - 2 \sum_{w\in \text{ solutions}} |w\rangle\!\langle w|\ , \tag{3.1.20}$$
   where $|w\rangle$ is solution.

3. apply the flip operation about the axis $|s\rangle$ to all state
   The unitary operator U_s is defined as
   $$U_s = 2\,|s\rangle\!\langle s| - \mathrm{I}\,. \tag{3.1.21}$$
   Then applying this operator to current state $|\psi_{\text{current}}\rangle = \alpha\,|s\rangle + \beta\,|s_\perp\rangle$ makes state change the phase about the state of $|s_\perp\rangle$, where $|s_\perp\rangle$ is perpendicular unit vector about $|s\rangle$ and $\langle s|s_\perp\rangle = 0$:
   $$U_s\,|\psi_{\text{current}}\rangle = (2\,|s\rangle\!\langle s| - \mathrm{I})(\alpha\,|s\rangle + \beta\,|s_\perp\rangle) \tag{3.1.22}$$
   $$= \alpha\,|s\rangle\,\langle s|s\rangle + 2\beta\,|s\rangle\,\langle s|s_\perp\rangle - \alpha\,|s\rangle - \beta\,|s_\perp\rangle \tag{3.1.23}$$
   $$= \alpha\,|s\rangle - \beta\,|s_\perp\rangle\ . \tag{3.1.24}$$

4. repeat the step 2 and 3 by k times

5. measure qubits

To evaluate the success probability to solve the problem after k times, we introduce two state $|u\rangle$ and $|v\rangle$:

$$|u\rangle := \frac{1}{\sqrt{N-M}} \sum_{x \notin \text{solutions}} |x\rangle \ , \tag{3.1.25}$$

$$|v\rangle := \frac{1}{\sqrt{M}} \sum_{x \in \text{solutions}} |x\rangle \ . \tag{3.1.26}$$

Here, $|u\rangle$ and $|v\rangle$ separate the Hilbert space, thus, initial superposition state $|s\rangle$ is decomposed by these two basis.

$$|s\rangle = \frac{1}{\sqrt{N}} \sum_x |x\rangle = \sqrt{\frac{N-M}{N}}\, |u\rangle + \sqrt{\frac{M}{N}}\, |v\rangle \tag{3.1.27}$$

$$= \cos\frac{\theta}{2}\, |u\rangle + \sin\frac{\theta}{2}\, |v\rangle \tag{3.1.28}$$

where θ satisfies $\cos\frac{\theta}{2} = \sqrt{\frac{N-M}{N}}$ and $\sin\frac{\theta}{2} = \sqrt{\frac{M}{N}}$ shown in figure 3.1.1. The unitary operator U_w flip the state vector $|s\rangle$ about the $|u\rangle$ because

$$U_w\, |u\rangle = |u\rangle \tag{3.1.29}$$

$$U_w\, |v\rangle = -\, |v\rangle \tag{3.1.30}$$

The unitary operator U_s flip the vector about the $|s\rangle$ axis. Thus, these two unitary operations $U_s U_w$ rotate the $|s\rangle$ by θ. Then, in the Gorover's algorithm, since this operation $U_s U_w$ is repeated by k time, the last state is given by

$$(U_s U_w)^k\, |s\rangle = \cos\left(\frac{2k+1}{2}\theta\right) |u\rangle + \sin\left(\frac{2k+1}{2}\theta\right) |v\rangle \ . \tag{3.1.31}$$

Here, in the most common case of the search problem, the number of the solution is much less than the number of data $M \ll N$. In that time, since $\sin\theta = \sqrt{\frac{M}{N}} \sim 0$, $\theta \sim 0$. Therefor, the probability of $|u\rangle$ become 0 and the one of the $|v\rangle$ become 1 as increasing the repetition time k. This show that the probability that the solution will be outcome when measured is much large.

To evaluate the proper times k, we consider the case that the vector $(U_s U_w)^k\, |s\rangle$ is

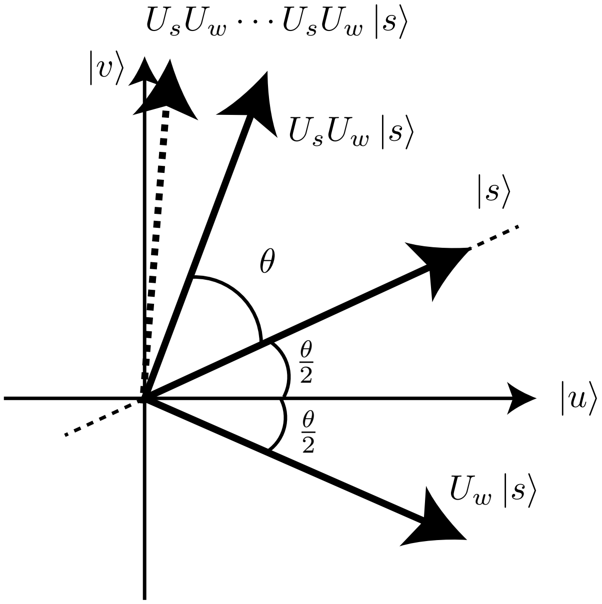

Figure 3.1.1: Dynamics of Grover's algorithm

closest to $|v\rangle$. In this case, for closest integer k_{closest} satisfy

$$\frac{2k_{\text{closest}}+1}{2}\theta \to \frac{\pi}{2}, \tag{3.1.32}$$

$$k_{\text{closest}} = \left[\frac{\pi}{2\theta} - \frac{1}{2}\right]_{\text{int}} \tag{3.1.33}$$

When $\theta > 0$,

$$\frac{\theta}{2} \geq \sin\frac{\theta}{2} = \sqrt{\frac{M}{N}}\,. \tag{3.1.34}$$

So thus, the k_{closest} is up to

$$k_{\text{closest}} \leq \left(\frac{\pi}{2\theta} - \frac{1}{2}\right) + 1 = \frac{\pi}{2\theta} + \frac{1}{2} \leq \frac{\pi}{4}\sqrt{\frac{N}{M}} + \frac{1}{2}\,. \tag{3.1.35}$$

Therefor, the number of the calling quantum oracle to search data of interest is $\mathcal{O}(N)$.

3.2 Quantum Error correction

Either in the classical or in the quantum system, noise in real physical systems cannot be completely eliminated. The basic principle for protecting information from noise is the method of encoding data by giving redundant information. By encoding the extended information, the original data is restored.

In classical computing, errors can be detected by redundant the original data replicating them. In quantum computing, howevee,due to the quantum no-cloning theorem from quantum mechanics [237], error correction cannot be performed in similar way to classical [57]. This is one of the difficulties of quantum error correction. Although various methods have been proposed for quantum error correction, the surface code [81, 220, 109, 40, 90, 79, 32, 31, 30, 111, 92, 232, 99, 142, 53, 225, 26, 41, 156] is one of the most popular methods of quantum error correction due to its relatively low threshold and similarity to classical computer error correction, and groups such as Google, IBM and Intel are aiming to implement it in superconducting quantum circuits [72, 114, 73]. In the case of classical bits, only simple bit flip errors need to be considered, so they can be cloned. On the other hand, in quantum systems, cloning is impossible in principle and has phase errors in addition to bit flip errors. Quantum error correction theory has evolved to extend classical error correction theory to take these considerations into account.

The first quantum error correction theory was proposed in 1995 as Shore's 9-bit code, and then D. Gottesman formulated the general concept as a stabilized code in 1997 [90]. The surface code, which is currently the most actively discussed in the field of superconducting quantum circuits, is one of the formulations of the stabilized code introduced by A. Y. Kittaev in 2003 [136]. This error rate threshold is close to the quantum Gilbert Varshamov limit, which represents the upper limit of the general quantum error correction capability, and is much larger than many other quantum error correction methods.

Errors of information are often expressed using the expression channel. Information is transmitted using signal paths, such as wiring, and in doing so is exposed to noise. This can cause the information to be rewritten. In classical computing, information is stored as 0s or 1s, so an error represents an inversion of these 0s and 1s to become 1s and 0s, respectively. With qubits, however, the use of superposition means that not only does the 0 and 1 information have to be inverted, but also its relative phase error.

3.2.1 Quantum error

Bit-flip error

Bit flip errors in quantum bits are represented as X-errors. This error correction can increase the probability of correcting the error by storing the information redundantly [219]. That is, instead of representing $|0\rangle$ and $|1\rangle$ in a single qubit, multiple qubits are used to represent it, $|000\rangle$, $|111\rangle$ and so on.

$$|\psi\rangle\,|0\rangle\,|0\rangle \rightarrow a\,|000\rangle + b\,|111\rangle \tag{3.2.1}$$

Now consider the case where there is an X error in this. Then, since the error occurs in one of the qubits, the result of the projection measurement will be divided into error-free and other cases, and we can find up to a certain number of errors.

Phase-flip error

Then for phase errors, unlike bit flips and errors as described earlier, they cannot be detected by simple projection measurements. Therefore, we perform gate operation of basis transformation on the qubit and convert the phase error into a bit flip error using 5 qubits [13, 144]. In this way, we can find bit flip errors in the same way as we have found bit flip errors in the past. Phase flip error (Z-error) reverse the sign of the coefficient of the block in three qubits, therefor we need to check the parity for sign between blocks. As quantum circuit,after operate H-gate to all nine qubits, then operate CNOT-gate to S_1 and S_1 with one to six and three to nine as control qubit, respectivily. After CNOT, S_1 and S_1 will measured and all nine qubit will be operate H-gate to return the state. Syndrome bit's states will change $|0\rangle$ or $|1\rangle$ according to the sign of coefficient in the blocks, therefore we can know which block has phase error. To correcting error, it is not need to know which qubit's phase has filiped, and error correcting operator for the first three qubit's block is, for example, $\mathrm{Z}_1\mathrm{Z}_2\mathrm{Z}_3\sigma_z^{\otimes 3}$

3.2.2 Quantum correction codes in a small system

9-qubit code

Here, the basic concept of quantum error correction method will described using Shore's nine qubit code. This code is earliest proposed quantum error correction theory with three bit and 5 bit code [13, 144] and easy to be understand the basic idea of quantum error correction [219]. From the quantum Hamming bond, to correct one qubit error, at least five qubit is necessary, therefore the Shore's code can correct any kind of one bit error. But here we consider only the error which can be represented by linear combination of Pauli operators, and ignore the qubit readout error. The operations show in the figure of the quantum circuit make nine qubit encode to logical one qubit. The block of three physical qubits state $|\psi\rangle = |0\rangle$ first be operate H-gate ($|\psi\rangle = (|0\rangle + |1\rangle)/\sqrt{2}$), then be operate CNOT gate with qubit one as control and two and three as target $|\psi_l\rangle = (|000\rangle +$

$|111\rangle)/\sqrt{2}$. Finally, each logical $|0_L\rangle$ and $|1_L\rangle$ states represent

$$|0_L\rangle = \frac{1}{\sqrt{8}}(|000\rangle + |111\rangle)(|000\rangle + |111\rangle)(|000\rangle + |111\rangle) \tag{3.2.2}$$

$$|1_L\rangle = \frac{1}{\sqrt{8}}(|000\rangle - |111\rangle)(|000\rangle - |111\rangle)(|000\rangle - |111\rangle) \tag{3.2.3}$$

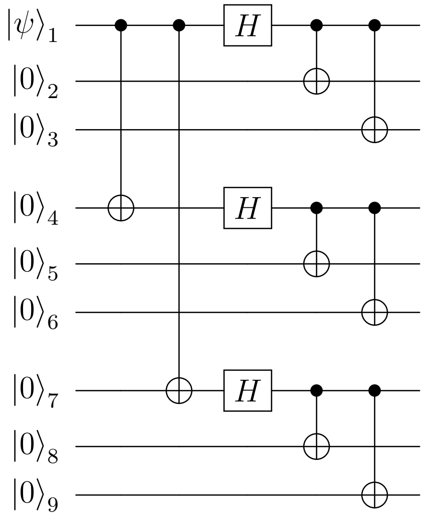

Using this logical qubit, the state during computation is describe $|\psi_L\rangle = \alpha|0_L\rangle + \beta|1_L\rangle$ where $\alpha, \beta \in \mathbb{C}$. When detecting error, we must never know the coefficients α and β, otherwise the state will convergent to digital state. This is the reason why the syndrome measurement is needed to quantum error correction. In this code, Parity check in each block of three qubit tell us bit flip error (X error). To detect the error, another two ancillary qubits will be used in the figure of quantum circuit.

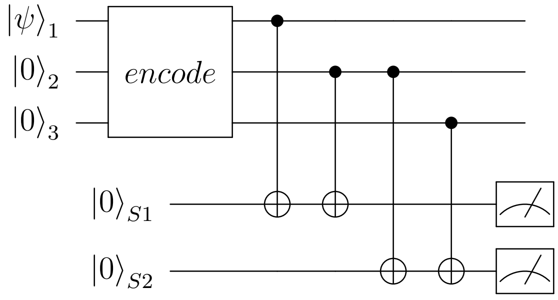

Measurement results of S_1 and S_2 will show $|1\rangle$ state only when there is the state difference between the qubit one and two or, two and three, respectively. For example, if $|1\rangle_{S1}$ and $|0\rangle_{S2}$ is detected, we know qubit one has bit flip error. This syndrome is equal to measure the projection operator $Z_1Z_2 = (|00\rangle\langle 00| + |11\rangle\langle 11|) \otimes I - (|01\rangle\langle 01| + |10\rangle\langle 10|) \otimes I$ and Z_2Z_3 for the logical qubit state $|\psi_L\rangle$. Observable $\langle\psi_L| Z_1Z_2 |\psi_L\rangle = \pm 1$ enable to get only the Parity without to detect the information of α and β.

In real system, quantum bit may has any angle disagreement in Bloch sphere, but when the qubit is measured, the error digitized to the each Pauli measurement basis. Therefore the only we need to correct the error in stabilizer is flip the bit or phase.

3.2.3 Stabilizer formalism

The stabilizer formalism was introduced by Daniel Gottesman [90]. In quantum error correction, the quantum information are encoded into the huge Hilbart space with multi-qubit state to protect error. However, description of the a quantum state using state vector becomes complicated with increasing a number of qubits. One of the efficient description of such a state vector is the stabilizer formalism using stabilizer operators to describe the quantum information, not using the state.

For n-qubit, the Hilbart space is $\mathbb{C}^{2^n}$. In this space, the Pauli group $\mathcal{P}_n$ is defined as that tensor product of the n-qubit Pauli operators and eigenvalues:

$$\mathcal{P}_n = \{\pm 1, \pm i\} \otimes \{\mathrm{I}, \mathrm{X}, \mathrm{Y}, \mathrm{Z}\}\,. \tag{3.2.4}$$

Then the Stabilizer group $\mathcal{S}$ is defined as the Abelian subgroup of the Pauli group containing none of the identity operator of the n-qubit $\mathrm{I}_d = \mathrm{I}^{\otimes n}$. The stabilizer group has many degrees of freedom to choose. To identify the stabilizer group, one can define the generator of the stabilizer group $\mathcal{S}$ as which commutes with every element of $\mathcal{S}$. A element of the generator divides the space into two eigenspace either with $+1$ or -1 eigenvalues. When a system of interest has $m \equiv n - k$ generators, the 2^n-dimension Hilbert space is divided into 2^m spaces and remained 2^k-dimension space forms "Stabilizer state".

Logical Pauli operators

After coding, computing is execute on the code using logical gates and logical gate must project circuit's states to stabilizer states. For surface code, for example, X gate operation to all data qubits in raw which include Z syndrome can be used as logical X gate. Logical Z gate is achieved by applying physical Z gate to the all qubit in the column which include X syndrome qubits, also it can be combined another stabilizers [74, 110, 156]. Hadamard gate is equivalent to exchange the X and Z axis on the Bloch sphere, hence the logical Hadamard is operated by applying physical Hadamard to all qubit and exchange the Z and X stabilizer and the logical Z and X gate.

Surface code

Here we describe the basic concept of surface code which has advantage for implementation to solid material. Topological surface code only need the nearest neighbor interaction between physical qubits, and it is comparably easy to arrange in superconducting circuit [74, 110, 156]. The simplest way to construct nearest neighbor interaction is arrange the qubits on two dimensional lattice points, and the boundary condition of the lattice is set what the qubits are arranged on the surface of the torus.

X stabilizer code for 1D

To detect phase flip error, we define one dimensional surface code by stabilizer. Let us consider a graph $G_1 = (V, E)$, where qubits represent edges $i \in E$. Stabilizer generators are given on vertexes by

$$B_v = \prod_{i \in \delta v} \mathrm{X}_i \tag{3.2.5}$$

where $\delta v \subset E$ represents a set of edges connecting a vertex v. In this case, logical operator is encoded as $\mathrm{Z_L} = \prod_{i \in E}$ and $\mathrm{X_L} = \mathrm{X}_i$. Since $\mathrm{X_L}$ does not commute with B_v, bit flip error cannot be corrected.

When ith qubit receive phase flip error Z_i, stabilizers of both side chain gives -1 eigenvalues. Then, we can detect the error. Generally, when n phase flip errors are happen, it is useful to define error operator as $\mathrm{Z}(c) = \prod_i \mathrm{Z}_i^{c_i}$, where ith qubit gets phase flip error. When error positions are neighbour, inside stabilizer is not effected by error because both side of the qubit have error then stabilizer gives $+1$ eigenvalue. Then, we can just know ends of the error chain, and define the set of the error chain $\partial c \subset V$, where ∂ represents the operation to pick up the ends of the error chain from V. The error $\mathrm{Z}(c)$ flips the eigenvalue of the stabilizer B_v on $v \in \partial c$. Correcting the error is performed by a repair operator $\mathrm{Z}(r)$ giving $\partial r = \partial c$.

Z stabilizer code for 2D

To correct the both phase flip and bit flip error, not only X stabilizer but also Z stabilizer is required, where X stabilizer composes the Pauli X operators, and Z stabilizer composes the Pauli Z operators. Both stabilizer also should commute. Using one dimensional array of qubits cannot make these oprerators, but quantum error correction requires two dimensional array of qubit, so-called "surface code" [136].

Let us consider $n \times n$ qubit array $G_2 = (F, V, E)$, where F, V, and E represent sets of face, vertex, and edge, respectively. Qubits are put on edges and boundary condition is periodical (i.e. top side connects bottom one, and right side connects left one), thus array forms torus. Stabilizer operators are given by

$$A_f = \prod_{i \in \partial f} \mathrm{Z}_i \,, \quad B_v = \prod_{j \in \delta v} \mathrm{X}_j \,, \tag{3.2.6}$$

where ∂f represents a set of four edges around face f, and δv represents a set of four edges connecting vertex v. Using these stabilizer operators, a surface code state is given by $+1$ eigenstate satisfying

$$A_f \left|\Psi\right\rangle = + \left|\Psi\right\rangle \ , \ \ B_v \left|\Psi\right\rangle = + \left|\Psi\right\rangle \tag{3.2.7}$$

For f and v, since operators A_f and B_v share even numbers (0 or 2) of edges, both operator commute $[A_f, B_v] = 0$. Error chains of phase flip error $Z(c)$ are also defined on vertex V as same as one dimensional code: ends of the chain δc gets the flip of eigenvalue -1 of the vertex operator B_v. For bit flip error, error chains $X(\tilde{c})$ are defined on vertex $\tilde{V}$ of the dual-lattice, in which face and vertex are exchanged, as same as phase flip error: ends of the chain $\delta\tilde{c}$ gets the flip of eigenvalue -1 of the face operator A_f.

To find logical operator $\mathrm{Z_L}$ and $\mathrm{X_L}$, first we count the number of edges $|E| = n^2$, on the other hand, the number of stabilizer operators equals the total number of faces and vertexes $|V| + |F| = n^2$. However, since the product operator of all face operators is identity operator, one operator is not independent. For vertex operator, one is also not independent. So thus, the number of stabilizer generator is $|V| + |F| - 2 = 2n^2 - 2$. When we use a surface of torus, we can encode two qubit into the array of physical qubit. Any loop in the surface can be decomposed as product state by stabilizer operators, however, a set of the loop with $\partial c = \emptyset$ can become the logical operator. Thus, we can choose two non-trvial loops l_1 and l_2 on the torus

$$\mathrm{Z_{L1}} = \mathrm{Z}(l_1) \,, \quad \mathrm{Z_{L2}} = \mathrm{Z}(l_2) \,. \tag{3.2.8}$$

The anti-commuting operator $\mathrm{X}_{\mathrm{L}i}$ with $\mathrm{Z}_{\mathrm{L}i}$ is also selected as $\mathrm{X}_{\mathrm{L}i}(\tilde{l}_i)$ on the dual-lattice.

On general surface graph, the Euler characteristic of the number is known:

$$|F| + |V| - |E| = 2 - 2g \tag{3.2.9}$$

where g is genus. $|E|$ represents the number of qubits, and the number of stabilizer is given by the total number of faces and vertexes $|F| + |V| - 2$. Thus, $2g$ logical qubits is encoded into the surface.

3.3 Fault-tolerant Quantum Computing

Logical CNOT gate is little bit harder than single gate. As a result of the CNOT gate operation, the parity of the target bit is the classical XOR of the parity, and the phase of the control bit is the phase summation. Lattice surgery is one method to operate the logical CNOT gate using this protocol[114]. In lattice surgery, operating this summation by combining and dividing ancillary(intermediate) logical bit to the target and control logical qubit.

Finally, T-gate is implemented using ancillary logical qubit $|\psi_T\rangle = \big(|0_L\rangle + e^{i\pi/4}|1_L\rangle\big)/\sqrt{2}$ and it can not operate on the surface code. This ancillary qubit is generated from each physical qubit which operated single T-gate. These physical qubit will be made redundant without enough error correction, and subsequently, measurement and control operation are performed using multiple this ancillary logical qubits to generate a low-error $|\psi_T\rangle$ state. Then logical T-gate is implemented by applying CNOT with this logical qubit and another control qubit. This process called magic state distillation [25] and it needs the most number of physical qubit for fault tolerant quantum computation.

There is some methods to constructing the logical qubit, most discussed one is the defect based surface code which consists from the gate operation using the boundary condition of the defect(qubit hole) in two dimensional lattice. Consider the size of superconducting qubit, it is hard to reduce from a few hundreds microns, the way to construct the one logical qubits on the one chip and connect each other via external classical buss is seems to be practical[112].

Recent situation as ante-NISQ era, while a processor as a utilitarian machine is required, there is still a need for a theoretical approach, such as reducing the number of physical qubits, or considering a structure that is easier to implement in an actual physical system.

3.4 Quantum Annealing

Annealing is process that is used to change the structure og a material. In this process, one raises the temperature of a material and slowly cools it down to obtain a lower-energy state - a more ordered, well-structured state. Simulated annealing is an application of this concept to the computation of optimization problems [130]. The optimization problem is generally to find a state in which a given cost function is minimized, analogous to this annealing behavior when the cost function is viewed as the energy or entropy of the system.

For example, the traveling salesman problem is a typical combinatorial optimization problem. where each city's traveling way is given its total distance, which is the cost function. Finding the minimum value of the cost function by simulated annealing can be easily understood when considering the motion of a particle moving on a potential. At the beginning the thermal energy of the particle is high and has a large fluctuation of the temperature. If you cool it down slowly enough, eventually the probability of finding the particle at the potential minimum approaches unity. Therefore, an annealing machine needs only a physical system that can represent a cost function and introduction of fluctuations.

Although thermal fluctuations are sometimes used in quantum annealing, in general we use quantum fluctuations. The quantum tunneling effect also helps, and the advantage over classical. The original idea was that we could obtain a superconducting qubit in the form of an artificial spin. In superconducting circuits, we use a spin glass system in which qubits are artificial spins. In quantum annealing, a strong transverse magnetic field is applied to the entire spin glass in order to prepare an easily recognizable ground state in which all the spins are oriented transversely. From there, the transverse magnetic field is slowly removed so that the system is always in the ground state, and the solution is finally obtained.

3.4.1 Adiabatic quantum computing

The stage for the quantum annealing is the Ising model applied transverse magnetic field. Controlling the transverse magnetic field allows to find the solution of the optimization problem. However, during the quantum annealing, usually phase transition are happen and become the bottleneck. To avoid the phase transition, the requirements are given.

Spin glass Hamiltonian

The most typical physical system for performing quantum annealing is the spin glass. The spin glass have the We assume that a magnetic field is applied to the system in the X and Z directions. In this case, the Hamiltonian of this spin system is

$$\mathcal{H}_{\text{spin}}(t) = \Lambda(t)\sum_{i}\tilde{\varepsilon}_i\sigma_i^z + \Gamma(t)\sum_{i}\tilde{\Delta}_i\sigma_i^x + \Lambda(t)\sum_{\substack{i_r\in\text{site}(n)\\ r\leq n}} J_{ir} \tag{3.4.1}$$

Although there are many possible forms of coupling between spins on a spin glass, we have represented X, Z coupling of arbitrary length as an ideal Hamiltonian annealing.

Ising model

Most famous model of the spin glass is Ising model which have only the two site interaction J_{ij} about the both z axis Pauli operators (1.2.14). When magnetic fields can apply about z and x axes, Hamiltonain of the Ising model has also the energy of each spin $\tilde{\varepsilon}_i$ for z Pauli operator, and $\tilde{\Delta}$ for the x Pauli operator (1.2.12):

$$\mathcal{H}_{\text{Ising}} = \Lambda(t)\sum_i \tilde{\varepsilon}_i \sigma_i^z + \Lambda(t)\sum_{\langle i,j\rangle} \tilde{J}_{ij}\sigma_i^z\sigma_j^z + \Gamma(t)\sum_i \tilde{\Delta}_i \sigma_i^x \tag{3.4.2}$$

$$:= \mathcal{H}_0 + \Gamma(t)\sum_i \tilde{\Delta}_i \sigma_i^x\,, \tag{3.4.3}$$

where $\Lambda(t)$, and $\Gamma(t)$ represents the time dependence from the external magnetic fields. To control the system properly, the amplitude and directions of external magnetic fields can be tuned.

Quantum annealing process

The optimization problem to be solved is encoded in the first and second terms $\mathcal{H}_0$ of the Ising Hamiltonian (3.4.2). The problem is mathematically represented as interactions formed as Hamiltonian [160]. The final goal of the computation by the quantum annealing is the find the most lowest ground state of the Hamiltonian encoded for optimization problem of interest [170, 171]. To approach the goal, the initial state is prepared and the state evolves belong the Schrödinger equation with satisfying the adiabatic condition (later introduced 3.4.2).

The Quantum annealing process start from the initial state of the Ising Hamiltonian with the much large transverse magnetic field applied

$$\mathcal{H}_{\text{Isign}}(t=0) = \Gamma(0)\sum_i \tilde{\Delta}_i \sigma_i^x\,, \tag{3.4.4}$$

where other two terms is much smaller than transverse terms.

The ground state $|\Psi_0\rangle$ of this initial Hamiltonian is the product state of superposition state at each site

$$|\Psi_0\rangle = \bigotimes_{i\in\text{site}} |+\rangle_i\,. \tag{3.4.5}$$

This state have 2^N superposition states with same probability, which well represents the fact that initial Hamiltonian have the unknown ground state.

During the quantum annealing process, the transverse magnetic field is very gradually decrease (remove) into zero field at the $t = \tau$ (theoretically $\tau = \infty$). In this process, changing the transverse magnetic field $\Gamma(t)$, the system evolves belong the Schrödinger equation of the Hamiltonian of the Ising model encoded for the optimization problem:

$$i\hbar\frac{\partial}{\partial t}\left|\Psi(t)\right\rangle = \mathcal{H}_{\text{Ising}}(t)\left|\Psi(t)\right\rangle \ . \tag{3.4.6}$$

Then, the solution of the optimization problem is represented by the final state after the natural evolution of the Schrödinger equation.

3.4.2 Adiabatic theorem and convergence condition

When performing quantum annealing, we need to know to some extent how slowly the Hamiltonian coefficients should be reduced. After all, the computation time of annealing corresponds to the change time of this parameter, so estimating it is an assessment of the performance of the machine. In the time evolution of a general quantum mechanical system (in the absence of dissipation), we can guarantee that in the limit satisfying the condition described by adiabatic theorem, the system will follow the ground state reliably.

To derive the adiabatic theorem, we consider the evolution of the system with time-dependent Hamiltonian $\mathcal{H}(t)$ from $t = 0$ to $t = \tau$. Introducing dimensionless variable $s = t/\tau$, using $\mathrm{d}s/\mathrm{d}t = \tau$. the Schöredinger equation for the Hamiltonian $\tilde{\mathcal{H}}(s)$ is derived as

$$i\hbar\frac{\mathrm{d}}{\mathrm{d}s}\left|\psi(s)\right\rangle = \tau\tilde{\mathcal{H}}(s)\left|\psi(s)\right\rangle \ . \tag{3.4.7}$$

Here, we assume that the eigenvalues and eigenvectors of the Hamiltonian $\tilde{\mathcal{H}}(s)$ are $e_j(s)$ and $\left|e_j(s)\right\rangle$ with parameter s

$$\tilde{\mathcal{H}}(s)\left|e_j(s)\right\rangle = e_j(s)\left|e_j(s)\right\rangle \ . \tag{3.4.8}$$

Then the state vector in equation (3.4.7) is assumed to be decomposed by these eigenvectores as following representation with parameter s:

$$\left|\psi(s)\right\rangle = \sum_j c_j(s)\mathrm{e}^{-i\tau\phi_j(s)/\hbar}\left|e_j\right\rangle \ , \tag{3.4.9}$$

where c_j is coefficient for each eigenvector and $\phi_j(s)$ is defined as the integration of the eigenenergy from 0 to s

$$\phi_j(s) = \int_0^s e_j(s')\mathrm{d}s' \, . \tag{3.4.10}$$

Then the state vector (3.4.9) is substituted into the Schrödinger equation (3.4.7): the left hand side is expanded as

$$
\begin{aligned}
& i\hbar \frac{\mathrm{d}}{\mathrm{d}s} |\psi(s)\rangle && (3.4.11)\\
& = i\hbar \frac{\mathrm{d}}{\mathrm{d}s} \left(\sum_j c_j(s) \mathrm{e}^{-i\tau\phi_j(s)/\hbar} |e_j(s)\rangle \right) && (3.4.12)\\
& = i\hbar \sum_j \Bigg[\quad \frac{\mathrm{d}c_j(s)}{\mathrm{d}s} \mathrm{e}^{-i\tau\phi_j(s)/\hbar} |e_j(s)\rangle \\
& \qquad - \frac{i}{\hbar} \tau c_j(s) \frac{\mathrm{d}\phi_j(s)}{\mathrm{d}s} \mathrm{e}^{-i\tau\phi_j(s)/\hbar} |e_j(s)\rangle \\
& \qquad + c_j(s) \mathrm{e}^{-i\tau\phi_j(s)/\hbar} \frac{\mathrm{d}}{\mathrm{d}s} |e_j(s)\rangle \quad \Bigg] && (3.4.13)\\
& = i\hbar \sum_j \mathrm{e}^{-i\tau\phi_j(s)/\hbar} \left[\frac{\mathrm{d}c_j(s)}{\mathrm{d}s} |e_j(s)\rangle - \frac{i}{\hbar} \tau e_j(s) c_j(s) |e_j(s)\rangle + c_j(s) \frac{\mathrm{d}}{\mathrm{d}s} |e_j(s)\rangle \right], && (3.4.14)
\end{aligned}
$$

where to derive equation (3.4.14) from (3.4.13), deviation of $\dot{\phi}_j(s) = e_j(s)$ is used. The other right side is expanded as

$$
\begin{aligned}
\tau \tilde{\mathcal{H}}(s) |\psi(s)\rangle &= \tau \tilde{\mathcal{H}}(s) \sum_j c_j(s) \mathrm{e}^{-i\tau\phi_j(s)/\hbar} |e_j(s)\rangle && (3.4.15)\\
&= \tau \sum_j c_j(s) \mathrm{e}^{-i\tau\phi_j(s)/\hbar} \tilde{\mathcal{H}}(s) |e_j(s)\rangle && (3.4.16)\\
&= \tau \sum_j c_j(s) \mathrm{e}^{-i\tau\phi_j(s)/\hbar} e_j(s) |e_j(s)\rangle , && (3.4.17)
\end{aligned}
$$

where (3.4.2) are used. Finally, the Schrödinger equation is

$$
\begin{aligned}
& i\hbar \sum_j \mathrm{e}^{-i\tau\phi_j(s)/\hbar} \left[\frac{\mathrm{d}c_j(s)}{\mathrm{d}s} |e_j(s)\rangle - \frac{i}{\hbar} \tau e_j(s) c_j(s) |e_j(s)\rangle + c_j(s) \frac{\mathrm{d}}{\mathrm{d}s} |e_j(s)\rangle \right] \\
& = \tau \sum_j \mathrm{e}^{-i\tau\phi_j(s)/\hbar} c_j(s) e_j(s) |e_j(s)\rangle . && (3.4.18)
\end{aligned}
$$

To analyze this equation (3.4.18), we prepare some equations. Taking deviation of equation about s and scalar product by $\langle e_k|$, the left side is

$$\langle e_k(s)| \frac{\mathrm{d}}{\mathrm{d}s}\Big(\tilde{\mathcal{H}}(s)\,|e_j(s)\rangle\Big) = \langle e_k(s)| \left(\frac{\mathrm{d}}{\mathrm{d}s}\tilde{\mathcal{H}}(s)\right)|e_j(s)\rangle + \langle e_k(s)|\,\tilde{\mathcal{H}}(s)\Big(\frac{\mathrm{d}}{\mathrm{d}s}\,|e_j(s)\rangle\Big) \tag{3.4.19}$$

$$= \left\langle e_k(s)\middle|\frac{\mathrm{d}}{\mathrm{d}s}\tilde{\mathcal{H}}(s)\middle|e_j(s)\right\rangle + e_k(s)\left\langle e_k(s)\middle|\frac{\mathrm{d}}{\mathrm{d}s}\middle|e_j(s)\right\rangle . \tag{3.4.20}$$

The right side is

$$\langle e_k(s)| \frac{\mathrm{d}}{\mathrm{d}s}\Big(e_j(s)\,|e_j(s)\rangle\Big) = \langle e_k(s)| \left(\frac{\mathrm{d}}{\mathrm{d}s}e_j(s)\right)|e_j(s)\rangle + \langle e_k(s)|\,e_j(s)\Big(\frac{\mathrm{d}}{\mathrm{d}s}\,|e_j(s)\rangle\Big) \tag{3.4.21}$$

$$= \left(\frac{\mathrm{d}}{\mathrm{d}s}e_j(s)\right)\langle e_k(s)|e_j(s)\rangle + e_j(s)\left\langle e_k(s)\middle|\frac{\mathrm{d}}{\mathrm{d}s}\middle|e_j(s)\right\rangle . \tag{3.4.22}$$

Then the equation for the matrix element of the Hamiltonian can be derived as

$$\left\langle e_k(s)\middle|\frac{\mathrm{d}}{\mathrm{d}s}\tilde{\mathcal{H}}(s)\middle|e_j(s)\right\rangle = \left(\frac{\mathrm{d}}{\mathrm{d}s}e_j(s)\right)\langle e_k(s)|e_j(s)\rangle + (e_j(s)-e_k(s))\left\langle e_k(s)\middle|\frac{\mathrm{d}}{\mathrm{d}s}\middle|e_j(s)\right\rangle . \tag{3.4.23}$$

When $k \neq j$, $e_j(s) - e_k(s) \neq 0$ and $\langle e_k(s)|e_j(s)\rangle = 0$, thus, this equation is written as

$$\left\langle e_k(s)\middle|\frac{\mathrm{d}}{\mathrm{d}s}\middle|e_j(s)\right\rangle = \frac{1}{e_j(s)-e_k(s)}\left\langle e_k(s)\middle|\frac{\mathrm{d}}{\mathrm{d}s}\tilde{\mathcal{H}}(s)\middle|e_j(s)\right\rangle . \tag{3.4.24}$$

When $k = j$, using arbitrary property of the state vector $|e_j(s)\rangle = \mathrm{e}^{i\theta}\,|e_j(s)\rangle$, we can choose the proper θ to satisfy the equation

$$\left\langle e_j(s)\middle|\frac{\mathrm{d}}{\mathrm{d}s}\middle|e_j(s)\right\rangle = 0 . \tag{3.4.25}$$

Therefor, to derive the deviation of the coefficient $\dot{c}_j(s)$ of the state vectorusing these equations (3.4.24)- (3.4.25) and taking the matrix element by $\langle e_k(s)|$, the left side of the equation (3.4.18) is

$$\langle \mathrm{e}_k(s)|\, i\hbar \sum_j \mathrm{e}^{-i\tau\phi_j(s)/\hbar}\left[\frac{\mathrm{d}c_j(s)}{\mathrm{d}s}\,|e_j(s)\rangle - \frac{i}{\hbar}\tau e_j(s)c_j(s)\,|e_j(s)\rangle + c_j(s)\frac{\mathrm{d}}{\mathrm{d}s}\,|e_j(s)\rangle\right] \tag{3.4.26}$$

$$=i\hbar \sum_j \mathrm{e}^{-i\tau\phi_j(s)/\hbar}\left[\frac{\mathrm{d}c_j(s)}{\mathrm{d}s}\,\langle \mathrm{e}_k(s)|e_j(s)\rangle - \frac{i}{\hbar}\tau e_j(s)c_j(s)\,\langle \mathrm{e}_k(s)|e_j(s)\rangle + c_j(s)\,\langle \mathrm{e}_k(s)|\,\frac{\mathrm{d}}{\mathrm{d}s}\,|e_j(s)\rangle\right] \tag{3.4.27}$$

$$=i\hbar\left[\mathrm{e}^{-i\tau\phi_k(s)/\hbar}\left(\frac{\mathrm{d}c_k(s)}{\mathrm{d}s} - \frac{i}{\hbar}\tau e_k(s)c_k(s)\right) + \sum_{j\neq k} c_j(s)\mathrm{e}^{-i\tau\phi_j(s)/\hbar}\left\langle \mathrm{e}_k(s)\middle|\frac{\mathrm{d}}{\mathrm{d}s}\middle|e_j(s)\right\rangle\right] \tag{3.4.28}$$

$$=i\hbar\mathrm{e}^{-i\frac{\phi_k(s)}{\hbar}\tau}\frac{\mathrm{d}c_k(s)}{\mathrm{d}s} + \mathrm{e}^{-i\frac{\phi_k(s)}{\hbar}\tau}\tau e_k(s)c_k(s) + i\hbar\sum_{j\neq k} c_j(s)\mathrm{e}^{-i\frac{\phi_j(s)}{\hbar}\tau}\frac{\left\langle e_k(s)\middle|\frac{\mathrm{d}}{\mathrm{d}s}\tilde{\mathcal{H}}(s)\middle|e_j(s)\right\rangle}{e_k(s)-e_j(s)}\,. \tag{3.4.29}$$

The right side of the equation (3.4.18) is

$$\begin{aligned}
&\langle e_k(s)|\left(\tau\sum_j \mathrm{e}^{-i\tau\phi_j(s)/\hbar}c_j(s)e_j(s)\,|e_j(s)\rangle\right)\\
=&\sum_j \tau\mathrm{e}^{-i\tau\phi_j(s)/\hbar}c_j(s)e_j(s)\,\langle e_k(s)|e_j(s)\rangle \qquad (3.4.30)\\
=&\tau\mathrm{e}^{-i\tau\phi_k(s)/\hbar}c_k(s)e_k(s)\,. \qquad (3.4.31)
\end{aligned}$$

Then the equation (3.4.18) is

$$\frac{\mathrm{d}}{\mathrm{d}s}c_k(s) = \sum_{j\neq k} c_j(s)\frac{\mathrm{e}^{\frac{i}{\hbar}[\phi_k(s)-\phi_j(s)]\tau}}{e_k(s)-e_j(s)}\left\langle e_k(s)\middle|\frac{\mathrm{d}}{\mathrm{d}s}\tilde{\mathcal{H}}(s)\middle|e_j(s)\right\rangle\,. \tag{3.4.32}$$

Let the system evolve in the long time $\tau \gg 1$ with initial condition

$$c_0(0) = 1\,,\; c_k(0) = 0\,(\text{for } k \neq 0)\,, \tag{3.4.33}$$

which represent the system initially is at the ground state. We assume the system take the almost ground state during the evolution:

$$c_0(s) = 1 - \mathcal{O}\left(\tau^{-1}\right)\,,\; c_k(s) = \mathcal{O}\left(\tau^{-1}\right) = \mathcal{O}(s)\,(\text{for } k \neq 0)\,. \tag{3.4.34}$$

This assumption will be checked later for consistency.

To solve the equation (3.4.18) with using the initial condition and analyse the probability of the excitation of the Hamiltonian, firstly we integrate the equation from 0 to s

$$c_k(s) = c_k(0) + \sum_{j\neq k} \int_0^s \mathrm{d}s' c_j(s') \frac{\mathrm{e}^{\frac{i}{\hbar}[\phi_k(s')-\phi_j(s')]\tau}}{e_k(s') - e_j(s')} \left\langle e_k(s') \middle| \frac{\mathrm{d}}{\mathrm{d}s'} \tilde{\mathcal{H}}(s') \middle| e_j(s') \right\rangle . \tag{3.4.35}$$

Here we interest the excitation state of the system, so $k \neq 0$. In this case, $c_k(0) = 0$ from assumption (3.4.33) and $c_k(s)$ is approximated as

$$\begin{aligned} c_k(s) &= \int_0^s \mathrm{d}s'(1 - \mathcal{O}(s')) \frac{\mathrm{e}^{\frac{i}{\hbar}[\phi_k(s')-\phi_0(s')]\tau}}{e_k(s') - e_0(s')} \left\langle e_k(s') \middle| \frac{\mathrm{d}}{\mathrm{d}s'} \tilde{\mathcal{H}}(s') \middle| e_0(s') \right\rangle & (3.4.36) \\ &\quad + \sum_{\substack{j\neq k, j\neq 0 \\ k\neq 0}} \int_0^s \mathrm{d}s' \mathcal{O}(s') \frac{\mathrm{e}^{-\frac{i}{\hbar}[\phi_j(s')-\phi_k(s')]\tau}}{e_j(s') - e_k(s')} \left\langle e_k(s') \middle| \frac{\mathrm{d}}{\mathrm{d}s'} \tilde{\mathcal{H}}(s') \middle| e_j(s') \right\rangle & (3.4.37) \\ &= \int_0^s \mathrm{d}s' \left[\frac{\mathrm{e}^{\frac{i}{\hbar}[\phi_k(s')-\phi_0(s')]\tau}}{e_k(s') - e_0(s')} \left\langle e_k(s') \middle| \frac{\mathrm{d}}{\mathrm{d}s'} \tilde{\mathcal{H}}(s') \middle| e_0(s') \right\rangle \right] + \mathcal{O}(s^2) & (3.4.38) \\ &= \int_0^s \mathrm{d}s' \left[\frac{\mathrm{e}^{\frac{i}{\hbar}[\phi_k(s')-\phi_0(s')]\tau}}{e_k(s') - e_0(s')} \left\langle e_k(s') \middle| \frac{\mathrm{d}}{\mathrm{d}s'} \tilde{\mathcal{H}}(s') \middle| e_0(s') \right\rangle \right] + \mathcal{O}(\tau^{-2}) & (3.4.39) \end{aligned}$$

We define functions $f(s)$ and $g(s)$ as

$$\begin{aligned} f(s) &:= \frac{i\hbar}{\tau} \mathrm{e}^{\frac{i}{\hbar}[\phi_k(s)-\phi_0(s)]\tau} & (3.4.40) \\ \frac{\mathrm{d}f(s)}{\mathrm{d}s} &= \Delta_k(s) \mathrm{e}^{\frac{i}{\hbar}[\phi_k(s)-\phi_0(s)]\tau} & (3.4.41) \\ \Delta_k(s) &:= e_k(s) - e_0(s) = \frac{\mathrm{d}}{\mathrm{d}s}[\psi_k(s) - \psi_0(s)] & (3.4.42) \\ g(s) &= \frac{\left\langle e_k(s) \middle| \frac{\mathrm{d}}{\mathrm{d}s} \tilde{\mathcal{H}}(s) \middle| e_0(s) \right\rangle}{(e_k(s) - e_0(s))^2} = \frac{\left\langle e_k(s) \middle| \frac{\mathrm{d}}{\mathrm{d}s} \tilde{\mathcal{H}}(s) \middle| e_0(s) \right\rangle}{\Delta_k(s)^2} . & (3.4.43) \end{aligned}$$

Then $c_k(s)$ is

$$\begin{aligned} c_k(s) &= \int_0^s \mathrm{d}s'\, f'(s') g(s') + \mathcal{O}(\tau^{-2}) & (3.4.44) \\ &= -f(s')g(s') \Big|_0^s + \mathcal{O}(\tau^{-2}) & (3.4.45) \\ &= f(0)g(0) - f(s)g(s) + \mathcal{O}(\tau^{-2}) . & (3.4.46) \end{aligned}$$

Here function $f(s)$ depending on the $1/\tau$, so thus, this satisfies the assumption of (3.4.34). Then, for the low probability of the exiting state $c_k(s) \ll 1$ at the long evolution time

$t \gg 1$, the requirement condition is

$$\tau \gg \frac{\left|\left\langle \mathrm{e}_k(s) \middle| \frac{\mathrm{d}\tilde{\mathcal{H}}(s)}{\mathrm{d}s} \middle| \mathrm{e}_0(0) \right\rangle\right|}{\Delta_k(s)^2} \tag{3.4.47}$$

Therefor, in original time t form, this is

$$\frac{\left|\left\langle \mathrm{e}_k(t) \middle| \frac{\mathrm{d}\mathcal{H}(t)}{\mathrm{d}t} \middle| \mathrm{e}_0(0) \right\rangle\right|}{\Delta_k(t)^2} \ll 1 \tag{3.4.48}$$

This is so-called "adiabatic theorem".

However above analysis is most based on that the first order dependency of the τ^{-1} and we ignore the total effect from the higher order terms. When the total terms of the higher order have the dependency more than $\mathcal{O}(\tau^{-1})$, such effect cannot be ignored even if each term only depends $\mathcal{O}(\tau^{-2})$ [60]. Moreover, when Hamiltonian have the degeneracy, we can also derive the general adiabatic theorem [121].

3.4.3 Convergence condition

To execute the quantum annealing operation on the Ising Hamiltonian (3.4.2), when the Hamiltonian evolves with satisfying the adiabatic condition (3.4.48), we analyse the convergence condition for the $\Gamma(t)$ to ground state of the Hamiltonian at $t \to \infty$ [170].

We assume $\Gamma(t)$ is the monotonically decreasing function at $t > t_0$. For arbitrary Ising Hamiltonian, the convergence condition is given by

$$\Gamma(t) = a \left(\frac{\left|\left\langle \mathrm{e}_k(t) \middle| \frac{\mathrm{d}\mathcal{H}(t)}{\mathrm{d}t} \middle| \mathrm{e}_0(0) \right\rangle\right|}{\Delta_k(t)^2} t + c \right)^{\frac{-1}{2N+1}}, \tag{3.4.49}$$

where a and c is constant value, not depending on the number of site N.

3.4.4 Optimization problems

There are many research to encode the optimization problem into the Ising model to solve by the quantum annealing [160, 207]. Here, to compare the algorithm between quantum annealing computing and gate model quantum computing, we briefly introduce the search database in quantum annealing [208], instead of the Grover's algorithm 3.1.3

Search database in quantum annealing

The situation is same as the Grovers' algorithm. We search M data of interest from the database with N data. The final goal to evaluate the method of the quantum annealing is to evaluate how the time scale τ depends on the number of the database N (to remind, classical algorithm cost $\mathcal{O}(N)$).

1. prepare the cost function (Hamiltonian) $\tilde{\mathcal{H}}_w$
   By using the state vector of the data interest $|w\rangle$, the Hamiltonian is defined as

   $$\tilde{\mathcal{H}}_w = 1 - |w\rangle\langle w| \ , \tag{3.4.50}$$

   $$|w\rangle = \frac{1}{\sqrt{M}} \sum_{x \in \text{solution}} |x\rangle \tag{3.4.51}$$

   This Hamiltonian selects the data in the database:

   $$\tilde{\mathcal{H}}_w \, |x\rangle = \begin{cases} |x\rangle & (x \text{ is not solution}) \\ 0 & (x \text{ is solution}) \end{cases} \tag{3.4.52}$$

2. prepare the initial Hamiltonian defined as

   $$\tilde{\mathcal{H}}_{\mathrm{init}} = 1 - |\Psi_0\rangle\langle\Psi_0| = 1 - \frac{1}{\sqrt{N}} \sum_x |x\rangle \ . \tag{3.4.53}$$

3. let the total Hamiltonian $\mathcal{H}_{\mathrm{t}}$ evolve from $t = 0$ to $t = \tau$ Total Hamiltonian is given by

   $$\tilde{\mathcal{H}}_{\mathrm{t}} = [1 - f(s)]\tilde{\mathcal{H}}_{\mathrm{t}} + f(s)\tilde{\mathcal{H}}_{\mathrm{t}} \, , \tag{3.4.54}$$

   where $s = t/\tau$ and the range of s is $0 \leq s \leq t$, and the function f is monotonically increasing and represents the external transverse magnetic field.

To analyse the evolution of the total Hamiltonian, we introduce the perpendicular state vector $|w_\perp\rangle$ about the $|w\rangle$:

$$|w_\perp\rangle = \frac{1}{\sqrt{N - M}} \sum_{x \notin \text{solution}} |x\rangle \ . \tag{3.4.55}$$

Then Hamiltonian is represented in matrix form as

$$\tilde{\mathcal{H}}_{\mathrm{t}} = \begin{pmatrix} \langle w|\tilde{\mathcal{H}}_{\mathrm{t}}|w\rangle & \langle w|\tilde{\mathcal{H}}_{\mathrm{t}}|w_\perp\rangle \\ \langle w_\perp|\tilde{\mathcal{H}}_{\mathrm{t}}|w\rangle & \langle w_\perp|\tilde{\mathcal{H}}_{\mathrm{t}}|w_\perp\rangle \end{pmatrix} . \tag{3.4.56}$$

Using these two state vector, the initial state can be decomposed as

$$|\Psi_0\rangle = \sqrt{\frac{M}{N}}\,|w\rangle + \sqrt{\frac{N-M}{N}}\,|w_\perp\rangle \ . \tag{3.4.57}$$

We can calculate each matrix element:

$$\begin{aligned}
\langle w|\tilde{\mathcal{H}}_{\mathrm{t}}|w\rangle &= (1-f)\,\langle w|\tilde{\mathcal{H}}_{\mathrm{init}}|w\rangle + f\,\langle w|\tilde{\mathcal{H}}_{\mathrm{w}}|w\rangle && (3.4.58)\\
&= (1-f)\,\langle w|(1-|\Psi_0\rangle\langle\Psi_0|)|w\rangle + f\,\langle w|(1-|w\rangle\langle w|)|w\rangle && (3.4.59)\\
&= (1-f)\left(1-\frac{M}{N}\right), && (3.4.60)
\end{aligned}$$

$$\begin{aligned}
\langle w|\tilde{\mathcal{H}}_{\mathrm{t}}|w_\perp\rangle &= (1-f)\,\langle w|\tilde{\mathcal{H}}_{\mathrm{init}}|w_\perp\rangle + f\,\langle w|\tilde{\mathcal{H}}_{\mathrm{w}}|w_\perp\rangle && (3.4.61)\\
&= (1-f)\,\langle w|(1-|\Psi_0\rangle\langle\Psi_0|)|w_\perp\rangle + f\,\langle w|(1-|w\rangle\langle w|)|w_\perp\rangle && (3.4.62)\\
&= -(1-f)\sqrt{\frac{M}{N}}\sqrt{\frac{N-M}{N}}\,, && (3.4.63)
\end{aligned}$$

$$\begin{aligned}
\langle w_\perp|\tilde{\mathcal{H}}_{\mathrm{t}}|w\rangle &= (1-f)\,\langle w_\perp|\tilde{\mathcal{H}}_{\mathrm{init}}|w\rangle + f\,\langle w_\perp|\tilde{\mathcal{H}}_{\mathrm{w}}|w\rangle && (3.4.64)\\
&= (1-f)\,\langle w_\perp|(1-|\Psi_0\rangle\langle\Psi_0|)|w\rangle + f\,\langle w_\perp|(1-|w\rangle\langle w|)|w\rangle && (3.4.65)\\
&= -(1-f)\sqrt{\frac{M}{N}}\sqrt{\frac{N-M}{N}}\,, && (3.4.66)
\end{aligned}$$

$$\begin{aligned}
\langle w_\perp|\tilde{\mathcal{H}}_{\mathrm{t}}|w_\perp\rangle &= (1-f)\,\langle w_\perp|\tilde{\mathcal{H}}_{\mathrm{init}}|w_\perp\rangle + f\,\langle w_\perp|\tilde{\mathcal{H}}_{\mathrm{w}}|w_\perp\rangle && (3.4.67)\\
&= (1-f)\,\langle w_\perp|(1-|\Psi_0\rangle\langle\Psi_0|)|w_\perp\rangle + f\,\langle w_\perp|(1-|w\rangle\langle w|)|w_\perp\rangle && (3.4.68)\\
&= (1-f)\left(1-\frac{N-M}{N}\right) + f\,. && (3.4.69)\\
&= 1-(1-f)\frac{N-M}{N} && (3.4.70)
\end{aligned}$$

Then, the Hamiltonian is changed as

$$\tilde{\mathcal{H}}_{\mathrm{t}} = \frac{1}{2}\begin{pmatrix} 1 & 0 \\ 0 & 1 \end{pmatrix} - \frac{1}{2}\begin{pmatrix} \cos 2\theta & \sin 2\theta \\ \sin 2\theta & -\cos 2\theta \end{pmatrix} \tag{3.4.71}$$

where,

$$\cos 2\theta = \frac{1}{\Delta_w}\left[1 - 2(1-f)\left(1 - \frac{M}{N}\right)\right], \tag{3.4.72}$$

$$\sin 2\theta = \frac{1}{\Delta_w}\left[2(1-f)\sqrt{\frac{M}{N}}\sqrt{\frac{N-M}{N}}\right], \tag{3.4.73}$$

$$\Delta_w = \sqrt{1 - 4(1-f)f\left(1 - \frac{M}{N}\right)}. \tag{3.4.74}$$

Then, the Hamiltonian can be diagonalized and eigenenergies are given by

$$\varepsilon_0 = \frac{1}{2}(1 - \Delta_w)\,,\ \varepsilon_1 = \frac{1}{2}(1 + \Delta_w) \tag{3.4.75}$$

Therefor, the energy gap is $\Delta_w = \varepsilon_1 - \varepsilon_0$.

The adiabatic condition is rewritten in this case as,

$$\tau \gg \frac{1}{\Delta_w^2}\left|\left\langle \varepsilon_1 \middle| \frac{\mathrm{d}\tilde{\mathcal{H}}}{\mathrm{d}s} \middle| \varepsilon_0 \right\rangle\right| \tag{3.4.76}$$

$$= \frac{1}{\Delta_w^2}\left|\left\langle \varepsilon_1 \middle| \frac{\mathrm{d}\tilde{\mathcal{H}}}{\mathrm{d}f}\frac{\mathrm{d}f(s)}{\mathrm{d}s} \middle| \varepsilon_0 \right\rangle\right| \tag{3.4.77}$$

$$= \frac{1}{\Delta_w^2}\left|\frac{\mathrm{d}f(s)}{\mathrm{d}s}\right|\left|\left\langle \varepsilon_1 \middle| \frac{\mathrm{d}\tilde{\mathcal{H}}}{\mathrm{d}f} \middle| \varepsilon_0 \right\rangle\right| \tag{3.4.78}$$

$$\left|\frac{\mathrm{d}f(s)}{\mathrm{d}s}\right| \le \frac{\tau\Delta_w^2}{\left|\left\langle \varepsilon_1 \middle| \frac{\mathrm{d}\tilde{\mathcal{H}}}{\mathrm{d}f} \middle| \varepsilon_0 \right\rangle\right|}\epsilon \tag{3.4.79}$$

where $\epsilon \ll 1$ represents the small number.

When the number of the database N is large $N \gg M$,

$$\cos 2\theta = \frac{2f-1}{\Delta_w} + \mathcal{O}\left(\frac{M}{N}\right), \tag{3.4.80}$$

$$\sin 2\theta = \frac{2(f-1)}{\Delta_w}\sqrt{\frac{M}{N}} + \mathcal{O}\left(\left(\frac{M}{N}\right)^{2/3}\right), \tag{3.4.81}$$

$$\Delta_w = 1 - 2f + \mathcal{O}\left(\frac{M}{N}\right). \tag{3.4.82}$$

Then Hamiltonian and its derivation is approximately

$$\tilde{\mathcal{H}}_{\mathrm{t}} \approx -\frac{1}{2}\begin{pmatrix} 2f-1 & 2(1-f)\sqrt{\frac{M}{N}} \\ 2(1-f)\sqrt{\frac{M}{N}} & -2f+1 \end{pmatrix} \tag{3.4.83}$$

$$\frac{\mathrm{d}\tilde{\mathcal{H}}_{\mathrm{t}}}{\mathrm{d}f} = -\frac{1}{2}\begin{pmatrix} -1 & \sqrt{\frac{M}{N}} \\ \sqrt{\frac{M}{N}} & +1 \end{pmatrix} \tag{3.4.84}$$

Therefor, a constant number $c\,(> 0)$ exists to be upper the term $\left|\langle\varepsilon_1|\frac{\mathrm{d}\tilde{\mathcal{H}}}{\mathrm{d}f}|\varepsilon_0\rangle\right| < c$ Then, the upper of the adiabatic condition (3.4.79) is given by

$$\frac{\mathrm{d}f(s)}{\mathrm{d}s} = c\epsilon\tau\Delta_w^2 = c\epsilon\tau\left[1 - 4(1-f)f\left(1 - \frac{M}{N}\right)\right]. \tag{3.4.85}$$

This differential equation can be solved for s by integration as

$$s = \frac{1}{2c\epsilon\tau}\frac{N}{\sqrt{N-M}}\left[\arctan\left(\sqrt{N-M}(2f-1)\right) + \arctan\sqrt{N-M}\right]. \tag{3.4.86}$$

At the last of the quantum annealing process, $s = 1$, thus, $f(s = 1) = 1$ and τ is given by

$$\tau = \frac{1}{\epsilon}\frac{N}{\sqrt{N-M}}\arctan\left(\sqrt{N-M}\right) \tag{3.4.87}$$

$$\approx \frac{1}{\epsilon}\frac{\pi}{2}\sqrt{N} \gg \sqrt{N} = \mathcal{O}\left(\sqrt{N}\right). \tag{3.4.88}$$

Chapter 4

Experiments and Engineering of Superconducting Quantum Circuit

In this chapter, cryogenic environment and microwave experiments are briefly introduced. The cryogenic environment is required to make chips fabricated become superconductor and to measure such chip. To prepare the cryogenic environment stably, most commonly used equipment is "Dilution refrigerator" using Helium. So thus, to understand the capability of the dilution refrigerator, the principle and application is also introduced together with designed cold finger and cable wiring. As for the microwave experiment, the basic experiment methods is explained together with the measured data.

4.1 Cryogenic engineering

In order to make measurements on superconducting quantum circuits, a cryogenic environment of about 10 mK is required. This is because the minimum energy gap due to the Josephson junction, which is the basis of the superconducting qubit, is in the GHz band. Denoting the energy gap as $\hbar\omega = hf$, corresponding characteristic temperature is given by

$$T_{gap} = \frac{h}{k_b} f \xrightarrow{at\,10[\mathrm{GHz}]} \frac{6.62607004 \times 10^{-34}\,[\mathrm{m^2 kg\,s^{-1}}]}{1.38064852 \times 10^{-23}\,[\mathrm{m^2 kg\,s^{-2} K^{-1}}]} 10\,[\mathrm{GHz}] \approx 480\,[\mathrm{mK}] \quad (4.1.1)$$

For this reason, the environmental temperature T_{env} must be low enough so that the energy gap is not buried in the ambient temperature noise.

In order to carry out the experiment for a long time in such an extremely low temperature environment, it is necessary to maintain the temperature. The dilution refrigerator (DR) is the only cooling system that can continuously achieve extremely low temperature environments of hundreds to tens of mK (Cryogenic environment). It is also necessary to design an environment in which microwaves can be measured in the dilution refrigerator. For this microwave measurement, it is also necessary to wire from room temperature to extremely low temperature in order to apply microwaves. We will construct a measuring device for a superconducting quantum circuit that meets these requirements.

4.1.1 Properties of the helium mixture gas

To understand the principle and mechanics of the dilution refrigerator, firstly we focus on the properties of the mixture gas of ^{3}He and ^{4}He [138].

Particle statistics

Whole particles are classified either Fermi particle (fermion) or Bose particle (boson). The electron, proton, and neutron are most famous and typical particles of the fermion. A system of multi particles of felmion have unique characteristic that only one fermion can occupy a given quantum state, and others can not occupy the quantum state. Two or more statistics particles cannot occupy the same quantum state. This is well known as Pauli exclusion principle, and for felmion are called as Fermi statistics. On the other hand, in a system of bosons, such as photon, cooper pair and so on, two or more particles cannot occupy the same quantum state.

At zero temperature, in the system of fermions, particles occupy energy level from the bottom. Then maximum energy occupied by the particle is called Fermi enrgy $\mathscr{E}_{\mathrm{F}}$, and it is converted to temperature unit $T_{\mathrm{F}} = \mathscr{E}_{\mathrm{F}}/k_{\mathrm{B}}$:

$$T_{\mathrm{F}} = \frac{\hbar(3\pi^2\rho_f)^{2/3}}{2m_f k_B} \tag{4.1.2}$$

where m_f is Fermi particle mass, and ρ_f is the density of the particles.

On the other hand, in the system of bosons under the T_{BEC}, all particles occupy the lowest energy levels. This is called Bose–Einstein condensation (BEC) [138].

$$T_{\mathrm{BEC}} = \frac{2\pi\hbar}{m_b k_B}\left(\frac{\rho_b}{2.612}\right)^{2/3}, \tag{4.1.3}$$

where m_b is boson mass, and ρ_b is the density of the boson.

Particle have also wave function $\psi(x)$ with position x. When distance between particles are closer and wave functions of the nearest neighbour particles become overlap, one must take account of the exchanging position of particles. There is two way to exchange the position: one is $\psi(x_1) = \psi(x_2)$ (represents the Bose statistic), the other is $\psi(x_1) =$

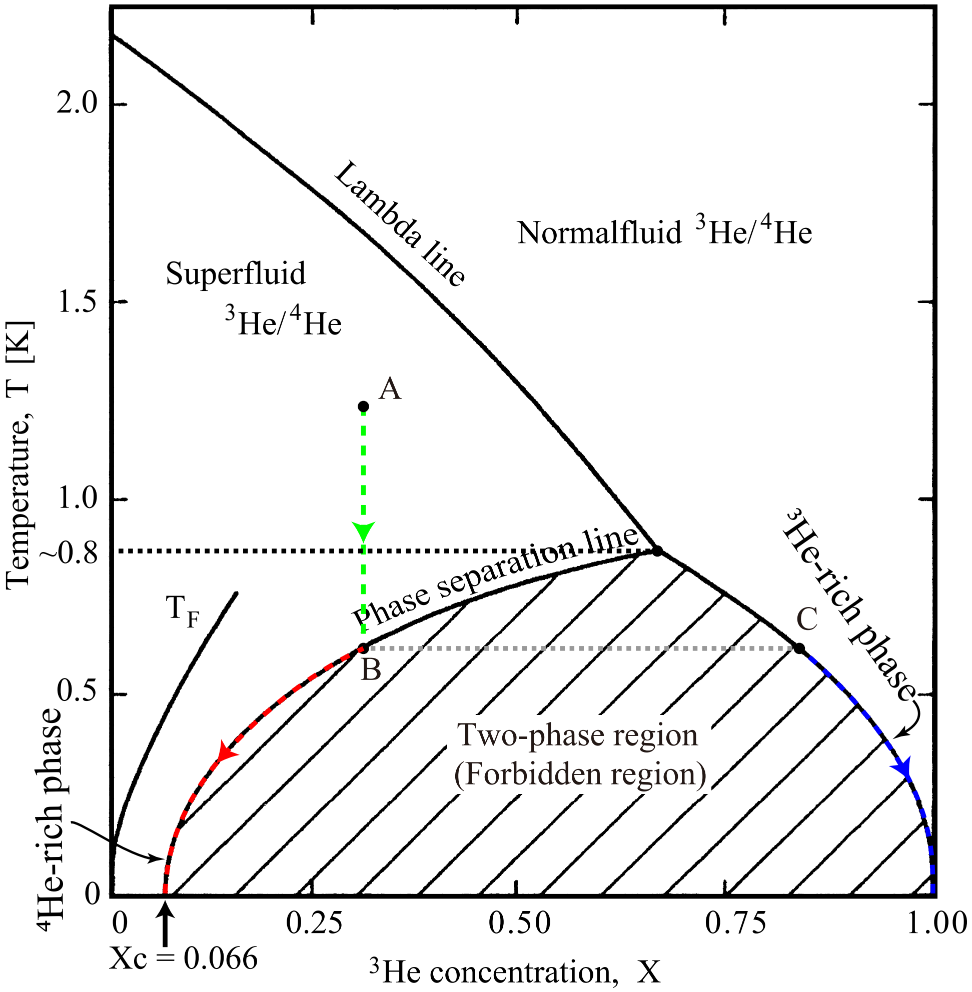

Figure 4.1.1: Phase diagram of ^{3}He -^{4}He mixture under cryogenic temperature at saturated vapour pressure [194] The diagram shows the λ line for the phase transition of the ^{4}He between normal fluid and super fulid. The λ line separates into ^{4}He -rich phase (dilute phase) and ^{3}He -rich phase (concentrated phase). The line shows the Fermi temperatures T_F depending on the ^{3}He component. [194, 15, 234]

$-\psi(x_2)$ (represents the Fermi statistic).

^{3}He / ^{4}He mixture liquid

We explain the principle of dilution cooling of He used in the dilution refrigerator. Figure 4.1.1 shows a phase diagram ^{3}He - ^{4}He mixture. This phase diagram contains several interesting physics. First of all, it is noticeable that ^{3}He and ^{4}He cannot mix uniformly in the shaded region, which is defined as the forbidden region, i.e., they are phase separated.

For example, if we start from point A in the figure 4.1.1 ($T = 1\mathrm{K}, X = 30\%$) and cool along the green line, the phase separation begins at point B, where the ^{3}He component

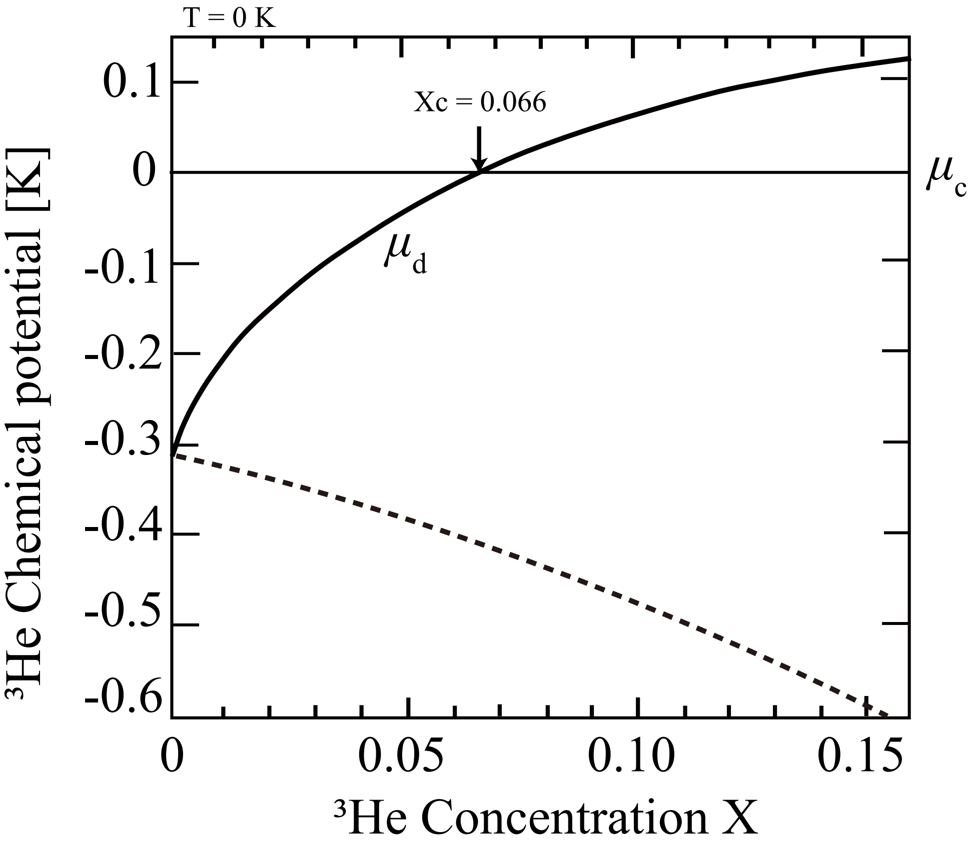

Figure 4.1.2: Chemical potential energy μ_d in ^{4}He rich phase of ^{3}He - ^{4}He mixture []. μ_c is the chemical potential energy of pure liquid of the ^{3}He . To compare μ_d with μ_c, μ_c is reference energy $\mu_c = 0$. The dash line represents the internal energy due to the interaction between ^{3}He atoms (Pauli principle). Dash line represents the chemical potential of a ^{3}He in pure ^{3}He liquid. This corresponds to the binding energy of a ^{3}He in ^{3}He liquid. [217, 63]

is separated into a large concentrated phase (point C) and a small dilute phase (point B). where X is the mole fraction of ^{3}He component. Since the molar volume of the concentrated phase is larger and the specific gravity is lower, the two phases coexist in the container with the concentrated phase floating on top of the dilute phase. At $T = 0$, the concentration of X in the dilute phase is 100%, i.e. pure liquid ^{3}He , while the dilute phase is 6.6%. Thus, it is one of the major points of dilution cooling that the concentration of ^{3}He in the dilute phase remains at a finite value rather than zero even at absolute zero.

Let us look at the phase diagram in more detail. The lambda line in figure 4.1.1 shows the temperature at which the ^{4}He component undergoes a phase transition to the superfluid state with Bose-Einstein condensation, which is on the order of 1K. In contrast, the transition temperature is sufficiently low, mK, for the dilute phase. In contrast, at sufficiently low temperatures of mK, thermally excited elementary excitations of the superfluid ^{4}He component is negligible. The ^{4}He component of the dilute phase interferes only slightly with the free motion of the ^{3}He atoms mixed into it, but they have almost no effect to the thermodynamic property of ^{4}He component. This is called a "mechanical vacuum". Conversely, from the viewpoint of ^{3}He atoms, one can say that they are in a Fermi degenerate state with a slight increase in effective particle mass.

Figure 4.1.2 shows the X dependence of the chemical potential μ_d of the ^{3}He component in the dilute phase. For simplicity, we consider the case of $T = 0$. The chemical potential is the change in energy of the system when a particle is added to or removed from the system. The chemical potential mu_d at $X = 0$ (the situation where one ^{3}He atom is in the superfluid ^{4}He) is lower than the chemical potential in the concentrated phase (μ_c). This is because a ^{3}He atom in a dense liquid ^{4}He is subject to stronger van der Waals attraction from its surroundings than in a less dense liquid ^{3}He (dash line shown in Figure 4.1.2). Here, the liquid ^{3}He is less dense than liquid ^{4}He because ^{3}He atoms have smaller mass than ^{4}He atom and thus need more free space around themselves to lower their zero-point vibration energy due to Heisenberg's uncertainty relation.

We next consider slowly increasing the concentration of dilute phase ^{3}He from zero. Since the ^{3}He component is Fermi degenerate, μ_d should increase as $\mu_d \propto X^{2/3}$. As a result, $\mu_d \le \mu_c$ for $X \le 6.6\%$, and thus the dense phase is a more stable for ^{3}He . Therefore, the concentration of ^{3}He in the dilute phase is upper bounded by 6.6% and does not increase further. Newly added ^{3}He atoms will be phase separated as a concentrated phase.

Entropy and cooling power

The ^{3}He atoms in the dilute phase can move relatively freely in the mechanical vacuum of ^{4}He . In this case, the concentrated phase plays the role of a "liquid". If one can selectively remove or depressurize only the ^{3}He component of the dilute phase in some way, one can expect a cooling effect by absorbing the latent heat due to evaporation of the ^{3}He in the dilute phase. Thus, the principle of dilution cooling is essentially the same as that of adiabatic evaporative cooling.

Let us consider the cooling power of the dilution refrigerator. In general, at a sufficiently degenerate low temperature region ($T \ll T_F$), the entropy S per particle of degenerate Fermi gas is given by

$$S = \frac{\pi^2 k_B}{2} \frac{T}{T_F} = \frac{\pi^2 k_B^2 m}{\hbar^2 [3\pi^2 n(X)]^{2/3}} T \,. \tag{4.1.4}$$

This equation (4.1.4) shows the temperature variation the of the entropy depending on the dilute and concentrated phases concentration X. Therefore, the entropy of the dilute

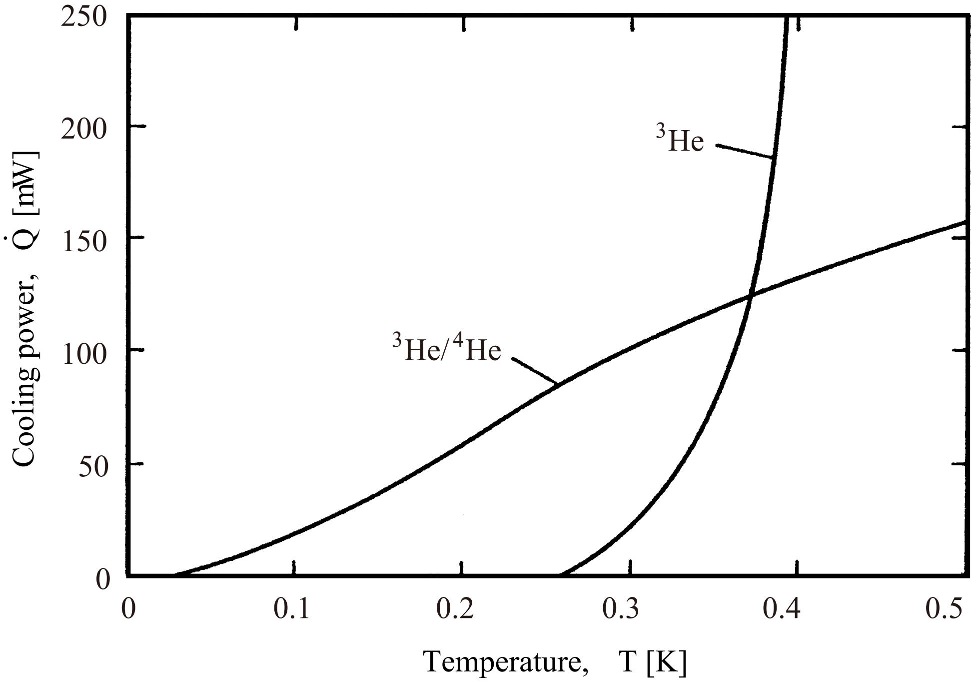

Figure 4.1.3: Competition of cooling power of refrigerator using ^{3}He - ^{4}He and ^{3}He only.

phase is higher than that of the concentrated phase at the same temperature. This view of the entropy represent the analogy of that the diluted phase corresponds "gas" and the concentrated phase corresponds "liquid". The latent heat that is taken away from the environment during evaporation is $L = T(S_d - S_c)$.

The cooling power $\dot{Q}$ of an evaporating ^{3}He into concentrated phase at low temperature is given by

$$\dot{Q} = \dot{n}_3 L \propto T^2 \,, \tag{4.1.5}$$

where $\dot{n}_3$ represents the flow of ^{3}He . The cooling power at the low temperature still exists in figure 4.1.3. This allow us get the cryogenic environment about 10 mK. On the other hand, the cooling by ^{3}He liquid has only reached at about 250 mK (see figure 4.1.3), however, at high temperature, helium gas has larger cooling power than dilution cooling. Thus, we should use proper methods to make cryogenic environment, matching range of temperate.

4.1.2 Dilution refrigerator

DR provides temperatures below 10 mK and can be operated without moving parts in low temperature phases, such as cylinders. The DR uses the mixed heat of the two isotopes of helium, ^{3}He and ^{4}He , to provide cooling. In order to be able to perform a dilution re-

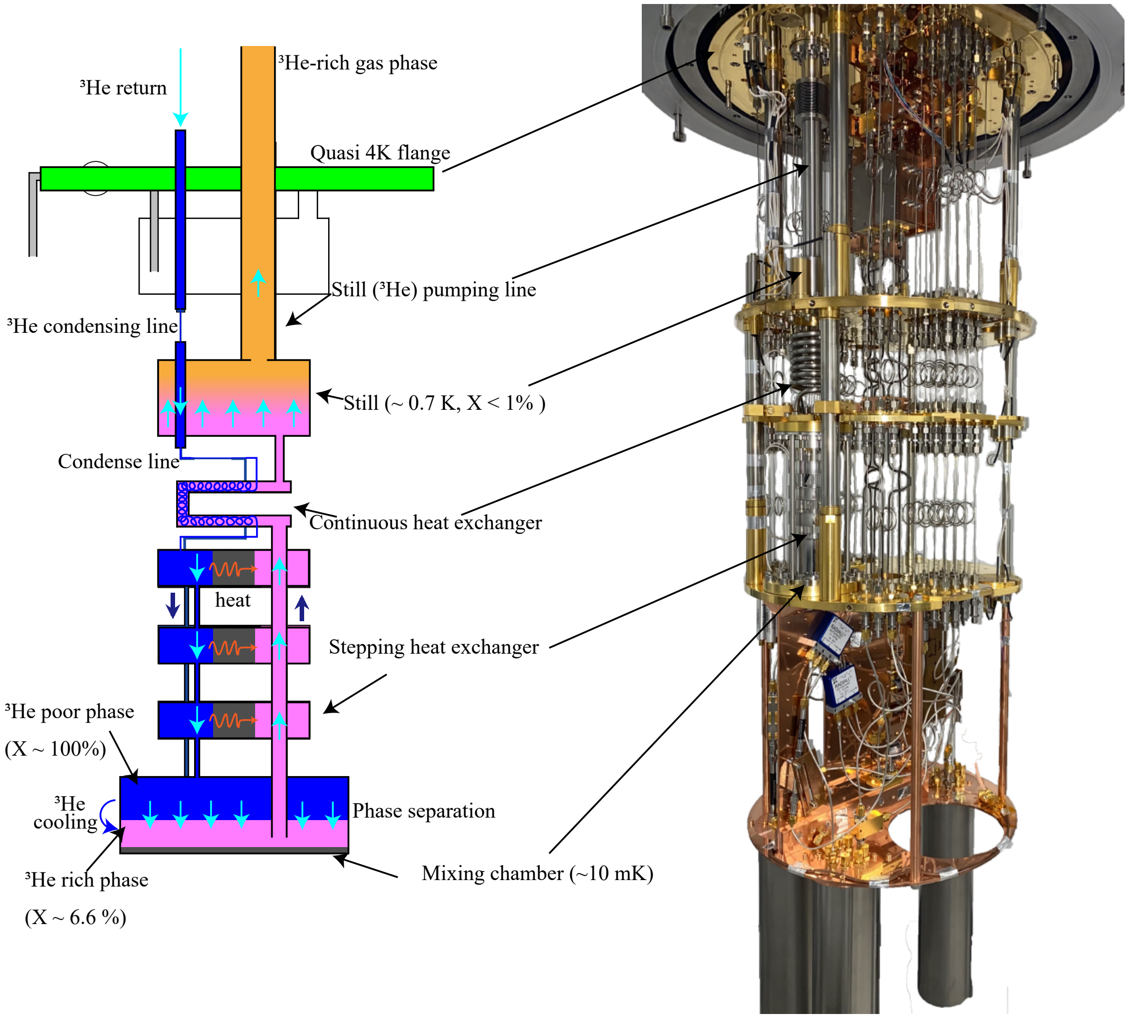

Figure 4.1.4: Schematic diagram of the dilution refrigerator (figure talking from the manual document of the LD250 Bluefors.inc)

frigerator cooling cycle, one must first obtain a starting temperature of liquid helium (4.2 K) or a degree below it. Such a refrigerator uses the cooling heat generated by mixing the helium isotopes ^{3}He and ^{4}He for cooling. This cooling cycle is possible due to the special and fortunate properties of the ^{3}He /^{4}He mixture at low temperatures. At saturated vapor pressure, pure ^{4}He undergoes a phase transition from ordinary liquid to superfluid at 2.17 K (below this transition temperature the properties of the two isotopes result in completely different); diluting ^{4}He with ^{3}He decreases the superfluid transition temperature. The ^{4}He - ^{3}He mixture separates into two phases: the ^{3}He -rich phase (enriched phase) and the ^{3}He -poor phase (dilute phase). Approaching absolute zero, the enriched phase becomes pure ^{3}He , while 6.4% of the ^{3}He remains in the dilute ^{4}He rich phase. The enthalpy of ^{3}He in the dilute phase is greater than in the enriched phase. Therefore, energy is required to transfer the ^{3}He atoms from the enriched phase to the dilute phase; in

DR, this energy is taken from a well isolated environment (mixing chamber), so cooling occurs.

To do this, it must first be cooled below 4.2 K, below which the helium becomes a liquid. The special properties of the ^{3}He - ^{4}He mixture allow for a low-temperature cooling cycle: when the ^{3}He / ^{4}He mixture is cooled below 0.8 K, the ^{3}He and ^{4}He are separated into two phases, with the ^{3}He being the most enriched phase and the ^{4}He being the other. On the one hand, ^{3}He is the most enriched phase; on the other hand, ^{4}He and about 6% of ^{3}He are dissolved in the dilute phase; the ^{3}He rich concentrated phase is at the top because it is lighter in mass than the dilute phase.

Therefore, when the temperature of Still is adjusted to about 0.7 K, only ^{3}He will evaporate selectively due to the difference in vapor pressure. As this evaporation takes place, the ^{3}He in the dilute phase is reduced, so the ^{3}He flows from the concentrated phase to the dilute phase by osmotic pressure. As this ^{3}He moves from the concentrated phase to the dilute phase, it removes heat from the surroundings (cooling). This is because ^{4}He is a superfluid below 0.5 K and has almost zero viscosity (since the normal fluid also exists in the dilute phase, total viscosity is still not zero, but much smaller than normal fluid). Thus in the dilute phase ^{3}He can be considered a gas.

In the concentrated phase, however, interaction in ^{3}He is so strong that it can be considered a liquid. Therefore, when ^{3}He changes its state from liquid to gas (evaporation), it loses heat. This evaporated ^{3}He can be recovered and cooled again from the other side to return to the concentrated phase to complete the cooling cycle. ^{3}He can be constantly cooled around the surroundings while circulating the ^{3}He , resulting in a continuous and stable mK temperature.

Detail of dilution refrigerator

Figure 4.1.4 is a schematic diagram of the dilution refrigerator. The ^{3}He - ^{4}He mixture is phase-separated in the lowermost vessel, called the mixing chamber. The dilute phase in the mixing chamber is connected to the upper vessel, called the still. The liquid level (domain between liquid and gas) of the mixture is kept always at the still to get large and static evaporation rate. The role of the still is to selectively evaporate the ^{3}He from the mixture by pumping the mixture vapor through a relatively large cross-sectional tube (still line) connected on top of the still. The evaporation also decrease the temperature at still, but this cause the decrease of the evaporating rate. To prevent decreasing the still temperature, the still also has the a external heater to maintain a constant temperature of about 0.7 K which can keep the evaporation rate high although the mixing chamber is cooled.

The idea to selectively exhaust ^{3}He from the mixed vapor with an exhaust pump is re-

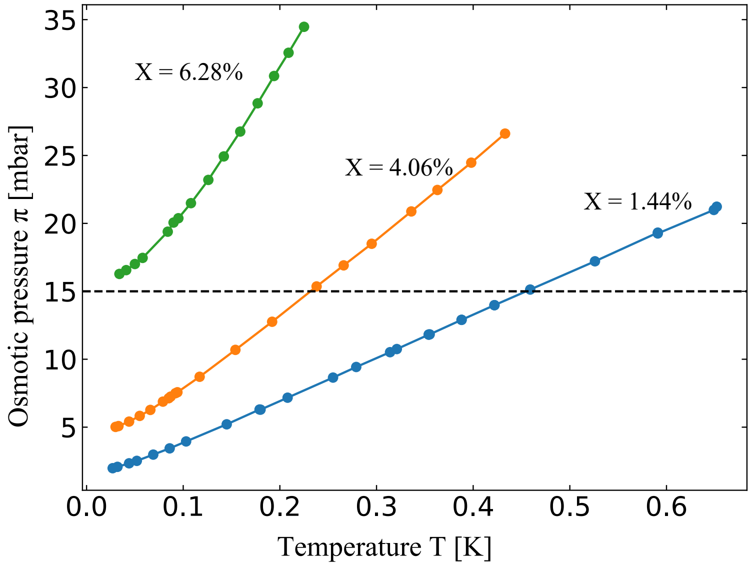

Figure 4.1.5: Osmotic pressure of dilute ^{3}He - ^{4}He mixture at a pressure 0.26 bar.

alized by using the difference of the osmotic pressure of the ^{3}He from one of the ^{4}He , and using the thermal isolation between the still and the mixing chamber. At mechanical equilibrium, the osmotic pressure of the ^{3}He component π_3 is equivalent between the diluted phase in the mixing chamber and the liquid in the still. Therefor, in the equilibrium, the osmotic pressure should be constant anywhere in the still line connected to mixing chamber. On the other hand, the temperature of the still is well isolated from the mixing chamber by the stepping heat exchanger.

The osmotic pressure is an increasing function of X and T (Figure 4.1.5). So thus, the temperature and the concentration of ^{3}He in the dilute phase at the mixing chamber is $T \approx 10\,\mathrm{mK}$, $X \approx 6.6\%$, to equivalent the osmotic pressure of the ^{3}He , the concentration of ^{3}He X_{still} in the still ($T \approx 0.7\,\mathrm{K}$) is less than 1% [145, 214].

The vapor pressure of ^{3}He at still, however, is three orders of magnitude higher than one of ^{4}He (shown in figure 4.1.6). This difference between ^{3}He and ^{4}He come from the zero point fluctuation with different mass. Thus, 90% of the exhausted mixture is ^{3}He , which means that ^{3}He can be exhausted almost selectively.

When ^{3}He is exhausted, the concentration of ^{3}He in still is decrease. To make balance of the osmotic pressure, the flow of ^{3}He $\dot{n}_3$ arise from the concentrated phase into diluted phase. This flow $\dot{n}_3$ is belong the cooling around environment and the cooling power is depending on the flow rate (4.1.5). This process is so-called "dilution cooling".

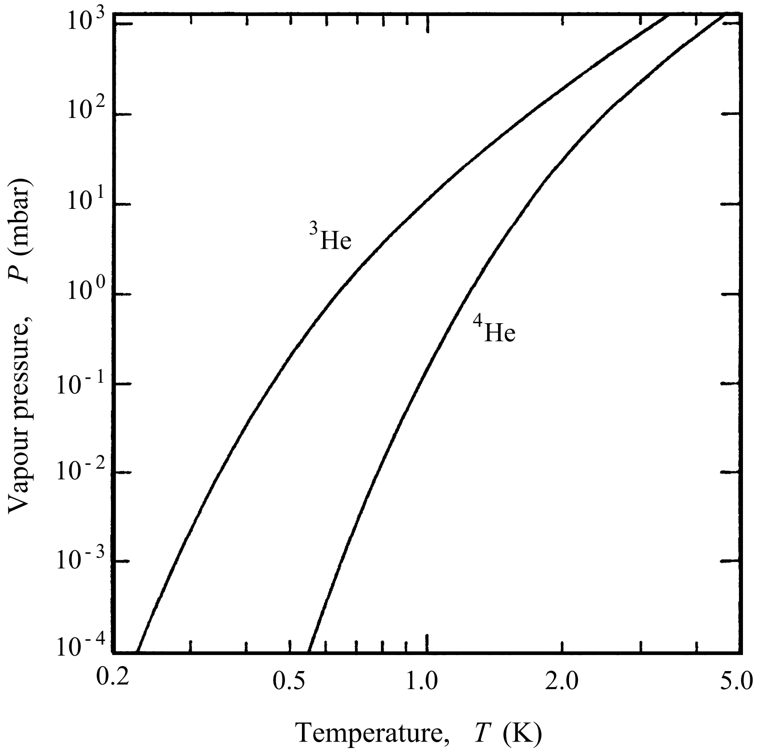

Figure 4.1.6: Vapour pressures of ^{3}He and ^{4}He

Mechanics of dilution refrigerator

If the ^{3}He vapor is continuously evacuated from the still, the concentrated phase in the mixing chamber will be eventurally exhausted and the cooling will end. Therefore, continuous cooling can be achieved by using a well-sealed ^{3}He evacuation pump operating at room temperature to return the evacuated ^{3}He gas to the concentrated phase. The return path (condense line) is described according to figure 4.1.4. First, the ^{3}He gas is re-liquefied in a small liquid ^{4}He depressurized cooling chamber with $T \approx 1.5\mathrm{K}$, called a 1 K pot. It is then thermally contacted with the still and cooled to 0.7 K before being continuously cooled in a decompressor. ^{3}He vapor is then transferred through the continuous heat exchanger and step heat exchangers, both of which exchange the heat with a dilute phase ^{3}He - ^{4}He mixture through the separating metal wall, and finally return to the concentrated phase in the mixing chamber. The minimum temperature reached by a dilution refrigerator is determined by the performance of these heat exchangers (moreover, when we install the measurement cable, they also cause the heat leak into mixing chamber.). This is because the majority of the heat input into the mixer is provided by ^{3}He returning from room temperature through the condense line.

In general, it is known that high cooling efficiency can be obtained by immersing the sample directly in the liquid refrigerant due to the large contact area. However, when the temperature is lower than 1 K, the interfacial thermal resistance between the liquid helium and a solid such as a metal becomes a serious problem. This is called "Kapitzer resistance". which is known to increase as T^3. Liquid ^{3}He , ^{3}He - ^{4}He mixtures and high purity metals themselves have high thermal conductivities in the mK temperature range. To prevent this resistance, exchnagers should have large surface area. Such a large surface area in continuous heat exchnager is realized by the using coiled line in still line. In the step heat exhanger, scince the temperature is more lower than still, surface is more required. So thus silver or copper powder is used, of which particle has the size 100 nm.

4.1.3 Cryogenic wiring for microwave

Quantum signals generated by superconducting quantum circuits are transmitted as microwaves. This microwave path travels over superconducting circuits, through non-magnetic copper coaxial cables, through low-temperature high-frequency isolators, and then to NbTi superconducting cables, up to 4K (shown in figure 4.1.8). The signal that reaches 4K is amplified again by the low noise amplifier (HEMT AMP) after passing through the low temperature isolator again. After amplification, signal is carried to the electronic equipment at room temperature using a low-loss core wire (copper) plated with silver. At room temperature, a total of about 100 dB of amplification is performed between the superconducting circuit and the measuring instrument using two stages of amplified air.

Next, the reason for using each component will be described. First, the reason why the cable directly connected to the superconducting circuit is non-magnetic is that the superconducting circuit is protected by a magnetic shield (described later), so that the non-magnetic cable is placed inside the magnetic shield. Furthermore, the reason for the flexible cable is that the wiring can be freely routed for the rearrangement of the experimental circuit.

Using a superconducting cable to connect Sample Stage to 4K protect a very weak quantum signal from chip. The signal is very easily buried in noise. In mixing chamber, the temperature is about 10 mK, there is a very large temperature difference with respect to mK up to 4 K, where amplifies the signal in the first stage. Therefore, the signal is protected from this thermal noise by using an NbTi cable that becomes superconducting at 4 K or less, has a large electrical resistance, and has a very small thermal conduction.

The reason why the low temperature isolator is sandwiched between the non-magnetic cable and the superconducting cable is to prevent the backflow of thermal noise from the superconducting cable, which is connected to the part hotter than MXC. An isolator is one of the high-frequency components, and one of the three terminals called a circulator (that transmits signals only in the direction of the arrow) can be used for 50Ω. It is terminated. As a result, the signal from In to Out flows, and the noise signal from Out

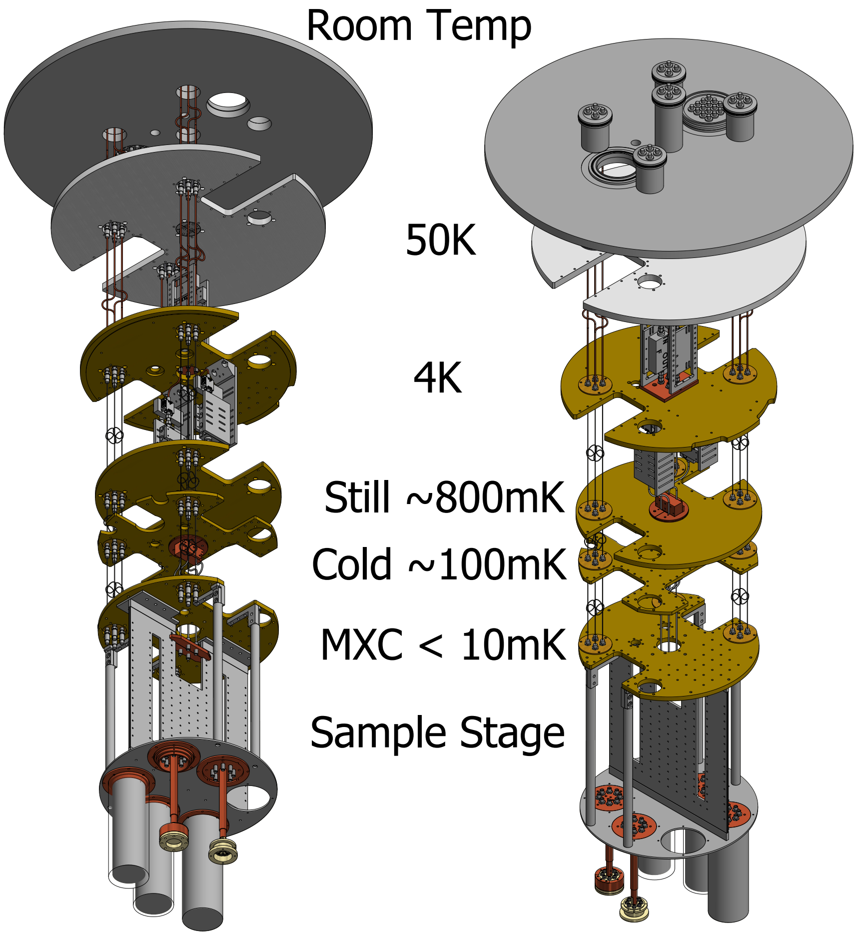

Figure 4.1.7: DR design and cold finger to measure for superconducting quantum circuit

to In is cut off. For the same reason, an isolator is also installed in the part connected to the superconducting cable or HEMT amplifier. In this case, not only the temperature but also the purpose of preventing the backflow of noise generated by the HEMT itself. In any case, the isolator acts as a valve that directs the flow of the signal in one direction, preventing noise and the backflow of the signal itself.

Although it is a HEMT amplifier, it is necessary to pay close attention to various things because the amplification here is the first for a weak signal. First, it is, of course, better that the HEMT amplifier body has sufficiently low noise if its amplification factor is large. In addition, it is important to have a solid thermal anchor to allow the heat generated by the HEMT amplifier to escape sufficiently. Even if the HEMT amplifier body is good, it is not good if the DC bias current used for amplification has noise. In other words, it is also essential to use a low-noise bias power supply.

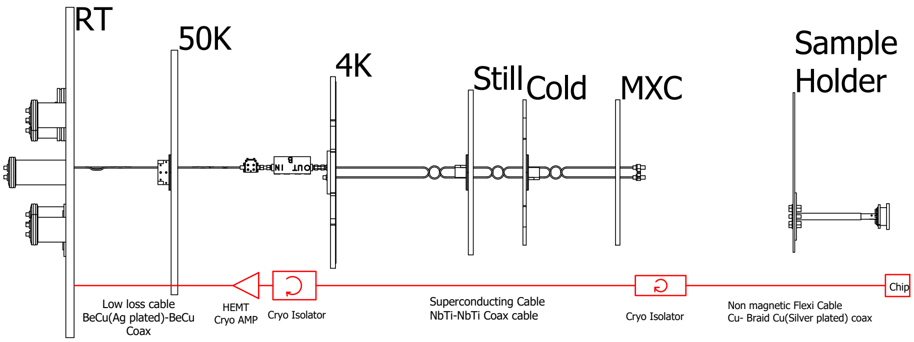

Figure 4.1.8: Wiring arrangement to measure for superconducting quantum circuit

In this way, the 4K amplified signal is transmitted to room temperature by a low-loss, silver-plated copper coaxial cable. At this time, the temperature is already 4K or higher, so there is no material that becomes superconducting in general distribution. Therefore, a material with good electrical conductivity is used, but with a coaxial wire made entirely of silver, the heat inflow from room temperature becomes extremely large. At high frequencies, there is a phenomenon called the skin effect in which a current flows only on the metal surface, so only the surface needs to be made of silver, and the other conductors are BeCu, which does not become a resistor and has a heat conduction smaller than that of silver. I am using it.

In addition, the superconducting coaxial cable is directly connected and penetrates each temperature layer to connect MXC and 4K. Therefore, thermal anchors are provided so as to make thermal contact with each temperature layer. Figure 4.1.7 is the overall picture of the designed superconducting quantum circuit measuring device in the refrigerator. This whole thing is called Cold Finger. The Big Plate has a large number of M4 screw holes to which each microwave component can be fixed. The BigPlate also has two windows. This is to allow wiring to go back and forth on both sides of this plate. It also has the purpose of reducing the weight of the entire Cold Finger as much as possible. If the weight increases, the cooling time increases proportionally. As a rule of thumb, it is said that 1 kg of copper will increase the cooling time by about 1 hour.

4.2 Microwave engineering

4.2.1 Spectroscopy

One of the most useful and famous experiment methods are spectroscopy to observe a static state of a system of interest. A static state show the information of the system such as energy diagram through frequency domain measurement. When spectroscopy are conducted, a signal with a frequency of interest are applied into the system of interest, which are called *probe signal*. The probe signal are spirited in two paths, one is for a device under test (DUT), the other is for a reference. Then refraction or transmission signal from DUT are detected, and also compared with reference signal. This procedure allows us to know what effect are from DUT, namely DUT interact probe signal, and to track physics and mechanism behind the system.

This method is very useful and convenient because usually we do not know so much information what we are interesting and want to know inside, so the spectroscopy requires just scattering parameters. Then it is easy to perform experiment while we have almost no information of the system. Almost any system can be applied and give us many knowledge.

4.2.2 Measurement resonator

One of the fundamental elements is resonator in quantum electromagnetic dynamics. The resonator or cavity are characterized by resonant frequency and characteristic impedance.

Quality factor and S_{21} of notched resonator

In order to give microwaves to the resonator, it is necessary to locally couple with the resonator called feedline, and the circuit The figure is shown in Figure 3.4. V in represents the power supply, and L 1 and C c of the Feed line are coupled to the resonator with respect to the LCR resonator. 33 Think of a system. Such a shape is called notch type, and when it is calculated using Kirchhoff's law etc., it is finally The obtained S parameter S 21 can be obtained by referring to [32] and [33].

$$S_{21}^{notch}(f) = \frac{V_{out}}{V_{in}} = a\mathrm{e}^{i\alpha}\mathrm{e}^{-2\pi i f\tau}\left[1 - \frac{(Q_l/|Q_e|)\mathrm{e}^{i\phi}}{1 + 2iQ_l(f/f_r - 1)}\right] \tag{4.2.1}$$

where, amplitude a, phase shift α, τ electrical delay due to length of a cable. All these coefficients can be calculated at the off-Resonant point $f = \pm\infty$. The resonator is represented by a frequency-dependent Lorentz function. It was possible to divide the S-parameters into two terms, an environment-dependent term and an LCR resonator term. If we define an external Q_e value Q_e consisting of a Q value Q_l, a feedline and a resonator coupling term, the internal Q_i factor is

$$Q_l^{-1} = Q_i^{-1} + \mathrm{Re}[Q_e^{-1}] \tag{4.2.2}$$

The external Q_e value can be adjusted depending on the strength of the coupling between the resonator and the feedline, but the internal Q_i value is determined by other qualities and is difficult to design intentionally. For example, if the quality of the board and a lot of CPW are accumulated, the adjacent ground conductor will float and the voltage 0 cannot be maintained, inducing other modes. Therefore, a higher internal Q value is a requirement to obtain a higher Q_l. In the experiment, the obtained S-parameters are fitted with this equation (4.2.2) to calculate the co-promotion frequency and internal Q_i value.

4.2.3 Spectrum measurement of transmon qubit

The transmon spectrum measured is shown in figure **??** depending on the external flux.

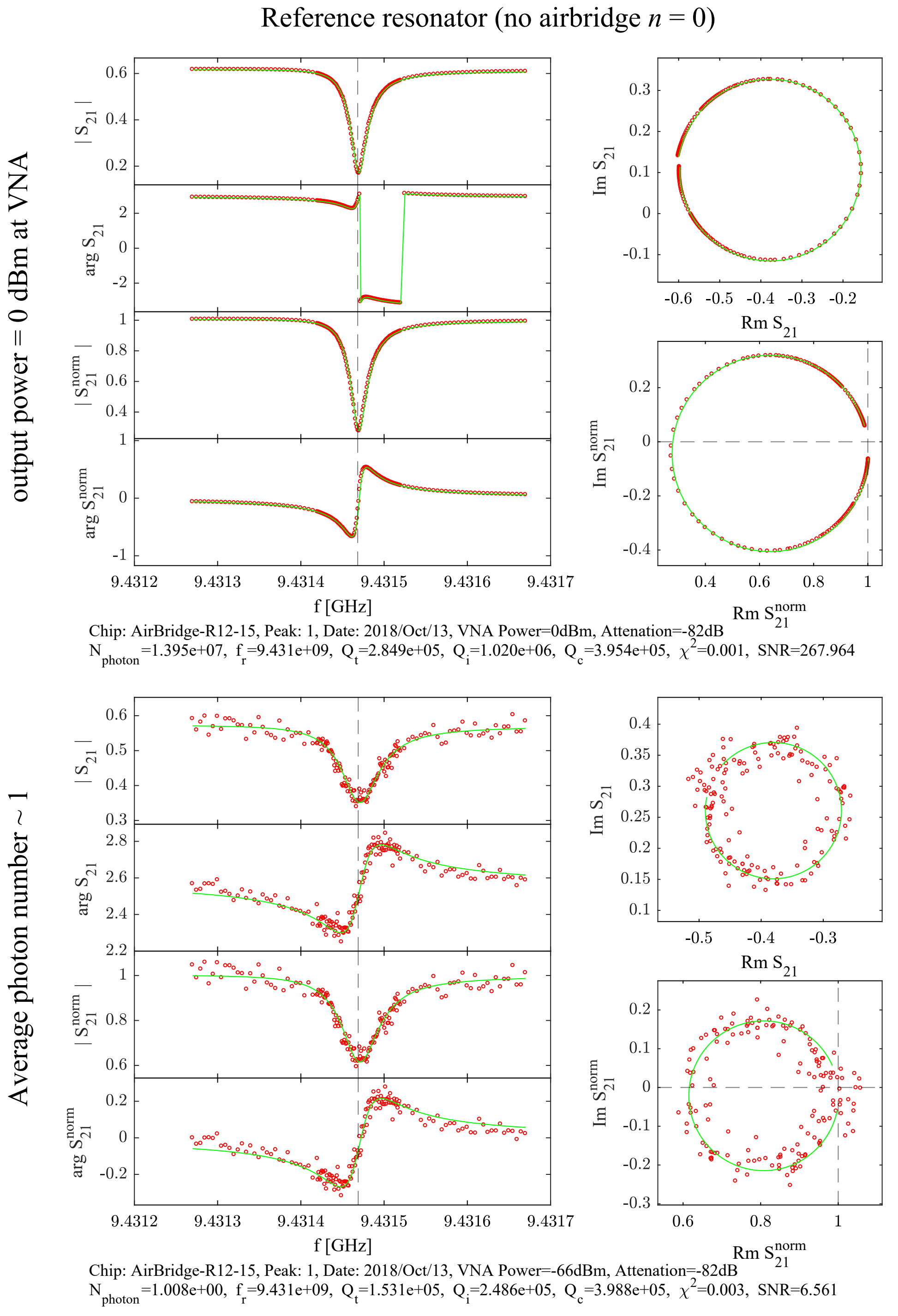

Chip: AirBridge-R12-15, Peak: 1, Date: 2018/Oct/13, VNA Power=0dBm, Attenation=-82dB
N_{photon}=1.395e+07, f_r=9.431e+09, Q_t=2.849e+05, Q_i=1.020e+06, Q_c=3.954e+05, χ^2=0.001, SNR=267.964

Chip: AirBridge-R12-15, Peak: 1, Date: 2018/Oct/13, VNA Power=-66dBm, Attenation=-82dB
N_{photon}=1.008e+00, f_r=9.431e+09, Q_t=1.531e+05, Q_i=2.486e+05, Q_c=3.988e+05, χ^2=0.003, SNR=6.561

Figure 4.2.1: Measurement result S_{21} and normalized data of resonator with 15 airbridges in center conducting line

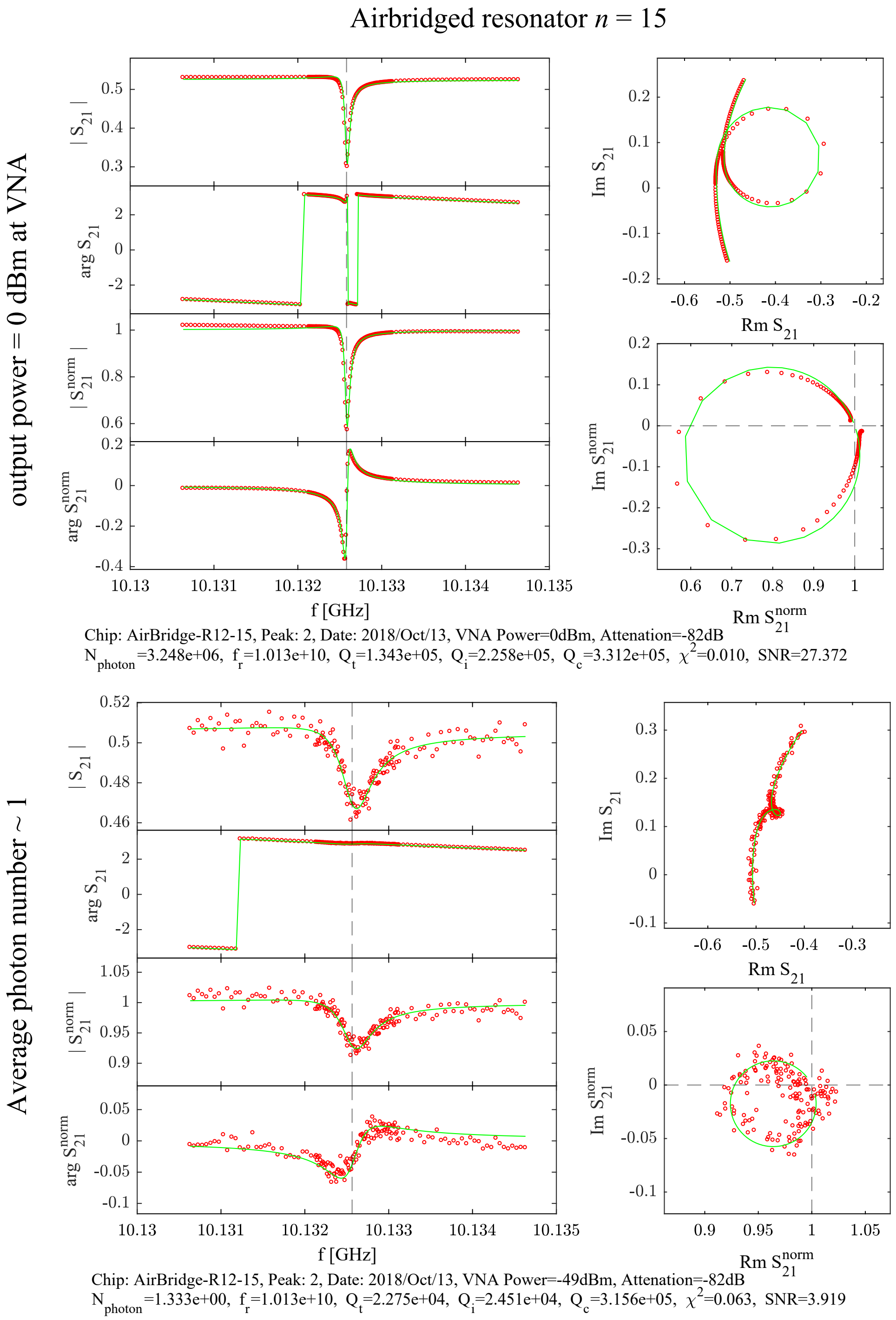
Airbridged resonator $n = 15$

Chip: AirBridge-R12-15, Peak: 2, Date: 2018/Oct/13, VNA Power=0dBm, Attenation=-82dB
N_{photon}=3.248e+06, f_r=1.013e+10, Q_t=1.343e+05, Q_i=2.258e+05, Q_c=3.312e+05, χ^2=0.010, SNR=27.372

Chip: AirBridge-R12-15, Peak: 2, Date: 2018/Oct/13, VNA Power=-49dBm, Attenation=-82dB
N_{photon}=1.333e+00, f_r=1.013e+10, Q_t=2.275e+04, Q_i=2.451e+04, Q_c=3.156e+05, χ^2=0.063, SNR=3.919

Figure 4.2.2: Measurement result S_{21} and normalized data of resonator with 15 airbridges in center conducting line

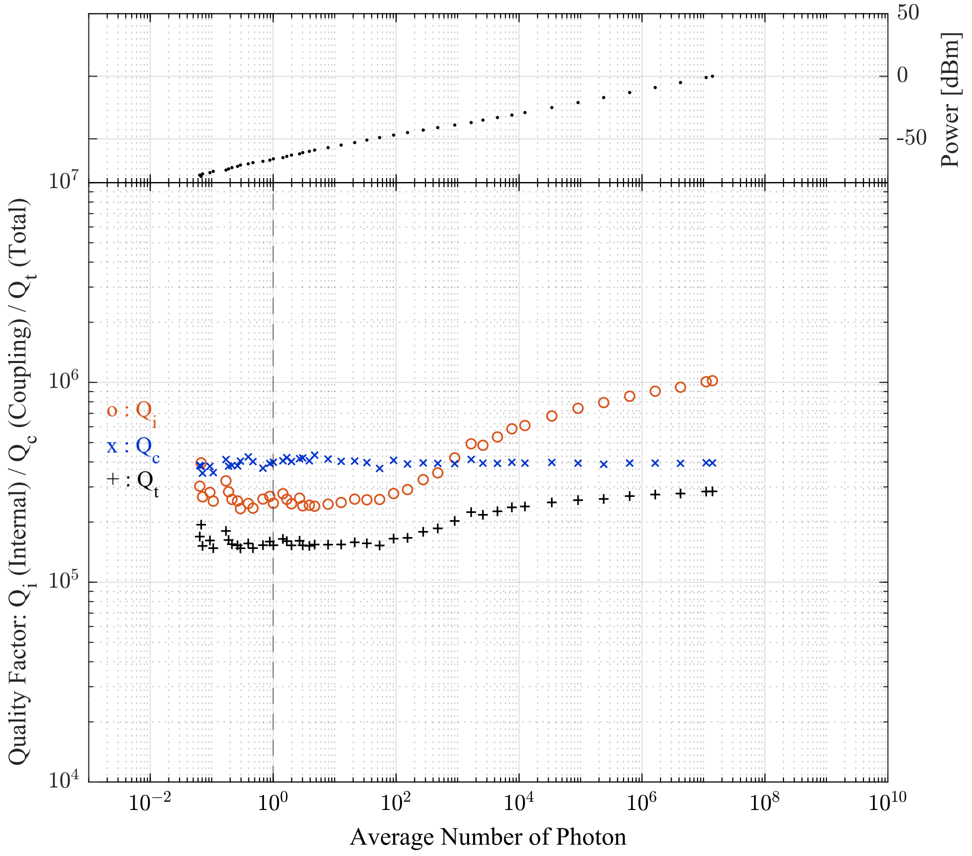

Chip: AirBridge-R12-15, Peak: 1, Average fr: 9.431[GHz], Date: 2018Oct13

Figure 4.2.3: Measurement result total, internal, and coupling quality factors of resonator without 15 airbridges in center conducting line

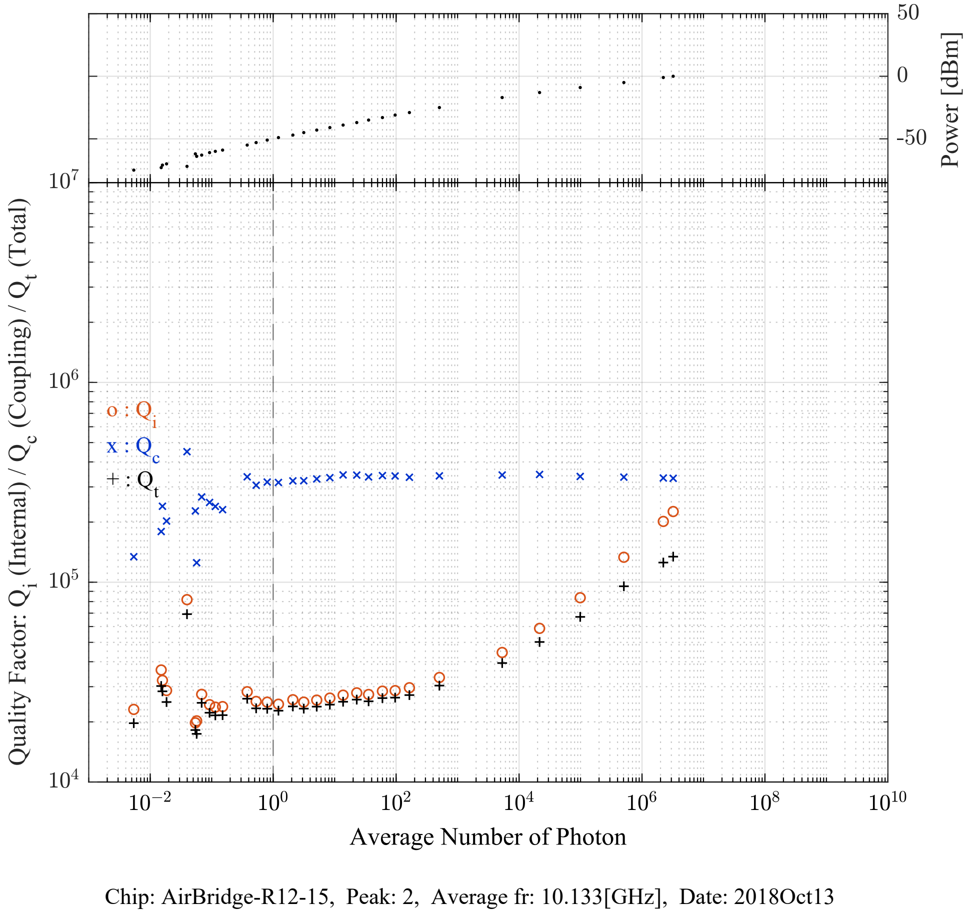

Figure 4.2.4: Measurement result total, internal, and coupling quality factors of resonator with 15 airbridges in center conducting line

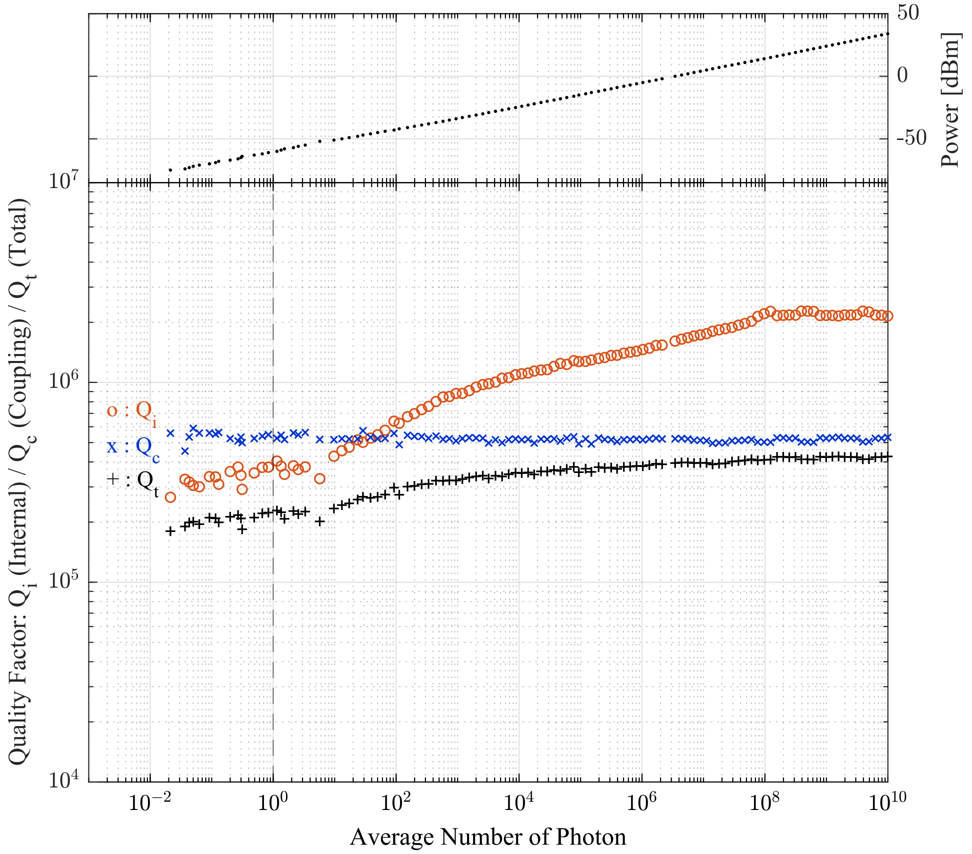

Chip: AirBridge-ab1-20, Peak: 1, Average fr: 7.234[GHz], Date: 2018Dec27

Figure 4.2.5: Measurement result total, internal, and coupling quality factors of resonator without 20 airbridges in center conducting line

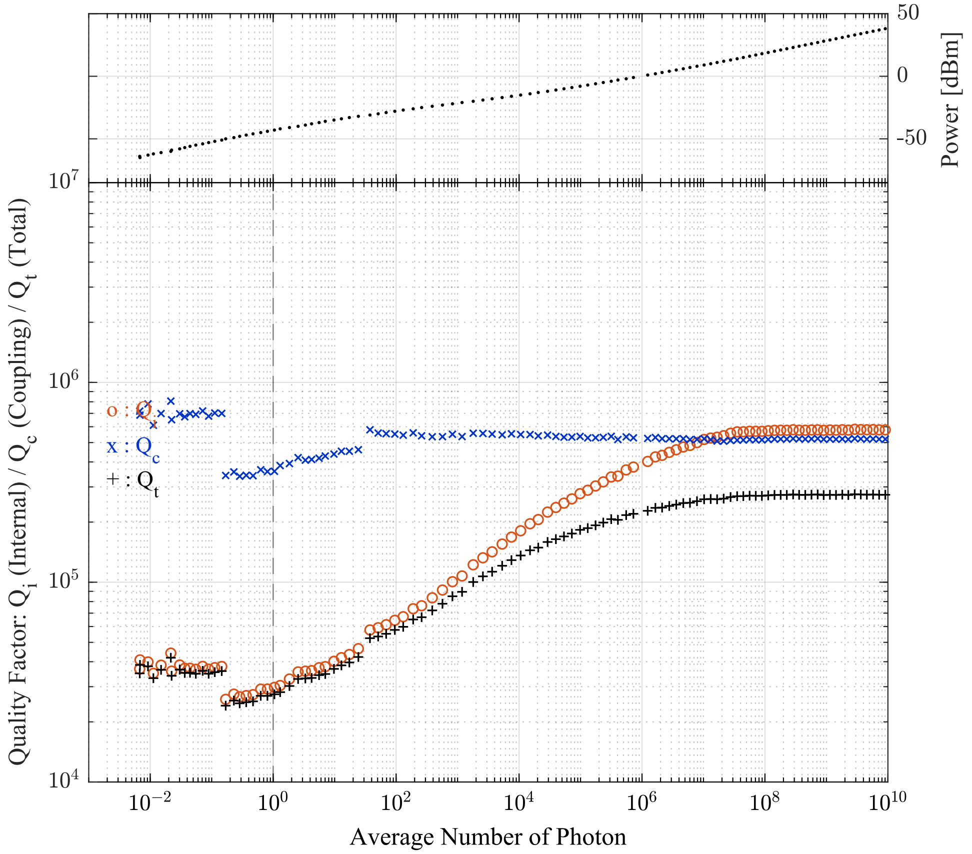

Chip: AirBridge-ab1-20, Peak: 2, Average fr: 7.805[GHz], Date: 2018Dec28

Figure 4.2.6: Measurement result total, internal, and coupling quality factors of resonator with 20 airbridges in center conducting line

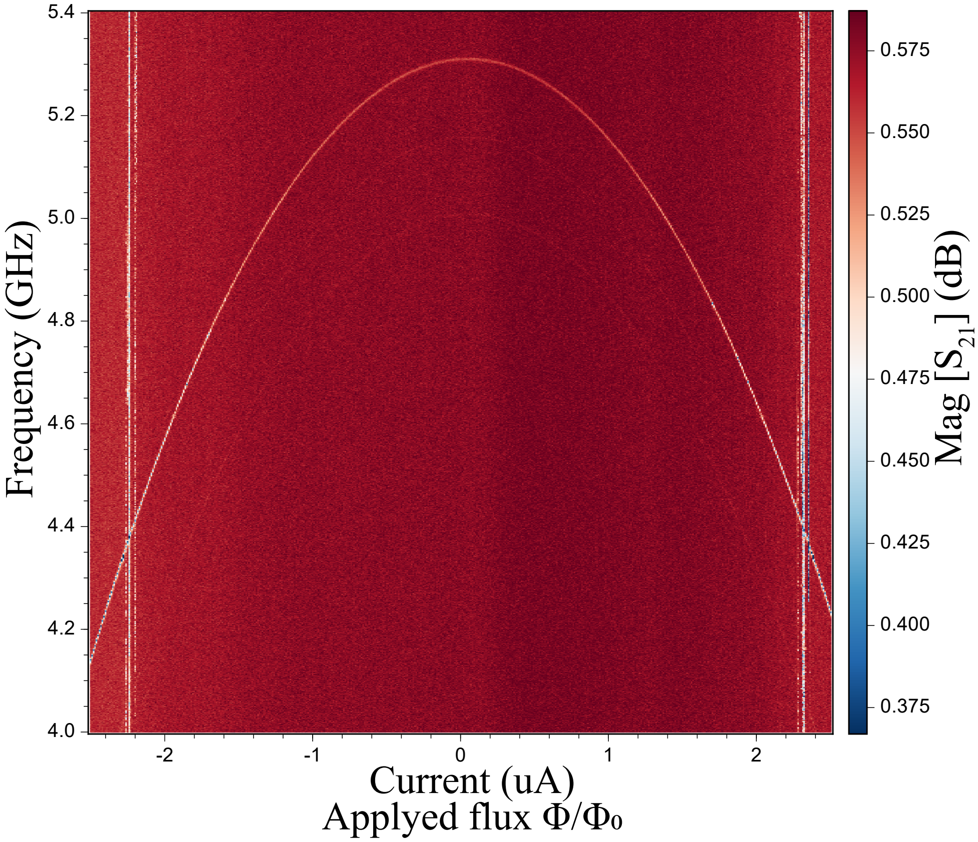

Figure 4.2.7: Spectrum of Transmon qubits

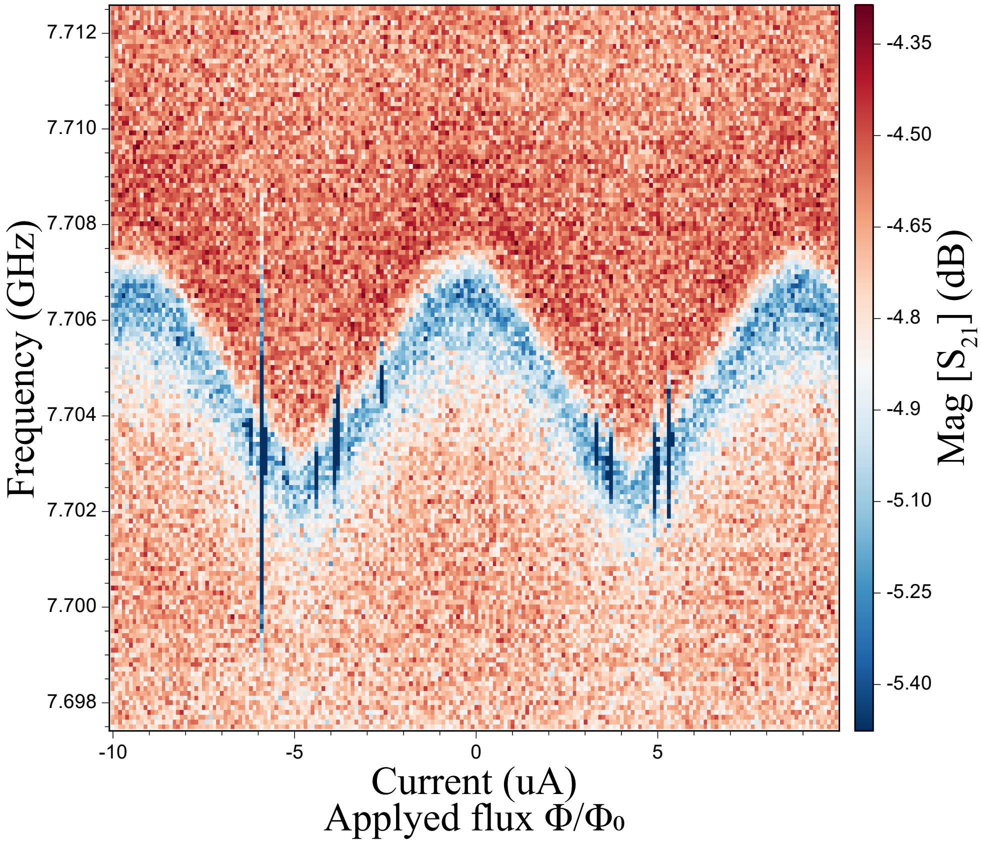

Figure 4.2.8: Spectrum of Transmon qubits

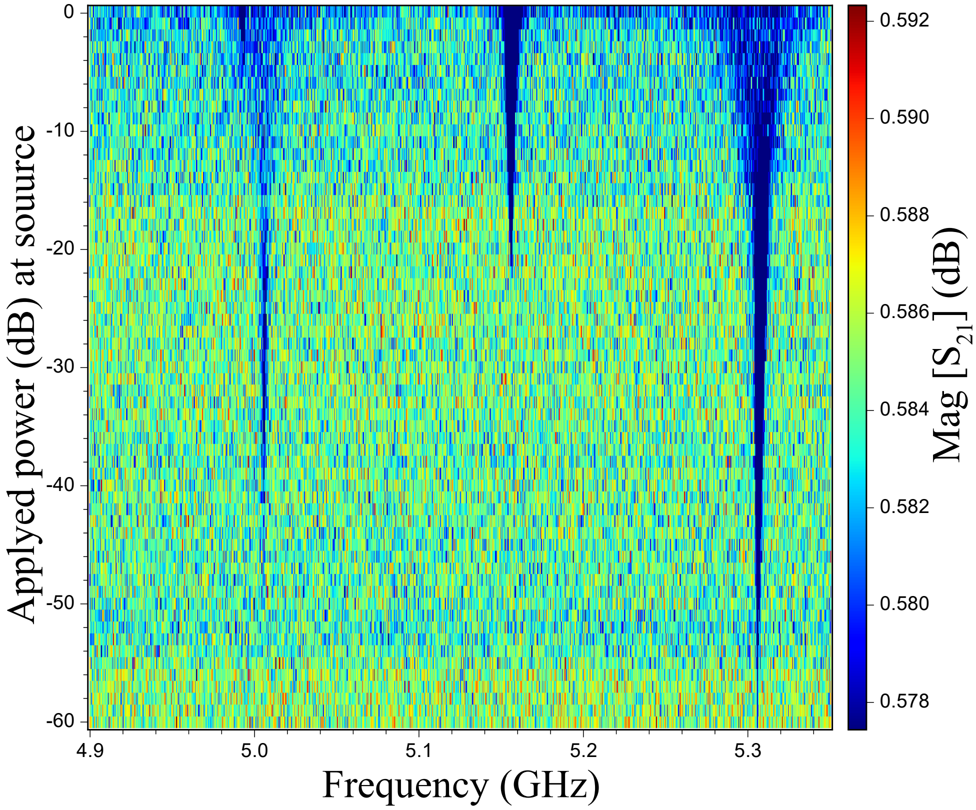

Figure 4.2.9: Spectrum of Transmon qubits vs power of drive

Part $|1\rangle$

Micro-architectures for Superconducting Quantum Computing Processor

Chapter 5

Micro-architecture of Quantum Computing Processor

5.1 Quantum Micro-architecture

Micro-architecture is a one fundamental layer to establish the quantum computer. In classical information processor field, micro-architecture of chip is one of the most crucial concepts to manage, design, fabricate, and verify the milestone. This concept allows us to simply consider and focus on the layout of the chip without higher level layer to quantum computer or much lower level physics. What could be so difficult to implement? As we have seen in the previous chapters, the source of all the difficulties can be reduced to noise. Reducing this wide variety of noise requires a great deal of diligent work. Each one of these tasks gives few visible results. However, as in the case of with the detection of gravitational waves [47], we are convinced that the endless reduction of noise will add up to a significant result.

5.2 Requirements of micro-architecture to build quantum computer

A particular solution that is being sought at the moment is the introduction of control wiring. Compared with the implementation of a classical computer, the quantum computer is very different as listed below. Therefore, there are various new technical challenges in implementation to be addressed.

1. The number and density of input and output lines to and from the external world are much larger in quantum arithmetic circuits. We have been working on the imple-

mentation of quantum logic circuits, which are spatially arranged, whereas quantum logic circuits are temporally arranged. As a result, all physical qubits must be connected externally to each other by control lines and controlled precisely in the time domain. A large amount of wiring with high density creates new challenges such as heat inflow to the refrigerator and crosstalk between the wires.

2. The frequency of the control signals used in a quantum computing circuit is around 10 GHz, about an order of magnitude higher than the clock frequency of a classical computer. This is a control microwave frequency that matches the energy of a typical superconducting qubit, and cannot be lowered easily. As a result, more advanced wideband interconnection technology and control measures for crosstalk between interconnects are required.

3. The multilayer interconnection technology of semiconductor integrated circuits cannot be applied directly to quantum arithmetic circuits. This is because the interlayer insulating film usually used in such technologies contains a lot of microscopic impurities that cause decoherence. The aforementioned high-density interconnection and interconnection crosstalk problems have been solved in conventional integrated circuits using multilayer interconnection/ground plane technology.

4. In quantum arithmetic circuits, all qubits need to be controlled in the time domain, so large scale multi-channel broadband signal generators need to be integrated and implemented. In addition, a large scale multichannel broadband classical logic circuit is also necessary for reading qubits. Therefore, to finally implement a 100-million-qubit universal quantum computer to solve real-world problems, we need to implement such broadband peripheral circuits on an unprecedented scale.

These requirement to integration of qubits is a very serious problem and cannot be avoided as long as the surface code scheme is used. Surface coding, as mentioned earlier, is done on multiple qubit circuits arranged in a grid. However, each qubit must be manipulated in order to perform the surface code. This means that wiring to the qubits located inside the chip is not possible on a two-dimensional circuit, entirely impossible. In a small circuit, only the intersection of the wires can be fabricated with Air Bridge [184, 43, 61] to pseudo-realize a two-dimensional circuit. However, as the circuit gets larger, there are more and more mixing wires. Thus, for integration, it is proposed to separate the classical circuits and qubits circuit into different layers.

Each research group is looking for its own way. For example, Google and some use the flip chip bonding technology to bond between the two layers [165, 210, 212, 150, 133, 115]; others uses small components called Pogo pins to mechanically create three-dimensional interconnects [34, 211]; and MIT uses the through silicon via (TSV) [247], which make hole on a silicon and connect between front and back sides conductor layers with impedance matched for microwave. The goal is to achieve multi-layered wiring by micromachining small holes in the substrate to conduct both sides of the substrate with matching impedance. In addition, the University of Tokyo group in Japan has proposed vertical wiring using TSVs from the back of the board. Each of these methods has its own advantage and disadvantage, and it is difficult to say which one is better. However, what they all have in common is that if the wiring layers are separated, wire mixtures are reduced, but another problem arises. Thus, there is no doubt that the technical problem of interconnections is confronting the development of quantum computers. Also, such three-dimensional wiring is a problem created by arranging qubits in a grid. Therefore, with the development of the theory of quantum error correction, circuits that are easier to wire may be devised.

Chapter 6

Micro-architecture of Surface Code

6.1 Pseudo-two-dimensional surface code micro-architecture

by Hiroto Mukai, Keiichi Sakata, Simon J Devitt, Rui Wang, Yu Zhou, Yukito Nakajima, and Jaw-Shen Tsai
published in New Journal of Physics [173].

6.2 Introduction

Recently, architectural designs for large-scale quantum computers have became increasingly comprehensive. This area of research requires a large amount of quantum engineering to specify how qubits will be manufactured, controlled, characterized, and packaged in a modular manner for fault-tolerant, error-corrected quantum computation [127, 178, 86, 113, 151]. The vast majority of architectures base their designs on the surface code because it has one of the highest fault-tolerant thresholds of any error-correction code, easing the physical fidelity requirements on the hardware, and is defined over a 2D, nearest neighbour array of physical qubits.

Superconducting quantum circuits have emerged as a major contender as a scalable hardware model for the surface code [**?** 75]. Superconducting qubits are fabricated with inter-qubit wiring for nearest-neighbor interactions, and each qubit requires external physical access for bias lines, control lines, and measurement devices. However, as two-dimensional (2D) arrays are scaled up, planar accessibility for control lines becomes a problem. Such challenges are sometimes referred to as the wiring problem, where physical qubits in the interior are no longer accessible in-plane from the edge [83].

Compared with classical silicon integrated circuits, it is much more difficult to achieve such wiring in superconducting quantum circuits. To individually access every qubit in

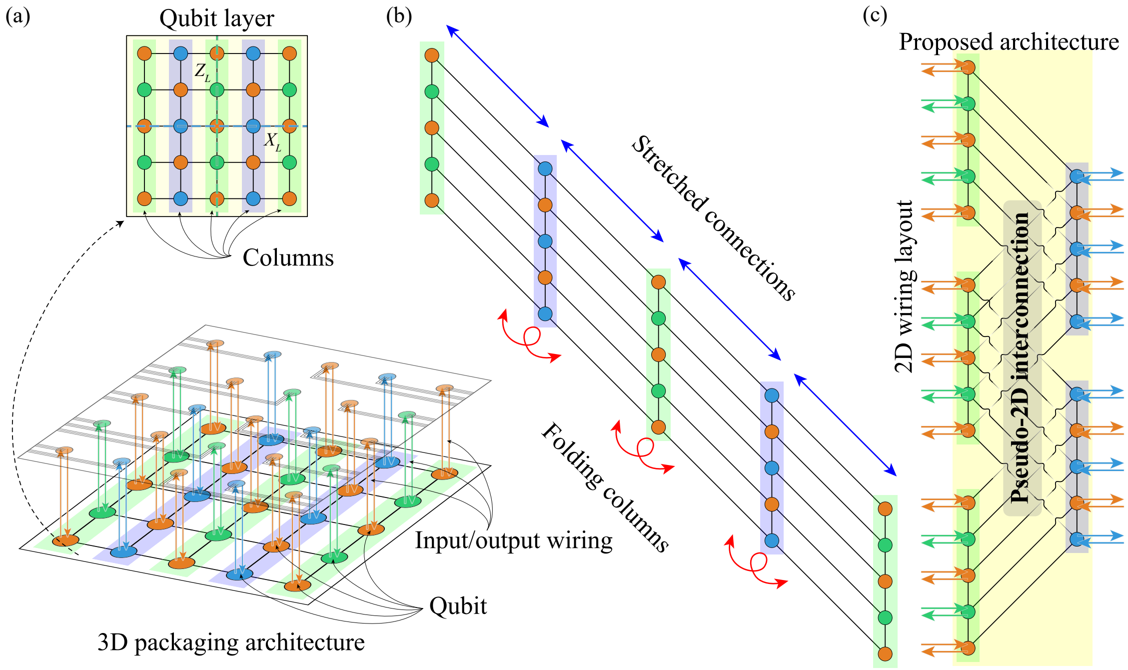

Figure 6.2.1: Standard circuit architecture and our proposed architecture for surface codes with 5×5 qubit array. (a) Standard system utilizing global multi-layer structures, a separated qubit layer (top figure), and a control/readout layer (clear layer in bottom figure). Qubits are divided into data qubits (orange circles) and X (blue circles) and Z (green circles) syndrome qubits, and all nearest-neighbor qubits are connected by inter-qubit wiring. Vertical arrows indicate input/output wiring. (b) Folding operation of proposed architecture. In the horizontal direction, interconnections of the 2D qubit array are stretched out while maintaining the resonator frequency. At each qubit column, the interconnection is folded. (c) Proposed planar architecture for surface code. After process (b), the proposed architecture has completely planar external wiring (no arrow intersect any wiring, external lines, and inter-qubit connections) with the help of pseudo-2D interconnections.

a 2D qubit array, standard multi-layer wiring technologies for silicon integrated circuits simply cannot be embraced as they generally require the introduction of decoherence enhancing and low-quality interlayer insulators [105, 126]. Therefore, many groups have been forced to utilize non-monolithic bulky three-dimensional (3D) wiring technologies in current superconducting systems [see figure 6.2.1(a)], such as flip-chip bonding, pogo pins, and through-silicon vias (TSVs) [9, 223, 205, 44, 10, 228, 78, 209, 4].

6.3 Proposed architecture

6.3.1 Concept

Our new architecture for the surface code is obtained by transforming a 2D qubit-array to a dual 1D qubit-array (we call it bi-linear array of qubits). Figure 6.2.1 shows the mapping before and after this transformation. The square lattice in figure 6.2.1(a) is divided into its constituent columns. Next, connections between columns, which take shape as resonators, are stretched [figure 6.2.1(b)] and then folded on top of each other successively, as shown in figure 6.2.1(c). As the connections are stretched out, the frequencies of the resonators are maintained, and it is a sign of scalability of our architecture. Such invariable frequencies do not survive in another 2D-array transformation [227].

Therefore, the circuits before and after the transformation both occupy approximately the same area, as shown by the yellow areas in figures 6.2.1(a) and (c). The resulting equivalent surface code circuit is a bi-linear array of the original 2D structure.

The folding operations liberate the columns locked deeply inside the original 2D lattice and bring them out to the edges of the bi-linear array. Therefore, the external control/readout lines connected to each qubit are accessible from the edges of the chip. This novel arrangement allows all these external connections to be prepared in a completely standard 2D layout.

The advantage gained in the external wiring as a result of the transformation, however, has a small cost in terms of the inter-qubit wiring between columns. These inter-qubit connections between neighboring columns require multilevel crossings. Nonetheless, these 3D structures only need to locally hop over inter-qubit connection lines. Thus, the cross-connections between the columns can be described as pseudo-2D.

In comparison, for the original surface code architecture, the multi-layer wiring grid involves an inter-qubit connection layer and an input/output wiring layer. Therefore, a global multi-layer structure, as shown in figure 6.2.1(a), is often adopted, which utilizes non-monolithic bulky 3D wiring technologies as mentioned earlier. Compared with the standard surface code arrangement, the new architecture has the following advantages:

(1) The complete separation of the input/output wiring and inter-qubit wiring will help suppress crosstalk between external lines and qubits as well as that between external lines and inter-qubit connection lines. Therefore, it is possible that the undesired decoherence of qubits owing to the external wiring will also be reduced.

(2) 2D planar layout of the input/output wiring which connects qubits to external electronics can be constructed by utilizing the standard 2D wide-band (microwave) technology. Superconducting resonators for the readout of qubits can also be prepared

with the standard 2D co-planar design.

(3) For local 3D (psuedo-2D) wiring, the ends of the inter-qubit connection lines always end up on the same qubit layer, regardless of the number of 3D hops involved in the connection. In such a case, the multi-layer crossing for this new architecture could be realized simply by using local monolithic 3D structures, such as superconducting airbridges.

Moreover, even though the original square lattice architecture can adopt a local 3D structure (airbridges) for the wire crossings between input/output and inter-qubit connections, compared with the new architecture, such an arrangement would produce strong crosstalk between external wiring and inter-qubit connection lines [cf. point (1) above].

Consequently, this architecture straightforwardly solves the challenging 3D external wiring problem. As mentioned, a convenient technology to realize cross wiring is an airbridge: a monolithic microstructure developed as low-loss wiring for superconducting qubits that can be fabricated in several ways, including a well-established standard fabrication process [43, 61]. It should be noted that, in standard superconducting architecture designs, a much larger number of airbridges - compared with the number additionally required for this proposed architecture - are already needed to maintain the uniform ground potential for all co-planar waveguide-based architectures.

6.3.2 Scaling estimation

To scale-up integration, one needs to consider that increasing the number of qubits M in a column will give rise to an increased number of airbriges in the scaled-up structure of this architecture [figure 6.3.1]. Therefore, one should limit M to the minimum required for the surface-code-based computer in an effective 2D array. This is the arrangement before the transformation shown in figure 6.3.3. This limitation posed by the number of airbridges results in a subtle change in the design compared with the standard 2D array for a surface-code design.

The typical logical structure of a computer shown in figure 6.3.2(b) is a 2D array of qubits used for the surface code computing utilizing braid-based logic [74]. Logical information is introduced by strategically switching on/off parts of the array to create and manipulate defects, which encode the logical qubits within the computer. The larger the 2D array at the physical layer, the more defects can be introduced for a given number of logically encoded qubits in the computer - or the error-correction strength of each logical qubits can be increased. Logic operations are then performed by topological braiding of the defects around each other. In figure 6.3.2(b), we illustrate a lattice that encodes two logical qubits via four pairs of defects (shaded regions), where two pairs are utilized for

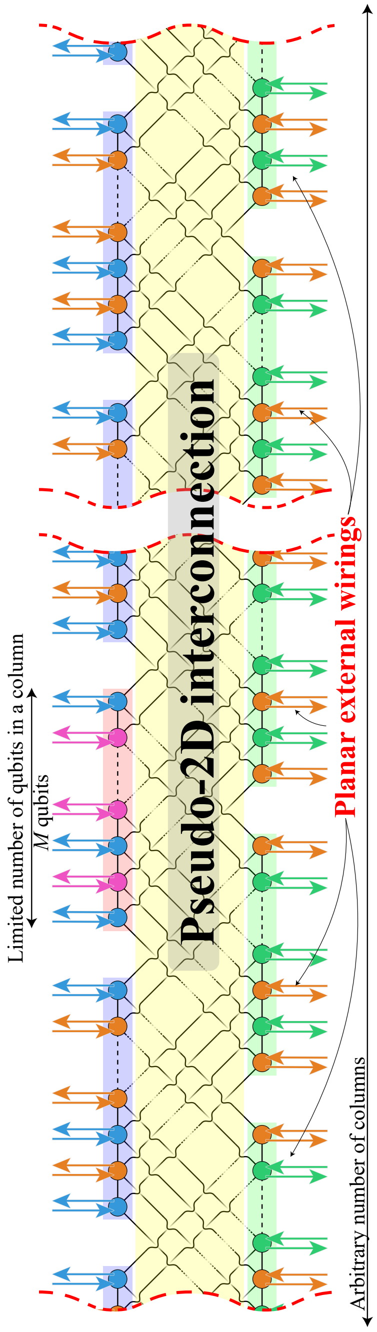

Figure 6.3.1: Physical layout of the new architecture. An arbitrarily long but fixed-width surface code can be created using a bi-linear arrangement of superconducting qubits that are cross-coupled with airbridged resonators. The fixed width of the surface code ensures that the airbridged resonators have a finite length and number of airbridged crossings. Each superconducting qubit can be accessed in the plane for the control, initialisation, and readout technology.

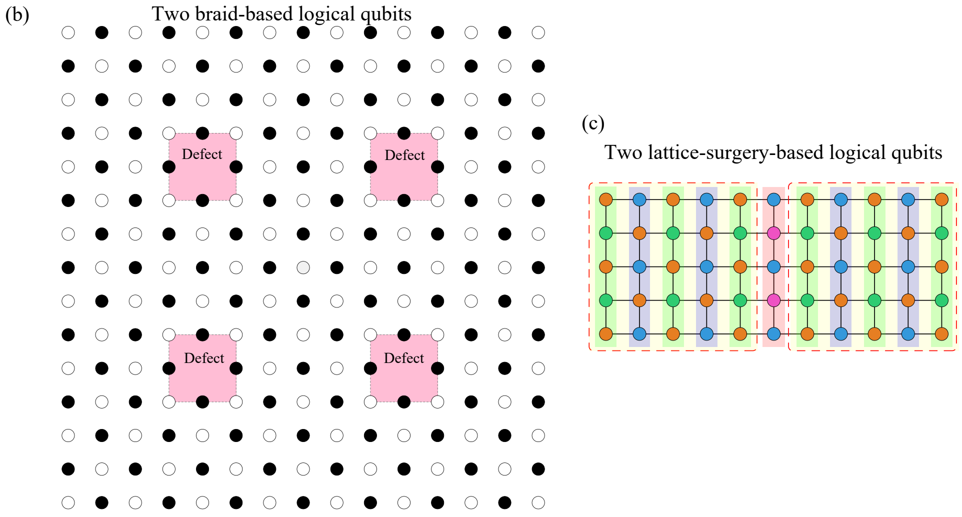

Figure 6.3.2: Standard braid-based arrangement of the surface code sufficient for encoding two logical qubits of information with a distance $d = 3$. (c) Standard arrangement of two lattice-surgery-based square patch as sufficient for encoding two logical qubits of information with a distance $d = 3$.

each logical qubit. The defects are encoded using a $d = 3$ surface code, which can correct an arbitrary single qubit error on either of the two encoded defect-based qubits. In order to realize this defect-based structure without significantly compromising the capability to efficiently enact arbitrary error-corrected circuits, scaling up is required in two dimensions.

In our new design the length of columns in the effective 2D array is limited owing to the number of airbridged crossings in an inter-qubit connection, but an arbitrary number of columns is allowed. Therefore, we envisage that a lattice-surgery-encoded logic will be used instead of the braid-based logic [shown in figure 6.3.2(c) for the $d = 3$ surface code] [114]. The lattice-surgery-encoded logic also can aid the realization of sufficiently fast classical error-correction decoding [54, 77]. In lattice surgery, isolated square patches of the planar code (*single logical qubit*, which is a surface code analogue that can encode a single piece of logical information) interact along a boundary to enact multi-qubit logic gates. This reduces the overall physical resource cost of each logical qubit, and results of several recent studies suggesting that lattice surgery techniques will always be more resource-efficient when implementing large-scale algorithms [110, 157, 73]. For a single logical qubit encoded with the planar code, a square 2D array of physical qubits is needed. For a quantum code with a distance d, $(2d-1) \times (2d-1)$ array of physical qubits is sufficient, the number of which can be reduced further by utilizing rotated planar lattices [114, 157] (see 6.4.4). This results in a linear nearest-neighbor (LNN) logical layout of encoded qubits [shown in figure 6.3.3], requiring less physical resources than defect-

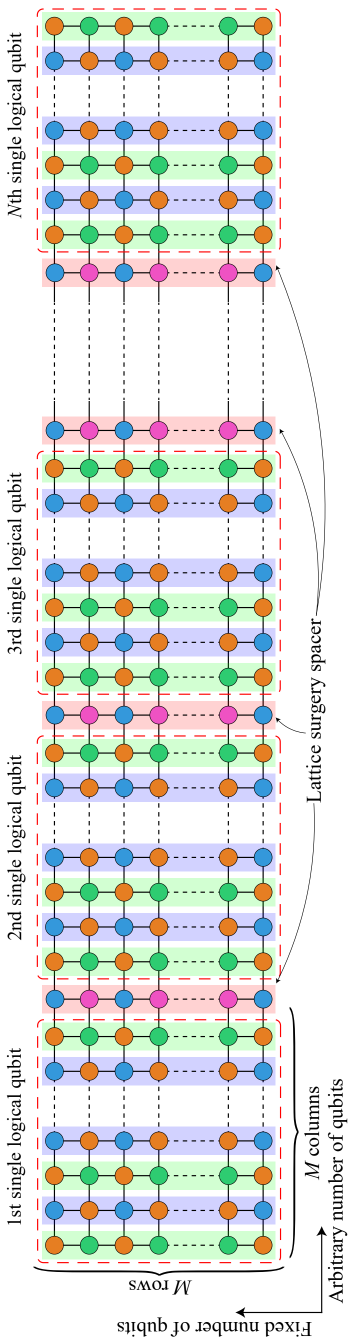

Figure 6.3.3: New logical qubit layout consisting of square patches of the surface code, each encoding a single logical qubit of information. Between the square patches there are spacer regions (red columns) to allow lattice-surgery-based logic operations. This layout maintains a small, fixed width of the physical lattice and converts the computer into an LNN logical qubit array. A technique for logical compilation and operation can include a single extra row of physical qubits stretching the length of the computer to enact a new data bus technique for logic operations using planar codes and lattice surgery [112].

based logical qubits. As shown in figure 6.3.3, there are additional columns of physical qubits (red columns) that are spacers between the encoded qubits, which are required to perform the lattice surgery operations.

It should be noted that the current methods for circuit compilation using lattice surgery still assume a 2D nearest-neighbor arrangement of logically encoded qubits [110, 157, 73]. This is because lattice surgery has two basic classes of operations (merges and splits) over two types of boundary for each planar code qubit (rough and smooth). As merge and split operations can only occur at a single boundary between logical qubit regions, we need to be able to convert between smooth and rough boundaries (as described in detail in Ref. [114]), and hence compilation into this LNN logical structure using a layout of pseudo-2D physical qubits will require some slight modifications over current techniques [110, 157]. However, a recent result of introducing additional rows of physical qubits to act as a data bus for logic operations can be used and is completely compatible with an LNN arrangement of qubits at the logical level [112].

Generally, to realize a square logical encoded qubit with given distance d of the surface code, a physical array contains $2d-1$ columns with $2d-1$ qubits for each column. Consequently, for a quantum computer containing N logical qubits on the planar code, an array of $M \times [NM + (N-1)]$ should be utilized. Here, $M = 2d-1$ is the number of qubits in a column, NM is the number of columns in the array for N logical qubits, and the extra factor of $(N-1)$ is the spacing region between adjacent logical qubits - needed for the lattice surgery (or a bus system [188]). This translates into a bi-linear array of $2\times\frac{1}{2}(2d-1)(2dN-1)$ [shown in figure 6.3.1]. The number of crossing points by interconnections is at most half the number of qubits in a column, at most $\lceil[(2d-1)-1]/2\rceil = d-1$, representing the number of airbridges per resonator. The factor of $1/2$ originates from the fact that alternate resonators (interconnections) are shared by two qubits. Hence, although the number of columns NM linearly increases with the number of logical qubits, the number of airbridges contained in a resonator will only be half the number of qubits in a column (which is fixed for a given code distance d).

In practice, the width of this array is related to the number of logical qubits, whereas its length is given by the distance of the planar code used to encode each logical qubit. For a large error-correcting code, each logical qubit requires $d = 15$–20 to be capable of correcting up to 7–10 errors (sufficient to heavily suppress the logical error rate). For a heavily error-corrected logical qubit with $d = 15$–21, the total number of qubits in a column will be $M = 29$–41 with a maximum number of airbridges for a given resonator of 14–20. By utilizing planar code encoding and lattice surgery [114] for fault-tolerant logic, we can define our computer as a long, rectangular structure consisting of an LNN array of *logical* qubits (requiring compilation of the high-level quantum algorithm with

LNN constraints [112, 110, 188]).

6.4 Preliminary tests

As a feasibility study of this new circuit scheme, we carried out preliminary evaluations of its most important new component, namely, the pseudo-2D interconnection consisting of crossed resonators with airbridges. We studied the dependence of the gate fidelity on the quality factor of resonators, where the centerline contains airbridges. We also studied the crosstalk between crossed co-planar resonators in the pseudo-2D interconnection network.

To examine whether airbridges can be used while still satisfying the error requirements for the surface code, we carried out an experimental test on chips containing the coupling airbridged resonator without qubits and a numerical simulation on a system containing a lossy resonator and two qubits without decoherence. Conventional research on superconducting quantum circuits employs a lossless resonator to eliminate its contribution. However, there has been little research related to the dependence of the gate fidelity on the resonator quality factor. Our numerical simulation reveals the lower limit of the internal quality factor, and the experimental test illustrates the possibility that this proposed architecture will be viable using current technology without special 3D techniques.

6.4.1 Quality factor of airbriged resonator

We prepared chips using a standard fabrication method for airbridges [**?**], with each chip containing both an airbriged resonator and a reference resonator made out of a 50-nm-thick Nb film. The film is sputtered on cleaned surface of non-doped Si substrate and etched by reactive ion etching (RIE). The airbridge design of each chip, including the interval between airbridge positions, is identical, and the only difference in fabrication is related to the number of airbridges (15 or 20). Each wafer was treated under the same conditions but wafers were not fabricated at the same time.

Figure 6.4.1(a) shows the measured internal quality factor, Q_i, of resonators containing 15 (black symbols) or 20 (red symbols) airbridges along the center conducting line [figure 6.4.1(b)], with the reference resonators also illustrated in figure 6.4.5 (measurement setup are described in 6.4.5). The quality factor of the resonators with airbridges along the centerline exceeds $> 2.3 \times 10^4$ at the power of a single photon level. In comparison with the reference co-planar resonators, which do not have airbridges, the quality factor of the resonators with airbridges is about one order of magnitude lower. However, the quality factor of the resonator with 20 airbridges is higher than that of the resonator with

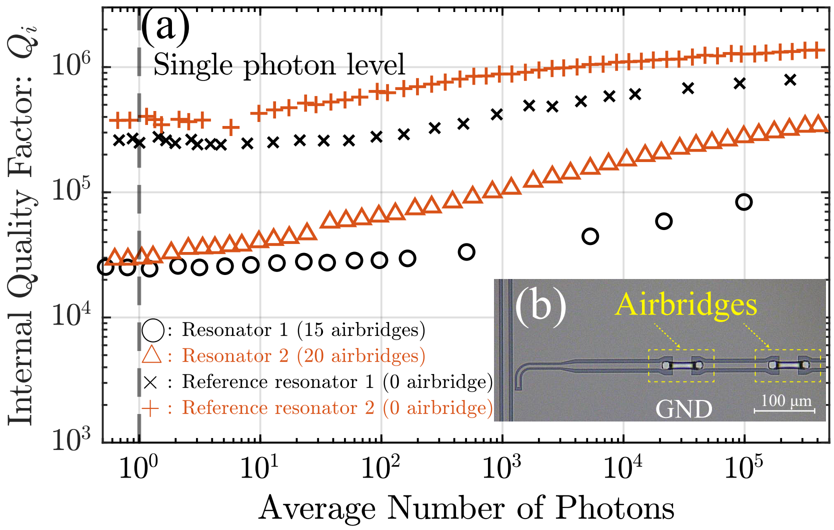

Figure 6.4.1: Measured internal quality factor versus average number of photons in resonators (a). Four datasets of measured coplanar resonator are shown in figure; resonator with 15 airbridges along the centerline (◯), resonator with 20 airbridges along the centerline (△), reference resonator with no airbridge for 15-airbriged resonator (×), and reference resonator with no airbridge for 20-airbriged resonator (+). We fabricated two chips; resonators ◯ and × were fabricated on one chip, △ and + were fabricated on the other chip. The dashed line corresponds to averaged single photon level. Q_i are fitted by standard methods [199]. In detail, a continuous ground plane is paved under the airbridge, which is forming a microstrip structure locally (b). Coupling quality factor Q_c and frequency of each resonator $\omega_r/2\pi$; $(Q_c, \omega_r/2\pi)$ = [◯ : $(3.141 \times 10^5$, 10.132 56 GHz), △ : $(5.273 \times 10^5$, 7.804 65 GHz), × : $(3.959 \times 10^5$, 9.431 47 GHz), + : $(5.162 \times 10^5$, 7.234 19 GHz)].

15 airbridges. These two resonators were fabricated in different wafers, so the result probably reflect imperfect reproducibility and parameter scattering in our fabrication process. Compare the airbridged resonators with the reference resonators fabricated on the same wafer, it shows a similar deviation trend in the quality factors.

6.4.2 Simulation of gate fidelity with lossy resonator

To appraise the effect of the extra loss resulting from the insertion of airbridges, we simulated the average gate infidelity of a CZ gate in our system, where two transmon-type qubits are coupled through a damped (lossy) resonator [161]. In the simulated system, each qubit has three energy levels and anharmonicity, η_i, the resonator has five energy levels with photon leakage rate $\kappa_i = \omega_r/Q_i$, and the coupling constant between each qubit and the resonator is g_i. In the system, we ignored the qubit–qubit direct coupling.

We adjusted the state of the system to the condition for the CZ gate, which is that the

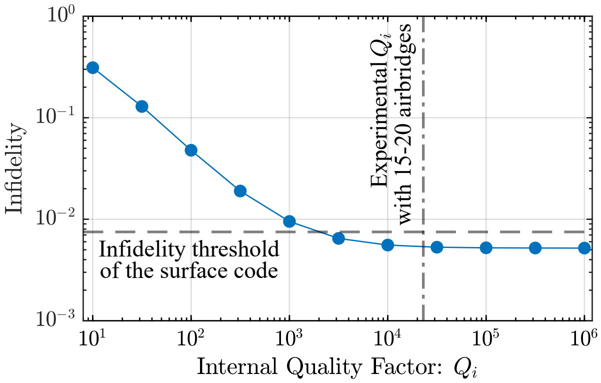

Figure 6.4.2: Simulated average gate infidelity of the CZ gate, via the resonator, versus the quality factor of the resonator. Frequency of the *i*th qubit between the ground and first excited levels: $\omega_i^{01}/2\pi = 5.6\,\mathrm{GHz}$ and $5.8\,\mathrm{GHz}$; anharmonicity of the *i*th qubit: $\eta_i/2\pi = -200\,\mathrm{MHz}$; resonator frequency: $\omega_r/2\pi = 6\,\mathrm{GHz}$; coupling constant between the *i*th qubit and resonator: $g_i/2\pi = 81.2\,\mathrm{MHz}$; effective coupling strength between qubits: $g_{eff}/2\pi = 3\,\mathrm{MHz}$; gate time; $117.9\,\mathrm{ns}$. The dashed line shows the threshold of the surface code. The dash-dotted line indicates the experimental Q_i with 15–20 airbridges.

energy difference from the ground level to the first excited level on one qubit is the same as the energy difference from the first excited level to the second excited level on the other qubit. Then, we calculated the time evolution of this system and finally obtained the average gate fidelity F (for more detail see the 6.4.6). To simplify the simulation, we ignore the pulse shape of the CZ gate operation. The leakage from the whole system to the external environment was also assumed to be entirely due to the resonator and not due to qubit decoherence, in order to leave no doubt that the error is caused by resonator loss. These assumptions were made to evaluate the dependence of the fidelity on the quality factor of the resonators.

Figure 6.4.2 shows the dependence of the infidelity on the quality factor of the resonator, Q_i, obtained by simulation. The result indicates that the value of Q_i required for the infidelity threshold of the surface code ($1 - F < 0.75\,\%$) is 2×10^3, and the infidelity is saturated at $Q_i > 10^4$.

The experimental internal quality factor of a resonator with airbridges at the centerline is one order of magnitude greater than what is required according to our simulation. In this experiment, ordinally airbridge technology were used. Therefore, this result strongly indicates that our proposed system, with realistic parameters, is feasible.

6.4.3 Crosstalk test

The crosstalk between two crossed resonator lines is also evaluated using another chip as shown in figure 6.4.3(a). A feed line crosses a resonator vertically using an airbridge

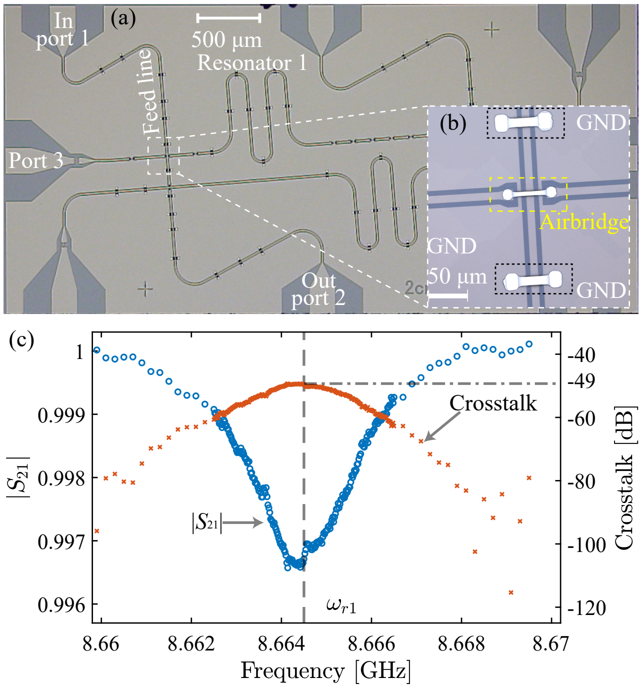

Figure 6.4.3: (a) Optical image of the chip for crosstalk measurements. The two parallel horizontal lines are half-wavelength resonators. The two parallel vertical lines are feed lines used to measure closstalk to the resonators at cross points via airbridges. (b) Detailed image of the cross point utilizing an airbridge. The center airbridge connects the left to right signal lines of the resonator over the vertical feed line. The top and bottom airbridges connect ground (GND) planes, which are separated. The width of the coplanar waveguide resonator is $10\,\mu\mathrm{m}$ and the gap to the ground is $6\,\mu\mathrm{m}$. The width of the airbsidges is $9\,\mu\mathrm{m}$, the length is $42.6\,\mu\mathrm{m}$, and the height is $3\,\mu\mathrm{m}$. (c) Datasets of $|S_{21}|$ (shown on left axis by blue circles) and crosstalk (shown on right axis by red crosses). The center vertical dashed line indicates the resonant frequency of the resonator 1, $\omega_{r1} 2\pi = 8.6645\,\mathrm{GHz}$, evaluated at port 3. The horizontal dash-dotted line indicates the maximum value of the crosstalk.

[figure 5(b)].

The frequency of the resonator ω_{r1} was measured by port 3. We subsequently measured the crosstalk between the feed line and the resonator around the resonant frequency ω_{r1}. The crosstalk is due to the airbridge structure that connects the center signal line of the resonator across the feed line. A continuous microwave signal reference was applied through the feed line from input port 1 to output port 2 in figure 6.4.3(a). Then, the signal was absorbed at the resonant frequency ω_{r1} of the airbridge resonator, which resulted in a small dip. In figure 6.4.3(c), the normalized measured data $|S_{21}|$ with the dip is shown (blue circles), and the crosstalk defined by $20\log_{10}(1-|S_{21}|)\,\mathrm{dB}$ is also shown (red crosses). The result shows that the crosstalk due to the crossing airbridge was at most $-49\,\mathrm{dB}$ when the frequencies are resonant.

Therefore, to realize the pseudo-2D interconnection network with airbridges, we should

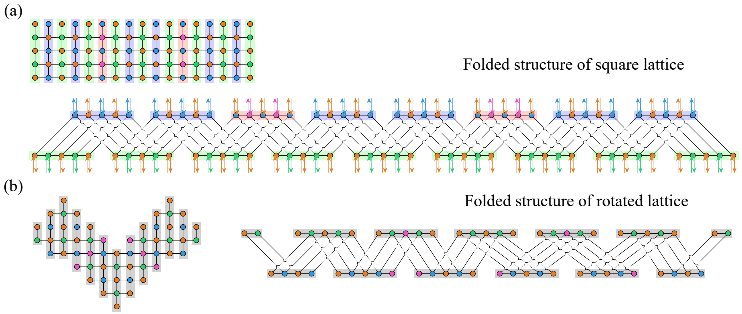

Figure 6.4.4: (a) LNN arrangement of three logical qubits of the square patch for the surface code with the distance 3. (b) LNN arrangement of three logical qubits of the rotated patch for the surface code with the distance 3.

detune all frequencies of crossed resonators sufficiently. This will suppress the effective crosstalk to an small value, even smaller than the characteristic background damping in a typical microwave measurement system.

6.4.4 Using the rotated lattice for logical qubit encoding

In the main text, we described the architectural layout using encoded qubits formed from a square lattice of $(2d-1)^2$ physical qubits. This number can be reduced by utilizing the rotated lattice encoding introduced in Ref. [114]. A rotated lattice will reduce the number of physical qubits in a logical block from $(2d-1)^2$ to $2d^2-1$, which can result in significant resource savings for large values of d.

Regarding the hardware architecture itself, there are no changes required for the underlying hardware. In figure 6.4.4 we illustrate how two encoded qubits in the rotated lattice are translated to the bi-linear design. Unlike the case when the encoded qubits are square patches, the airbridge connections become non-uniform. However, the maximum number of airbridges within a single resonator does not change between the cases of square encoding and rotated encoding, the square lattice encoding represents the upper bound for the rotated lattice. Consequently, the design in the main text is completely compatible with that using rotated lattice encoding.

6.4.5 Extra information on the experiment

We utilized a vector network analyzer (VNA) to measure the internal quality factor and crosstalk. To evaluate the internal quality factor of resonators, we prepare the chip with 15 airbridges shown in figure 6.4.5. The spectrum of the resonators was measured using the input and output ports of the feed line coupled to each resonator.

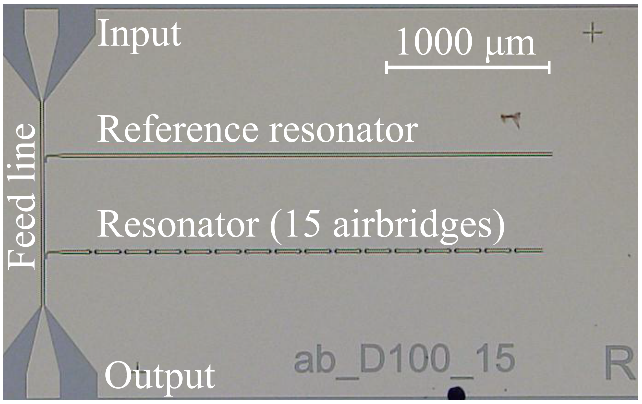

Figure 6.4.5: Measured chip for the resonator with 15 airbridges (top) and the reference resonator (bottom), which are capacitively coupled to the feed line. The resonators are made of Nb film on a non-doped Si wafer.

6.4.6 Information on the simulation

We modeled a part of our system as two qubits coupled via a damped resonator without leakage from qubits, so the Hamiltonian is

$$\mathcal{H}/\hbar = \omega_r a^\dagger a + \sum_{i=1,2}\left[\omega_i^{01} b_i^\dagger b_i + \frac{\eta_i}{2} b_i^\dagger b_i (b_i^\dagger b_i - 1) + g_i (a^\dagger b_i + a b_i^\dagger)\right], \tag{6.4.1}$$

and this indirect interaction of qubits (last term) is used for the CZ gate. The quantum map $\mathcal{E}$ can be derived solving by the Lindblad master equation, and then we calculate the average gate (in)fidelity in the computational subspace $|\psi_{\rm s}\rangle$ between the map $\mathcal{E}$ and an ideal CZ gate map $\mathcal{E}_{\rm CZ}$, which is defined as [236, 28]

$$\overline{F}(\mathcal{E}, \mathcal{E}_{\rm CZ}) = \int d\psi_{\rm s} \left\langle \psi_{\rm s} | \mathcal{E}_{\rm CZ}^{-1} \circ \mathcal{E}(\psi_{\rm s}) | \psi_{\rm s} \middle| \psi_{\rm s} | \mathcal{E}_{\rm CZ}^{-1} \circ \mathcal{E}(\psi_{\rm s}) | \psi_{\rm s} \right\rangle, \tag{6.4.2}$$

averaged over the Haar measure $d\psi_{\rm s}$. This simulation is performed using Quantum Toolbox in Python (QuTiP) [125].

6.4.7 Qubit chip fabrication feasibility

The new architecture might suggest that, as the number of the qubit scales up, the chip would become longer and longer. One may wonder if it is actually possible to fabricate such a chip. We consider the issue for a realistic logical qubit chips, in terms of its design and its fabrication feasibility. To circumvent the increasing chip length as it scales, we consider a case where inter-qubit coupling within qubit array in each column are achieved by a direct coupling manner, instead of coupled via resonators as in figure. 6.2.1(c). Such coupling scheme was shown to be very effective and able to achieve a highly accurate gate operations [132].

We considered an implementation of a 30 × 30 physical qubit array, for it is a sound logical qubit for a surface-code based quantum computer. Using realistic physical parameters, such logical qubit can be prepared on a $30\,\mathrm{mm} \times 200\,\mathrm{mm}$ chip, including readout resonators, as shown in figure 6.4.6, where qubits are arranged within the inline 1D array, with a pitch of $0.4\,\mathrm{mm}$. The resulted chip size, especially its length, would easily fit within the size of the largest chip of the day, the wafer scale processor chip having an area of approximately $46\,000\,\mathrm{mm}^2$ [222]. The input/output wirings of the chips can all be arranged in the ordinary 2D manner. Moreover, the above estimation was based on a preliminary design concept without any sort of area optimization, and the chip size could be further reduced in the future. Therefore, fabrication of such logical qubit chip should be possible with the current technology, in principal. Then, many of these logical qubit chips could be assembled and packaged further as a quantum computer. The inter logical qubit chip connections can be achieved using "quantum bus" architecture [112] for example. In this case, connection between two logical qubit chips could be established only with limited numbers of classical connection lines. It seems there is no immediately foreseeable fundamental physical limit preventing the chip fabrication and its packaging, at least now.

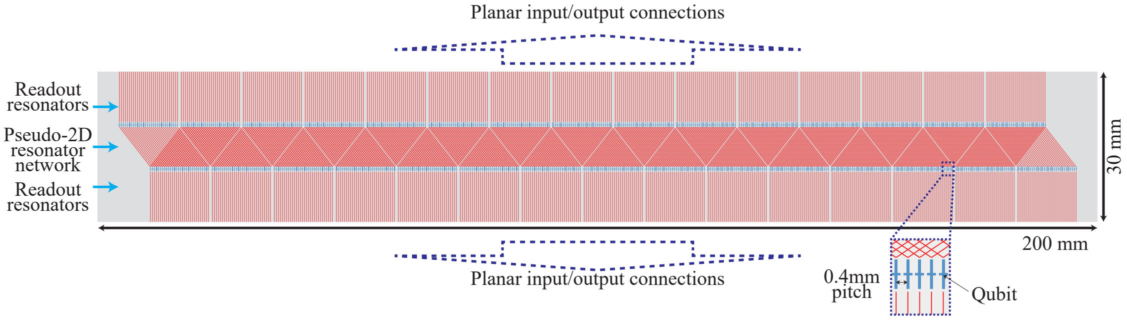

Figure 6.4.6: A design of single-logical-qubit chip consists of 30 × 30 physical qubits, arranged according to the proposed pseudo-2D coupling network architecture. Qubits are depicted as blue crosses (inset) and resonators are as red lines. All the external input and output connections can be achieved by the conventional planer wiring technology. The resulted chip size is approximately $30\,\mathrm{mm} \times 200\,\mathrm{mm}$ rectangular.

6.5 Conclusion

To conclude, we proposed a novel scalable architecture of superconducting quantum circuits for the surface codes, where standard planar 2D wiring can be adopted for the external wiring, with the help of an airbridge-incorporated inter-qubit pseudo-2D resonator network. We also carried out an experimental feasibility study of the pseudo-2D resonator network and showed that there are no fundamental difficulties in realizing it. Our results indicate that it may be possible to build a fault-tolerant, large-scale quantum computer using simple monolithic integration technologies. We are planning to construct a small-scale circuit to further examine and explore this possibility.

Chapter 7

Micro-architecture of Three Dimensional Cluster State

7.1 Surface Codes and the Raussendorf lattice

The surface code and the Raussendorf lattice are arguably the preferred method of error-correction for a large-scale, general purpose quantum computer is a variety of physical systems. Essentially all hardware systems under development today for scalable quantum computing prefer this coding technique over the plethora of other options for universal, error-corrected computation. While other coding techniques do have better theoretical properties, the surface code is generally chosen for three important reasons that make it amenable to architectural implementation.

- It has one of the highest fault-tolerant threshold of any error-correcting code, approaching $1\,\%$ depending on the underlying noise assumptions.
- It is defined over a 2-dimensional array of qubits with only nearest neighbor interactions required.
- It is a software driven model of computation, meaning that provided enough physical resources are available (i.e. the number of qubits), no further hardware redesign or reconfiguration is needed when changing the algorithm that is to be run.

Due to its adoption in many hardware designs, the surface code and Raussendorf model have been studied extensively. Not only is there significant research into the properties and behavior of the code (in regards to the value of the fault-tolerant threshold, logical error rate scaling as code distance is increased and resource benchmarking for large-scale algorithms) but a large amount of the classical support software has been developed. This includes classical error-correction decoders, compilers for both braid based logic and lattice surgery logic and mode resource friendly protocols for a universal set of fault-tolerant gates. Given the difficulty in architecturally building a system with the flexibility to implement more exotic error correction techniques, especially in superconducting hardware, it is widely anticipated that surface codes will remain the method of choice for large-scale quantum computers.

There are many excellent reviews of both the surface code and the Raussendorf model, how error correction is performed and how algorithms are compiled and run on a machine utilizing these techniques. We will only briefly review the basics, which are directly relevant to the systems layout for an actual architecture.

The surface code requires a 2-dimensional array of qubits with nearest neighbor coupling, as shown in Figure 7.1.1(a). This array of qubits is subdivided into two sets of parity check operators, known as plaquette and vertex stabilizers. For each plaquette, the circuit shown in Figure 7.1.1(b) is repeatedly run over the entire lattice to project each group of four qubits in each plaquette into an eigenstate of the associated $ZZZZ$ operator, with the ± 1 eigenvalue used as a syndrome, indicating the presence of X errors on an odd number of the four qubits in the plaquette. After projecting each plaquette into eigenstates of the associated $ZZZZ$ stabilizer, the circuit in Figure 7.1.1(c) is run over all the groups of four qubits associated with a vertex in Fig 7.1.1(a). These circuit are used to project the four associated qubits into an eigenstate of the $XXXX$ operator, with the

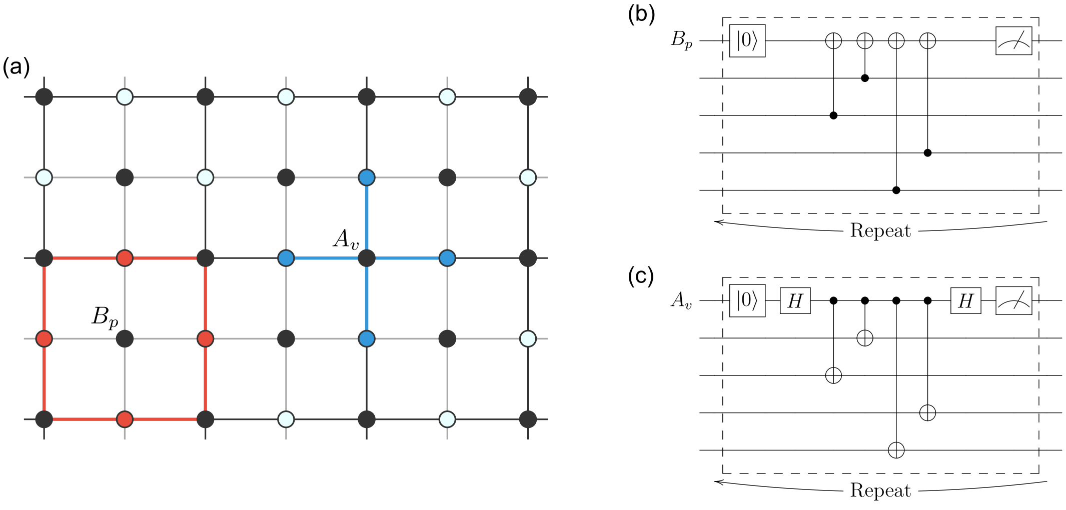

Figure 7.1.1: (a) Basic layout of the surface code. The qubits indicated by the circles are 2-dimensionally arranged, and coupled to nearest neighbors. The filled circles on the plaquettes of the black lattice B_p are syndrome qubits for $ZZZZ$ stabilizer, and these on the vertexes A_v are syndrome qubits for $XXXX$ stabilizer. (b) Quantum circuit for $ZZZZ$ stabilizer. (c) Quantum circuit for $XXXX$ stabilizer.

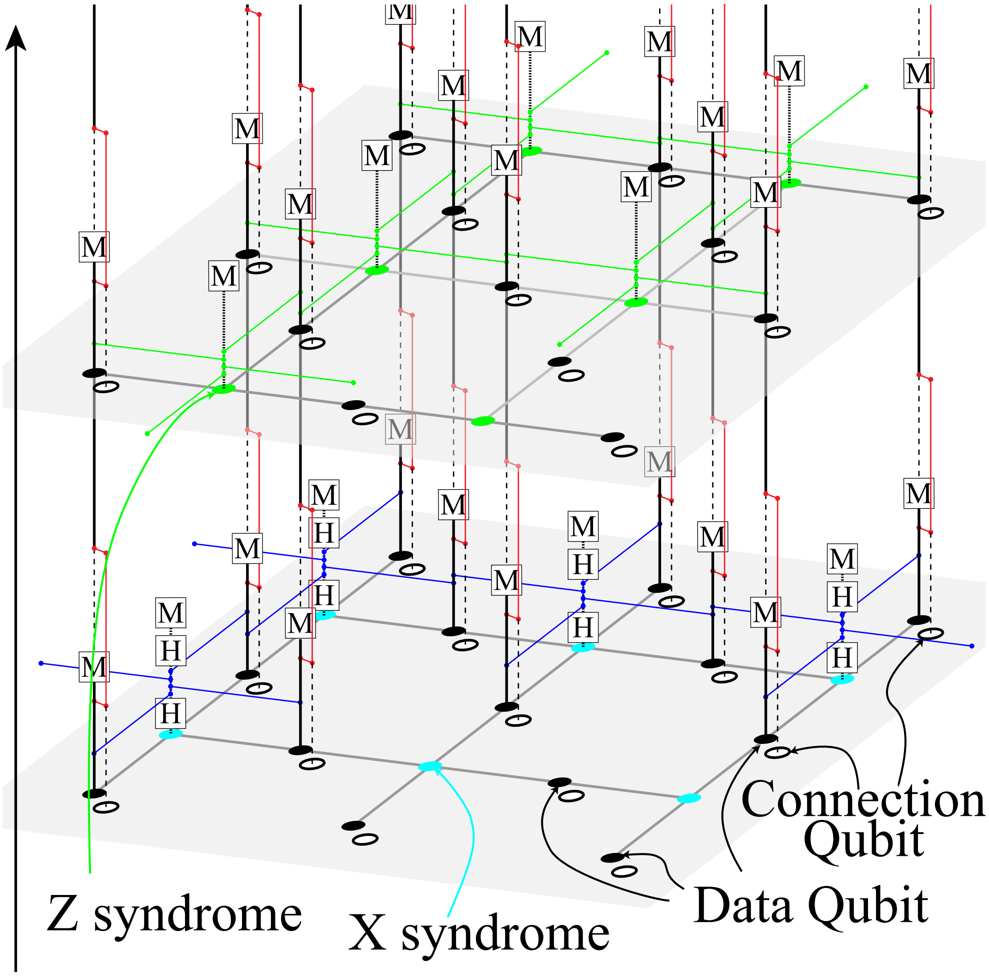

Figure 7.1.2: Quantum error correction on cluster state

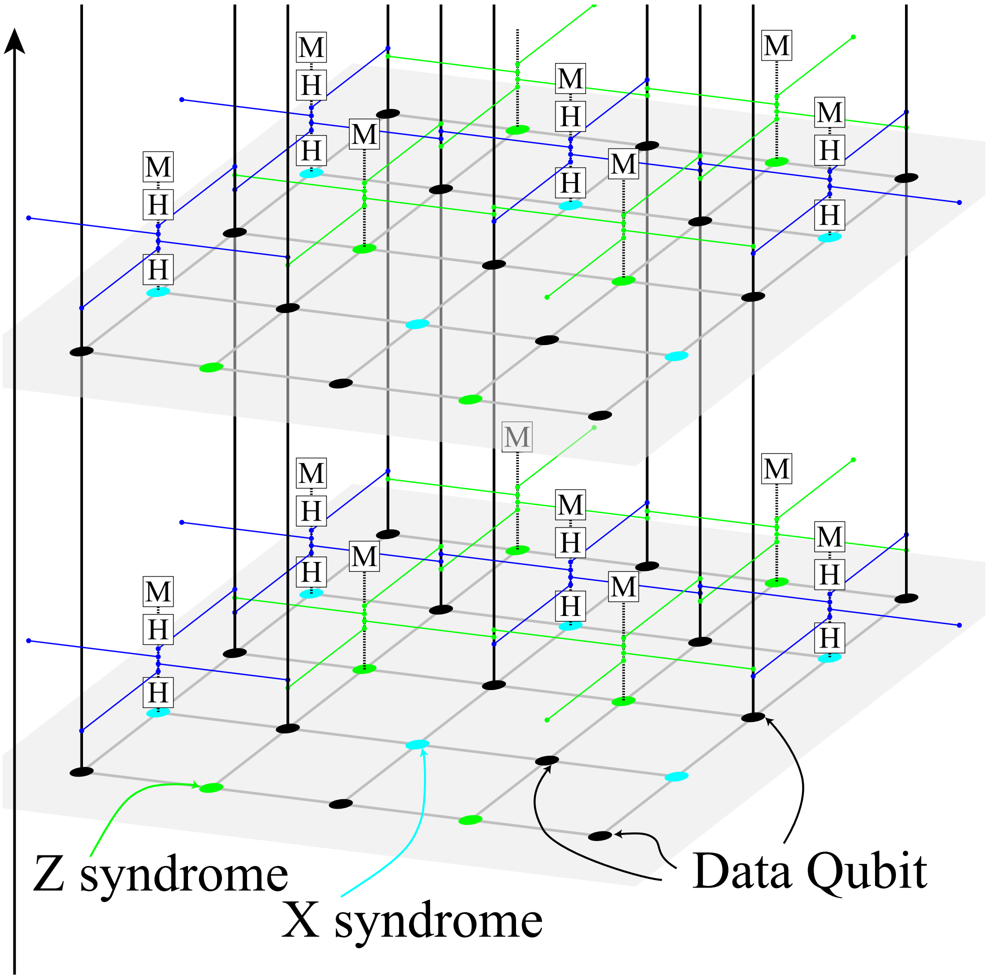

Figure 7.1.3: Quantum error correction on surface code

eigenvalue providing syndrome information regarding Z errors.

For a large surface code, these two circuits are run repeatedly and in the absence of any encoded information, syndrome information is extracted at each step and classically decoded to determine the most likely set of physical errors that have occurred. Provided that the physical error rate associated with each qubit and each gate in Figs 7.1.1(b) and (c) is below approximately $1\,\%$, the surface code will effectively provide protection to any encoded information introduced into the computer.

Computation on the surface code is a more complex discussion but it ultimately does not require any additional hardware considerations and can be omitted in this summary. Provided each physical qubit can be selectively measured and initialized in the architecture, all the hardware elements needed for a large-scale computer is encapsulated by being able to repeatedly run the circuits in Figs 7.1.1(b) and (c) across the whole computer and to achieve physical error rates at approximately one order of magnitude below the fault-tolerant threshold of the surface code. [200, 201, 202, 111, 204, 107, 154, 180, 203, 33]

The Raussendorf lattice is a cluster state extension of the surface code. As a code, it is no different from the surface code and was the first example of a more general technique, now known as foliation, which can convert and CSS quantum code into a cluster state equivalent. [64, 155, 185, 108, 35, 149, 129, 181, 87, 240, 116]

7.2 Traditional Superconducting architectures

Limiting ourselves to discussing to superconducting quantum computing architectures that have received heavy investment and are targeting error-corrected, large-scale digital computation, they all follow essentially the same design specifications. The three main contenders are currently the efforts at Google, IBM and Rigetti Computing who each are designing successively larger superconducting qubit arrays that will need to satisfy the 2-dimensional geometric constraints needed by the surface code.

While the devices currently reported from these laboratories are not yet a 2-dimensional nearest neighbor geometry, they are moving in the same direction. Figure 7.1.1 illustrates the layouts of the most advanced chips from each group reported to date. The Google chip Sychamore is a 54 qubit 2-dimensional array of Xmon qubits, the IBM 50Q is a 50 qubit 2-dimensinal array of transmon qubits coupled to microwave resonators while the Rigetti chip is a specific geometry of 19 transmon qubits. IBM has recently announced more advanced 20 and 50 qubit designs, but have only so far released diagrams related to their connection geometry (rather than pictures of the device itself)

Current targets for many of these experimental groups is the regime that has become known as “quantum supremacy”. Quantum supremacy refers to reaching a scale for quantum machines where certain sampling algorithms that could, in principle, be run on these devices would be classically intractable for the most powerful supercomputers. While there is a rich research history into these protocols, papers from Boxio *et al.* suggests that a quantum circuit operating over a 2-dimensional lattice of 7×7 qubits with a depth of approximately 40 would be classically intractable (or at best, extremely expensive) to simulate. An added goal of successfully demonstrating this protocol is that the algorithm is extremely sensitive to errors, even a single Pauli error can cause this algorithm to fail. Consequently physical error rates would need to be less that the inverse of the *circuit area* of the protocol, where circuit area is defined at the number of qubits (Q), times the circuit depth (K). In the results of Boxio *et al.*, $Q = 49$ and $K \approx 40$, implying that physical error rates need to be approximately $p < 1/2000 = 0.05\,\%$. An physical error rate this small would satisfy the fault-tolerant threshold condition of the surface code.

The ability to scale to larger 2-dimensional arrays of qubits, for either quantum supremacy protocols or for larger, more commercially practical quantum computers poses some difficult engineering challenges. One of the most prescient is the "wiring problem". As illustrated in figure 7.1.1, the control lines for qubit biasing, control and readout are fabricate in a planar manner. For the geometries illustrated, this is not a major concern. Each qubit in the system has planar access across the superconducting chip such that control, bias and readout lines can be fabricated along with the actual qubits. However, as you go to larger arrays, this planar access for control lines is no longer possible.

This is a well known problem within the superconducting quantum community and the current consensus is to develop techniques to bring in control lines vertically onto the chip. This type of 3-dimensional fabrication for control lines for each qubit has already seen success, but there has not yet been any reported experiments illustrating this type of qubit control in conjunction with the qubit protocols that have been demonstrated for designs with planar control lines. Maintaining high fidelities as qubits arrays are scaled is crucial to building large-scale superconducting qubits and it remains to be seen if this type of 3D control techniques will allow for qubit scaling into the 100's, 1000's or even higher while maintaining high fidelity operations for error-corrected computation.

This work proposes an alternative design that maintains the beneficial aspects of a surface code, error-corrected, superconducting architecture while eliminating the need for fabricating control lines into the middle of a large 2D array of qubits. Instead, our design uses a cluster based approach, utilizing the Raussendorf lattice on a bi-linear array of qubits. Planar control lines can be fabricated to control each qubit in our system and a large-scale machine would consists of a very long (and thin) array of qubits, implementing the same error-correction protocols as more traditional superconducting designs. Our approach offers a possible alternative architectural approach for large-scale superconducting machines if the wiring and control problem becomes insurmountable as superconducting quantum computers scale up.

7.3 Proposal to implement 3D cluster state generation on 2D circuit

The final purpose of this proposal is that using two physical dimensions and one time dimension, three dimensional "Cluster state" generation and its measurement are realized on completely planar superconducting circuit including external wiring for physical qubits. The three dimensional cluster state on measurement based quantum computation (MBQC), known as Raussendorf lattice, has ability to run fault-tolerant quantum computation.

To create and measure the one-dimensional cluster state, we refer to [181], shown a quantum circuit in equation 7.3.1 as a starting point for this proposal. A qubit stores the information as $|\psi\rangle$ and other qubits are prepared as ground state $|0\rangle$. A key point of our circuit is recursively utilizing the qubit for $|0\rangle$.

Start from following two quantum circuits which are equivalent when target qubit state is $|0\rangle$.

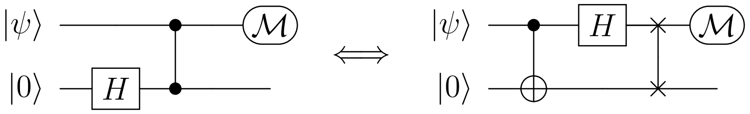

(7.3.1)

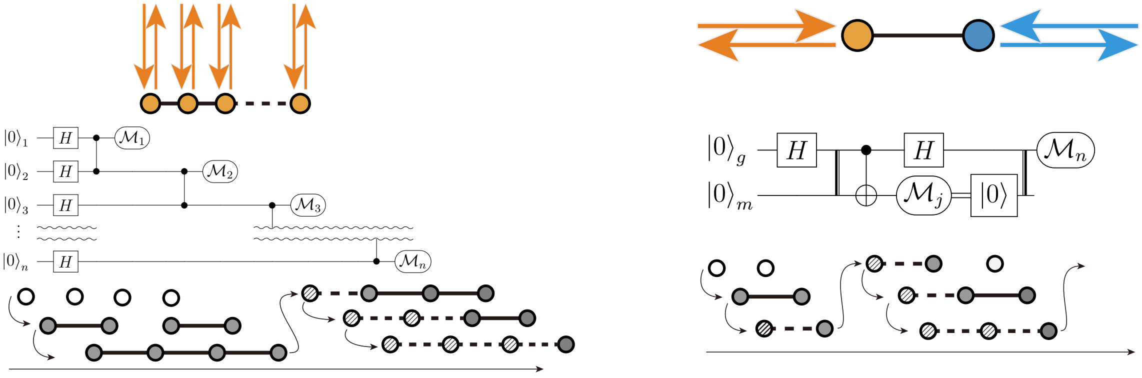

Figure 7.3.1: Superconducting circuit schematics.

because this equivalent are proof by following equations.

$$\begin{aligned} U_{\mathrm{CZ}}(I \otimes H)\left|\psi\right\rangle\left|0\right\rangle =& (\alpha\left|0\right\rangle\left|+\right\rangle + \beta\left|1\right\rangle\left|-\right\rangle) \\ =& U_{\mathrm{SWAP}}(\alpha\left|+\right\rangle\left|0\right\rangle + \beta\left|-\right\rangle\left|1\right\rangle) \\ =& U_{\mathrm{SWAP}}(H \otimes I)(\alpha\left|0\right\rangle\left|0\right\rangle + \beta\left|1\right\rangle\left|1\right\rangle) \\ =& U_{\mathrm{SWAP}}(H \otimes I)U_{\mathrm{CNOT}}\left|\psi\right\rangle\left|0\right\rangle \end{aligned} \tag{7.3.2}$$

where $\left|\psi\right\rangle = \alpha\left|0\right\rangle + \beta\left|1\right\rangle$, $\{\alpha, \beta\} \in \mathbb{C}$, $\left|\pm\right\rangle = (\left|0\right\rangle \pm \left|1\right\rangle)/\sqrt{2}$, U_k are unitary gate operators for $k \in \{\mathrm{SWAP}, \mathrm{CNOT}, \mathrm{CZ}\}$, I and H are Identity and Hadamard gates, respectively. Then quantum circuit of left of Eq. (7.3.1) is clearly equivalent to following quantum circuit by swapping operation of measurement.

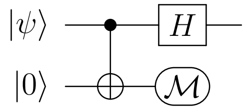

(7.3.3)

Utilizing equation (7.3.1), transformation are realized from original 1D cluster state generating quantum circuit 7.3.1(left) into recursive quantum circuit with two initial state (quantum circuit 7.3.1(right)), which require to prepare initial state for sufficient number that we want to create cluster. In quantum circuit, this transformation is shown as

where $\boxed{\left|0\right\rangle}$ is operation to initialize qubit into $\left|0\right\rangle$ state. In other words, this 1D cluster is generated in time by two physical qubits operation including Hadamard, CNOT, measurement, and reset gates. Final outcome $\mathcal{M}_n$ from equation 7.3.1 accumulate effects by prior operations, which allow us to run one-way operation by measurements. To implement this original quantum circuit, one-dimensional physical n-qubit-array are required (shown in figure 7.3.1). The number of qubit in the array is the same number of which you want to generate 1D-cluster. On the other hand, our transformation (shown in figure 7.3.1) be able to reduce physical resources to construct one-dimensional cluster state. The required resources are two physical qubits. Additionally introduced repeat operation are possible to realized utilizing initialization, which are required almost all quantum algorithms.

To create two dimensional cluster state, time-dependent 1D cluster are extended in physical space. Therefore, original machine-gun architecture in two dimensional physical space are converted into one dimensional physical space by one dimensional time. By using the quantum circuit equation (**??**), this transformation is described as following equation from 7.3.2 into 7.3.3.

Conducting the quantum circuit 7.3.2 requires two-dimensional square lattice of physical qubits. The other quantum ciruite 7.3.2 are implemented into bi-linear qubit-array

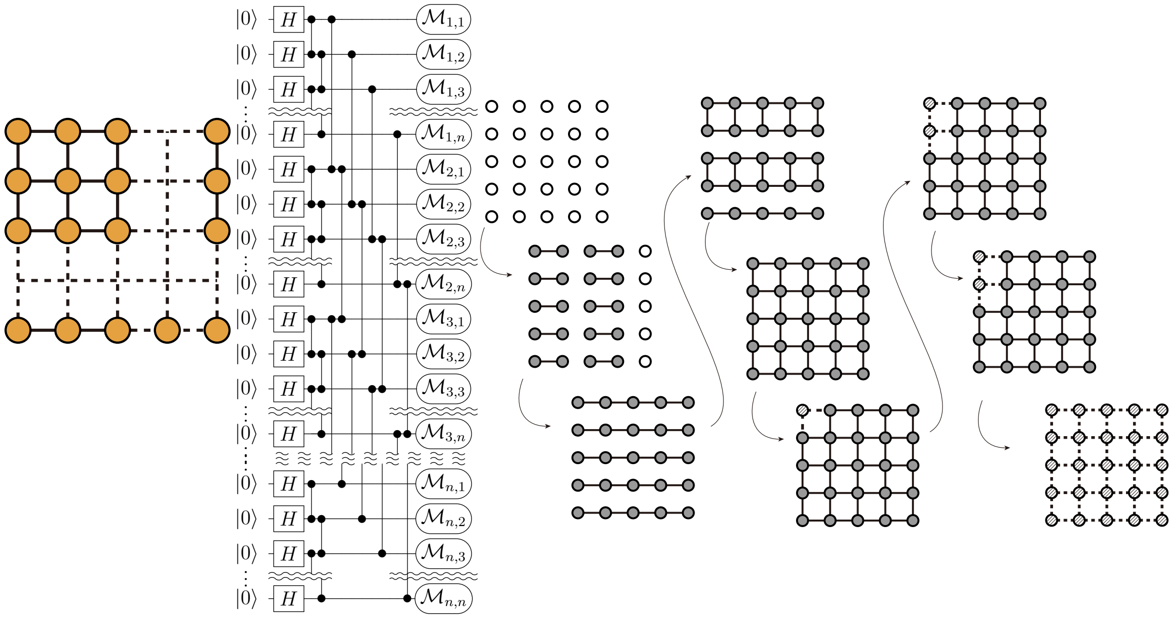

Figure 7.3.2: 2 dimensional cluster state generation on 2D array of qubits

(shown in figure 7.3.2). The transformation of generating two dimensional cluster state allow to use less resource of physical qubit array than original scheme. For instance, to generate 10 by 10 cluster state, 10 by 10 array of qubit are required in original scheme. On the other hand, in our transformation, 2 by 10 qubits array are sufficient for physical resources.

However, quantum circuit 7.3.3 are can not scale to three dimensional cluster state with planer wiring on practical chip. The reason why not scale is because generating three dimensional cluster state make a demand on connecting each qubit in one block to a qubit placed equivalent position in next block. This interconnection constrain cause difficulty to scale up this circuit given planer wiring.

To solve this scaling problem of wiring, another transformation are introduced for interconnection of a block, which are shown in quantum circuit 7.3.4. The transformation replace a line of measured qubits with just one qubit, whose physical qubits arrangement is shown in figure 7.3.4. This physical circuit are implemented on planar circuit together with planar external wiring (in figure represented as arrows). The transformation requires measured qubit have multi-qubits coupling independently.

To generate three dimensional cluster state by using planer wiring superconducting quantum circuit, multi-block of the 2D-cluster state generator circuit introduced above are utilized (show in figure 7.3.5). Connection between blocks are build between measurement qubits of next blocks. The circuit to generate 3D-cluster finally composes one dimensional measurement qubits array (blue) and generator qubit bunches for each mea-

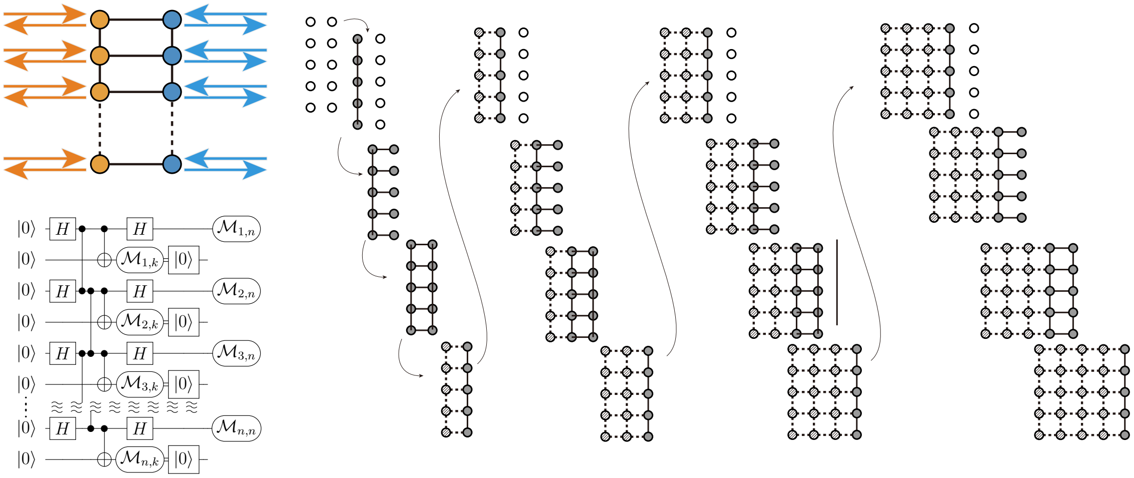

Figure 7.3.3: 2 dimensional cluster state generation on bilinear of qubits

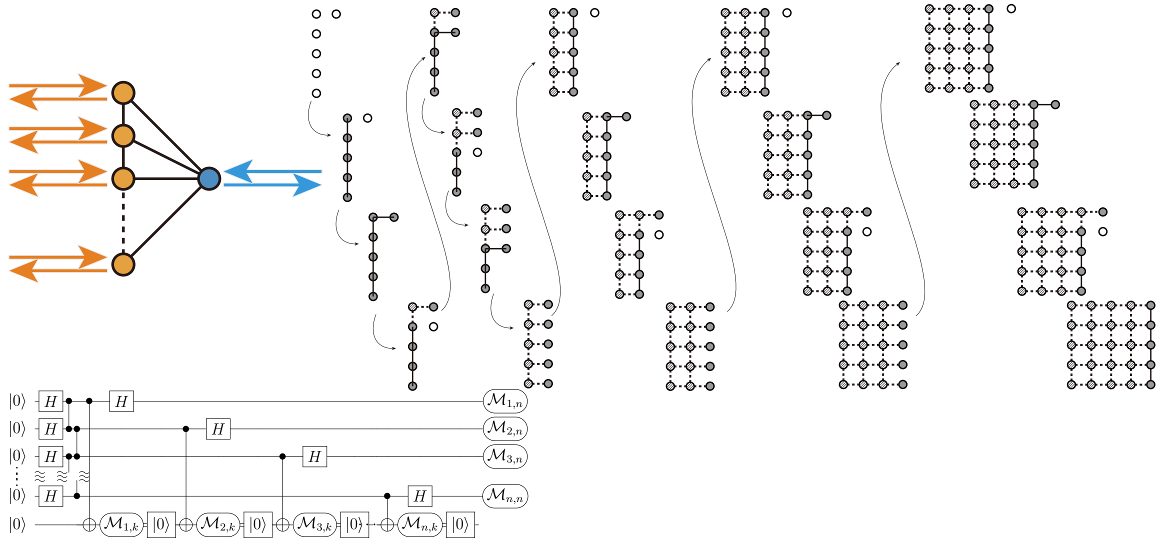

Figure 7.3.4: 2 dimensional cluster state generation on an array of qubits with multi-qubit coupling

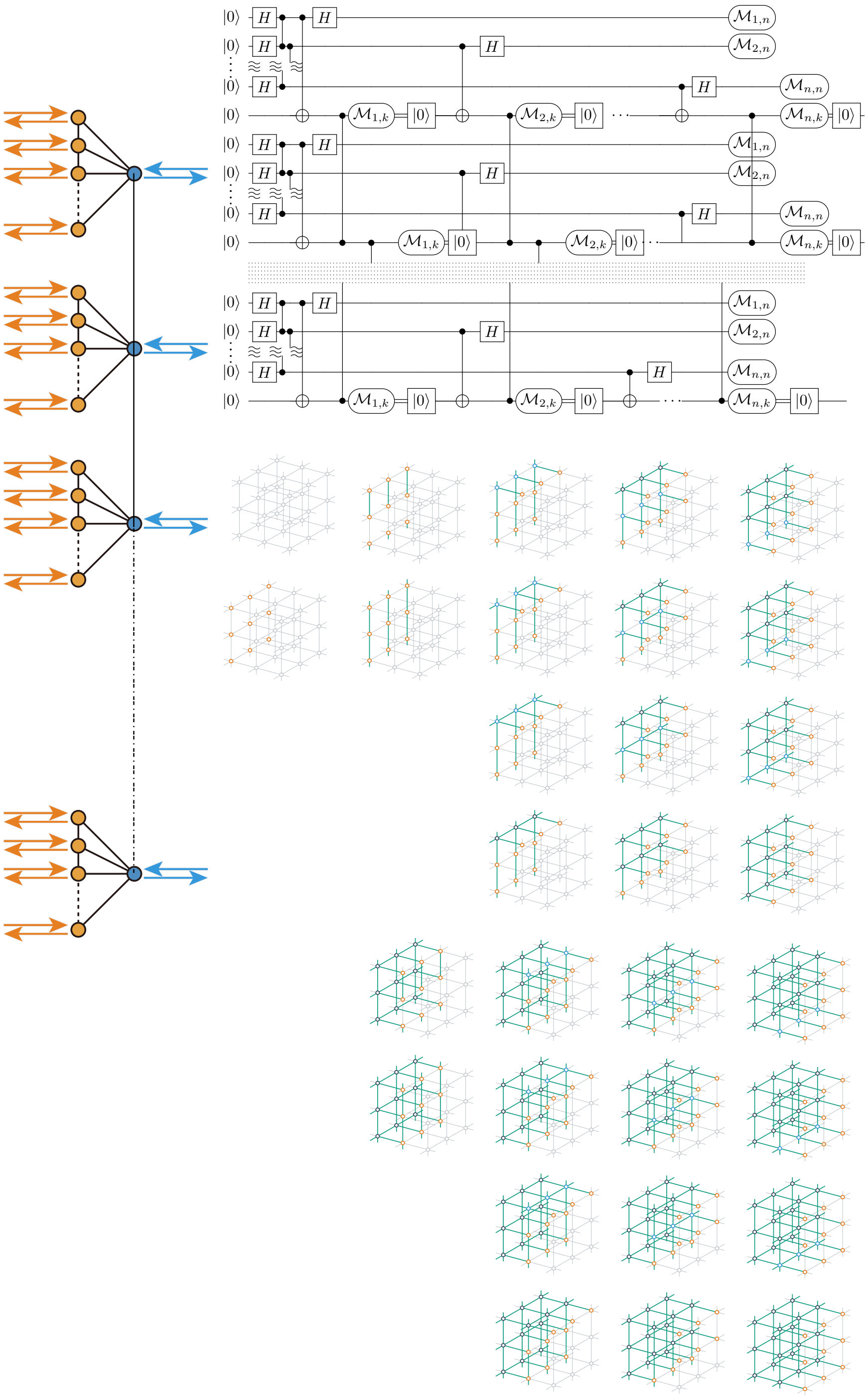

Figure 7.3.5: 3 dimensional cluster state generation on bilinear array of qubits

surement qubit. The bunch generate one-dimensional cluster state by using 1D-qubit array in time, which shapes a line cluster. Using connections between bunches connects 1D-cluster states generated by bunches one by one, which shapes a planner lattice cluster state. This sequence are repeated in time with using measurement, 3D-cluster state are constructed. The circuit have one advantage that arbitrary length in time dimension are used even if cluster state as resource for computation since it allow us to keep to generate arbitrary long cuboid cluster state while prepared cluster state is limited original physical resource.

Chapter 8

Micro-architecture of Quantum Annealing

Superconducting Quantum Annealing Architecture with LC Resonators

by Hiroto Mukai, Akiyoshi Tomonaga, and Jaw-Shen Tsai
published in Journal of the Physical Society of Japan [174].

8.1 Introduction

With the present information explosion in our society, it is indispensable to realize efficient quantum information-processing systems for the coming generation. Such quantum systems are being researched and developed. Among them, superconducting quantum circuits are making remarkable progress. Quantum annealing is a class of quantum information processing specialized for solving optimization problems [131, 69, 68]. In general, a wide range of real-world problems can be classified as optimization problems, which cover the fields of fundamental science, the improvement of productivity, and the development of infrastructure. However, it is practically impossible to solve these optimization problems with von Neumann computers when the size of the problems exceeds certain limits [85].

For quantum annealing, a problem to be solved is encoded as strengths of interactions in a “spin glass” that consists of many spins and interactions between spins [160]. By suitably encoding the time evolution of the spin glass, nature itself will find the minimum energy of the whole system, giving us the solution to the optimization problem. To build a quantum annealer, we need to consider what is required for such a physical system. When the number of the interactions for each qubit increases, the encoding of optimization problems becomes more efficient. Therefore, it is possible to reduce the overhead of the number of physical spins [27, 38]. Thus, a larger problem can be solved efficiently. In general, it is indispensable to increase the number of spins as well as couplings between these spins to efficiently solve large-scale problems by quantum annealing.

In this paper, we propose a novel architecture for scalable quantum annealing circuits with full coupling, in which a spin is coupled to all other spins. The existing superconductive quantum annealing systems [104, 37] utilize flux qubits as spins, which are coupled with each other by an rf-superconducting quantum interference device (SQUID)-based coupler [106]. On the other hand, in our proposed architecture, the coupling structure between qubits is mediated by superconducting resonators. Here, the pair of the qubit and resonator functions as a very long quantum system (spin), enabling it to be coupled to a large number of other spins. A strongly coupled qubit-resonator pair enables us to make a large quantum system compared with the size of a qubit. Additionally, to increase the coupling energy between spins, deep-strong coupling [246**?**] between the qubit and the resonator is introduced. It is also possible to introduce a dispersive readout [229, 123].

8.2 Proposed Architecture

We propose a novel architecture for superconducting circuits to realize a quantum annealing system that consists of flux qubits and lumped element (LC) resonators (Fig. 8.2.1).

Each flux qubit has longitudinal (Z) and transverse (X) degrees of freedom [186, 230]. Their Z and X energies are controlled by applied external magnetic fluxes to the main loop and α-loop [shown in Fig. 8.2.1(b)], respectively. It is common to use flux qubits for quantum annealing because the quadratic structure of the energy band of the flux qubit allows a transverse magnetic field and longitudinal magnetic field to easily and continuously increase or decrease [104]. For this reason, we also employ flux qubits for our proposed architecture.

In general, a lumped element resonator has a uniform current distribution on its inductive parts, in contrast to a distributed resonator such as those of the coplanar type, with the standing wave dependent on the resonant frequency. In our architecture, we utilize an LC resonator with a long inductive limb, which plays an important role in our architecture [see Fig. 8.2.1(a)]. The long inductive limbs make it possible to couple many spins. Accordingly, an LC resonant mode with a uniform current is realized, while other non-LC resonant modes inevitably exist. However, by optimizing the parameters of the circuit, the energy of the LC resonant mode can be realized in the vicinity of the qubit energy, while making the other modes far away from the energy. Thus, the coupling of

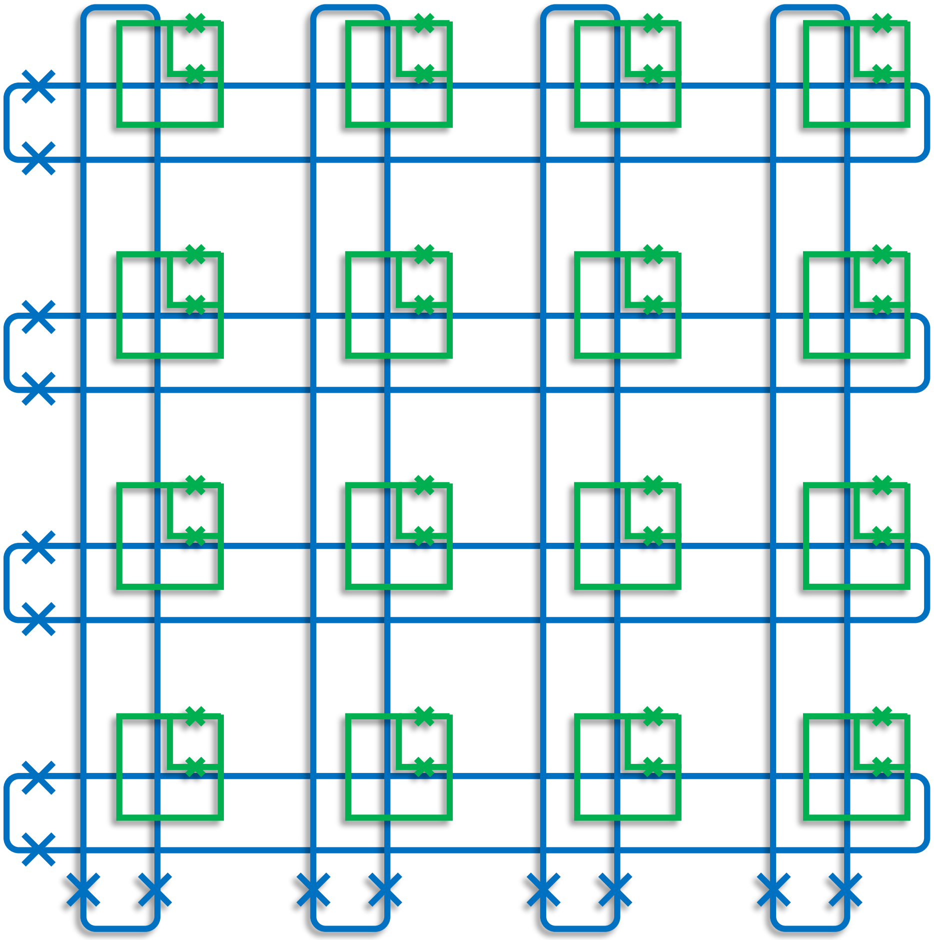

Figure 8.1.1: Commercially used annealing circuit on superconductor. Rectangular loop are qubit (blue). Square loop are couplers (green)

the other resonant modes to the qubit can be ignored.

In the architecture, N flux qubits are arranged on a line and each qubit is connected to a different LC resonator via a mutual inductance. The N LC resonators are braided so that they fully interact with each other by the long inductive limb through the rf-SQUID-based couplers as shown in Fig. 8.2.1(a). Thus, the N flux qubits effectively and fully interact with all other qubits via the network of LC resonators and couplers.

In contrast with the existing scheme, in which each qubit interacts with some qubits through an rf-SQUID-based coupler, the proposed system has the following advantages. The qubits fully interact with each other. The number of interactions between the qubits is $N(N-1)/2$ when there are N qubits in the proposed circuit. On the other hand, the existing scheme has a unit cell with $2N$ interactions [105]

In the mapping optimization problems to interactions of a system, the larger the number of spins and interactions between spins, the more efficiently the problems are mapped.

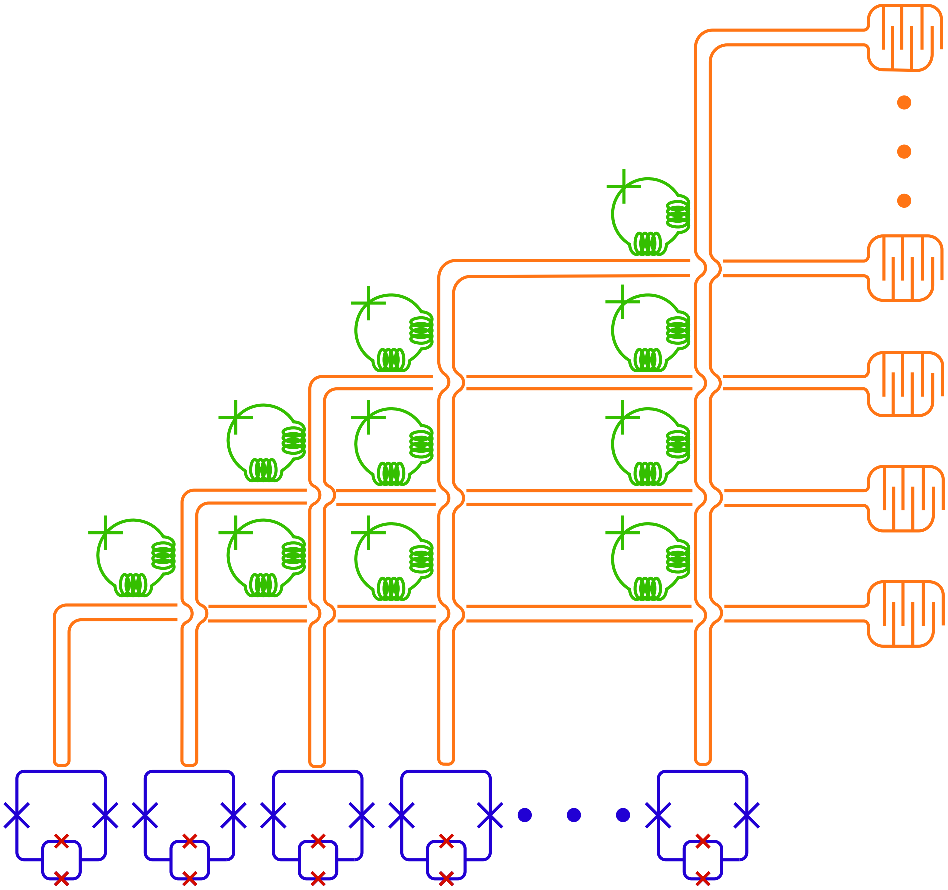

Figure 8.2.1: (Color online) Schematic representation of full-coupling quantum annealing circuit. The orange part is the LC resonator, which has a long inductive limb. All qubits (blue part) form a pair with the resonator, and each pair couples with all other pairs via an rf-SQUID-based coupler (green part). × (crosses) represent Josephson junctions. For simplicity, control lines are omitted in the N-qubit circuit. In the N-qubit circuit, control lines and resonators are arranged in a multilayer.

Because of the long inductive limbs of resonators for the proposed architecture, it is possible to increase the number of spins and interactions.

In the mapping optimization problems to interactions of a system, the larger the number of spins and interactions between spins, the more efficiently the problems are mapped. In our architecture, because of the long inductive limbs of resonators, it is possible to increase the number of spins and interactions.

Considering the actual realization of the quantum annealing circuit, as it is clear from Fig. 8.2.1(a), the resonator is interwoven in a stitchlike manner. Therefore, a standard multilayered superconducting integration is required. On the other hand, the qubit, which is the part most sensitive to decoherence, can be separately fabricated by the standard double-angle shadow evaporation of aluminum [58] that produces all the good superconducting qubits.

8.3 General Quantum Annealing

To perform the quantum annealing, the requirement is that a Hamiltonian of a physical system fits the form of the stoquastic Hamiltonian (H_{QA}), which is given by [?]

$$\mathcal{H}_{QA} = \Lambda(t) \sum_{i} \tilde{\varepsilon}_i \sigma_i^z + \Lambda(t) \sum_{\substack{i,j \\ i<j}} \tilde{J}_{ij} \sigma_i^z \sigma_j^z + \Gamma(t) \sum_{i} \tilde{\Delta}_i \sigma_i^x \ , \tag{8.3.1}$$

where $\tilde{\varepsilon}_i$ and $\tilde{\Delta}_i$ are the normalized energies of the *i*th spin corresponding to the longitudinal and transverse magnetic fields, respectively, $\tilde{J}_{ij}$ is the normalized energy of the interaction between the spins ($-1 \leq \{\tilde{\varepsilon}_i,\ \tilde{J}_{ij}\} \leq 1$), and Λ and Γ are time-dependently tunable values.

The optimization problem is mapped onto $\tilde{\varepsilon}_i$ and $\tilde{J}_{ij}$. After mapping the optimization problem to the system, the quantum annealing is performed in accordance with the following procedure. Initially ($t = t_0$), all spins are made to face the same direction by applying transverse magnetic fields, where $\Lambda(t_0) = 0$ and $\Gamma(t_0) = 1$. Then, the magnetic fields applied to the spins are gradually changed to the longitudinal direction. Finally, at $t = t_f$, $\Lambda(t_f) = 1$, and $\Gamma(t_f) = 0$, the states of the spins show us the solution to the problem. When the system is at the end of an annealing procedure, the energy of the spin and the strengths of the effective interactions between spins should be much larger than the transverse energy of the spin ($\tilde{\Delta}_i \ll \tilde{\varepsilon}_i\,, \tilde{J}_{ij}$). To satisfy these requirements, the characteristics of our proposed architecture must be estimated and calculated.

8.4 Requirements of Proposed Architecture

The proposed architecture is described by the following Hamiltonian, which considers the qubits, resonators, the longitudinal and transverse inductive coupling between each

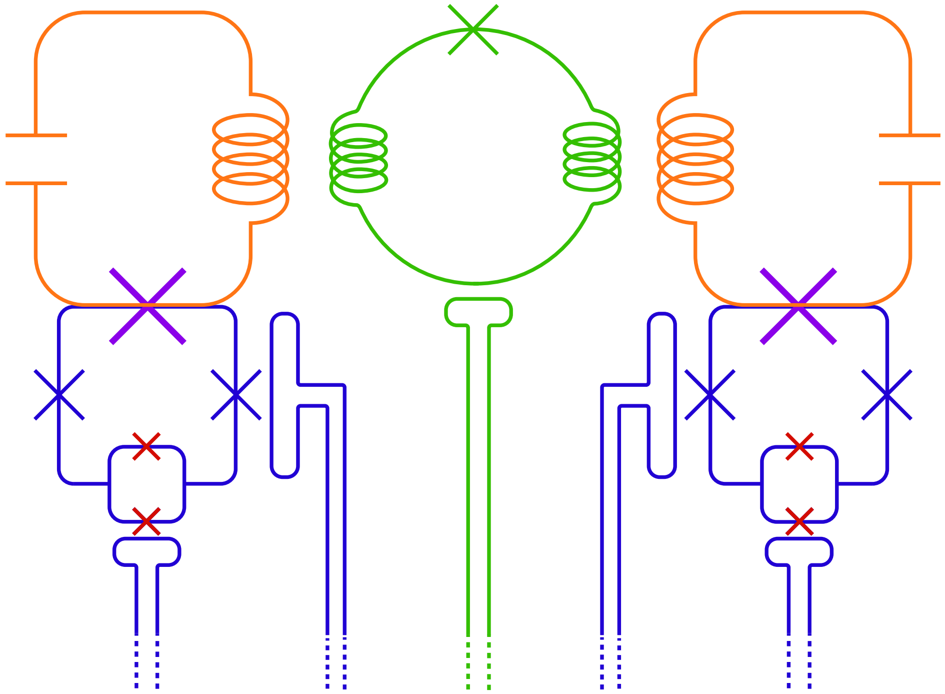

Figure 8.3.1: Schematic representation of two flux qubits coupled to two LC resonators via a SQUID-based coupler. The flux qubit and the resonator share a line with a β-junction. Blue crosses represent Josephson junctions. Red and purple crosses are α and β-junctions, respectively. φ is the phase difference across each junction. f_i^α and f_i^z are the α and main loop flux biases, respectively.

qubit and resonator, and the interactions between resonators [19]:

$$\begin{aligned}\mathcal{H}_N = &\sum_i \left(\varepsilon_i \sigma_i^z + \Delta_i \sigma_i^x\right) + \omega_i^r \left(a_i^\dagger a_i + \frac{1}{2}\right) \\ &+ \sum_i g_i^z \sigma_i^z \left(a_i^\dagger + a_i\right) + g_i^x \sigma_i^x \left(a_i^\dagger + a_i\right) \\ &+ \sum_{\substack{i,j \\ i<j}} g_{ij}^c \left(a_i^\dagger + a_i\right)\left(a_j^\dagger + a_j\right) \ , \end{aligned} \tag{8.4.1}$$

where *i* and *j* are integers from 1 to *N*, which is the total number of qubits (resonators), σ_i^z and σ_i^x are the *i*th spin operators of the longitudinal and transverse degrees of freedom, $\varepsilon_i = \varepsilon_i(f_i^z)$ and $\Delta_i = \Delta_i(f_i^\alpha)$ are the energies of each degree of freedom of the *i*th qubit, $f_i^z = \Phi_i^z/\Phi_0$ and $f_i^\alpha = \Phi_i^x/\Phi_0$, Φ_i^z and Φ_i^x are the fluxes of the *i*th qubit in the α-loop and the main loop, Φ_0 is the flux quantum, $a_i^\dagger$ and a_i are the bosonic creation and annihilation operators of the *i*th resonator, ω_i^r is the energy of the *i*th resonator, g_i^z and g_i^x are the longitudinal and transverse coupling constants between the *i*th qubit and resonator, and

g^c_{ij} is the coupling constant between the *i*th and *j*th resonators, respectively.

When the applied flux of the main loop changes away from a half-integer multiple of the flux quantum, the Z and X energies of the *i*th qubit $(\varepsilon_i, \Delta_i)$ become $\Delta_i = 0$ and $\varepsilon_i = \varepsilon^f_i$, and the transverse coupling g^x_i is neglected. The third term of the Hamiltonian $(\mathcal{H}_N)$, which describes the qubit-resonator interactions, is exactly diagonalized (following and expanding Billangeon's method in Refs. [17] and [18]) by the unitary operator given by

$$\mathcal{U}_N = \exp\left[\sum_{k=1}^{N}\sum_{l=1}^{N} -\theta_{kl}\sigma^z_k\left(a^\dagger_l - a_l\right)\right] . \tag{8.4.2}$$

Here, θ_{ij} are set to satisfy the following simultaneous equations for all *i* and *j*:

$$\forall i, j \quad g^z_i\delta_{ij} - \sum_{k=1}^{N}\left(2g^c_{kj} + \omega^r_k\delta_{kj}\right)\theta_{ik} = 0 \,, \tag{8.4.3}$$

where we impose $g^c_{ij} = g^c_{ji}$ because the coupling strength of the resonators is symmetric, and $g_{ii} = 0$ because the self-coupling refers to the self-energy of the resonator ω^r_i, which has already been included. Under this constraint, using the Baker–Campbell–Hausdorff (BCH) formulation, the first-order terms cancel out, the effective interaction terms remain, and the higher-order terms equal zero,

$$\begin{aligned}\mathcal{H}'_N \equiv& \mathcal{U}^\dagger_N \mathcal{H}^f_N \mathcal{U}_N \\ =& \sum_i \varepsilon^f_i \sigma^z_i + \sum_{\substack{i,j\\ i<j}} J_{ij}\sigma^z_i\sigma^z_j \\ &+ \sum_i \omega^r_i\left(a^\dagger_i a_i + \frac{1}{2}\right) + \sum_{\substack{i,j\\ i<j}} g^c_{ij}\left(a^\dagger_i + a_i\right)\left(a^\dagger_j + a_j\right) ,\end{aligned} \tag{8.4.4}$$

where $J_{ij} = -g^z_i\theta_{ji}$.

J_{ij} is the strength of the effective interaction between the *i*th and *j*th qubits. We can obtain J_{ij} by applying Cramer's rule to Eq. (8.4.3). θ_{ij} denotes the route from the *i*th qubit to the *j*th qubit through the network of resonators. In the proposed architecture, the full interactions between qubits are effectively realized. In the Hamiltonian in Eq. (8.4.4), the qubit-resonator interaction term has already been diagonalized. The remaining terms of resonator couplings change the eigenenergies of the resonators only and not the other terms. Therefore, to evaluate the energies of qubits and effective couplings between qubits for the quantum annealing Hamiltonian in Eq. (8.3.1), it is not necessary to consider the 3rd and 4th terms of the Hamiltonian in Eq. (8.4.4) that depend only on the resonators themselves.

To map a particular optimization problem that we wish to solve, it is necessary that the set of interactions (J_{ij}) is encoded to the set of coupling constants of the system (g^c_{ij}). If the encoding time is not polynomial when using a classical computer, it makes no sense to build the system. In our proposed circuit, once the set of interactions of the problem is fixed, it can be converted to the set of g^c_{ij} by a common matrix method using a classical computer in polynomial time with Eq. (8.4.3).

We define the coupling matrix G with non-diagonal elements $2g^c_{ij}$ and diagonal elements ω^r_i. Then, using Cramer's rule, we obtain $J_{ij} = -g^z_i(\det G'_{ij}/\det G)$, where G'_{ij} is G with the *i*th columns replaced with the vector $(0, \cdots, 0, g^z_j, 0, \cdots, 0)^T$, which has the *j*th qubit-resonator coupling strength at the *j*th element with other elements equal to zero. The highest orders of $\det G$ and $\det G'_{ij}$ for the resonator energy are

$$\det G \propto \prod_{k=1}^{N} \omega^r_k, \qquad \det G'_{ij} \propto 2g^z_j g^c_{ij} \prod_{k=1,\, k\neq i,j}^{N} \omega^r_k \,. \tag{8.4.5}$$

Therefore, we can estimate the strength of the effective interaction through just two (*i* and *j*) resonators as

$$|J_{ij}| \propto (g^z_i/\omega^r_i)(g^z_j/\omega^r_j)g^c_{ij} \,, \tag{8.4.6}$$

where the lower-order terms of ω^r are ignored, which are much smaller than the highest-order term because the lower-order terms correspond to coupling through more than two resonators.

In the strong-coupling regime, which is usually used in the field of superconducting circuits, the resonator energy ω^r is larger than the coupling constant g between a qubit and resonator $(\kappa, \gamma \ll g < \omega^r)$, where κ and γ are the photon leakage rate from the resonator and the relaxation rate from the qubit, respectively. In this regime, the value of $|J_{ij}|$ is much smaller than the sufficient strength of the interactions: $|J_{ij}| \ll 1$.

For example, when $N = 2$, J_{ij} is given by

$$J_{12} = \frac{4g^z_1 g^z_2 g^c_{12}}{\omega^r_1\omega^r_2 - (2g^c_{12})^2} \,. \tag{8.4.7}$$

The value of J_{12} is lower than the order of MHz when common values of the qubit-resonator coupling strength [21] $(\sim 100\,\mathrm{MHz})$ are used in the strong-coupling regime. To satisfy the requirement of the final procedure (see Sect. 8.3) of the quantum annealing, ε must also be lower than the order of MHz. However, the thermal fluctuation of a quantum circuit in a $10\,\mathrm{mK}$ environment is equivalent to a frequency fluctuation of around $200\,\mathrm{MHz}$. Thus, this system cannot give the correct solution to problems because the final state of the qubits is easily buried in thermal noise.

The ultrastrong-coupling regime [183, 71] is stronger than the strong coupling regime. However, the coupling strength is still smaller than the energy of the resonator by one order of magnitude ($g \sim 0.1\omega^r$), so the strength of the effective interactions is also insufficient in this regime. To resolve this problem of the strength, we adopt the deep-strong-coupling regime, which has recently been realized in experiments [246**?**].

In the deep-strong-coupling regime, the coupling strength between the qubits and resonators is similar to the energy of the resonator ($g \sim \omega^r$). A large inductance, generated by the qubit and the resonator sharing a line and a large Josephson junction (called β-junction), allows the coupling strength to increase. In this regime, the strength of the effective interaction is larger and Eq. (8.4.6) becomes

$$|J_{ij}| \propto g_{ij}^c \, . \tag{8.4.8}$$

The order of the strength of J_{ij} depend the order of the strength of g_{ij}^c.

Although in this regime, the approximation of the Jaynes–Cummings model fails, the second-order term of the resonator $g_i^{z,2}(a_i^\dagger + a_i)^2$ appears in the system Hamiltonian without the approximation of the Rabi model. Fortunately, following the method of Ref. [246], this second-order term can be transformed into a first-order term and eliminated to obtain the form of the Hamiltonian in Eq. (8.4.1).

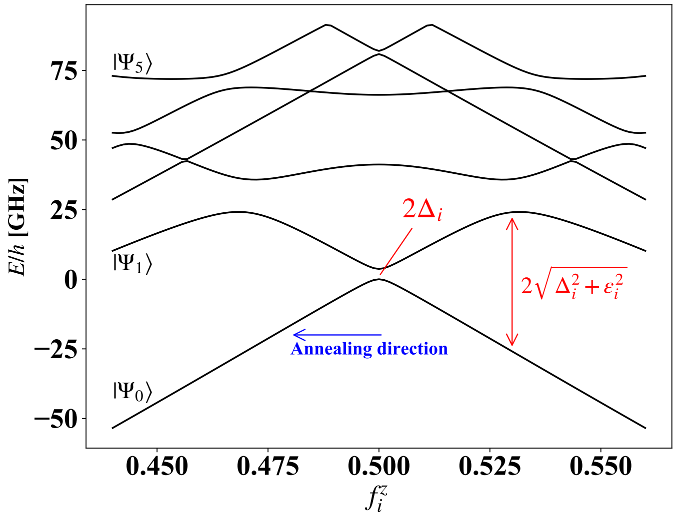

Figure 8.4.1: (Color online) Calculated energy levels of a flux qubit with a β-junction as a function of main loop flux bias. The energy gap between E_1 and E_0 is $2\sqrt{\Delta_i^2 + \varepsilon_i^2}$. $|\Psi_\xi\rangle$ is the ξth eigenstate given E_ξ. We take the calculation space maximum value of k, l, and m of 7 for a good approximation. The parameters are $E_c/h = 5\,\text{GHz}$, $E_J/h = 250\,\text{GHz}$, $\alpha = 0.7$, and $\beta = 4$.

Next, we calculate the energy levels and the coupling strengths of the qubit in the deep-strong-coupling regime. From Fig. 8.2.1(b), the Hamiltonian of the *i*th qubit is given by

$$\begin{aligned}\mathcal{H}_i^q =& \frac{1}{2(\alpha+\beta+2\alpha\beta)C}\left[(\alpha+\beta+\alpha\beta)\left(q_a^2+q_b^2\right)\right.\\ &\left.-(1+2\alpha)q_\beta^2-2\alpha\beta q_a q_b-2\alpha(q_a+q_b)q_\beta\right]\\ &-E_J\left\{\cos\varphi_a+\cos\varphi_b+\cos\varphi_\beta\right.\\ &\left.+\alpha\cos\left(\pi f_i^\alpha\right)\cos\left[\varphi_a+\varphi_b+\varphi_\beta+\pi(2f_i^z-f_i^\alpha)\right]\right\}\ ,\end{aligned} \tag{8.4.9}$$

where q_j is the conjugate momentum of $\phi_j=\varphi_j\Phi_0/2\pi$, $j\in\{a,\,b,\,\beta\}$, C is the capacitance of the Josephson junction, E_J is the energy of the Josephson junction, and $0.5\alpha E_J$ and βE_J are the energies of the α-junction and β-junction, respectively. To derive the energy levels, we calculate the Schrödinger equation of the Hamiltonian ($\mathcal{H}_i^q$) by using the wave function $|\Psi_\xi\rangle=\sum_{k,l,m}C_{k,l,m}^\xi|\psi_k^{(a)}\rangle|\psi_l^{(b)}\rangle|\psi_m^{(\beta)}\rangle$, where $|\psi_\eta^{(j)}\rangle=(2\pi)^{-1/2}\exp(-i\eta\varphi_j)$, $C_{k,l,m}^\xi$ is an arbitrary complex number for $\eta\in\{k,l,m\}$ and ξ is the number of energy states. The energy band structure is shown in Fig. 8.4.1.

The coupling constant between the qubit and the resonator via the β-junction is also calculated [191] (shown in Fig. 8.4.2) as

$$g_i^{\|}=\frac{1}{2}I_r\times\frac{1}{2}\Phi_0\left(\langle\Psi_1|\,\varphi_\beta\,|\Psi_1\rangle-\langle\Psi_0|\,\varphi_\beta\,|\Psi_0\rangle\right)\ , \tag{8.4.10}$$

$$g_i^{\perp}=\frac{1}{2}I_r\times\frac{1}{2}\Phi_0\left(\langle\Psi_0|\,\varphi_\beta\,|\Psi_1\rangle+\langle\Psi_1|\,\varphi_\beta\,|\Psi_0\rangle\right)\ , \tag{8.4.11}$$

where φ_β is the phase difference at the β-junction.

As shown in Fig. 8.4.1, a flux qubit can be well approximated as a two-level system around the optimal point ($f_i^z\sim 0.5$) because of its large anharmonicity [186]. Using the Hamiltonian in Eq. (8.4.9) and both of the coupling constants in Eqs. (8.4.10) and (8.4.11), the Hamiltonian of the resonator-qubit pair is given by

$$\mathcal{H}_i^{qr}=\omega_i^r\left(a_i^\dagger a_i+\frac{1}{2}\right)+\omega_i^q\sigma_i^{z'}+\left(g_i^{\|}\sigma_i^{z'}+g_i^{\perp}\sigma_i^{x'}\right)\left(a_i^\dagger+a_i\right), \tag{8.4.12}$$

where $\omega_i^q=\sqrt{\Delta_i^2+\varepsilon_i^2}$ and the Pauli matrix $\sigma_i^{z'}$ basis is $|\Psi_0\rangle$ and $|\Psi_1\rangle$. g_i^z and g_i^x in the coordinate σ_i^z of the Hamiltonian in Eq. (8.4.1) can be calculated using $g_i^{\|}$, $g_i^{\perp}$, ε_i, and Δ_i (Fig. 8.4.2). Thereby, g_i^x is negligible because it is much smaller than g_i^z.

In the deep-strong-coupling regime, the state of the pair of the qubit and resonator is displaced. When the qubit energy is sufficiently smaller than the resonator energy, the state of the pair at the transverse magnetic field can be approximated [5] to $|{\leftarrow}\rangle_i\equiv$

$|+\rangle_i \otimes \exp\left[-(g_i^z/\omega_i^r)(a_i^\dagger - a_i)\right]|n_i\rangle$. Here, $|+\rangle_i \equiv (|\circlearrowleft\rangle_i + |\circlearrowright\rangle_i)/\sqrt{2}$, $|\circlearrowleft\rangle_i$ and $|\circlearrowright\rangle_i$ are the basis of the *i*th qubit and correspond to the current directions, and n_i is the photon number of the Fock state in the *i*th resonator.

Next, we describe a procedure to perform quantum annealing using the parameters in the proposed circuit (Δ_i, ε_i, g_i^z, g_i^x, g_{ij}^c). An example of the procedure for each parameter during annealing is shown in Fig. 8.4.3. This graph is based on the assumption that the flux biases are linearly changed at each loop.

In the beginning of the quantum annealing procedure, the state of each qubit is $|{\leftarrow}\rangle$. Then, to fit the Hamiltonian of the proposed architecture [Eq. (8.4.1)] to the form of Eq. (8.3.1), J_{ij}, Δ_i, and ε_i must be controlled with time. To control the parameters, they are time-dependently tuned by external flux biases. The four parameters (Δ_i, ε_i, J_{ij}^z, J_{ij}^x) depend on the flux biases of the main loop and the α-loop because J_{ij} depends on $g_{i,j}^z$, $g_{i,j}^x$, and the set of g_{ij}^c. Such a standard annealing path is shown in Fig. 8.4.3.

In the proposed system, we can freely choose ε_i and $|J_{ij}^z|$ in the range of 0 to around 2 GHz. At the end of the path, Δ_i should be set much smaller than ε_i and $|J_{ij}^z|$ [93]. Fortunately, Δ_i is reduced by the factor $\exp[-2(g_i^z/\omega_i^r)^2]$ in the deep-strong-coupling regime [5]. Therefore, the final state of the system should correspond to the solution to an optimization problem. After the annealing, the flux qubit can be measured by dispersive readout with high accuracy.

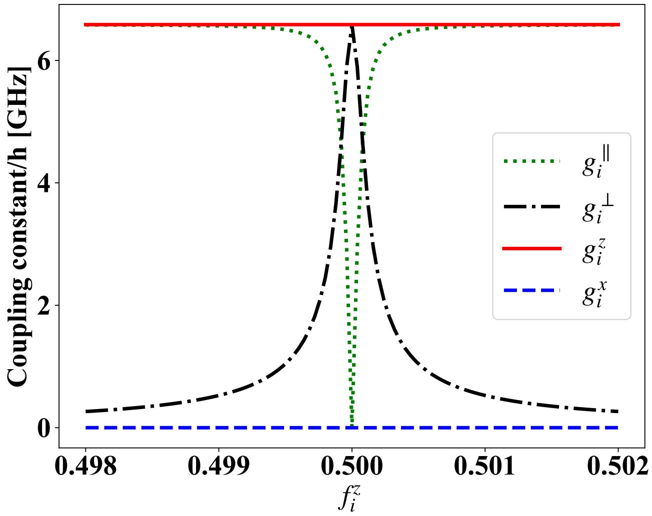

Figure 8.4.2: (Color online) Calculated coupling constant of each degree of freedom as a function of the main loop flux bias. The solid and dashed curves represent g_i^z and g_i^x, respectively. These constants are calculated from $g_i^{\parallel}$, $g_i^{\perp}$, ε_i, and Δ_i. The other parameters are shown in Table 8.4.1.

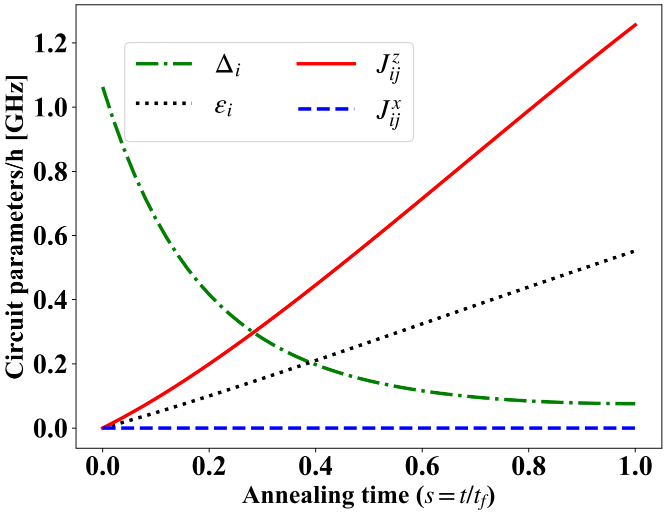

Figure 8.4.3: (Color online) Calculated circuit parameter dynamics for a typical annealing path. This graph is based on the assumption that g^c_{ij} is linearly increased from 0 to 400 MHz. f^z_i and f^α_i are also linearly changed from 0.5 to 0.4997 and from 0.21 to 0, respectively. During the annealing path, J^z_{ij} (solid curve) and J^x_{ij} (dashed curve) are calculated from g^z_i and g^x_i in Eq. (8.4.1). The other parameters are shown in Table 8.4.1.

From Eq. (8.4.7), the coupling strength (J_{12}) is expressed in terms of the circuit parameters as

$$J_{12} \approx \frac{M^2}{L_r^2} M_c I^q_1 I^q_2 \ , \tag{8.4.13}$$

where M is the mutual inductance between a qubit and a resonator, and M_c is the effective mutual inductance between resonators (1 and 2) through the coupler. I^q_i is the screening current of the *i*th qubit ($i = 1, 2$). L_r is the effective inductance of resonators.

To realize antiferromagnetic and ferromagnetic interactions between qubits for the mapping of problems in Eq. (8.4.7), the rf-SQUID-based coupler connecting the resonators requires that the coupling must be able to take positive and negative values under external biases [106, 239]. To meet the requirement from the coupler, the circuit parameters are chosen to obtain the coupling strength (J_{12}) on the order of GHz. The parameters are listed in Table 8.4.1.

Parasitic direct couplings exist between resonators because of geometric mutual inductance at their limbs. However, in the case that two resonators with the parameters given in Table 8.4.1 are positioned 100 $\mu\mathrm{m}$ apart, the parasitic direct couplings should be lower than the order of MHz. The simulation showed that such small parasitic couplings can be ignored. When the length of the resonator limb is elongated to the order of cm, the

Table 8.4.1: Parameters for annealing calculation. I_i^r is the root-mean-square current of the resonator. I_c and I_s are critical currents of Josephson junctions in an rf-SQUID-based coupler and a qubit, respectively. $E_J = I_c\Phi_0/2\pi, E_c = e^2/2C$. The resonator with the parameters below has a 2-mm-long inductor limb.

Parameter	Value	Unit
E_c/h	5	GHz
E_J/h	250	GHz
ω_r	7.2	GHz
I_r	41	nA
L_r	1.4	nH
M_c	154	pH
I_s	10	µm
α	0.8	-
β	1.1	-

parasitic couplings probably need to be suppressed with a superconducting ground plane.

An *N*-qubit system can clearly be realized in the same way. In this *N*-pair circuit, we can show that the order of coupling strengths is not reduced by the increase in *N*. We deal with this *N*-qubit system as a unit cell because the number of qubits in the unit cell is limited by the length of the long inductive limb of the LC resonators. From Eq. (8.4.13), to make J_{ij} as large as possible, the inductance of the resonator cannot be made too large. It is necessary to suppress L_r to nH order or below to construct a fully coupled circuit with dozens of qubits. For this reason, the length of the long inductive limb is limited to cm order.

8.5 Resonator network analysis

Let the Hamiltonian $\mathcal{H}_{rn}$ describe a system with fully coupled harmonic oscillators. For *i*-th resonator, annihilation and creation operators are $a_i^\dagger$ and a_i, resonator frequency is

ω_i^r, and coupling constant is g_{ij}, respectably. Then Hamiltonian is expressed as,

$$\mathcal{H}_{rn} = \sum_i \omega_i^r \left(a_i^\dagger a_i + \frac{1}{2}\right) + \sum_{i<j} g_{ij} \left(a_i^\dagger + a_i\right)\left(a_j^\dagger + a_j\right) \tag{8.5.1}$$

$$= \sum_i \frac{1}{2}\omega_i^r \left(a_i^\dagger a_i + a_i a_i^\dagger\right) + \frac{1}{2}\sum_{i\neq j} g_{ij} \left(a_i^\dagger a_j^\dagger + a_j^\dagger a_j + a_i a_j^\dagger + a_i a_j\right) \tag{8.5.2}$$

$$= \frac{1}{2}\sum_{\langle i,j\rangle} \left[\left(\omega_i^r \delta_{ij} + g_{ij}(1-\delta_{ij})\right)\left(a_i^\dagger a_j + a_i a_j^\dagger\right) + g_{ij}(1-\delta_{ij})\left(a_i^\dagger a_j^\dagger + a_i a_j\right)\right]. \tag{8.5.3}$$

For conciseness, following definitions are introduced

$$A_{ij} := \omega_{ij}^r \delta_{ij} + gij(1-\delta_{ij}), \tag{8.5.4}$$

$$B_{ij} := gij(1-\delta_{ij}). \tag{8.5.5}$$

The Hamiltonian (8.5.3) is then concisely written as

$$\mathcal{H}_{rn} = \frac{1}{2}\sum_{\langle i,j\rangle} \left[A_{ij}\left(a_i^\dagger a_j + a_i a_j^\dagger\right) + B_{ij}\left(a_i^\dagger a_j^\dagger + a_i a_j\right)\right] \tag{8.5.6}$$

$$= \frac{1}{2}\sum_{\langle i,j\rangle} \left(a_i^\dagger A_{ij} a_j + a_i A_{ij} a_j^\dagger + a_i^\dagger B_{ij} a_j^\dagger + a_i B_{ij} a_j\right) \tag{8.5.7}$$

$$= \frac{1}{2}\mathbf{a}^\dagger \mathbf{A}\mathbf{a} + \mathbf{a}^{\mathrm{T}}\mathbf{A}\left(\mathbf{a}^\dagger\right)^{\mathrm{T}} + \mathbf{a}^\dagger \mathbf{B}\left(\mathbf{a}^\dagger\right)^{\mathrm{T}} + \left(\mathbf{a}^\dagger\right)^{\mathrm{T}}\mathbf{B}\mathbf{a} \tag{8.5.8}$$

$$= \frac{1}{2}\begin{pmatrix}\mathbf{a}^\dagger & \mathbf{a}^{\mathrm{T}}\end{pmatrix}\begin{pmatrix}\mathbf{A} & \mathbf{B}\\ \mathbf{B} & \mathbf{A}\end{pmatrix}\begin{pmatrix}\mathbf{a}\\ \left(\mathbf{a}^\dagger\right)^{\mathrm{T}}\end{pmatrix} \tag{8.5.9}$$

where annihilation and creation vectors are $\mathbf{a}^\dagger := (a_1^\dagger \; a_2^\dagger \; \ldots)$ and $\mathbf{a} := (a_1 \; a_2 \; \ldots)^{\mathrm{T}}$, and coefficient matrices are $\mathbf{A} := (A_{ij})$, $\mathbf{B} := (B_{ij})$, respectably. Introducing the transformation (called Bogoliubov transformation)

$$b_i = \sum_j \left(u_j^{(i)} a_j + v_j^{(i)} a_j^\dagger\right), \tag{8.5.10}$$

$$\tag{8.5.11}$$

we diagonalize the Hamiltonian (8.5.9) as

$$\mathcal{H}_{rn} = \sum_i \frac{1}{2}\Omega_i \left(b_i^\dagger b_i + b_i b_i^\dagger\right). \tag{8.5.12}$$

New operators b_i and b_j are required to satisfy bosonic commutation relation,

$$\begin{aligned}\left[b_i, b_j^\dagger\right] &= \sum_{k,l} \left[\left(u_k^{(i)} a_k + v_k^{(i)} a_k^\dagger\right), \left(u_l^{(j)*} a_l^\dagger + v_l^{(j)*} a_l\right)\right] && (8.5.13)\\ &= \sum_k \left(\left[u_k^{(i)} a_k, u_k^{(j)*} a_k^\dagger\right]\right) + \left[v_k^{(i)} a_k^\dagger, v_k^{(j)*} a_k\right]) && (8.5.14)\\ &= \sum_k \left(u_k^{(i)} u_k^{(j)*} - v_k^{(i)} v_k^{(j)*}\right) && (8.5.15)\\ &:= \delta_{ij} && (8.5.16)\end{aligned}$$

Equations (8.5.15) and (8.5.16) imposes the orthogonal relation on the coefficients $u_k^{(i)}$ and $v_k^{(i)}$, named the Bogolibov amplitude. The coefficients $u_k^{(i)}$ and $v_k^{(i)}$ are determined by the following Bogolibov equations:

$$\begin{aligned}\Omega_i u_j^{(i)} &= \sum_k \left(u_k^{(i)} A_{jk} - v_k^{(i)} B_{jk}\right), && (8.5.17)\\ \Omega_i v_j^{(i)} &= \sum_k \left(u_k^{(i)} B_{jk} - v_k^{(i)} A_{jk}\right), && (8.5.18)\end{aligned}$$

They can be written in a matrix form as

$$\begin{pmatrix} \mathbf{A} & -\mathbf{B} \\ \mathbf{B} & -\mathbf{A} \end{pmatrix} \begin{pmatrix} \mathbf{u} \\ \mathbf{v} \end{pmatrix} = \Omega_i \begin{pmatrix} \mathbf{u} \\ \mathbf{v} \end{pmatrix}. \tag{8.5.19}$$

8.5.1 Coupled two-resonator system

Let us consider the circuit of two resonators coupled via mutual inductance. We denote the capacitance, inductance, charge, current of resonators the mutual inductance, as C_i, L_i, $Q_i(t)$, $I_i(t)$, M, $i = \{1, 2\}$, respectably. Lagrangian $\mathcal{L}$ of this circuit is given by

$$\begin{aligned}\mathcal{L} =& \left(\frac{1}{2} L_1 I_1^2 + \frac{1}{2} L_2 I_2^2 + M I_1 I_2\right) - \left(\frac{1}{2}\frac{Q_1^2}{C_1} + \frac{1}{2}\frac{Q_2^2}{C_2}\right) && (8.5.20)\\ =& \mathcal{L}\left(t, Q_1(t), Q_2(t), \dot{Q}_1(t) = I_1(t), \dot{Q}_2(t) = I_2(t)\right). && (8.5.21)\end{aligned}$$

The canonical momentums conjugate p_i to Q_1 and Q_2 are

$$p_1 = \frac{\partial \mathcal{L}}{\partial \dot{Q}_1} = \frac{\partial \mathcal{L}}{\partial I_1} \tag{8.5.22}$$

$$= L_1 I_1 + M I_2 \,. \equiv \Phi_1 \tag{8.5.23}$$

$$p_2 = \frac{\partial \mathcal{L}}{\partial \dot{Q}_2} = \frac{\partial \mathcal{L}}{\partial I_2} \tag{8.5.24}$$

$$= L_2 I_2 + M I_1 \,. \equiv \Phi_2 \tag{8.5.25}$$

Here, canonical momentum $p_i = \Phi_i$ is flux penetrating i resonator.The relation between the flux and current given in equations (8.5.23) and (8.5.25) is written in the matrix form as

$$\begin{pmatrix} \Phi_1 \\ \Phi_2 \end{pmatrix} = \begin{pmatrix} L_1 & M \\ M & L_2 \end{pmatrix} \begin{pmatrix} I_1 \\ I_2 \end{pmatrix} . \tag{8.5.26}$$

$$\Leftrightarrow \begin{pmatrix} I_1 \\ I_2 \end{pmatrix} = \begin{pmatrix} L_1 & M \\ M & L_2 \end{pmatrix}^{-1} \begin{pmatrix} \Phi_1 \\ \Phi_2 \end{pmatrix} \tag{8.5.27}$$

$$= \frac{1}{L_1 L_2 - M^2} \begin{pmatrix} L_2 & -M \\ -M & L_1 \end{pmatrix} \begin{pmatrix} \Phi_1 \\ \Phi_2 \end{pmatrix} . \tag{8.5.28}$$

Then Lagrange equation is given by

$$\begin{cases} \frac{\mathrm{d}}{\mathrm{d}t} \frac{\partial \mathcal{L}}{\partial \dot{Q}_1} - \frac{\partial \mathcal{L}}{\partial Q_1} = 0 \\ \frac{\mathrm{d}}{\mathrm{d}t} \frac{\partial \mathcal{L}}{\partial \dot{Q}_2} - \frac{\partial \mathcal{L}}{\partial Q_2} = 0 \end{cases} \Leftrightarrow \begin{cases} \frac{\mathrm{d}\Phi_1}{\mathrm{d}t} + \frac{Q_1}{C_1} = 0 \\ \frac{\mathrm{d}\Phi_2}{\mathrm{d}t} + \frac{Q_2}{C_2} = 0 \end{cases} \tag{8.5.29}$$

Equation (8.5.29) is circuit equation of motion (differential type Kirchhoff equation). Then taking Legendre transformation of the Lagrangian $\mathcal{L}$, we obtain the Hamiltonian $\mathcal{H}$,

$$\mathcal{H} = \sum_{i=\{1,2\}} p_i \dot{q}_i - \mathcal{L} \tag{8.5.30}$$

$$= \sum_{i=\{1,2\}} \Phi_i I_i - \left[\left(\frac{1}{2}\Phi_1 I_1 + \frac{1}{2}\Phi_2 I_2\right) - \left(\frac{1}{2}\frac{Q_1^2}{C_1} + \frac{1}{2}\frac{Q_1^2}{C_1}\right)\right] \tag{8.5.31}$$

$$=\left(\frac{1}{2}\Phi_1 I_1 + \frac{1}{2}\Phi_2 I_2\right) + \left(\frac{1}{2}\frac{Q_1^2}{C_1} + \frac{1}{2}\frac{Q_1^2}{C_1}\right) \tag{8.5.32}$$

$$=\left(\frac{1}{2}\Phi_1 \frac{L_2\Phi_1 - M\Phi_2}{L_1L_2 - M^2} + \frac{1}{2}\Phi_2 \frac{-M\Phi_1 + L_1\Phi_2}{L_1L_2 - M^2}\right) + \left(\frac{1}{2}\frac{Q_1^2}{C_1} + \frac{1}{2}\frac{Q_1^2}{C_1}\right) \tag{8.5.33}$$

$$=\frac{1}{2}\frac{L_2}{L_1L_2 - M^2}\Phi_1^2 + \frac{1}{2}\frac{L_1}{L_1L_2 - M^2}\Phi_2 - \frac{M}{L_1L_2 - M^2}\Phi_1\Phi_2 + \left(\frac{1}{2}\frac{Q_1^2}{C_1} + \frac{1}{2}\frac{Q_1^2}{C_1}\right) \tag{8.5.34}$$

$$=\frac{1}{2}\frac{\Phi_1^2}{L_1'} + \frac{1}{2}\frac{\Phi_2^2}{L_2'} - \frac{\Phi_1\Phi_2}{M'} + \left(\frac{1}{2}\frac{Q_1^2}{C_1} + \frac{1}{2}\frac{Q_1^2}{C_1}\right) \tag{8.5.35}$$

where,

$$L_1' \equiv \frac{L_1L_2 - M^2}{L_2} = L_1 - \frac{M^2}{L_2} \tag{8.5.36}$$

$$L_2' \equiv \frac{L_1L_2 - M^2}{L_1} = L_2 - \frac{M^2}{L_1} \tag{8.5.37}$$

$$M' \equiv \frac{L_1L_2 - M^2}{M} = \frac{L_1L_2}{M} - M \tag{8.5.38}$$

To quantize the Hamiltonian, we introduce the canonical commutation relation

$$\left[\hat{Q}_j, \hat{\Phi}_i\right] = i\hbar\delta_{ij}\,, \tag{8.5.39}$$

$$\left[\hat{\Phi}_i, \hat{\Phi}_j\right] = 0\,, \tag{8.5.40}$$

$$\left[\hat{Q}_i, \hat{Q}_j\right] = 0\,. \tag{8.5.41}$$

We then introduce the annihilation and creation operators as

$$a_k^\dagger = \frac{1}{\sqrt{2\hbar Z_k'}}\left(Z_k'\hat{Q}_k - i\hat{\Phi}_k\right), \tag{8.5.42}$$

$$a_k = \frac{1}{\sqrt{2\hbar Z_k'}}\left(Z_k'\hat{Q}_k + i\hat{\Phi}_k\right), \tag{8.5.43}$$

where characteristic impedance is $Z_k' = \sqrt{L_k'/C_k}$ and resonant frequency is $\omega_k' = 1/\sqrt{L_k' C_k}$.

One can express Φ_k and Q_k in terms of a_k and $a_k^\dagger$ as

$$Q_k = \sqrt{\frac{\hbar}{2}\frac{1}{Z_k'}}\left(a_k^\dagger + a_k\right), \tag{8.5.44}$$

$$\Phi_k = i\sqrt{\frac{\hbar}{2}Z_k'}\left(a_k^\dagger - a_k\right). \tag{8.5.45}$$

Finally, the Hamiltonian is given by

$$\mathcal{H} = \frac{1}{2}\hbar\omega_1^{'}\left(a_1^\dagger a_1 + a_1 a_1^\dagger\right) + \frac{1}{2}\hbar\omega_2^{'}\left(a_2^\dagger a_2 + a_2 a_2^\dagger\right) + g^c\left(a_1^\dagger - a_1\right)\left(a_2^\dagger - a_2\right), \tag{8.5.46}$$

where coupling constant and eigen-frequencies are described as

$$g^c \equiv \frac{1}{2}\hbar\sqrt{\frac{Z_1'Z_2'}{M'^2}} = M\sqrt{\frac{\hbar^2\omega_1\omega_2}{4(L_1L_2 - M^2)}} > M\sqrt{\frac{\hbar\omega_1}{2L_1}\frac{\hbar\omega_2}{2L_2}}, \tag{8.5.47}$$

$$\omega_1 = \frac{1}{\sqrt{L_1C_1}}, \quad \omega_2 = \frac{1}{\sqrt{L_2C_2}}. \tag{8.5.48}$$

8.5.2 Coupled N-resonator

Lagrangian of circuit with N resonators fully coupled is described as

$$\mathcal{L} = \left(\sum_i \frac{1}{2}L_iI_i^2 + \sum_{i<j} M_{ij}I_iI_j\right) - \left(\frac{1}{2}\frac{Q_i^2}{C_i}\right) \tag{8.5.49}$$

$$= \left(\sum_i \frac{1}{2}L_iI_i^2 + \sum_{i,j} \frac{1}{2}M_{ij}I_iI_j\right) - \left(\frac{1}{2}\frac{Q_i^2}{C_i}\right) \tag{8.5.50}$$

$$= \mathcal{L}\left(t, Q(t), \dot{Q}(t) = I(t)\right), \tag{8.5.51}$$

where mutual inductance is symmetric,

$$M_{ij} = M_{ji}, \tag{8.5.52}$$

$$M_{ii} = 0, \tag{8.5.53}$$

$$\tag{8.5.54}$$

and charge and current vector of resonators are defined as,

$$\mathbf{Q}(t) = \Big(Q_1(t), Q_2(t), \ldots, Q_N(t)\Big)^T , \tag{8.5.55}$$

$$\begin{aligned}\mathbf{I}(t) &= \frac{\mathrm{d}}{\mathrm{d}t}\Big(Q_1(t), Q_2(t), \ldots, Q_N(t)\Big)^T \\ &= \Big(I_1(t), I_2(t), \ldots, I_N(t)\Big)^T .\end{aligned} \tag{8.5.56}$$

The canonical momentum p_i conjugate to Q_i is given by

$$p_i = \frac{\partial \mathcal{L}}{\partial I_i} = L_i I_i + \sum_j \frac{1}{2} M_{ij} I_j \equiv \Phi_i , \tag{8.5.57}$$

where the vector $\mathbf{\Phi}$ is defined as

$$\mathbf{\Phi} = \Big(\Phi_1(t), \Phi_2(t), \ldots, \Phi_N(t)\Big)^T . \tag{8.5.58}$$

Introducing the matrices of self inductance and mutual inductance

$$L = \begin{pmatrix} L_1 & 0 & 0 & 0 \\ 0 & L_2 & 0 & 0 \\ 0 & 0 & \ddots & 0 \\ 0 & 0 & 0 & L_N \end{pmatrix} , \tag{8.5.59}$$

$$M = \begin{pmatrix} 0 & M_{12} & \cdots & M_{1N} \\ M_{21} & 0 & \cdots & M_{2N} \\ \vdots & \vdots & \ddots & \vdots \\ M_{N1} & M_{N2} & \cdots & 0 \end{pmatrix} , \tag{8.5.60}$$

$$\Lambda = L + M , \tag{8.5.61}$$

one can express the relation between the flux and current in the following matrix form:

$$\Phi = \Lambda I , \tag{8.5.62}$$

$$I = \Lambda^{-1} \Phi , \tag{8.5.63}$$

$$I^T = \Phi^T \Lambda^{-1} . \tag{8.5.64}$$

Then Hamiltonian of this system is

$$\begin{aligned} \mathcal{H} &= \sum_i p_i \dot{q}_i - \mathcal{L} \qquad &(8.5.65)\\ &= \sum_i \Phi_i I_i - \left[\left(\sum_i \frac{1}{2} L_i I_i^2 + \sum_{i,j} \frac{1}{2} M_{ij} I_i I_j \right) - \left(\sum_i \frac{1}{2} \frac{Q_i^2}{C_i} \right) \right] \qquad &(8.5.66)\\ &= \frac{1}{2} \Phi^T I + \sum_i \frac{1}{2} \frac{Q_i^2}{C_i} \qquad &(8.5.67)\\ &= \frac{1}{2} \Phi^T \Lambda^{-1} \Phi + \sum_i \frac{1}{2} \frac{Q_i^2}{C_i} \,. \qquad &(8.5.68) \end{aligned}$$

Finally, quantized the Hamiltonian is obtained by introducing the canonical commutation relation

$$\begin{aligned} [Q_i, \Phi_j] &= i\hbar \delta_{ij} \,, \qquad &(8.5.69)\\ [Q_i, Q_j] &= [\Phi_i, \Phi_j] = 0 \,. \qquad &(8.5.70) \end{aligned}$$

We can then introduce the creation and annihilation operators as

$$\begin{aligned} a_i^\dagger &= \frac{1}{\sqrt{2\hbar Z_i^{'}}} \left(Z_i^{'} \hat{Q}_i - i \hat{\Phi}_i \right) , \qquad &(8.5.71)\\ a_i &= \frac{1}{\sqrt{2\hbar Z_i^{'}}} \left(Z_i^{'} \hat{Q}_i + i \hat{\Phi}_i \right) , \qquad &(8.5.72) \end{aligned}$$

where impedance is

$$Z_i = \sqrt{\frac{L_i^{'}}{C_i}} \,. \tag{8.5.73}$$

Then total Hamiltonian of the N resonator circuit is expressed as

$$\mathcal{H} = \sum_i \hbar \omega_i \left(a_i^\dagger a_i + \frac{1}{2} \right) + \sum_{i,j} g_{ij}^c \left(a_i^\dagger - a_i \right) \left(a_j^\dagger - a_j \right) , \tag{8.5.74}$$

where eigen-frequency is $\omega_i^{'} = 1/\sqrt{L_i^{'} C_i}$.

8.6 Conclusion

We have described the architecture of a quantum annealing circuit with lumped element resonators to considerably increase the number of coupled qubits, which is important for an efficient quantum annealing system. Although the total number of fully coupled qubits is considered to be limited to around 100 in a unit at present, this unit can be scaled up by combining with other units via other couplers.

Quantum annealing machines with dozens of fully coupled qubit unit cells should have an obvious advantage in mapping problems such as social networks, economics, and categorized advertisements. These problems can be decomposed into many subsets, where tight relationships exist within the subset, while only shallow relationships are required among subsets.

Conclusion

In this paper, we have proposed and described in detail three micro-architectures for quantum information processors.

First, we have shown that we can eliminate the wiring problem in real superconducting quantum circuits by cleverly folding the two-dimensional lattice to perform the surface code, while maintaining the geometric connection. Next, we studied the arrangement of the circuit and way how to make it work so that a cluster state, which can realize quantum error correction, can be generated using superconducting quantum circuits. The two micro-architectures, which had been considered completely independent of each other in order to realize different things, became almost equivalent by adding the constraint of using two-dimensional wiring to solve the wiring problem in the implementation of superconducting quantum circuits. This means that the equivalence between the surface code (2D lattice) and the cluster state (3D lattice), which is used for quantum error correction using the stabilizer code for universal quantum computation, has been revealed in the real system of superconducting quantum circuits.

In addition, the micro-architecture of quantum annealing uses a network of woven resonators to achieve full coupling. Based on the conditions of the mapping of the cost function of quantum annealing and the adiabatic theorem, deep-strong coupling is introduced as the coupling between the qubit and the resonator. As a development, if we were to use this system as a gate model instead of quantum annealing, these constraints would change to something else. Therefore, this all-coupled micro-architecture can be used in quantum computers such as NISQ.

Finally, since much of the experimental work has not yet been presented in this paper, I would like to make this microarchitecture feasible by experimentally realizing it in the future.

Appendix

Appendix A

Fabrication

A.1 Fabrications

Airbridge

In determining the parameters of the Air-Birdge, the Air-Birdge must be long enough to span the resonators. The commonly used CPW parameters require at least $22\,\mu\mathrm{m}$ or more to pass through the center conductor, where the width of the center conductor is $10\,\mu\mathrm{m}$ and the width between the center conductor and the ground conductor is $6\,\mu\mathrm{m}$. To minimize the impedance mismatch, the characteristic impedance of the CPW is kept constant until the air bridge scaffold. to $50\,\Omega$.

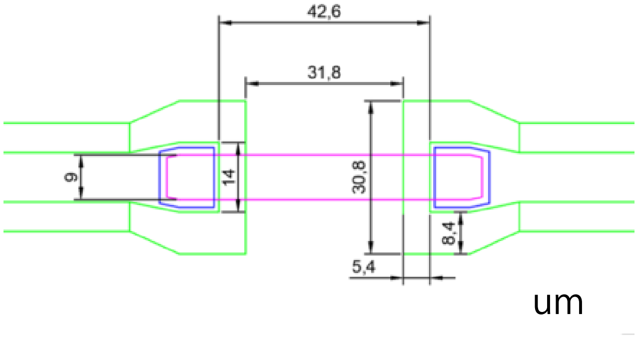

Figure A.1.1: Design of airbridge

Appendix B

Mathematical Derivations

B.1 Annihilation and creation operators

For p and q with $[p, q] = i$,

$$[q, \exp(\pm ip)] = \left[q, \sum_{k=0}^{\infty} \frac{(\pm ip)^k}{k!}\right] = \sum_{k=0}^{\infty} \frac{(\pm i)^k}{k!} [q, p^k] \tag{B.1.1}$$

$$= \sum_{k=0}^{\infty} \frac{(\pm i)^k}{k!} k p^{k-1} [q, p] = \sum_{k=0}^{\infty} \frac{(\pm i)^k}{k!} (-i) k p^{k-1} \tag{B.1.2}$$

$$= \pm \sum_{k=1}^{\infty} \frac{(\pm ip)^{k-1}}{(k-1)!} = \pm \exp(\pm ip) \tag{B.1.3}$$

B.2 Schwarz-Chistoffer mapping

By the Riemann Mapping Theorem, there exists a function S that conformally maps the upper half plane onto P for given a polygonal curve Γ, its interior P is a simply connected domain. The Schwarz-Christoffel theorem provides a concrete description of such maps [59]. When using this SC-theorem, relation of angle between before and after mapping are maintained. In physics, this fact are very useful to calculate electric and magnetic field with maintaining orthogonality relation of Maxwell equation.

> Theorem: *Let P be the interior of a polygon Γ having vertices $w_1, \ldots, w_n$ and interior angles $\alpha_1\pi, \ldots, \alpha_n\pi$ in counter clockwise order. Let S be any conformal, one-to-one map from the upper half plane H onto P satisfying $S(\infty) = w_n$.*

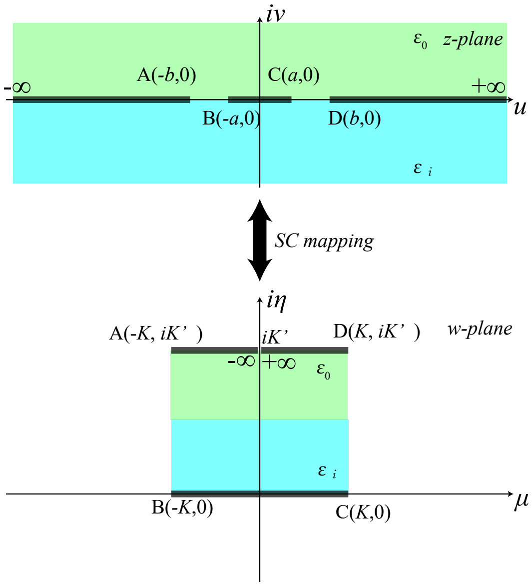

Figure B.2.1: Schwarz-Chistoffer mapping of across section of the coplaner waveguide: top is z-plane, and bottom is w-plane

Then S can be written in the form:

$$S(z) = a_{scm} + c_{scm} \int_{z_0}^{z} \prod_{k=1}^{n-1} (\zeta - z_k)^{\alpha_k - 1} \, \mathrm{d}\zeta \tag{B.2.1}$$

where a_{scm} and c_{scm} are complex constants, and $z_0 < z_1 < \cdots < z_{n-1}$ are complex numbers satisfying $S(z_k) = w_k$ for $k = 1, \ldots, n-1$

To calculate a capacitance and an inductance of coplanar waveguide, conformal mapping are introduced. Let consider across section of coplanar waveguide SC-mapping function is writen as,

$$S(z) = \int_0^z \frac{1}{\sqrt{(1-\zeta^2)(1-k^2\zeta^2)}} \mathrm{d}\zeta \tag{B.2.2}$$

where the complete elliptic integral of the first kind K are introduced. Capacitance and inductance of CPW are

$$C_{CPW} = (1+\epsilon_r) C_{air} = \frac{1+\epsilon_r}{2} \epsilon_0 \frac{4K(k)}{K(k')} \, , \tag{B.2.3}$$

$$L_{CPW} = \frac{\epsilon_0 \mu_0}{C_{air}} = \mu_0 \frac{K(k')}{4K(k)} \tag{B.2.4}$$

Moreover when thickness are finite, there is some correction,

List of Figures

List of Tables

Bibliography

[1] Scott Aaronson and Lijie Chen. Complexity-Theoretic Foundations of Quantum Supremacy Experiments. In Ryan O'Donnell, editor, *32nd Computational Complexity Conference (CCC 2017)*, volume 79 of *Leibniz International Proceedings in Informatics (LIPIcs)*, pages 22:1–22:67, Dagstuhl, Germany, 2017. Schloss Dagstuhl–Leibniz-Zentrum fuer Informatik.

[2] Vinay Ambegaokar and Alexis Baratoff. Tunneling between superconductors. *Phys. Rev. Lett.*, 10:486–489, Jun 1963.

[3] P. W. Anderson and J. M. Rowell. Probable observation of the josephson superconducting tunneling effect. *Phys. Rev. Lett.*, 10:230–232, Mar 1963.

[4] Frank Arute, Kunal Arya, Ryan Babbush, Dave Bacon, Joseph C. Bardin, Rami Barends, Rupak Biswas, Sergio Boixo, Fernando G.S.L. Brandao, David A. Buell, Brian Burkett, Yu Chen, Zijun Chen, Ben Chiaro, Roberto Collins, William Courtney, Andrew Dunsworth, Edward Farhi, Brooks Foxen, Austin Fowler, Craig Gidney, Marissa Giustina, Rob Graff, Keith Guerin, Steve Habegger, Matthew P. Harrigan, Michael J. Hartmann, Alan Ho, Markus Hoffmann, Trent Huang, Travis S. Humble, Sergei V. Isakov, Evan Jeffrey, Zhang Jiang, Dvir Kafri, Kostyantyn Kechedzhi, Julian Kelly, Paul V. Klimov, Sergey Knysh, Alexander Korotkov, Fedor Kostritsa, David Landhuis, Mike Lindmark, Erik Lucero, Dmitry Lyakh, Salvatore Mandrà, Jarrod R. McClean, Matthew McEwen, Anthony Megrant, Xiao Mi, Kristel Michielsen, Masoud Mohseni, Josh Mutus, Ofer Naaman, Matthew Neeley, Charles Neill, Murphy Yuezhen Niu, Eric Ostby, Andre Petukhov, John C. Platt, Chris Quintana, Eleanor G. Rieffel, Pedram Roushan, Nicholas C. Rubin, Daniel Sank, Kevin J. Satzinger, Vadim Smelyanskiy, Kevin J. Sung, Matthew D. Trevithick, Amit Vainsencher, Benjamin Villalonga, Theodore White, Z. Jamie Yao, Ping Yeh, Adam Zalcman, Hartmut Neven, and John M. Martinis. Quantum supremacy using a programmable superconducting processor. *Nature*, 574(7779):505–510, 2019.

[5] S. Ashhab and Franco Nori. Qubit-oscillator systems in the ultrastrong-coupling

regime and their potential for preparing nonclassical states. *Physical Review A - Atomic, Molecular, and Optical Physics*, 81(4):1–17, 2010.

[6] Alain Aspect, Philippe Grangier, and Gérard Roger. Experimental tests of realistic local theories via bell's theorem. *Phys. Rev. Lett.*, 47:460–463, Aug 1981.

[7] J. Bardeen, L. N. Cooper, and J. R. Schrieffer. Microscopic theory of superconductivity. *Phys. Rev.*, 106:162–164, Apr 1957.

[8] J. Bardeen, L. N. Cooper, and J. R. Schrieffer. Theory of superconductivity. *Phys. Rev.*, 108:1175–1204, Dec 1957.

[9] R. Barends, J. Kelly, A. Megrant, A. Veitia, D. Sank, E. Jeffrey, T. C. White, J. Mutus, A. G. Fowler, B. Campbell, Y. Chen, Z. Chen, B. Chiaro, A. Dunsworth, C. Neill, P. O'Malley, P. Roushan, A. Vainsencher, J. Wenner, A. N. Korotkov, A. N. Cleland, and John M. Martinis. Superconducting quantum circuits at the surface code threshold for fault tolerance. *Nature*, 508(7497):500–503, apr 2014.

[10] J. H. Béjanin, T. G. McConkey, J. R. Rinehart, C. T. Earnest, C. R. H. McRae, D. Shiri, J. D. Bateman, Y. Rohanizadegan, B. Penava, P. Breul, S. Royak, M. Zapatka, A. G. Fowler, and M. Mariantoni. Three-dimensional wiring for extensible quantum computing: The quantum socket. *Phys. Rev. Applied*, 6:044010, Oct 2016.

[11] J. S. Bell. On the einstein podolsky rosen paradox. *Physics Physique Fizika*, 1:195–200, Nov 1964.

[12] Charles Bennett. Gb: Quantum cryptography: public key distributions and coin tossing. *Theor. Comput. Sci*, 560:7–11, 2014.

[13] Charles H. Bennett, David P. DiVincenzo, John A. Smolin, and William K. Wootters. Mixed-state entanglement and quantum error correction. *Phys. Rev. A*, 54:3824–3851, Nov 1996.

[14] A J Berkley, M W Johnson, P Bunyk, R Harris, J Johansson, T Lanting, E Ladizinsky, E Tolkacheva, M H S Amin, and G Rose. A scalable readout system for a superconducting adiabatic quantum optimization system. *Superconductor Science and Technology*, 23(10):105014, 2010.

[15] David S Betts and David Sheridan Betts. *An introduction to millikelvin technology.* Number 1. Cambridge University Press, 1989.

[16] Kishor Bharti, Alba Cervera-Lierta, Thi Ha Kyaw, Tobias Haug, Sumner Alperin-Lea, Abhinav Anand, Matthias Degroote, Hermanni Heimonen, Jakob S. Kottmann, Tim Menke, Wai-Keong Mok, Sukin Sim, Leong-Chuan Kwek, and Alán Aspuru-Guzik. Noisy intermediate-scale quantum (nisq) algorithms, 2021.

[17] P. M. Billangeon, J. S. Tsai, and Y. Nakamura. Circuit-QED-based scalable architectures for quantum information processing with superconducting qubits. *Physical Review B - Condensed Matter and Materials Physics*, 91(9), 2015.

[18] P. M. Billangeon, J. S. Tsai, and Y. Nakamura. Scalable architecture for quantum information processing with superconducting flux qubits based on purely longitudinal interactions. *Physical Review B - Condensed Matter and Materials Physics*, 92(2):1–6, 2015.

[19] Alexandre Blais, Jay Gambetta, A. Wallraff, D. I. Schuster, S. M. Girvin, M. H. Devoret, and R. J. Schoelkopf. Quantum-information processing with circuit quantum electrodynamics. *Physical Review A - Atomic, Molecular, and Optical Physics*, 75(3):1–21, 2007.

[20] Alexandre Blais, Arne L. Grimsmo, S. M. Girvin, and Andreas Wallraff. Circuit quantum electrodynamics. *arXiv*, 2020.

[21] Alexandre Blais, Ren Shou Huang, Andreas Wallraff, S. M. Girvin, and R. J. Schoelkopf. Cavity quantum electrodynamics for superconducting electrical circuits: An architecture for quantum computation. *Physical Review A - Atomic, Molecular, and Optical Physics*, 69(6):1–14, 2004.

[22] Alexandre Blais, Alexander Maassen van den Brink, and Alexandre M. Zagoskin. Tunable Coupling of Superconducting Qubits. *Physical Review Letters*, 90(12):4, 2003.

[23] Rainer Blatt and David Wineland. Entangled states of trapped atomic ions. *Nature*, 453(7198):1008–1015, 2008.

[24] Sergio Boixo, Sergei V. Isakov, Vadim N. Smelyanskiy, Ryan Babbush, Nan Ding, Zhang Jiang, Michael J. Bremner, John M. Martinis, and Hartmut Neven. Characterizing quantum supremacy in near-term devices. *Nature Physics*, 14(6):595–600, 2018.

[25] H. Bombin and M. A. Martin-Delgado. Topological quantum distillation. *Physical Review Letters*, 97(18):1–4, 2006.

[26] H. Bombin and M. A. Martin-Delgado. Statistical mechanical models and topological color codes. *Physical Review A - Atomic, Molecular, and Optical Physics*, 77(4):1–10, 2008.

[27] Tomas Boothby, Andrew D. King, and Aidan Roy. Fast clique minor generation in Chimera qubit connectivity graphs. *Quantum Information Processing*, 15(1):495–508, 2016.

[28] Mark D. Bowdrey, Daniel K.L. Oi, Anthony J. Short, Konrad Banaszek, and Jonathan A. Jones. Fidelity of single qubit maps. *Physics Letters A*, 294(5):258 – 260, 2002.

[29] Jochen Braumüller, Joel Cramer, Steffen Schlör, Hannes Rotzinger, Lucas Radtke, Alexander Lukashenko, Ping Yang, Sebastian T. Skacel, Sebastian Probst, Michael Marthaler, Lingzhen Guo, Alexey V. Ustinov, and Martin Weides. Multiphoton dressing of an anharmonic superconducting many-level quantum circuit. *Phys. Rev. B*, 91:054523, Feb 2015.

[30] S. B. Bravyi and A. Yu. Kitaev. Quantum codes on a lattice with boundary. (96):1–6, 1998.

[31] Sergey Bravyi and Jeongwan Haah. Magic-state distillation with low overhead. *Physical Review A - Atomic, Molecular, and Optical Physics*, 86(5):1–10, 2012.

[32] Sergey Bravyi and Alexei Kitaev. Universal quantum computation with ideal Clifford gates and noisy ancillas. *Physical Review A - Atomic, Molecular, and Optical Physics*, 71(2):1–14, 2005.

[33] Hans J. Briegel and Robert Raussendorf. Persistent entanglement in arrays of interacting particles. *Physical Review Letters*, 86(5):910–913, 2001.

[34] Nicholas T Bronn, Vivekananda P Adiga, Salvatore B Olivadese, Xian Wu, Jerry M Chow, and David P Pappas. High coherence plane breaking packaging for superconducting qubits. *Quantum science and technology*, 3(2):024007, 2018.

[35] Dan E. Browne and Hans J. Briegel. One-way Quantum Computation - a tutorial introduction. pages 1–23, 2006.

[36] C. C. Bultink, M. A. Rol, T. E. O'Brien, X. Fu, B. C. S. Dikken, C. Dickel, R. F. L. Vermeulen, J. C. de Sterke, A. Bruno, R. N. Schouten, and L. DiCarlo. Active resonator reset in the nonlinear dispersive regime of circuit qed. *Phys. Rev. Applied*, 6:034008, Sep 2016.

[37] P. I. Bunyk, Emile M. Hoskinson, Mark W. Johnson, Elena Tolkacheva, Fabio Altomare, Andrew J. Berkley, Richard Harris, Jeremy P. Hilton, Trevor Lanting, Anthony J. Przybysz, and Jed Whittaker. Architectural Considerations in the Design of a Superconducting Quantum Annealing Processor. *IEEE Transactions on Applied Superconductivity*, 24(4):1–9, 2014.

[38] Jun Cai, William G. Macready, and Aidan Roy. A practical heuristic for finding graph minors. pages 1–16, 2014.

[39] Daniel L. Campbell, Yun-Pil Shim, Bharath Kannan, Roni Winik, Alexander Melville, Bethany M. Niedzielski, Jonilyn L. Yoder, Charles Tahan, Simon Gustavsson, and William D. Oliver. Universal non-adiabatic control of small-gap superconducting qubits. *Physical Review X*, 10(4):41051, 2020.

[40] Earl T. Campbell, Barbara M. Terhal, and Christophe Vuillot. Roads towards fault-tolerant universal quantum computation. *Nature*, 549(7671):172–179, 2017.

[41] M. Cerezo, Alexander Poremba, Lukasz Cincio, and Patrick J. Coles. Variational Quantum Fidelity Estimation. 2019.

[42] Josephine B. Chang, Michael R. Vissers, Antonio D. Córcoles, Martin Sandberg, Jiansong Gao, David W. Abraham, Jerry M. Chow, Jay M. Gambetta, Mary Beth Rothwell, George A. Keefe, Matthias Steffen, and David P. Pappas. Improved superconducting qubit coherence using titanium nitride. *Applied Physics Letters*, 103(1):012602, 2013.

[43] Zijun Chen, A. Megrant, J. Kelly, R. Barends, J. Bochmann, Yu Chen, B. Chiaro, A. Dunsworth, E. Jeffrey, J. Y. Mutus, P. J.J. O'Malley, C. Neill, P. Roushan, D. Sank, A. Vainsencher, J. Wenner, T. C. White, A. N. Cleland, and John M. Martinis. Fabrication and characterization of aluminum airbridges for superconducting microwave circuits. *Applied Physics Letters*, 104(5):1–4, 2014.

[44] Kevin S. Chou, Jacob Z. Blumoff, Christopher S. Wang, Philip C. Reinhold, Christopher J. Axline, Yvonne Y. Gao, L. Frunzio, M. H. Devoret, Liang Jiang, and R. J. Schoelkopf. Deterministic teleportation of a quantum gate between two logical qubits. *Nature*, 561(7723):368–373, sep 2018.

[45] J Clarke and A I Braginski. *The SQUID handbook Vol 2 Applications of SQUIDs and SQUID systems.* Wiley-VCH, Germany, 2006.

[46] Claude Cohen-Tannoudji, Bernard Diu, and Franck Laloe. Quantum mechanics. ed. rev., amend. 1977.

[47] LIGO Scientific Collaboration and Virgo Collaboration. Observation of gravitational waves from a binary black hole merger. *Physical Review Letters*, 116(6):1–16, 2016.

[48] Leon N. Cooper. Bound electron pairs in a degenerate fermi gas. *Phys. Rev.*, 104:1189–1190, Nov 1956.

[49] R. Dassonneville, T. Ramos, V. Milchakov, L. Planat, Dumur, F. Foroughi, J. Puertas, S. Leger, K. Bharadwaj, J. Delaforce, C. Naud, W. Hasch-Guichard, J. J. García-Ripoll, N. Roch, and O. Buisson. Fast High-Fidelity Quantum Nondemolition Qubit Readout via a Nonperturbative Cross-Kerr Coupling. *Physical Review X*, 10(1):11045, 2020.

[50] E B Davies. Markovian master equations. *Communications in Mathematical Physics*, 39(2):91–110, 1974.

[51] Christopher M Dawson and Michael A Nielsen. The solovay-kitaev algorithm. *arXiv preprint quant-ph/0505030*, 2005.

[52] David Deutsch. Quantum theory, the church–turing principle and the universal quantum computer. *Proceedings of the Royal Society of London. A. Mathematical and Physical Sciences*, 400(1818):97–117, 1985.

[53] Simon J. Devitt, William J. Munro, and Kae Nemoto. Quantum error correction for beginners. *Reports on Progress in Physics*, 76(7):1–41, 2013.

[54] Simon J. Devitt, Ashley M. Stephens, William J. Munro, and Kae Nemoto. Requirements for fault-tolerant factoring on an atom-optics quantum computer. *Nature Communications*, 4:2524 EP –, 10 2013.

[55] Michel H Devoret et al. Quantum fluctuations in electrical circuits. *Les Houches, Session LXIII*, 7(8):133–135, 1995.

[56] Oliver Dial, Douglas T McClure, Stefano Poletto, G A Keefe, Mary Beth Rothwell, Jay M Gambetta, David W Abraham, Jerry M Chow, and Matthias Steffen. Bulk and surface loss in superconducting transmon qubits. *Superconductor Science and Technology*, 29(4):044001, mar 2016.

[57] DGBJ Dieks. Communication by epr devices. *Physics Letters A*, 92(6):271–272, 1982.

[58] G. J. Dolan. Offset masks for lift-off photoprocessing. *Applied Physics Letters*, 31(5):337–339, 1977.

[59] Tobin A Driscoll and Lloyd N Trefethen. *Schwarz-Christoffel Mapping*. Cambridge Monographs on Applied and Computational Mathematics. Cambridge University Press, 2002.

[60] Jiangfeng Du, Lingzhi Hu, Ya Wang, Jianda Wu, Meisheng Zhao, and Dieter Suter. Experimental study of the validity of quantitative conditions in the quantum adiabatic theorem. *Physical Review Letters*, 101(6):8–11, 2008.

[61] A. Dunsworth, R. Barends, Yu Chen, Zijun Chen, B. Chiaro, A. Fowler, B. Foxen, E. Jeffrey, J. Kelly, P. V. Klimov, E. Lucero, J. Y. Mutus, M. Neeley, C. Neill, C. Quintana, P. Roushan, D. Sank, A. Vainsencher, J. Wenner, T. C. White, H. Neven, John M. Martinis, and A. Megrant. A method for building low loss multi-layer wiring for superconducting microwave devices. *Applied Physics Letters*, 112(6):063502, February 2018.

[62] W. Dür, G. Vidal, and J. I. Cirac. Three qubits can be entangled in two inequivalent ways. *Phys. Rev. A*, 62:062314, Nov 2000.

[63] Charles Ebner and David O Edwards. The low temperature thermodynamic properties of superfluid solutions of 3he in 4he. *Physics Reports*, 2(2):77–154, 1971.

[64] Sophia E. Economou, Netanel Lindner, and Terry Rudolph. Optically generated 2-dimensional photonic cluster state from coupled quantum dots. *Physical Review Letters*, 105(9):1–4, 2010.

[65] A. Einstein, B. Podolsky, and N. Rosen. Can quantum-mechanical description of physical reality be considered complete? *Phys. Rev.*, 47:777–780, May 1935.

[66] Suguru Endo, Iori Kurata, and Yuya O. Nakagawa. Calculation of the green's function on near-term quantum computers. *Phys. Rev. Research*, 2:033281, Aug 2020.

[67] Suguru Endo, Jinzhao Sun, Ying Li, Simon C. Benjamin, and Xiao Yuan. Variational quantum simulation of general processes. *Phys. Rev. Lett.*, 125:010501, Jun 2020.

[68] E. Farhi, J. Goldstone, S. Gutmann, J. Lapan, A. Lundgren, and D. Preda. A quantum adiabatic evolution algorithm applied to random instances of an NP-complete problem. *Science*, 292(5516):472–476, 2001.

[69] Edward Farhi, Jeffrey Goldstone, Sam Gutmann, and Michael Sipser. Quantum computation by adiabatic evolution. *arXiv preprint quant-ph/0001106*, 2000.

[70] Richard P. Feynman. Simulating physics with computers. *International Journal of Theoretical Physics*, 21(6-7):467–488, 1982.

[71] P. Forn-Díaz, J. Lisenfeld, D. Marcos, J. J. García-Ripoll, E. Solano, C. J.P.M. Harmans, and J. E. Mooij. Observation of the bloch-siegert shift in a qubit-oscillator system in the ultrastrong coupling regime. *Physical Review Letters*, 105(23):3–6, 2010.

[72] A. G. Fowler, S. J. Devitt, and L. C.L. Hollenberg. Implementation of shor's algorithm on a linear nearest neighbour qubit array. *Quantum Information and Computation*, 4(4):237–251, 2004.

[73] Austin G. Fowler and Craig Gidney. Low overhead quantum computation using lattice surgery, 2018.

[74] Austin G. Fowler, Matteo Mariantoni, John M. Martinis, and Andrew N. Cleland. Surface codes: Towards practical large-scale quantum computation. *Physical Review A - Atomic, Molecular, and Optical Physics*, 86(3), 2012.

[75] Austin G. Fowler, Matteo Mariantoni, John M. Martinis, and Andrew N. Cleland. Surface codes: Towards practical large-scale quantum computation. *Phys. Rev. A*, 86:032324, Sep 2012.

[76] Austin G. Fowler and John M. Martinis. Quantifying the effects of local many-qubit errors and nonlocal two-qubit errors on the surface code. *Physical Review A - Atomic, Molecular, and Optical Physics*, 89(3):1–7, 2014.

[77] Austin G. Fowler, Adam C. Whiteside, and Lloyd C. L. Hollenberg. Towards practical classical processing for the surface code. *Phys. Rev. Lett.*, 108:180501, May 2012.

[78] B Foxen, J Y Mutus, E Lucero, R Graff, A Megrant, Yu Chen, C Quintana, B Burkett, J Kelly, E Jeffrey, Yan Yang, Anthony Yu, K Arya, R Barends, Zijun Chen, B Chiaro, A Dunsworth, A Fowler, C Gidney, M Giustina, T Huang, P Klimov, M Neeley, C Neill, P Roushan, D Sank, A Vainsencher, J Wenner, T C White, and John M Martinis. Qubit compatible superconducting interconnects. *Quantum Science and Technology*, 3(1):014005, nov 2017.

[79] Michael H. Freedman and David A. Meyer. Projective Plane and Planar Quantum Codes. *Foundations of Computational Mathematics*, 1(3):325–332, 2001.

[80] L. Frunzio, A. Wallraff, D. Schuster, J. Majer, and R. Schoelkopf. Fabrication and characterization of superconducting circuit qed devices for quantum computation. *IEEE Transactions on Applied Superconductivity*, 15(2):860–863, 2005.

[81] Keisuke Fujii and Yuuki Tokunaga. Error and loss tolerances of surface codes with general lattice structures. *Physical Review A*, 86(2):020303, aug 2012.

[82] Jay Gambetta, W. A. Braff, A. Wallraff, S. M. Girvin, and R. J. Schoelkopf. Protocols for optimal readout of qubits using a continuous quantum nondemolition measurement. *Physical Review A - Atomic, Molecular, and Optical Physics*, 76(1):1–11, 2007.

[83] Jay M. Gambetta, Jerry M. Chow, and Matthias Steffen. Building logical qubits in a superconducting quantum computing system. *npj Quantum Information*, 3(1), jan 2017.

[84] Bryan T. Gard, Kurt Jacobs, José Aumentado, and Raymond W. Simmonds. Fast, High-Fidelity, Quantum Non-demolition Readout of a Superconducting Qubit Using a Transverse Coupling. pages 1–10, 2018.

[85] Michael R Garey and David S Johnson. Computers and intractability. *A Guide to the*, 1979.

[86] Mercedes Gimeno-Segovia, Pete Shadbolt, Dan E. Browne, and Terry Rudolph. From three-photon greenberger-horne-zeilinger states to ballistic universal quantum computation. *Phys. Rev. Lett.*, 115:020502, Jul 2015.

[87] Ming Gong, Ming Cheng Chen, Yarui Zheng, Shiyu Wang, Chen Zha, Hui Deng, Zhiguang Yan, Hao Rong, Yulin Wu, Shaowei Li, Fusheng Chen, Youwei Zhao, Futian Liang, Jin Lin, Yu Xu, Cheng Guo, Lihua Sun, Anthony D. Castellano, Haohua Wang, Chengzhi Peng, Chao Yang Lu, Xiaobo Zhu, and Jian Wei Pan. Genuine 12-Qubit Entanglement on a Superconducting Quantum Processor. *Physical Review Letters*, 122(11), 2019.

[88] Vittorio Gorini, Alberto Frigerio, Maurizio Verri, Andrzej Kossakowski, and E.C.G. Sudarshan. Properties of quantum markovian master equations. *Reports on Mathematical Physics*, 13(2):149 – 173, 1978.

[89] Vittorio Gorini, Andrzej Kossakowski, and E. C. G. Sudarshan. Completely positive dynamical semigroups of n-level systems. *Journal of Mathematical Physics*, 17(5):821–825, 1976.

[90] Daniel Gottesman. Stabilizer Codes and Quantum Error Correction. 2008, 1997.

[91] Daniel Gottesman. The heisenberg representation of quantum computers. *arXiv preprint quant-ph/9807006*, 1998.

[92] Daniel Gottesman. An introduction to quantum error correction and fault-tolerant quantum computation. 0000:13–58, 2010.

[93] M. Grajcar, A. Izmalkov, and E. Il'Ichev. Possible implementation of adiabatic quantum algorithm with superconducting flux qubits. *Physical Review B - Condensed Matter and Materials Physics*, 71(14):1–8, 2005.

[94] Daniel M. Greenberger, Michael A. Horne, and Anton Zeilinger. *Going Beyond Bell's Theorem*, pages 69–72. Springer Netherlands, Dordrecht, 1989.

[95] Lov K Grover. A fast quantum mechanical algorithm for database search. In *Proceedings of the twenty-eighth annual ACM symposium on Theory of computing*, pages 212–219, 1996.

[96] Lov K Grover. From schrödinger's equation to the quantum search algorithm. *Pramana*, 56(2):333–348, 2001.

[97] A. I. Gubin, K. S. Il'in, S. A. Vitusevich, M. Siegel, and N. Klein. Dependence of magnetic penetration depth on the thickness of superconducting Nb thin films. *Physical Review B - Condensed Matter and Materials Physics*, 72(6):1–8, 2005.

[98] Otfried Gühne and Géza Tóth. Entanglement detection. *Physics Reports*, 474(1-6):1–75, 2009.

[99] Laszlo Gyongyosi and Sandor Imre. State stabilization for gate-model quantum computers. *Quantum Information Processing*, 18(9), 2019.

[100] G. Haack, F. Helmer, M. Mariantoni, F. Marquardt, and E. Solano. Resonant quantum gates in circuit quantum electrodynamics. *Physical Review B - Condensed Matter and Materials Physics*, 82(2):1–6, 2010.

[101] Thomas Häner and Damian S. Steiger. 0.5 petabyte simulation of a 45-Qbit qantum circuit. *Proceedings of the International Conference for High Performance Computing, Networking, Storage and Analysis, SC 2017*, 2017.

[102] Serge Haroche and J-M Raimond. *Exploring the quantum: atoms, cavities, and photons.* Oxford university press, 2006.

[103] R. Harris, A. J. Berkley, M. W. Johnson, P. Bunyk, S. Govorkov, M. C. Thom, S. Uchaikin, A. B. Wilson, J. Chung, E. Holtham, J. D. Biamonte, A. Yu Smirnov, M. H.S. Amin, and Alec Maassen Van Den Brink. Sign- and magnitude-tunable coupler for superconducting flux qubits. *Physical Review Letters*, 98(17), 2007.

[104] R. Harris, J. Johansson, A. J. Berkley, M. W. Johnson, T. Lanting, Siyuan Han, P. Bunyk, E. Ladizinsky, T. Oh, I. Perminov, E. Tolkacheva, S. Uchaikin, E. M. Chapple, C. Enderud, C. Rich, M. Thom, J. Wang, B. Wilson, and G. Rose. Experimental

demonstration of a robust and scalable flux qubit. *Physical Review B - Condensed Matter and Materials Physics*, 81(13):1–19, 2010.

[105] R. Harris, M. W. Johnson, T. Lanting, A. J. Berkley, J. Johansson, P. Bunyk, E. Tolkacheva, E. Ladizinsky, N. Ladizinsky, T. Oh, F. Cioata, I. Perminov, P. Spear, C. Enderud, C. Rich, S. Uchaikin, M. C. Thom, E. M. Chapple, J. Wang, B. Wilson, M. H.S. Amin, N. Dickson, K. Karimi, B. MacReady, C. J.S. Truncik, and G. Rose. Experimental investigation of an eight-qubit unit cell in a superconducting optimization processor. *Physical Review B - Condensed Matter and Materials Physics*, 82(2):1–15, 2010.

[106] R. Harris, T. Lanting, A. J. Berkley, J. Johansson, M. W. Johnson, P. Bunyk, E. Ladizinsky, N. Ladizinsky, T. Oh, and S. Han. Compound Josephson-junction coupler for flux qubits with minimal crosstalk. *Physical Review B - Condensed Matter and Materials Physics*, 80(5):2–5, 2009.

[107] Philipp Hauke, Helmut G. Katzgraber, Wolfgang Lechner, Hidetoshi Nishimori, and William D. Oliver. Perspectives of quantum annealing: Methods and implementations. 2019.

[108] M. Hein, J. Eisert, and H. J. Briegel. Multiparty entanglement in graph states. *Physical Review A - Atomic, Molecular, and Optical Physics*, 69(6), 2004.

[109] Daniel Herr. *Software for Quantum Computation.* PhD thesis, 2019.

[110] Daniel Herr, Franco Nori, and Simon J. Devitt. Lattice surgery translation for quantum computation. *New Journal of Physics*, 19(1):1–23, 2017.

[111] Daniel Herr, Alexandru Paler, Simon J. Devitt, and Franco Nori. Lattice surgery on the Raussendorf lattice. *Quantum Science and Technology*, 3(3):1–9, 2018.

[112] Daniel Herr, Alexandru Paler, Simon J. Devitt, and Franco Nori. Time versus Hardware: Reducing Qubit Counts with a (Surface Code) Data Bus. 2019.

[113] Charles D. Hill, Eldad Peretz, Samuel J. Hile, Matthew G. House, Martin Fuechsle, Sven Rogge, Michelle Y. Simmons, and Lloyd C. L. Hollenberg. A surface code quantum computer in silicon. *Science Advances*, 1(9), 2015.

[114] Clare Horsman, Austin G. Fowler, Simon Devitt, and Rodney Van Meter. Surface code quantum computing by lattice surgery. *New Journal of Physics*, 14, 2012.

[115] Sihao Huang, Benjamin Lienhard, Greg Calusine, Antti Vepsäläinen, Jochen Braumüller, David K. Kim, Alexander J. Melville, Bethany M. Niedzielski, Jonilyn L. Yoder, Bharath Kannan, Terry P. Orlando, Simon Gustavsson, and William D. Oliver. Microwave package design for superconducting quantum processors, 2020.

[116] Joni Ikonen, Jan Goetz, Jesper Ilves, Aarne Keränen, Andras M. Gunyho, Matti Partanen, Kuan Y. Tan, Dibyendu Hazra, Leif Grönberg, Visa Vesterinen, Slawomir Simbierowicz, Juha Hassel, and Mikko Möttönen. Qubit Measurement by Multichannel Driving. *Physical Review Letters*, 122(8):80503, 2019.

[117] K. Inomata, M. Watanabe, T. Yamamoto, K. Matsuba, Y. Nakamura, and J. S. Tsai. Superconducting non-linear resonator for non-destructive readout of a flux qubit. *Journal of Physics: Conference Series*, 150(5):8–12, 2009.

[118] Kunihiro Inomata, Tsuyoshi Yamamoto, Michio Watanabe, Kazuaki Matsuba, and Jaw Shen Tsai. Film-thickness dependence of 10 GHz Nb coplanar-waveguide resonators. *Journal of Vacuum Science and Technology B: Microelectronics and Nanometer Structures*, 27(5):2286–2291, 2009.

[119] A. Izmalkov, M. Grajcar, E. Il'ichev, Th Wagner, H. G. Meyer, A. Yu Smirnov, M. H.S. Amin, Alec Maassen Van Den Brink, and A. M. Zagoskin. Evidence for entangled states of two coupled flux qubits. *Physical Review Letters*, 93(3):037003–1, 2004.

[120] R. C. Jaklevic, John Lambe, A. H. Silver, and J. E. Mercereau. Quantum interference effects in josephson tunneling. *Phys. Rev. Lett.*, 12:159–160, Feb 1964.

[121] Sabine Jansen, Mary Beth Ruskai, and Ruedi Seiler. Bounds for the adiabatic approximation with applications to quantum computation. *Journal of Mathematical Physics*, 48(10), 2007.

[122] Evan Jeffrey, Daniel Sank, J. Y. Mutus, T. C. White, J. Kelly, R. Barends, Y. Chen, Z. Chen, B. Chiaro, A. Dunsworth, A. Megrant, P. J. O'Malley, C. Neill, P. Roushan, A. Vainsencher, J. Wenner, A. N. Cleland, and John M. Martinis. Fast accurate state measurement with superconducting qubits. *Physical Review Letters*, 112(19):1–5, 2014.

[123] Evan Jeffrey, Daniel Sank, J. Y. Mutus, T. C. White, J. Kelly, R. Barends, Y. Chen, Z. Chen, B. Chiaro, A. Dunsworth, A. Megrant, P. J. O'Malley, C. Neill, P. Roushan, A. Vainsencher, J. Wenner, A. N. Cleland, and John M. Martinis. Fast accurate state measurement with superconducting qubits. *Physical Review Letters*, 112(19):1–5, 2014.

[124] M. Jerger, S. Poletto, P. MacHa, U. Hübner, E. Il'Ichev, and A. V. Ustinov. Frequency division multiplexing readout and simultaneous manipulation of an array of flux qubits. *Applied Physics Letters*, 101(4):1–5, 2012.

[125] J. R. Johansson, P. D. Nation, and Franco Nori. QuTiP 2: A Python framework for the dynamics of open quantum systems. *Computer Physics Communications*, 184(4):1234–1240, April 2013.

[126] B. R. Johnson, M. D. Reed, A. A. Houck, D. I. Schuster, Lev S. Bishop, E. Ginossar, J. M. Gambetta, L. Dicarlo, L. Frunzio, S. M. Girvin, and R. J. Schoelkopf. Quantum non-demolition detection of single microwave photons in a circuit. *Nature Physics*, 6(9):663–667, 2010.

[127] N. Cody Jones, Rodney Van Meter, Austin G. Fowler, Peter L. McMahon, Jungsang Kim, Thaddeus D. Ladd, and Yoshihisa Yamamoto. Layered architecture for quantum computing. *Phys. Rev. X*, 2:031007, Jul 2012.

[128] B.D. Josephson. Possible new effects in superconductive tunnelling. *Physics Letters*, 1(7):251 – 253, 1962.

[129] Richard Jozsa. An introduction to measurement based quantum computation. pages 1–22, 2005.

[130] Tadashi Kadowaki. Study of Optimization Problems by Quantum Annealing. 2002.

[131] Tadashi Kadowaki and Hidetoshi Nishimori. Quantum annealing in the transverse Ising model. *Physical Review E - Statistical Physics, Plasmas, Fluids, and Related Interdisciplinary Topics*, 58(5):5355–5363, 1998.

[132] J. Kelly, R. Barends, A. G. Fowler, A. Megrant, E. Jeffrey, T. C. White, D. Sank, J. Y. Mutus, B. Campbell, Yu Chen, Z. Chen, B. Chiaro, A. Dunsworth, I.-C. Hoi, C. Neill, P. J. J. O'Malley, C. Quintana, P. Roushan, A. Vainsencher, J. Wenner, A. N. Cleland, and John M. Martinis. State preservation by repetitive error detection in a superconducting quantum circuit. *Nature*, 519(7541):66–69, mar 2015.

[133] Julian Shaw Kelly and Evan Jeffrey. Low footprint resonator in flip chip geometry, October 8 2020. US Patent App. 16/753,431.

[134] Werner Kern. The evolution of silicon wafer cleaning technology. *Journal of The Electrochemical Society*, 137(6):1887–1892, jun 1990.

[135] Mun Dae Kim and K. Moon. Strong coupling of a cavity QED architecture for a current-biased flux qubit. *Journal of the Korean Physical Society*, 58(6):1599–1604, 2011.

[136] A Yu Kitaev. Fault-tolerant quantum computation by anyons. *Annals of Physics*, 303(1):2–30, 2003.

[137] C. Kittel. *Introduction to Solid State Physics*. Wiley, 2004.

[138] Charles Kittel and Herbert Kroemer. Thermal physics, 1998.

[139] P. Kittel, A. Kashani, J. M. Lee, and P. R. Roach. General pulse tube theory. *Cryogenics*, 36(10):849–857, 1996.

[140] Jens Koch, Terri M. Yu, Jay Gambetta, A. A. Houck, D. I. Schuster, J. Majer, Alexandre Blais, M. H. Devoret, S. M. Girvin, and R. J. Schoelkopf. Charge-insensitive qubit design derived from the cooper pair box. *Phys. Rev. A*, 76:042319, Oct 2007.

[141] Philip Krantz, Andreas Bengtsson, Michaël Simoen, Simon Gustavsson, Vitaly Shumeiko, W. D. Oliver, C. M. Wilson, Per Delsing, and Jonas Bylander. Single-shot read-out of a superconducting qubit using a Josephson parametric oscillator. *Nature Communications*, 7(May):1–8, 2016.

[142] Lasse Bjørn Kristensen, Morten Kjaergaard, Christian Kraglund Andersen, and Nikolaj Thomas Zinner. Hybrid Quantum Error Correction in Qubit Architectures. pages 1–37, 2019.

[143] Sangil Kwon, Akiyoshi Tomonaga, Gopika Lakshmi Bhai, Simon J. Devitt, and Jaw-Shen Tsai. Tutorial: Gate-based superconducting quantum computing. (July):1–54, sep 2020.

[144] Raymond Laflamme, Cesar Miquel, Juan Pablo Paz, and Wojciech Hubert Zurek. Perfect quantum error correcting code. *Phys. Rev. Lett.*, 77:198–201, Jul 1996.

[145] J. Landau, J. T. Tough, N. R. Brubaker, and D. O. Edwards. Temperature, pressure, and concentration dependence of the osmotic pressure of dilute He3-He4 mixtures. *Physical Review A*, 2(6):2472–2482, 1970.

[146] R. Landauer. Irreversibility and heat generation in the computing process. *IBM Journal of Research and Development*, 5(3):183–191, 1961.

[147] Christian Lang. Read-Out Strategies for Multi-Qubit States in Circuit Quantum Electrodynamics. 2009.

[148] T. Lanting, A. J. Berkley, B. Bumble, P. Bunyk, A. Fung, J. Johansson, A. Kaul, A. Kleinsasser, E. Ladizinsky, F. Maibaum, R. Harris, M. W. Johnson, E. Tolkacheva, and M. H.S. Amin. Geometrical dependence of the low-frequency noise in superconducting flux qubits. *Physical Review B - Condensed Matter and Materials Physics*, 79(6):1–4, 2009.

[149] Mikkel V. Larsen, Xueshi Guo, Casper R. Breum, Jonas S. Neergaard-Nielsen, and Ulrik L. Andersen. Deterministic generation of a two-dimensional cluster state. *Science*, 366(6463):369–372, 2019.

[150] Chan U Lei, Lev Krayzman, Suhas Ganjam, Luigi Frunzio, and Robert J Schoelkopf. High coherence superconducting microwave cavities with indium bump bonding. *Applied Physics Letters*, 116(15):154002, 2020.

[151] Bjoern Lekitsch, Sebastian Weidt, Austin G. Fowler, Klaus Mølmer, Simon J. Devitt, Christof Wunderlich, and Winfried K. Hensinger. Blueprint for a microwave trapped ion quantum computer. *Science Advances*, 3(2), 2017.

[152] E. Leonard, M. A. Beck, J. Nelson, B. G. Christensen, T. Thorbeck, C. Howington, A. Opremcak, I. V. Pechenezhskiy, K. Dodge, N. P. Dupuis, M. D. Hutchings, J. Ku, F. Schlenker, J. Suttle, C. Wilen, S. Zhu, M. G. Vavilov, B. L.T. Plourde, and R. McDermott. Digital Coherent Control of a Superconducting Qubit. *Physical Review Applied*, 11(1):1–13, 2019.

[153] G Lindblad. On the generators of quantum dynamical semigroups. *Communications in Mathematical Physics*, 48(2):119–130, 1976.

[154] Netanel H. Lindner and Terry Rudolph. A photonic cluster state machine gun. pages 1–10, 2008.

[155] Netanel H. Lindner and Terry Rudolph. Proposal for pulsed On-demand sources of photonic cluster state strings. *Physical Review Letters*, 103(11):1–4, 2009.

[156] Daniel Litinski. A Game of Surface Codes: Large-Scale Quantum Computing with Lattice Surgery. *Quantum*, 3(c):128, 2019.

[157] Daniel Litinski and Felix von Oppen. Lattice Surgery with a Twist: Simplifying Clifford Gates of Surface Codes. *Quantum*, 2:62, May 2018.

[158] Yanbing Liu, Srikanth J. Srinivasan, D. Hover, Shaojiang Zhu, R. McDermott, and A. A. Houck. High fidelity readout of a transmon qubit using a superconducting low-inductance undulatory galvanometer microwave amplifier. *New Journal of Physics*, 16:0–8, 2014.

[159] F. London, H. London, and Frederick Alexander Lindemann. The electromagnetic equations of the supraconductor. *Proceedings of the Royal Society of London. Series A - Mathematical and Physical Sciences*, 149(866):71–88, 1935.

[160] Andrew Lucas. Ising formulations of many NP problems. *Frontiers in Physics*, 2(February):1–14, 2014.

[161] Xin-You Lü, S Ashhab, Wei Cui, Rebing Wu, and Franco Nori. Two-qubit gate operations in superconducting circuits with strong coupling and weak anharmonicity. *New Journal of Physics*, 14(7):073041, jul 2012.

[162] P. Magnard, P. Kurpiers, B. Royer, T. Walter, J. C. Besse, S. Gasparinetti, M. Pechal, J. Heinsoo, S. Storz, A. Blais, and A. Wallraff. Fast and Unconditional All-Microwave Reset of a Superconducting Qubit. *Physical Review Letters*, 121(6):60502, 2018.

[163] François Mallet, Florian R. Ong, Agustin Palacios-Laloy, François Nguyen, Patrice Bertet, Denis Vion, and Daniel Esteve. Single-shot qubit readout in circuit quantum electrodynamics. *Nature Physics*, 5(11):791–795, 2009.

[164] B. W. Maxfield and W. L. McLean. Superconducting penetration depth of niobium. *Phys. Rev.*, 139:A1515–A1522, Aug 1965.

[165] CRH McRae, JH Béjanin, Z Pagel, AO Abdallah, TG McConkey, CT Earnest, JR Rinehart, and M Mariantoni. Thermocompression bonding technology for multilayer superconducting quantum circuits. *Applied Physics Letters*, 111(12):123501, 2017.

[166] A. Megrant, C. Neill, R. Barends, B. Chiaro, Yu Chen, L. Feigl, J. Kelly, Erik Lucero, Matteo Mariantoni, P. J. J. O'Malley, D. Sank, A. Vainsencher, J. Wenner, T. C. White, Y. Yin, J. Zhao, C. J. Palmstrøm, John M. Martinis, and A. N. Cleland. Planar superconducting resonators with internal quality factors above one million. *Applied Physics Letters*, 100(11):113510, 2012.

[167] W Meissner and R Ochsenfeld. Ein neuer Effekt bei Eintritt der Supraleitfähigkeit. *Naturwissenschaften*, 21(44):787–788, 1933.

[168] Mb Metcalfe. A new microwave resonator readout scheme for superconducting qubits. *Thesis*, 2008.

[169] Ashley Montanaro. Quantum algorithms: An overview. *npj Quantum Information*, 2(1):1–17, 2016.

[170] Satoshi Morita and Hidetoshi Nishimori. Convergence of quantum annealing with real-time Schrödinger dynamics. *Journal of the Physical Society of Japan*, 76(6):21–23, 2007.

[171] Satoshi Morita and Hidetoshi Nishimori. Mathematical foundation of quantum annealing. *Journal of Mathematical Physics*, 49(12), 2008.

[172] Sarah Mostame, Patrick Rebentrost, Alexander Eisfeld, Andrew J. Kerman, Dimitris I. Tsomokos, and Alán Aspuru-Guzik. Quantum simulator of an open quantum system using superconducting qubits: Exciton transport in photosynthetic complexes. *New Journal of Physics*, 14, 2012.

[173] Hiroto Mukai, Keiichi Sakata, Simon J Devitt, Rui Wang, Yu Zhou, Yukito Nakajima, and Jaw-Shen Tsai. Pseudo-2d superconducting quantum computing circuit for the surface code: proposal and preliminary tests. *New Journal of Physics*, 22(4):043013, apr 2020.

[174] Hiroto Mukai, Akiyoshi Tomonaga, and Jaw Shen Tsai. Superconducting quantum annealing architecture with LC resonators. *Journal of the Physical Society of Japan*, 88(6):1–6, 2019.

[175] Y Nakamura, Yu. A. Pashkin, and J. S. Tsai. Coherent control of macroscopic quantum states in a single-Cooper-pair box. *Nature*, 398(6730):786–788, apr 1999.

[176] Y. Nakamura, H. Terai, K. Inomata, T. Yamamoto, W. Qiu, and Z. Wang. Superconducting qubits consisting of epitaxially grown nbn/aln/nbn josephson junctions. *Applied Physics Letters*, 99(21):212502, 2011.

[177] C. Neill, P. Roushan, K. Kechedzhi, S. Boixo, S. V. Isakov, V. Smelyanskiy, A. Megrant, B. Chiaro, A. Dunsworth, K. Arya, R. Barends, B. Burkett, Y. Chen, Z. Chen, A. Fowler, B. Foxen, M. Giustina, R. Graff, E. Jeffrey, T. Huang, J. Kelly, P. Klimov, E. Lucero, J. Mutus, M. Neeley, C. Quintana, D. Sank, A. Vainsencher, J. Wenner, T. C. White, H. Neven, and J. M. Martinis. A blueprint for demonstrating quantum supremacy with superconducting qubits Supplementary. *Science*, 360(6385):195–199, 2018.

[178] Kae Nemoto, Michael Trupke, Simon J. Devitt, Ashley M. Stephens, Burkhard Scharfenberger, Kathrin Buczak, Tobias Nöbauer, Mark S. Everitt, Jörg Schmiedmayer, and William J. Munro. Photonic architecture for scalable quantum information processing in diamond. *Phys. Rev. X*, 4:031022, Aug 2014.

[179] Ani Nersisyan, Stefano Poletto, Nasser Alidoust, Riccardo Manenti, Russ Renzas, Cat-Vu Bui, Kim Vu, Tyler Whyland, Yuvraj Mohan, Eyob A. Sete, Sam Stanwyck, Andrew Bestwick, and Matthew Reagor. Manufacturing low dissipation superconducting quantum processors, 2019.

[180] Michael A. Nielsen. Optical quantum computation using cluster states. *Physical Review Letters*, 93(4):040503–1, 2004.

[181] Michael A. Nielsen. Cluster-state quantum computation. *Reports on Mathematical Physics*, 57(1):147–161, 2006.

[182] Michael A Nielsen and Isaac Chuang. Quantum computation and quantum information, 2002.

[183] T. Niemczyk, F. Deppe, H. Huebl, E. P. Menzel, F. Hocke, M. J. Schwarz, J. J. Garcia-Ripoll, D. Zueco, T. Hümmer, E. Solano, A. Marx, and R. Gross. Circuit quantum electrodynamics in the ultrastrong-coupling regime. *Nature Physics*, 6(10):772–776, 2010.

[184] A. A. Omar and Y. L. Chow. Coplanar Waveguide with Top and Bottom Shields in Place of Air-Bridges. *IEEE Transactions on Microwave Theory and Techniques*, 41(9):1559–1563, 1993.

[185] S. Omkar, Y. S. Teo, and H. Jeong. Resource-efficient and fault-tolerant topological quantum computation with hybrid entanglement of light. 2019.

[186] T. P. Orlando, J. E. Mooij, Lin Tian, Caspar H. Van Der Wal, L. S. Levitov, Seth Lloyd, and J. J. Mazo. Superconducting persistent-current qubit. *Physical Review B - Condensed Matter and Materials Physics*, 60(22):15398–15413, 1999.

[187] Hanhee Paik, D. I. Schuster, Lev S. Bishop, G. Kirchmair, G. Catelani, A. P. Sears, B. R. Johnson, M. J. Reagor, L. Frunzio, L. I. Glazman, S. M. Girvin, M. H. Devoret, and R. J. Schoelkopf. Observation of high coherence in josephson junction qubits measured in a three-dimensional circuit qed architecture. *Phys. Rev. Lett.*, 107:240501, Dec 2011.

[188] Alexandru Paler, Ilia Polian, Kae Nemoto, and Simon J Devitt. Fault-tolerant, high-level quantum circuits: form, compilation and description. *Quantum Science and Technology*, 2(2):025003, 2017.

[189] Z. H. Peng, Yu Xi Liu, Y. Nakamura, and J. S. Tsai. Fast generation of multiparticle entangled state for flux qubits in a circle array of transmission line resonators

with tunable coupling. *Physical Review B - Condensed Matter and Materials Physics*, 85(2):1–10, 2012.

[190] T. Peronnin, D. Marković, Q. Ficheux, and B. Huard. Sequential dispersive measurement of a superconducting qubit. *Phys. Rev. Lett.*, 124:180502, May 2020.

[191] B. Peropadre, D. Zueco, D. Porras, and J. J. García-Ripoll. Nonequilibrium and nonperturbative dynamics of ultrastrong coupling in open lines. *Physical Review Letters*, 111(24):1–5, 2013.

[192] Alex P. M. Place, Lila V. H. Rodgers, Pranav Mundada, Basil M. Smitham, Mattias Fitzpatrick, Zhaoqi Leng, Anjali Premkumar, Jacob Bryon, Sara Sussman, Guangming Cheng, Trisha Madhavan, Harshvardhan K. Babla, Berthold Jaeck, Andras Gyenis, Nan Yao, Robert J. Cava, Nathalie P. de Leon, and Andrew A. Houck. New material platform for superconducting transmon qubits with coherence times exceeding 0.3 milliseconds, 2020.

[193] B. L.T. Plourde, J. Zhang, K. B. Whaley, F. K. Wilhelm, T. L. Robertson, T. Hime, S. Linzen, P. A. Reichardt, C. E. Wu, and John Clarke. Entangling flux qubits with a bipolar dynamic inductance. *Physical Review B - Condensed Matter and Materials Physics*, 70(14):1–4, 2004.

[194] Frank Pobell. *Matter and methods at low temperatures*, volume 2. Springer, 2007.

[195] Stefan Pogorzalek, Kirill G. Fedorov, Ling Zhong, Jan Goetz, Friedrich Wulschner, Michael Fischer, Peter Eder, Edwar Xie, Kunihiro Inomata, Tsuyoshi Yamamoto, Yasunobu Nakamura, Achim Marx, Frank Deppe, and Rudolf Gross. Hysteretic flux response and nondegenerate gain of flux-driven josephson parametric amplifiers. *Physical Review Applied*, 8(2):1–10, 2017.

[196] David M Pozar. *Microwave engineering*. John wiley & sons, 2011.

[197] John Preskill. Quantum computing and the entanglement frontier. pages 1–18, 2012.

[198] John Preskill. Quantum Computing in the NISQ era and beyond. *Quantum*, 2(July):79, 2018.

[199] S. Probst, F. B. Song, P. A. Bushev, A. V. Ustinov, and M. Weides. Efficient and robust analysis of complex scattering data under noise in microwave resonators. *Review of Scientific Instruments*, 86(2), 2015.

[200] R. Raussendorf and H. J. Briegel. A one-way quantum computer. *Physical Review Letters*, 86(22):5188–5191, 2001.

[201] R. Raussendorf, J. Harrington, and K. Goyal. A fault-tolerant one-way quantum computer. *Annals of Physics*, 321(9):2242–2270, 2006.

[202] R. Raussendorf, J. Harrington, and K. Goyal. Topological fault-tolerance in cluster state quantum computation. *New Journal of Physics*, 9:1–20, 2007.

[203] Robert Raussendorf, Daniel E. Browne, and Hans J. Briegel. The one-way quantum computer - A non-network model of quantum computation. *Journal of Modern Optics*, 49(8):1299–1306, 2002.

[204] Robert Raussendorf and Jim Harrington. Fault-tolerant quantum computation with high threshold in two dimensions. *Physical Review Letters*, 98(19):1–4, 2007.

[205] Matthew Reagor, Christopher B. Osborn, Nikolas Tezak, Alexa Staley, Guenevere Prawiroatmodjo, Michael Scheer, Nasser Alidoust, Eyob A. Sete, Nicolas Didier, Marcus P. da Silva, Ezer Acala, Joel Angeles, Andrew Bestwick, Maxwell Block, Benjamin Bloom, Adam Bradley, Catvu Bui, Shane Caldwell, Lauren Capelluto, Rick Chilcott, Jeff Cordova, Genya Crossman, Michael Curtis, Saniya Deshpande, Tristan El Bouayadi, Daniel Girshovich, Sabrina Hong, Alex Hudson, Peter Karalekas, Kat Kuang, Michael Lenihan, Riccardo Manenti, Thomas Manning, Jayss Marshall, Yuvraj Mohan, William O'Brien, Johannes Otterbach, Alexander Papageorge, Jean-Philip Paquette, Michael Pelstring, Anthony Polloreno, Vijay Rawat, Colm A. Ryan, Russ Renzas, Nick Rubin, Damon Russel, Michael Rust, Diego Scarabelli, Michael Selvanayagam, Rodney Sinclair, Robert Smith, Mark Suska, Ting-Wai To, Mehrnoosh Vahidpour, Nagesh Vodrahalli, Tyler Whyland, Kamal Yadav, William Zeng, and Chad T. Rigetti. Demonstration of universal parametric entangling gates on a multi-qubit lattice. *Science Advances*, 4(2):eaao3603, feb 2018.

[206] T. L. Robertson, B. L.T. Plourde, T. Hime, S. Linzen, P. A. Reichardt, F. K. Wilhelm, and John Clarke. Superconducting quantum interference device with frequency-dependent damping: Readout of flux qubits. *Physical Review B - Condensed Matter and Materials Physics*, 72(2):1–9, 2005.

[207] Christoph Roch, Thomy Phan, Sebastian Feld, Robert Müller, Thomas Gabor, and Claudia Linnhoff-Popien. A Quantum Annealing Algorithm for Finding Pure Nash Equilibria in Graphical Games. 2019.

[208] Jérémie Roland and Nicolas J. Cerf. Quantum search by local adiabatic evolution. *Physical Review A - Atomic, Molecular, and Optical Physics*, 65(4):6, 2002.

[209] D. Rosenberg, D. Kim, R. Das, D. Yost, S. Gustavsson, D. Hover, P. Krantz, A. Melville, L. Racz, G. O. Samach, S. J. Weber, F. Yan, J. L. Yoder, A. J. Kerman, and W. D. Oliver. 3d integrated superconducting qubits. *npj Quantum Information*, 3(1):42, October 2017.

[210] D Rosenberg, D Kim, R Das, D Yost, S Gustavsson, D Hover, P Krantz, A Melville, L Racz, GO Samach, et al. 3d integrated superconducting qubits. *npj quantum information*, 3(1):1–5, 2017.

[211] Danna Rosenberg, Steven J Weber, David Conway, Donna-Ruth W Yost, Justin Mallek, Gregory Calusine, Rabindra Das, David Kim, Mollie E Schwartz, Wayne Woods, et al. Solid-state qubits: 3d integration and packaging. *IEEE Microwave Magazine*, 21(8):72–85, 2020.

[212] Sami Rosenblatt, Jason S Orcutt, Martin O Sandberg, Markus Brink, Vivekananda P Adiga, and Nicholas T Bronn. Flip chip integration on qubit chips, July 16 2019. US Patent 10,355,193.

[213] Yves Salathé, Philipp Kurpiers, Thomas Karg, Christian Lang, Christian Kraglund Andersen, Abdulkadir Akin, Sebastian Krinner, Christopher Eichler, and Andreas Wallraff. Low-Latency Digital Signal Processing for Feedback and Feedforward in Quantum Computing and Communication. *Physical Review Applied*, 9(3):1–22, 2018.

[214] Anssi Salmela, Alexander Sebedash, Juho Rysti, Elias Pentti, and Juha Tuoriniemi. Osmotic pressure of He3/He4 mixtures at the crystallization pressure and at millikelvin temperatures. *Physical Review B - Condensed Matter and Materials Physics*, 83(13):1–8, 2011.

[215] Martin Sandberg, Michael R. Vissers, Jeffrey S. Kline, Martin Weides, Jiansong Gao, David S. Wisbey, and David P. Pappas. Etch induced microwave losses in titanium nitride superconducting resonators. *Applied Physics Letters*, 100(26):262605, 2012.

[216] J. A. Schreier, A. A. Houck, Jens Koch, D. I. Schuster, B. R. Johnson, J. M. Chow, J. M. Gambetta, J. Majer, L. Frunzio, M. H. Devoret, S. M. Girvin, and R. J. Schoelkopf. Suppressing charge noise decoherence in superconducting charge qubits. *Phys. Rev. B*, 77:180502, May 2008.

[217] P. Seligmann, D. O. Edwards, R. E. Sarwinski, and J. T. Tough. Heat of mixing and ground-state energy of liquid He3-He4 mixtures. *Physical Review*, 181(1):415–423, 1969.

[218] P. W. Shor. Algorithms for quantum computation: discrete logarithms and factoring. In *Proceedings 35th Annual Symposium on Foundations of Computer Science*, pages 124–134, 1994.

[219] Peter W. Shor. Scheme for reducing decoherence in quantum computer memory. *Phys. Rev. A*, 52:R2493–R2496, Oct 1995.

[220] Andrew Steane. Multiple-particle interference and quantum error correction. *Proceedings of the Royal Society A: Mathematical, Physical and Engineering Sciences*, 452(1954):2551–2577, 1996.

[221] Matthias Steffen, M. Ansmann, R. McDermott, N. Katz, Radoslaw C. Bialczak, Erik Lucero, Matthew Neeley, E. M. Weig, A. N. Cleland, and John M. Martinis. State tomography of capacitively shunted phase qubits with high fidelity. *Phys. Rev. Lett.*, 97:050502, Aug 2006.

[222] Cerebras Systems. The cerebras wafer scale engine: https://www.cerebras.net/, 2019.

[223] Maika Takita, Andrew W. Cross, A. D. Córcoles, Jerry M. Chow, and Jay M. Gambetta. Experimental demonstration of fault-tolerant state preparation with superconducting qubits. *Physical Review Letters*, 119(18), oct 2017.

[224] M. Tinkham. *Introduction to Superconductivity*. Dover Books on Physics Series. Dover Publications, 2004.

[225] Yu Tomita and Krysta M. Svore. Low-distance surface codes under realistic quantum noise. *Physical Review A - Atomic, Molecular, and Optical Physics*, 90(6), 2014.

[226] A Torgovkin, S Chaudhuri, A Ruhtinas, M Lahtinen, T Sajavaara, and I J Maasilta. High quality superconducting titanium nitride thin film growth using infrared pulsed laser deposition. *Superconductor Science and Technology*, 31(5):055017, apr 2018.

[227] Dimitris I. Tsomokos, Sahel Ashhab, and Franco Nori. Using superconducting qubit circuits to engineer exotic lattice systems. *Phys. Rev. A*, 82:052311, Nov 2010.

[228] Mehrnoosh Vahidpour, William O'Brien, Jon Tyler Whyland, Joel Angeles, Jayss Marshall, Diego Scarabelli, Genya Crossman, Kamal Yadav, Yuvraj Mohan, Catvu Bui, Vijay Rawat, Russ Renzas, Nagesh Vodrahalli, Andrew Bestwick, and Chad Rigetti. Superconducting through-silicon vias for quantum integrated circuits, 2017.

[229] A. Wallraff, D. I. Schuster, A. Blais, L. Frunzio, J. Majer, M. H. Devoret, S. M. Girvin, and R. J. Schoelkopf. Approaching unit visibility for control of a superconducting qubit with dispersive readout. *Physical Review Letters*, 95(6):1–4, 2005.

[230] Steven J. Weber, Gabriel O. Samach, David Hover, Simon Gustavsson, David K. Kim, Alexander Melville, Danna Rosenberg, Adam P. Sears, Fei Yan, Jonilyn L. Yoder, William D. Oliver, and Andrew J. Kerman. Coherent Coupled Qubits for Quantum Annealing. *Physical Review Applied*, 8(1):1–13, 2017.

[231] Dave Wecker, Bela Bauer, Bryan K. Clark, Matthew B. Hastings, and Matthias Troyer. Gate-count estimates for performing quantum chemistry on small quantum computers. *Physical Review A - Atomic, Molecular, and Optical Physics*, 90(2):1–13, 2014.

[232] Zack Weinstein, Gerardo Ortiz, and Zohar Nussinov. Universality Classes of Stabilizer Code Hamiltonians. (1), 2019.

[233] James D. Whitfield, Jacob Biamonte, and Alan Aspuru-Guzik. Simulation of electronic structure Hamiltonians using quantum computers. *Molecular Physics*, 109(5):735–750, 2011.

[234] John Wilks and David Sheridan Betts. An introduction to liquid helium. 2. 1987.

[235] Patrick Winkel, Kiril Borisov, Lukas Grünhaupt, Dennis Rieger, Martin Spiecker, Francesco Valenti, Alexey V. Ustinov, Wolfgang Wernsdorfer, and Ioan M. Pop. Implementation of a transmon qubit using superconducting granular aluminum. *Phys. Rev. X*, 10:031032, Aug 2020.

[236] Christopher J. Wood and Jay M. Gambetta. Quantification and characterization of leakage errors. *Physical Review A*, 97(3):032306, March 2018.

[237] William K Wootters and Wojciech H Zurek. A single quantum cannot be cloned. *Nature*, 299(5886):802–803, 1982.

[238] X. Wu, J. L. Long, H. S. Ku, R. E. Lake, M. Bal, and D. P. Pappas. Overlap junctions for high coherence superconducting qubits. *Applied Physics Letters*, 111(3):032602, 2017.

[239] Friedrich Wulschner, Jan Goetz, Fabian R. Koessel, Elisabeth Hoffmann, Alexander Baust, Peter Eder, Michael Fischer, Max Haeberlein, Manuel J. Schwarz, Matthias Pernpeintner, Edwar Xie, Ling Zhong, Christoph W. Zollitsch, Borja Peropadre, Juan Jose Garcia Ripoll, Enrique Solano, Kirill G. Fedorov, Edwin P. Menzel, Frank Deppe, Achim Marx, and Rudolf Gross. Tunable coupling of transmission-line microwave resonators mediated by an rf SQUID. *EPJ Quantum Technology*, 3(1), 2016.

[240] Wenhu Xu, Xin Zhao, and Guilu Long. Efficient generation of multi-photon W states by joint-measurement. *Progress in Natural Science*, 18(1):119–122, 2008.

[241] T. Yamamoto, K. Inomata, K. Koshino, P. M. Billangeon, Y. Nakamura, and J. S. Tsai. Superconducting flux qubit capacitively coupled to an LC resonator. *New Journal of Physics*, 16:1–23, 2014.

[242] Fei Yan, Philip Krantz, Youngkyu Sung, Morten Kjaergaard, Daniel L. Campbell, Terry P. Orlando, Simon Gustavsson, and William D. Oliver. Tunable Coupling Scheme for Implementing High-Fidelity Two-Qubit Gates. *Physical Review Applied*, 10(5):1, 2018.

[243] A Chi-Chih Yao. Quantum circuit complexity. In *Proceedings of 1993 IEEE 34th Annual Foundations of Computer Science*, pages 352–361. IEEE, 1993.

[244] Biaoliang Ye, Zhen Fei Zheng, and Chui Ping Yang. Multiplex-controlled phase gate with qubits distributed in a multicavity system. *Physical Review A*, 97(6):30–33, 2018.

[245] F. Yoshihara, K. Harrabi, A. O. Niskanen, Y. Nakamura, and J. S. Tsai. Decoherence of flux qubits due to $1/f$ flux noise. *Phys. Rev. Lett.*, 97:167001, Oct 2006.

[246] Fumiki Yoshihara, Tomoko Fuse, Sahel Ashhab, Kosuke Kakuyanagi, Shiro Saito, and Kouichi Semba. Superconducting qubit-oscillator circuit beyond the ultrastrong-coupling regime Supplimental. *Nature Physics*, 13(1):44–47, 2017.

[247] Donna-Ruth W Yost, Mollie E Schwartz, Justin Mallek, Danna Rosenberg, Corey Stull, Jonilyn L Yoder, Greg Calusine, Matt Cook, Rabindra Das, Alexandra L Day, et al. Solid-state qubits integrated with superconducting through-silicon vias. *npj Quantum Information*, 6(1):1–7, 2020.

[248] Yiqing Zhou, E. Miles Stoudenmire, and Xavier Waintal. What limits the simulation of quantum computers? *arXiv*, 10(4):41038, 2020.

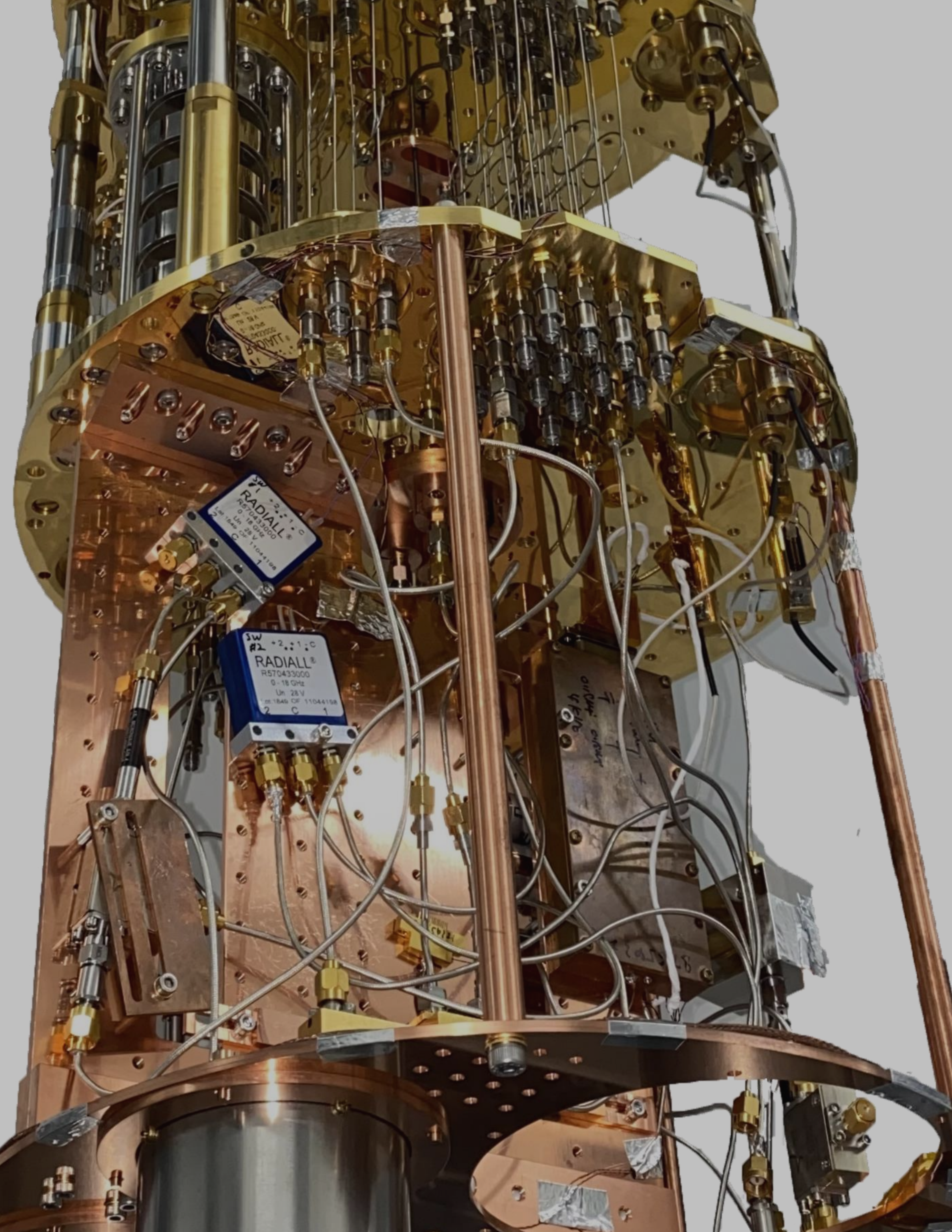
SW #1
RADIALL®
R570433000
0 - 18 GHz
Un: 28 V
2 C 1
SW #2
RADIALL®
R570433000
0 - 18 GHz
Un: 28 V
Lot 1849 OF 11044198
2 C 1